STRONG LIGHT-MATTER COUPLING IN ORGANIC MICROCAVITIES:

INVESTIGATING THE FUNDAMENTAL PRINCIPLES OF STRONG COUPLING IN STRONGLY DISORDERED MATERIALS EXPERIMENTALLY

Laura Christine Tropf

A Thesis Submitted for the Degree of PhD
at the
University of St Andrews

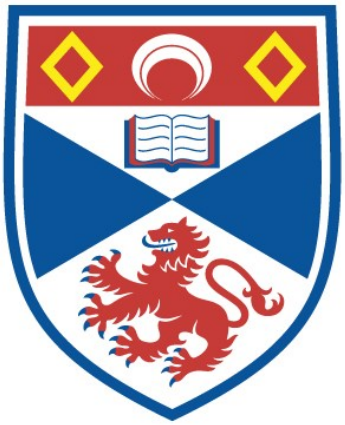

2019

Strong light–matter coupling in organic microcavities

Investigating the fundamental principles of strong coupling in strongly disordered materials experimentally

by

Laura Christine Tropf

University of
St Andrews

This thesis is submitted in partial fulfilment for the degree of Doctor of Philosophy (PhD) at the University of St Andrews

November 2018

Abstract

Strong light–matter coupling gives rise to intriguing possibilities like Bose-Einstein condensation at room temperature. In this context, organic semiconductors are particularly attractive because they combine large oscillator strengths with high exciton binding energies and thus readily enable large light–matter coupling strengths up to room temperature. Yet, in these commonly strongly disordered materials, the applicability of fundamental predictions developed for systems of high order needs to be verified.

Hence, the validity of the theoretically predicted form of the coupling strength and of the coupled oscillator model is tested for strongly coupled organic microcavities in this thesis. Experimental investigations of metal-clad microcavities confirm the coupling strength to be proportional to the electric field with which the excitons interact and to the square root both of the oscillator strength of the material and of the number of chromophores inside the microcavity. Systematically varying these parameters demonstrates a non-zero threshold for the onset of the strong coupling regime for the first time, which confirms the applicability of the coupled oscillator model also for strongly disordered systems.

Moreover, the effect of the coupling strength on the photoluminescence from organic microcavities is investigated. For metal-clad cavities, but not for microcavities with dielectric mirrors, an increase of the luminescence intensity with increasing coupling strength was found. For the latter system, a systematic study aimed to determine the properties of the cavity and of the organic material which are crucial for polariton lasing. However, experiments did not yield polariton lasing, for which two potential reasons are identified: (1) the vanishing of modes close to resonance and (2) pronounced bimolecular quenching in the studied material. Since organic microcavities are complex, systematic studies as presented in this thesis are an important step towards a more profound understanding of organic polaritons.

Declarations

Candidate's declaration

I, Laura Christine Tropf, do hereby certify that this thesis, submitted for the degree of PhD, which is approximately 50,000 words in length, has been written by me, and that it is the record of work carried out by me, or principally by myself in collaboration with others as acknowledged, and that it has not been submitted in any previous application for any degree.

I was admitted as a research student at the University of St Andrews in August 2014.

I received funding from an organisation or institution and have acknowledged the funder in the full text of my thesis.

Date Laura Tropf

Supervisor's declaration

I hereby certify that the candidate has fulfilled the conditions of the Resolution and Regulations appropriate for the degree of PhD in the University of St Andrews and that the candidate is qualified to submit this thesis in application for that degree.

Date Malte C. Gather

Permission for publication

In submitting this thesis to the University of St Andrews we understand that we are giving permission for it to be made available for use in accordance with the regulations of the Uni-

versity Library for the time being in force, subject to any copyright vested in the work not being affected thereby. We also understand, unless exempt by an award of an embargo as requested below, that the title and the abstract will be published, and that a copy of the work may be made and supplied to any bona fide library or research worker, that this thesis will be electronically accessible for personal or research use and that the library has the right to migrate this thesis into new electronic forms as required to ensure continued access to the thesis.

I, Laura Christine Tropf, confirm that I have obtained third-party copyright permissions that are required.

The following is an agreed request by candidate and supervisor regarding the publication of this thesis:

Printed copy

No embargo on print copy.

Electronic copy

No embargo on electronic copy.

Date Laura Tropf

Date Malte C. Gather

Underpinning Research Data or Digital Outputs

Candidate's declaration

I, Laura Christine Tropf, understand that by declaring that I have original research data or digital outputs, I should make every effort in meeting the University's and research funders' requirements on the deposit and sharing of research data or research digital outputs.

Date Laura Tropf

Permission for publication of underpinning research data or digital outputs

We understand that for any original research data or digital outputs which are deposited, we are giving permission for them to be made available for use in accordance with the requirements of the University and research funders, for the time being in force.

We also understand that the title and the description will be published, and that the underpinning research data or digital outputs will be electronically accessible for use in accordance with the license specified at the point of deposit, unless exempt by award of an embargo as requested below.

The following is an agreed request by candidate and supervisor regarding the publication of underpinning research data or digital outputs:

No embargo on on underpinning research data or digital outputs.

Date Laura Tropf

Date Malte C. Gather

Acknowledgements

Acknowledgements

Reflecting on the support I received during my PhD in many different ways, I realised how lucky I have been to be surrounded by so many helpful individuals. This section is too short to mention everyone who contributed to the friendly, collaborative base I could build on, so that I restrict myself to the people whose contributions I deem most important.

First of all, I want to thank Malte C. Gather for 'adopting' me three months into my project and starting the journey into strong-coupling science together with me. I am grateful for many long discussions about my work and the freedom I have had to take 'my polaritons' wherever I wanted. I have learned a lot about scientific method and strategy from you, Malte, and have always appreciated the efforts you make for creating a positive working environment in the group.

I also thank Jonathan Keeling for inspiring discussions and for sparing time to clarify my understanding of polaritons. In particular, I am indebted to Jonathan for bringing my attention to the non-zero threshold that should exist for the strong coupling regime. Moreover, I acknowledge Sven Höfling and Ifor D. W. Samuel for setting me off when I started my PhD and Christof P. Dietrich for introducing me to polaritons. I often—especially but not only in the beginning—relied on members of Ifor's group to perform measurements with me.

On the more technical side, the understanding of an experimentalist of their samples is often limited by the ways they can investigate them. There is a list of people I wish to thank because they have helped me overcome these limits by taking time to introduce me to a method or to investigate my samples with me: Sai K. Rajendran (fs-pump and cryogenic measurements), M. Tariq Sajjad (TCSPC measurements), Mingzhou Chen (Raman spectroscopy), Markus Karl

(maintenance and improvement of the biolaser setup), Nils M. Kronenberg (AFM measurements) and Marcel Schubert (last-minute re-investigations).

I am grateful to all the people in the School of Physics and Astronomy who contribute to make it the open and supportive workplace it is. My particular thanks goes to all present and former members of the Gather Lab, who have given me insight into the (for me) new field of bio-physics. I have valued the good working atmosphere and many constructive discussions during group meetings and lunch breaks. Furthermore, I thank all the administrative, technical and service staff of the School. Specifically, I am indebted to the administrative team of the CM-CDT—Julie Massey, Christine Edwards, Wendy Clark and Debra Thompson—for sorting out all small and big hiccups I encountered during my PhD and the technicians of the clean room—Callum Smith and Graeme Beaton—for never giving up on the sputterer and providing prompt fixes for urgent issues.

Finally and beside the scientific realm, thank you, everyone—i.e., people from the CM-CDT and the group, from tango, from the chorus and Transition,...—who has made my St Andrews experience so positive! In particular, thank you Max, Francisco, Maria and Nils, for spicing up my Swabian negativity with French sarcasm, Mexican warm-heartedness and Rhenish 'Frohmut'—time spent with you made me forget even the worst misbehaviour of the sputterer. Nils, I cannot thank you enough for your support in countless ways: you were never tired of discussing my data, helped me in the final phase by acting as my locistics manager and thorough proof reader and most importantly, you recharged me by simply being there with all your kindness and enthusiasm for all sorts of adventures. Last but not least, Mama, Papa, Jonas, Theresa and Kati: you always believed in me, encouraged me and shared my triumphs as well as my sorrows. I could not have made it to this point without the long-distance encouragement I received from you.

Funding Sources

This work was supported by the Engineering and Physical Sciences Research Council [grant number EP/L015110/1].

Research Data/Digital Outputs Access Statement

Research data underpinning this thesis are available at https://doi.org/10.17630/d0e6f5c4-bf95-464c-aa6d-534a481bc5fe.

Publications

1. Christof P. Dietrich, Anja Steude, Laura Tropf, Marcel Schubert, Nils M. Kronenberg, Kai Ostermann, Sven Höfling and Malte C. Gather. "An Exciton-Polariton Laser Based on Biologically Produced Fluorescent Protein", *Science Advances* **2**, e1600666 (2016).

2. Arko Graf, Laura Tropf, Yuriy Zakharko, Jana Zaumseil and Malte C. Gather. "Near-Infrared Exciton-Polaritons in Strongly Coupled Single-Walled Carbon Nanotube Microcavities", *Nature Communications* **7**, 13078 (2016).

3. Laura Tropf, Christof P. Dietrich, Stefanie Herbst, Alexander L. Kanibolotsky, Peter J. Skabara, Frank Würthner, Ifor D. W. Samuel, Malte C. Gather and Sven Höfling. "Influence of Optical Material Properties on Strong Coupling in Organic Semiconductor Based Microcavities", *Applied Physics Letters* **110**, 153302 (2017).

4. Arko Graf, Martin Held, Yuriy Zakharko, Laura Tropf, Malte C. Gather and Jana Zaumseil. "Electrical Pumping and Tuning of Exciton-Polaritons in Carbon Nanotube Microcavities", *Nature Materials* **16**, 911–917 (2017).

5. Martin Held, Arko Graf, Yuriy Zakharko, Pengning Chao, Laura Tropf, Malte C. Gather and Jana Zaumseil. "Ultrastrong Coupling of Electrically Pumped Near-Infrared Exciton-Polaritons in High Mobility Polymers", *Advanced Optical Materials* **6**, 1700962 (2018).

6. Laura Tropf and Malte C. Gather. "Investigating the Onset of the Strong Coupling Regime by Fine-Tuning the Rabi Splitting in Multilayer Organic Microcavities", *Advanced Optical Materials* **6**, 1800203 (2018).

7. Arko Graf, Laura Tropf, Jana Zaumseil and Malte C. Gather. "Strong light-matter interactions and exciton-polaritons in organic materials", Chapter 9 in "Handbook of organic materials for electronic and photonic devices", Woodhead Publishing, Elsevier, 2019.

Contents

List of Figures

List of Tables

1 Introduction

The reason why we can see or feel the warmth of the sun on our skin is that light interacts with matter, i.e., photons in the visible or infrared spectral range are absorbed by the receptors of our eyes or heat up the water molecules in our body.[1] The interaction between matter and light also enables plants to photosynthesise and is thus essential for most forms of life on this planet. From a scientific point of view, the interaction between light and matter gives rise to fascinating phenomena like the photo-electric effect[2,3] or lasers,[4,5] which over the last century have transformed the way we understand and use physics. Moreover, by exploiting the interaction, oranisations like the European Union aim to tackle the energy problem, thus bringing devices like solar cells and energy-efficient light-emitting devices into our every-day lives.[6,7]

Realising that the interaction of matter and light is in fact a ubiquitous phenomenon, one might ask in which way the *strong* light–matter coupling studied in this thesis differs from the previously discussed situations. All kinds of light–matter interaction involve the exchange of energy between light and matter. In the conventional scenario, the energy that is transferred

from photons to matter by absorption of light can excite particles which may then for example generate a current in a device. However, the interaction can also slightly change the properties of either the light or the matter, which is then called the coupled regime. For instance in lasers, the majority of excited particles emits into a single mode (or a few modes) of a broad gain spectrum. By contrast, strong light–matter coupling goes beyond 'slightly changing' the properties of interaction partners. Instead, it represents a regime where the two constituents of the coupled system, light and matter, can no longer be separated. Formally, this means that the coupled regime can no longer be adequately described by the isolated eigenstates of light and matter, which will be explained further below. Instead, new eigenstates arise, so-called polaritons, which are a mix between light and matter.

It is well-known from classical physics that interaction can lead to new eigenmodes of a coupled system. For instance, when two pendula of the same resonance frequency are coupled by a string, they will no longer oscillate at the same frequency as each individual, uncoupled pendulum would. Instead, the coupled system can be observed to oscillate at two new frequencies, one being faster than the uncoupled frequency, the other being slower.[8] Moreover, an oscillatory transfer of energy from one pendulum onto the other pendulum and back will occur (at the slow frequency). In order to gain some understanding from this mechanical analogue, three aspects of the light–matter system need to be clarified: (1) In what way do light and matter correspond to harmonic oscillators? (2) How do light and matter couple? (3) What is the consequence of the strong coupling for the system of polaritons? These questions will be answered in the following.

In order to answer the first question, it is necessary to specify the light–matter system further. For the light part, consider a photon confined between two mirrors. Due to self-interference, the photon can propagate in this so-called microcavity only if the length of the cavity equals an integer number of half wavelengths of the photon. If this condition is fulfilled, the energy of the cavity photon is called its eigenenergy. In order for the matter part to be able to interact with the photon, it should consist of a two-level system (or two levels of a multi-level system), which is occupied by electrons. This criterion is met for example by excitons, which are bound electron–hole pairs. In organic semiconductors, which are investigated in this thesis, the energy levels correspond to molecular orbitals. Here, the lowest excitation of the molecule leaves the highest occupied orbital electron-deficient (or populated with a hole) and transfers the electron to the lowest unoccupied orbital. The eigenenergy of the exciton is

then the energy difference between the ground state and the excited state of the molecule. The cavity photon and the exciton are thus analogous to mechanical oscillators in that they have eigenenergies, similar to the resonance frequencies of the pendula. This system—a microcavity filled with an organic semiconductor—will henceforth be referred to as organic microcavity.

The interaction between light and matter occurs via dipole interaction. When cavity photon and exciton are on resonance, the organic films can absorb a photon to generate an exciton. Likewise, the relaxation of an exciton will result in the emission of light at the energy of the cavity photon. The reason for the uniqueness of the strong coupling regime is that the exchange of energy between light and matter is coherent. This means that (1) the exchange of light and matter happens at a fixed frequency, the Rabi frequency, which is dictated by the coupling strength between photon and exciton; and (2) when there is more than one exciton present in the microcavity, the exchange will happen collectively, i.e., all excitons will be excited (and relax again) at the same time. The latter is reminiscent of all the energy of one pendulum being transferred to the other and vice versa. As a consequence of the strong light–matter coupling, the properties of the polaritons will be a mix of light and matter, which gives rise to an unusual combination of material properties for these mixed light–matter particles. The coupled system will also have new eigenenergies—one being lower and the other being higher than the eigenenergies of the uncoupled photon and exciton. The energy difference between the two new states is called the Rabi splitting and is a key characteristic of the strong coupling regime.

Note that strong light–matter interaction is not limited to the interaction of photons with excitons in organic microcavities, as specified above. Although the focus of the presented work is on exciton–polaritons, the matter part of polaritons is not restricted to excitons; light can also strongly couple to surface plasmons, to phonons in crystals or to vibronic modes of molecules.[9–13] In fact, the Rabi splittings predicted and observed in microcavities in the 1980s used ultra-cold ($T < 5$ K) Rydberg atoms as matter component.[14–16] Here, the collapse and revival of the Rabi oscillations was demonstrated in very complex and advanced experiments, which were necessary for the control of the atoms, including superconducting microcavities. The next step to facilitating the observation of microcavity polaritons was to use excitons of quantum wells in inorganic semiconductors in 1992 by Weisbuch *et al.* [17]: here, the entire cavity–exciton system could be reduced to one monolithic heterostructure of inorganic semiconducting layers and already the first experiments showed polaritons at $T = 20 \ldots 77$ K.

Even though the temperature for the observation of polaritons was soon after increased to room temperature,[18] the first observation of a Rabi splitting in organic semiconductors by Lidzey *et al.* [19] in 1998 was a break-through in several regards: (1) Due to the large oscillator strengths of organic materials, the Rabi splitting was increased with respect to inorganic exciton polaritons by an order of magnitude. This reduced the demands for the Q-factors of the microcavities, which, together with the large binding energies of organic excitons, greatly facilitated the generation and observation of polaritons. (2) Organic semiconductors represent a huge class of light-emitting materials, which is renowned for its tunability and the relative ease of device fabrication.[20]

This long—though by far not exhausting—list of experiments on exciton–polaritons in microcavities raises the question where the fascination with polaritons stems from and why one would want to study organic polaritons in particular. The answer to both questions is two-fold, since polaritons (organic or not) are attractive with respect to both fundamental research and potentially arising applications.

On the one hand, exciton–polaritons are an ideal platform to study non-equilibrium physics with nonlinearities, which originate from polaritonic interaction. For instance, the nonlinearities give rise to phenomena known from non-linear optics, like bistabilities and solitons, which can now be observed in polaritons.[21–23] Moreover, the combination of these non-linearities with the bosonic character of exciton–polaritons allows for their condensation,[24,25] and due to the light mass of these mixed light–matter particles, this can even persist up to room temperature.[26,27] The driven–dissipative nature of this system allows for investigating out-of-equilibrium condensates and leads to inherent instabilities.[28–33] Using organic materials for the excitonic part adds another level of complexity to the system, owing to the disorder and the vibronic progression in these materials. In this context, the extensive tunability of organic microcavities makes them an ideal platform to study these complex systems.

On the other hand, there are several ways in which the strong coupling regime could lead to new devices or improve existing ones. While some of the applications arise from general properties of polaritons, like using polaritons for quantum simulators,[34] the discussion here will focus on the practical consequences of organic polaritons in particular. There are mainly three aspects of polaritons which could potentially be exploited in devices with organic materials: the coherence and delocalisation of the coupled excited states, the shift in energy states

upon strong coupling and the lower threshold of polariton lasing compared to photon lasing. The coherence of polariton states could improve devices by e.g. increasing the exciton conductivity,[35,36] or even the conductivity of charges,[37] even though the latter findings have not been unanimously confirmed.[38,39] The delocalisation of the excitation has also been demonstrated to enable more efficient energy transfer between different exciton species in a microcavity[40] or to increase the luminescence quantum yield of organic materials[41] albeit not in all experiments.[42,43] The shift of energy levels when transitioning from weakly to strongly coupled systems could be used in polaritonic chemistry or organic electronics. For example, the control of photo-chemical reactions via interaction with light has been shown,[44,45] which could be useful e.g. for the design of catalysts.[46,47] The possibility to tune energy levels could also enhance organic electronic devices, for example exploiting singlet fission processes or by harvesting triplet states.[48–51] Furthermore, the tunable emission with low angular dispersion, which is found in microcavities with very large coupling strengths, could be of interest for devices where high purity of colour is required even at large angles.[52,53] Finally, polariton condensation is predicted and demonstrated to occur at lower thresholds than photon lasing.[25,54] This lower threshold has raised hopes in the organic community to realise an electrically driven, organic (polariton) laser—a long-standing and so far elusive goal. Even though the efficiency of final devices is low as of yet,[55,56] the microcavity system is considered promising due to the extensive control, which offers new possibilities for optimising devices.[39,57–59]

However appealing potential applications of organic polaritons may appear, an optimisation of devices is only possible once the fundamental properties of the exploited phenomenon are thoroughly understood. Although the research of the last 20 years has shed light on many aspects of organic polaritons, there are still numerous questions to be answered. For example, even though polariton lasing has been demonstrated in a variety of different organic materials to date,[27,60–63] there is no conclusive picture as to which properties of the system are critical for achieving polariton lasing. Moreover, most reports of strongly coupled, organic systems use the coupled oscillator model for analysing the coupling properties.[27,59–67] Yet, the coupled oscillator model has been proven to yield ambiguous results in the presence of disorder in the material,[68,69] so that its applicability to strongly coupled organic microcavities should be verified. Similarly, the coupling strength is assumed to follow a very simple form, being proportional to the electric field and to the square root of the number of absorbers, of the oscillator strength and of the inverse mode volume.[70] The validity of this form has been tested

and confirmed for organic semiconductors.[19,42,50,71,72] However, all these investigations use an organic material of particularly low disorder (a J-aggregate) and identify the Rabi splitting with the coupling strength. Thus, the reports do not probe regimes of large disorder that would be expected for most organic semiconductors and ignore the difference between the Rabi splitting and the coupling strength that is predicted by the coupled oscillator model.

Therefore, this thesis studies the fundamental properties of organic polaritons using materials that show the key signatures of many organic materials, i.e. large disorder-broadening and a vibronic progression. The first set of experiments investigates the coupling strength in metal-clad microcavities as a function of different parameters of the uncoupled system (Chapter 4). By studying different materials in microcavities and by changing the thickness of the organic film and its position inside a microcavity, the form of the coupling strength is confirmed to be proportional to the electric field and to the square root of the oscillator strength of the material and of the number of absorbers. These investigations also allowed to validate the coupled oscillator model by demonstrating a non-zero threshold for the onset of the strong coupling regime on the same order of magnitude as the losses of the system. Moreover, the luminescence from microcavities—with metallic and dielectric mirrors—is studied (Chapter 5). On the one hand, a highly tunable microcavity system is aimed to be optimised for polariton condensation, although not successfully. On the other hand, the photoluminescence intensity of weakly and strongly coupled microcavities is compared. While the results of microcavities with dielectric mirrors do not show any enhancement in photoluminescence intensity, a continuous enhancement with coupling strength is observed in metal-clad microcavities.

This thesis is structured as follows. After explaining the theoretical background (Chapter 2), the methods which were used to perform the experiments of this thesis are explained in Chapter 3. Chapter 4 is based on the work published in Tropf *et al.* [73] (Chapter 4.1) and in Tropf & Gather [74] (Chapter 4.2), i.e., on the work investigating the validity of the form of the coupling strength and of the coupled oscillator model as detailed above. The following chapter (5) then presents investigations of the luminescence of strongly coupled microcavities. After the characterisation of the photoluminescence from uncoupled, organic films (Chapter 5.1), Chapter 5.2 turns to the experimental challenges which were faced when optimising the microcavity for polariton lasing and Chapter 5.3 discusses the measured photoluminescence intensity for samples with different light–matter coupling strengths. The final chapter, Chapter 6, then summarises the main results and provides an outlook.

2

Theoretical background

This chapter provides the background knowledge for the experiments in this thesis. To understand an organic microcavity in the strong coupling regime, we first need to understand the uncoupled parts of the system, i.e., the exciton of the organic material (2.1) and the cavity photon (2.2). After that, light–matter coupling will be discussed in the weak (2.3) and in the strong coupling limits (2.4). In the strong-coupling regime, particular focus will be on the peculiarities of organic microcavities like the difference to inorganic microcavities and the prevailing disorder.

2.1 Organic semiconductors

Organic semiconductors are a subgroup of carbon-based molecules that are able to conduct charges at finite resistance. The origin of the semiconducting nature differs significantly from that observed in inorganic semiconductors, despite the similarity of name. In inorganic materials, semiconductivity arises from thermal excitation of charge carriers into the conduction band, which extends over the entire crystal. In organic semiconductors, semiconductivity

originates from extended, molecular orbitals, which are delocalised over one molecular unit. Because electron transfer between molecules is governed by incoherent hopping, coherent electron transport does not extend over the entire film. Electronic excitation or relaxation of the molecule is concomitant with the absorption or emission of a photon, which is why organic semiconductors can be used for photovoltaics as well as organic light emitting devices.
This section will look at aspects of organic semiconductors which are relevant for their coupling to light and it is based on the descriptions in Köhler & Bässler [75], Demtröder [76], and Riedel [77]. For this, first the origin of the energetic states of organic semiconductors and their distribution will be explained. Then, the transition between the states and the dynamics thereof will be discussed.

2.1.1 Properties from structural considerations

This section first describes the electronic structure of organic molecules and how this can result in semiconductivity at certain conditions. The second part distinguishes several types of organic semiconductors with distinct properties, which differ in their structure on a molecular level or in their arrangement within a film.

2.1.1.1 Electronic structure: the origin of semiconductivity in organic materials

Molecules are stable when the electron distributions of the atoms can be rearranged in a way to lower the energy of the multi-atom system. Two aspects of this rearrangement can lower the total energy. First, when atoms come into close proximity, their electron orbitals overlap and the charge density between the nuclei can be increased. In that case, the increased Coulomb attraction lowers the potential energy of the system. Second, the formation of molecular orbitals can result in a delocalisation of the electrons. It follows from the Heisenberg uncertainty relation that this delocalisation reduces the uncertainty of the momentum and hence the mean kinetic energy of the electrons, $\langle E_{\mathrm{kin}} \rangle = \frac{\langle p^2 \rangle}{2m_0}$.

Whether or not molecular orbitals form depends on whether or not the formation of molecular orbitals is energetically favourable. Figure 2.1 illustrates how the outer-most electronic wave functions of the atoms, which can have positive (yellow) or negative (grey) values, can interfere according to the linear combination of atomic orbitals (LCAO), here shown for the example of a diatomic molecule. LCAO is a simplified concept that neglects electron–electron interactions, but that is instructive for understanding the physical principle of molecular or-

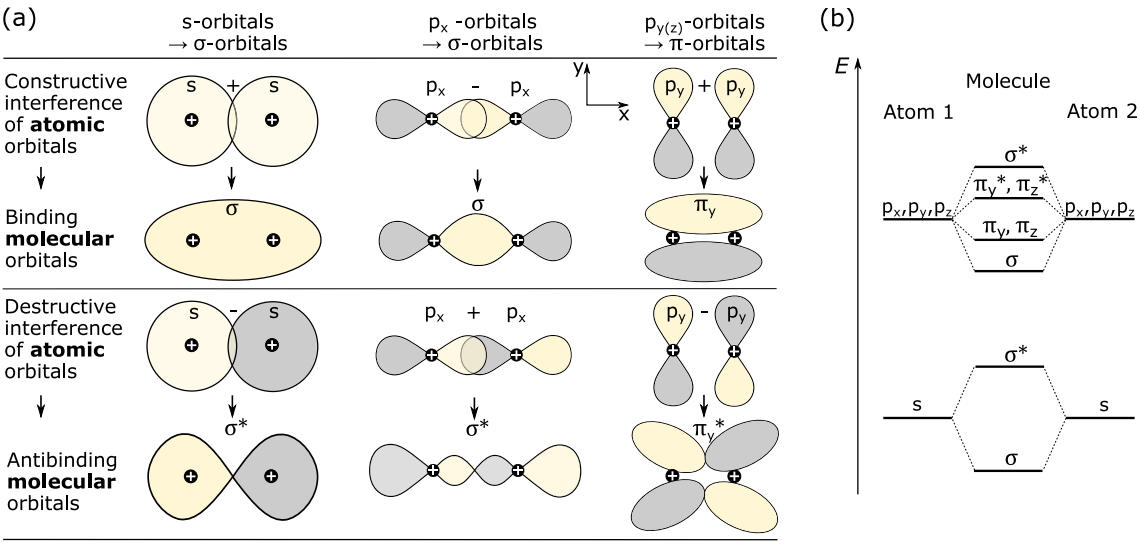

Figure 2.1: (a) Schematic illustration of the linear combination of atomic orbitals (LCAO) on the example of diatomic molecules. Yellow indicates a positive electron wave function, grey a negative electron wave function and black the nucleus. When two wave functions overlap, they interfere constructively or destructively, forming new binding (σ, π) or antibinding ($\sigma*$, $\pi*$) orbitals, respectively. (b) Energy levels resulting from the formation of the molecular orbitals in (a).

bitals. Depending on whether the interference is constructive or destructive, the electron density between the nuclei is increased or not. All superpositions are possible, but the energy of the resulting molecular orbital will be lower (higher) with respect to the atomic orbitals for constructive (destructive) interference (see Figure 2.1b). The extent of this increase and decrease in energy of the molecular orbitals relative to the atomic orbitals mainly depends on the resonance (or exchange) integral, which describes the interaction between the atomic orbitals and in turn depends on their overlap and energy difference. Molecular orbitals are distinguished between σ and π orbitals. The electron distribution of σ orbitals is on the axis between the nuclei whereas π orbitals lie away from this axis. Hence, σ orbitals correspond to a larger resonance integral and have a larger energetic difference to the isolated atomic orbitals. This applies to the shift of both the reduced energy in the binding orbital and the increased energy in the antibinding orbital. The energy difference between binding and antibinding π and π^* orbitals is smaller and often corresponds to light in the visible spectral range. The gain in energy by forming the molecule (i.e., the binding energy) then depends on which orbitals are occupied by which number of electrons. The orbitals will be filled with electrons starting at smallest energies with at most two electrons each (due to the Pauli exclusion principle) as the system minimises its energy.

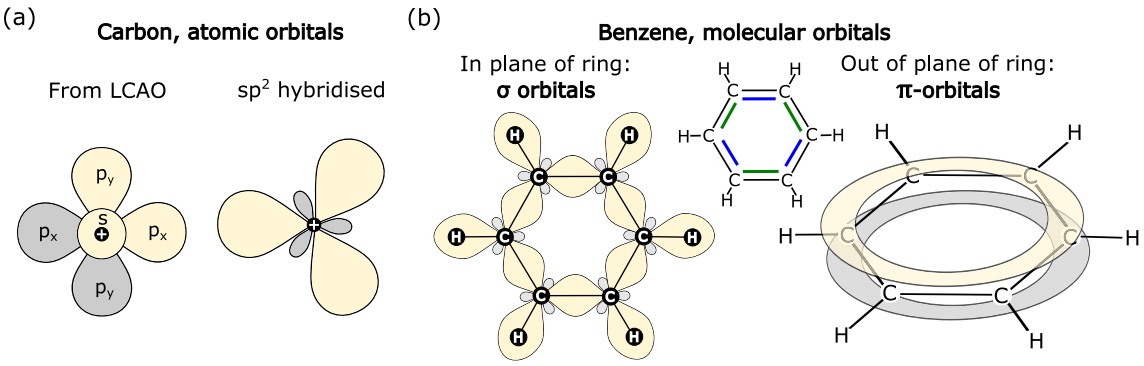

Figure 2.2: (a) Atomic orbitals of carbon from LCAO and the hybrid sp^2 orbital formed when the electrons of carbon interact with those of surrounding atoms (and with each other). (b) Molecular orbitals of a benzene molecule, where carbon is sp^2 hybridised, so that the ring lies in a plane. To the left, only σ orbitals in the plane of the ring are shown, to the right, only π orbitals above and below the plane of the ring. The inset shows the Lewis structure of benzene, where the carbon double bond is equally probable on the blue as on the green positions.

When moving to more complex molecules like organic compounds, the situation is changed and electron–electron interaction will influence the shape of the atomic orbitals before the bonding takes place. Carbon has six electrons, with four of them being valence electrons in the second shell. In the hypothetical case of an isolated carbon atom in space, one would expect two of the valence electrons in the s-orbital and one in the p_x and p_y orbital, each. However, depending on the environment of the carbon atoms, these three orbitals will mix to form three sp^2-'hybrid orbitals' so as to minimise the energy of the system (and thereby optimising the bonding to its available binding partners). These sp^2 orbitals lie in a plane with an angle of 120° between them and allow the carbon atom to form three σ-bonds to three different binding partners (typically one hydrogen and two carbon atoms), as illustrated in Figure 2.2a.

This hybridisation results in molecules with chains or rings of carbon, e.g. polyacetylene or benzene, which are planar with 120° between adjacent bonds (Figure 2.2b). Due to the shared occupation of the bonds, each carbon now has one 'spare' valence electron, which is not used in any of the σ bonds. These electrons populate the atomic p_z orbitals, which are perpendicular to the plane of the molecule and together, form the molecular π_z orbitals. Due to symmetry of the ring of benzene, there is no preference as to which orbitals are joined pairwise (in Figure 2.2b, both the blue and the green bonds are equally likely). Hence, the π_z orbital is delocalised over the entire ring structure (right side of Figure 2.2b), which is formally depicted as alternating single and double bonds between adjacent carbon atoms. The situation

is similar for chains like polyacetylene.

In fact, whenever carbon systems have alternating single and double bonds in their structure formulae, delocalised π_z orbitals will arise. These electrons can be considered as free electrons in a box (e.g. for calculating the energy of excited states), the length of which is given by the conjugation length. The conductivity along a conjugated path is thus higher than in any other direction. However, it is emphasised that the delocalisation, other than in inorganic semiconductors, does not occur across the entire bulk of the material, but only on the scale of molecular units (or effective conjugation units). Electron transport across the bulk is thus greatly reduced with respect to free electrons and is best described as hopping processes between molecular units.[78]

While all conjugated molecules share the delocalisation of electrons and thus, the semiconducting properties, they are not necessarily efficient chromophores. Chromophores are characterised by the transition between the ground state and the excited state being efficient and in the visible spectral range. The transition consists of the excitation of an electron from the highest occupied molecular orbital (HOMO) to the lowest unoccupied molecular orbital (LUMO). Its efficiency is described by the magnitude of the so-called transition dipole moment. The efficiency is an important quantity for describing chromophores, so that in addition to the transition dipole moment μ, one can define the macroscopic oscillator strength f:

$$f = 5.36 \cdot 10^6 \langle \nu \rangle |\mu|^2 = \frac{4.29 \cdot 10^{-9}}{n} \int \kappa(\tilde{\nu}) \, \mathrm{d}\tilde{\nu}. \tag{2.1}$$

Here, ν is the frequency of the transition in SI units, $\tilde{\nu}$ is the transition frequency in wave numbers, n is the refractive index of the material and κ is the decadic molar extinction coefficient. The prefactors represent a combination of different constants that originate from relating the probability of absorption and emission—more precisely, the Einstein A and B coefficients—to each other and relating the absorption cross section for a single chromophore to the absorption coefficient of a film. Equation 2.1 links a microscopic, quantum mechanical quantity (μ) to the macroscopic quantity of the measurable extinction coefficient. f will be small when a transition is quantum mechanically not allowed (e.g. by spin conservation) and so will be the absorption peak. The maximum oscillator strength for a single dipole is 1, but films with many dipoles will be described by a single, effective oscillator strength with $f \gg 1$.

Since the dipole operator is odd, only transitions from even states to odd states* and vice versa will be symmetry-allowed and will thus have significant transition dipole moments (or oscillator strength). Moreover, it turns out that transition dipole moments are larger when the transition from HOMO to LUMO is concomitant with a redistribution of charge.[79] This is realised in molecules containing additional functional units which donate and accept electron density within the conjugated domain (e.g. oxygen and nitrogen, respectively). While this usually leads to a decrease in charge mobility, the efficiency of the transition is increased. These functional units also influence the position of the HOMO and LUMO levels and hence, the frequency of the transition.

2.1.1.2 Structure of molecules and films: different classes of organic semiconductors

The conjugation, often in the form of aromatic rings as described above, can appear on different kinds of molecules. Organic semiconductors are classified as polymers or small molecules. Polymers are made of a chain of repeating units ($\gtrsim 20$)[80], with the conjugation occurring across the entire backbone of the chain. However, the effective conjugation length of a polymer will generally be shorter as different local environments will reduce the coherence length along which delocalisation can occur. Since the confinement of the electron determines the gap between the HOMO and the LUMO, the bandgap is a function of the effective conjugation length. The width of the transition is then influenced by the spread in effective conjugation lengths. In addition to the conjugated central unit, polymers generally have side groups attached to the semiconducting backbone. These increase their solubility—polymers are usually processed from solution—and can control the interaction between different polymer chains or the rigidity of the polymer. Small molecules, by contrast, have a lower molecular weight which allows for their evaporation in vacuum. The evaporation facilitates the fabrication of multilayer stacks. Like for polymers, side groups are often attached to the conjugated unit as a means to influence the inter-molecular interaction, the film structure or the solubility.

Because organic molecules used as organic semiconductors are overall neutral, the interaction between different molecular units is usually given by dipole–dipole interaction. In cases where the molecule has no permanent overall dipole moment, the dipoles will be induced and different molecules will interact via Van der Waals forces. The immediate environment will

*Even and odd operators and functions f correspond to a symmetric or antisymmetric behaviour around 0: $f_{\text{even}}(-x) = f_{\text{even}}(x)$ and $f_{\text{odd}}(-x) = -f_{\text{odd}}(x)$, respectively. This is fulfilled for example in polynomial functions or operators with exclusively even and odd terms, respectively.

affect the energetic position and shape of the molecular orbitals. This environment will differ between different conjugated units (i.e., molecules or effective conjugation domains on one molecule), so that different units will have slightly different energy levels. As a result, thin films of organic molecules do not have one sharp absorption energy but rather a broad band of transition energies. The width of the band depends of the degree of order in the film.

Both polymers and small molecules can have different degrees of order when deposited in a film. At the limits, they can form molecular crystals with perfect periodical order or fully amorphous films with the lowest degree of order. Regimes of intermediate order include aggregates, in which molecules are stacked in an orderly fashion, ensembles of microcrystallites or films in which all dipoles lie in one plane. The greater the order in the material, the more similar are the energetic levels of different molecules and thus, the narrower the band width of the absorption will be. This is observed for example in J-aggregates, where the stacking creates an extended coherent state with a narrower, red-shifted transition and a smaller Stokes shift compared to the monomer (the latter originating from a nearly resonant excitation and absorption process).[81,82] Likewise, increasing the rigidity of the molecule reduces the number of possible conformations and thus the disorder in the material.

Disorder will lead to inhomogeneous broadening of the transition. The distribution of energetic levels across different molecular units, arising from different effective conjugation lengths and different environments of each chromophore, will then have a Gaussian shape. In organic semiconductors, the inhomogeneous broadening is usually a lot larger than the homogeneous linewidth, which results from the finite lifetime of the excited state.

2.1.2 Excitation and relaxation of organic semiconductors

This section discusses the dynamic processes of excitation and relaxation in organic semiconductors. It will be seen that the absorption and emission of light generally not only involves electronic, but also vibronic transitions. The second part of this section then describes how competing non-radiative processes can influence the emission efficiency of a given material.

2.1.2.1 Absorption and emission spectra

The molecular orbitals discussed above show the energy levels which electrons can occupy. The energetic state of the molecule is then given by the way electrons are distributed over the orbitals, how their spins add up and how the nuclei move with respect to each other.

In the ground state S_0, the energy will be minimised and electrons will occupy the lowest levels, complying with the Pauli exclusion principle. The HOMO then plays the role of the valence band in inorganic semiconductors. From here, electrons can be excited into any of the unoccupied orbitals and the lowest excited state will excite an electron into the LUMO, which acts as the conduction band.

Assume an excitation from an electron of the HOMO (e.g. π_z, see Figure 2.1b) into the LUMO (e.g. π_z^*). The missing electron in π_z represents a hole, which will electrostatically interact with the extra electron in the LUMO, i.e., they will attract each other. Due to the Coulomb attraction, a bound electron–hole pair is formed in the molecule, which represents the excited state of the molecule and is called an exciton. It falls into the class of Frenkel excitons because its radius is small ($\sim$ 1 nm, defined by the extension of the orbitals) and its binding energy is strong. The binding energy of the exciton results from the interaction of the charges and is given by the difference in energy of the electrical and the optical gap. The electrical gap describes the energy difference between the LUMO and HOMO (or between the electron affinity and the ionisation potential). As mentioned before, the energetic position of these molecular orbitals does not take any electron–electron interaction into account. The optical gap, by contrast, is indicated by the absorption edge and shows the difference between the S_1 and S_0 state. These energetic states consider the attraction between the hole in the HOMO of the molecular ground state and the electron in the LUMO of the molecular ground state, which lowers the optical gap with respect to the electrical gap. The binding energy differs between different materials, but can safely be assumed to be $E_B \gtrsim 0.5$ eV, which means that excitons in organic materials are stable at room temperature since $E_B \gg k_B \cdot 300\ \mathrm{K} = 0.026$ eV.

In addition to the Coulomb interaction, the alignment of the spins of electron and hole will affect the energy levels of the excited state. The spins of the electrons can interfere constructively (i.e., total spin $S = 1$), forming a triplet state (notation T_i, $i > 0$) or destructively (i.e, $S = 0$) to form a singlet state (notation S_i, $i \geq 0$). The triplet state has its name from the three (degenerate) states which can form with the same spin quantum number $S = 1$ but different spin projections, $m_S = -1, 0, 1$. It usually has a lower energy than the singlet state. According to quantum mechanics, the total spin S is conserved in transitions when the spin–orbit coupling is small, as it is the case for the molecules discussed here. Since the ground state of conjugated molecules is a singlet state (as, in fact, for most molecules), only transitions to and from other singlet states are allowed—at least for molecules with little spin–orbit coupling. Thus, the

luminescence from singlet states (fluorescence) to the ground state S_0 is fast. In contrast, the radiative relaxation of triplet states (phosphorescence) is much slower ($\lesssim \times 0.01$) and is thus often suppressed by faster non-radiative relaxation channels. While this is of great importance under electrical excitation,* optical excitation does not create triplet states. The experiments in this thesis only use optical excitation of organic molecules with little spin–orbit coupling. Thus, singlet states will present the vast majority of excited states and the discussion in the following will be restricted to this situation.

So far, we have considered a rigid molecule, where all atoms sit at equilibrium distance from each other. However, molecules can vibrate in collective or normal modes, in which all nuclei move through their equilibrium position at the same time. These vibrations are quantised as a function of the vibration frequency ω_{vib} in the energy potential of the molecule. Close to the minimum, this can be approximated as a parabola, so the energies of the vibrational mode are given by $E_{\text{vib,n}} = \left(n + \frac{1}{2}\right)\hbar\omega_{\text{vib}}$, $n = 1, 2, ...$ A better approximation of the energy potential between two bound atoms is the Morse potential, which takes into account the dissociation of the molecule at large inter-nuclei distances R: $E_{\text{pot}} = E_{\text{M}}\left[1 - e^{a\left(R - R_{\text{eq}}\right)}\right]^2$. Here, E_{M} is the depth of the potential and relates to the dissociation energy E_{D} as $E_{\text{M}} = E_{\text{D}} + \frac{1}{2}\hbar\omega_{\text{vib}}$; R_{eq} is the equilibrium distance between the nuclei and a is a proportionality factor. As a consequence of the potential becoming wider away from the minimum, the vibronic energy states move closer with respect to vibronic states in a parabola.

The different potentials and energy levels of an organic molecule together with different transition mechanisms (radiative or non-radiative) are illustrated in Figure 2.3, which is similar to a Jablonski diagram. Since the energy of one vibrational quantum is roughly $\omega_{\text{vib}} \sim 0.1$ eV, only the lowest energy state will be significantly occupied at room temperature. The vibrational levels are nonetheless important, as we will see in the following. Upon excitation of one electron into the LUMO, the energy potential will not only be shifted to higher energies, but at the same time, the equilibrium distance between nuclei will increase (see Figure 2.3). The nuclear adaptation to the new energy potential will, however, be slow compared to the radiative excitation of the electron. Thus, radiative transitions will appear as vertical lines in the energy diagram, which is called the Franck–Condon principle. Since the transition

*Under electrical excitation, the occupation of HOMO and LUMO does not follow optical selection rules and hence, each combination of spins is excited with the same probability. However, since there exist three different spin combinations which will form a triplet state but only one that forms the singlet state, 75% of the electrical excitations will be triplet excitons. Due to their much slower decay, these can act as trap states in electrically driven devices with small spin–orbit coupling.

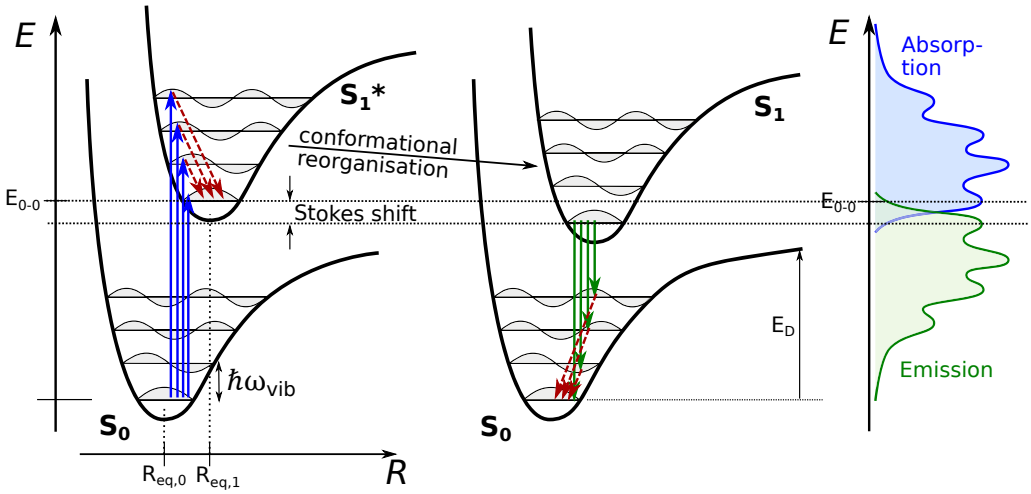

Figure 2.3: Schematic diagram of photo-excitation (blue) and subsequent relaxation (green) in organic materials. Radiative transitions are indicated by vertical, solid arrows and thermal relaxation by red, dashed arrows. Conformational relaxation of the excited state ($S_1^* \rightarrow S_1$) leads to the Stokes shift between the 0-0 transition in absorption and emission spectra.

matrix element depends on the density of states of the final state (see Fermi's golden rule in Section 2.2), the highest transition probability is to a vibrational state which is not necessarily the vibrational ground state. The absorption spectrum of an organic molecule will thus generally consist of several peaks corresponding to the excitation into different vibronic levels of the excited state. The thermal relaxation into the vibronic ground state of S_1 will then follow quickly with respect to electronic transition rates. Additionally, many molecules rearrange their atoms after excitation in order to minimise their energy with respect to the new electron distribution ('conformational reorganisation' in Figure 2.3). This conformational relaxation results in a shift of the emission spectrum towards lower energies, the extent of which is the so-called Stokes shift. The subsequent radiative relaxation will follow the same principles as the excitation and depend on the overlap of wave functions in the initial and final state. Thus, relaxation will not only occur into the vibronic ground state but also into vibronically excited states of S_0, yielding an emission spectrum that is mirror-symmetric to the absorption.

2.1.2.2 Dynamics of excited states

The photoluminescence quantum yield (PLQY) is an important measure for evaluating the radiative efficiency of a transition. It describes how many photons are emitted for each absorbed photon. From the processes discussed above, one might conclude that the PLQY is always equal to one. However, this is not the case as a consequence of non-radiative processes

competing with the radiative ones.

The non-radiative steps of the radiative process sketched above—i.e., the thermal relaxation and the conformational reorganisation—should not be confused with overall non-radiative processes. Generally, there is one radiative transition, e.g. $S_1 \rightarrow S_0$, which relaxes at a rate k_r. Additionally, there will be several fully non-radiative processes, in which no photon is emitted throughout the entire relaxation process. If the chromophore is in solution, this can mainly happen via internal conversion and intersystem crossing (at the rates k_IC and k_ISC). Internal conversion describes the transition from the electron in a low vibrational state of S_1 into a highly excited state of S_0 at the same energy, where upon the energy will be dissipated into the bulk. Intersystem crossing, by contrast, describes the spin flip of an excited electron, rendering the excited state into a triplet state. This is not generally a quantum mechanically allowed processes so that k_ISC will be small for organic materials which have little spin–orbit coupling (like the materials used here).

Even more non-radiative decay channels are available when the chromophore is in a dense thin film and the excitons can interact with each other. The interaction via non-radiative energy transfer—either via dipole–dipole interaction (Förster type) or via electron exchange interaction (Dexter type), depending on the multiplicity of the involved states*— results in bimolecular annihilation.[83] In principle, excitons can annihilate with other excitons (or charges, though not discussed here), independent of the spin:

$$X_1 + Y_1 \rightarrow S_0 + Z_n \rightarrow S_0 + Z_1 + \text{heat}. \tag{2.2}$$

Here, X, Y and Z can be either singlet or triplet states and S_0 is the ground state. The subscript n denotes a high vibronic excitation, which will decay thermally and via internal conversion into the vibronic ground state of the first excited state. Being a two-particle interaction, the annihilation scales with the concentration of both particles, $[X]$ and $[Y]$. The quenching process will dissipate the energy of one exciton, leaving only one excited exciton.

The rate equation for excitons can then be described by three terms: one pumping term, one term representing the radiative and non-radiative relaxation of excitons and an additional

*For the photoexcitation of primary relevance here, the majority of the excitons will be in singlet states, Förster type energy transfer will dominate due to its longer range.

term that depends on the square of the exciton density n:[84]

$$\frac{\mathrm{d}n}{\mathrm{d}t} = \alpha \cdot I_{\mathrm{pump}} - \left(k_r + \sum_i k_{nr,i} \right) \cdot n - \gamma \cdot n^2. \tag{2.3}$$

Here, α is the absorption coefficient, I_{pump} is the pumping intensity, k_r is the radiatve decay rate, $k_{nr,i}$ represents various non-radiative decay rates and γ is the bimolecular annihilation rate constant. Since the bimolecular quenching depends on the concentration of excitons, it scales both with density of the chromophores and with excitation density. When exciton–exciton annihilation dominates the overall decay, the emission will not scale linearly with the intensity, but rather with its square root. For the system discussed here, singlet–singlet annihilation, i.e., $X, Y, Z = S$, will dominate bimolecular quenching.

From the above considerations, it becomes clear that the PLQY Φ is determined by how the radiative decay rate compares to the overall decay rate:

$$\Phi = \frac{\#\text{ photons emitted}}{\#\text{ photons absorbed}} = \frac{k_r}{k_r + \sum_i k_{nr,i} + \gamma \cdot n}. \tag{2.4}$$

k_r thus competes with all non-radiative decay rates, k_{nr} and $\gamma \cdot n$. This shows that the PLQY can decrease both with increasing concentration of chromophores and with increasing excitation level because of the increase of exciton–exciton annihilation.

2.2 Microcavities

Cavity photons form the second ingredient necessary to obtain strong light–matter coupling. This section will give a brief overview of the dispersion relation of a photon in a Fabry-Pérot cavity and of the important characteristics of these microcavities depending on the type of confining mirrors.

2.2.1 The Fabry-Pérot cavity

A Fabry-Pérot cavity is defined by two plane-parallel mirrors, confining the light in the direction perpendicular ($\perp$) to the mirrors. In the plane of the mirrors ($\parallel$), however, translation invariance is maintained. This makes the wave vector parallel to the mirrors ($q_\parallel$, related to momentum p as $p_\parallel = \hbar q_\parallel$) a good variable to describe the system by, as will be shown in the following.

In vacuum, the propagation of the photon is solely determined by the speed of light, c, and its frequency ω depends on its wave vector q (related to the wavelength λ as $q = \frac{2\pi}{\lambda}$) according to $\omega = cq$. This is no longer valid when light travels through a medium of complex refractive index $\tilde{n} = n - ik$ with refractive index n and extinction coefficient k. In that case, the dispersion relation is changed to $\omega = \frac{cq}{\tilde{n}(q)}$ by the interaction with the medium, and is thus no longer linear for dispersive media.[85]

The dispersion relation becomes even more distorted from the linear behaviour when the light is confined between two mirrors. While literature often skims over the derivation and only states the resulting photonic dispersion relation,[70,86–89] it will be derived in detail here. This is important in order to understand where (and how well) approximations and hence final equations are valid. We start by considering light of wave vector q_0 outside and q_c inside the cavity performing a roundtrip in the cavity of effective length d, see Figure 2.4a. The phase shift experienced by the light during one roundtrip depends on the angle Θ_c ($\Theta_c = 0$ corresponds to light perpendicular to the mirrors) inside the cavity and is given by $2dq_c \cos\Theta_c$. After one roundtrip, only wave vectors q_c fulfilling

$$e^{i2dq_c \cos\Theta_c} = 1 \quad \Leftrightarrow \quad 2dq_c \cos\Theta_c = 2\pi \cdot m, \quad m = 1, 2, ... \tag{2.5}$$

will interfere constructively and hence form the cavity mode or dispersion relation. This is equivalent to the description of a standing wave forming between the mirrors at wavelengths $m \cdot \frac{\lambda_c}{2} = d \cdot \cos\Theta_c$ with nodes at the edges of the cavity. For simplicity, we will assume $m = 1$ in the following, which corresponds to a $\frac{\lambda}{2}$-cavity. Assuming that inside the cavity, we have the refractive index n_c and outside, $n_0 = 1$, q_c is related to q_0 via $q_c = n_c q_0$. Using furthermore the identity $\cos^2\Theta + \sin^2\Theta = 1$ and Snell's law ($n_0 \sin\Theta_0 = n_c \sin\Theta_c$), we can reformulate condition 2.5 to become a function of the observables outside the cavity (q_0 and Θ_0):

$$q_0 = \frac{\hbar c \pi}{n_c d} \cdot \frac{1}{\sqrt{1 - \frac{\sin^2\Theta_0}{n_c^2}}}. \tag{2.6}$$

Knowing the wave vectors for which constructive interference is fufilled, it is straightforward

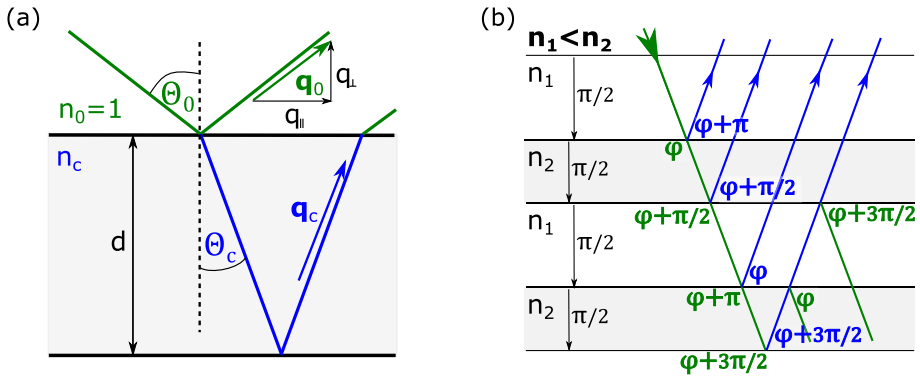

Figure 2.4: Illustration of interference (a) in a microcavity and (b) in a DBR. The beam path in (b) is only drawn at an angle for clarity. Due to the periodicity of trigonometric functions, we set $\varphi + 2\pi = \varphi$. All constructively interfering beams are drawn in blue.

to find an expression for the energy of the photon mode, E_{MC}:

$$\begin{aligned} E_{\mathrm{MC}} &= \hbar c q_0 \\ &\approx E_0 \cdot \left(1 + \frac{\sin^2 \Theta_0}{2n_c^2}\right), \qquad E_0 = \frac{\hbar c \pi}{n_c d}, \end{aligned} \tag{2.7}$$

where E_0 is the photon energy at $\Theta_0 = 0°$. The approximation was obtained by a Taylor series for $\frac{1}{\sqrt{1-x}}$. This error of this approximation depends on Θ_0 and n_c ($n_c \approx 1.8$ for organic materials), which is estimated to correspond to a $\sim 10\%$ (24%) deviation from the parabolic shape for $\Theta_0 = 40°$ ($\Theta_0 = 90°$) .

E_{MC} can also be expressed as a function of the wave vector parallel to the mirrors, for which continuity across the mirrors holds: $q_{\parallel} = q_{\parallel,0} = q_{\parallel,c}$. To obtain $E_{\mathrm{MC}}(q_{\parallel})$, Equation 2.5 is rearranged to yield $q_c = \frac{\pi}{d \cdot \cos\Theta_c}$. Combining this expression with $q_c = \sin\Theta_c \cdot q_{\parallel}$, the generally valid relationship between the angle inside the cavity, Θ_c, and $q_{\parallel}$ can be established: $\tan\Theta_c = \frac{d}{\pi} q_{\parallel}$. Moreover, it can be deduced from the trigonometric identity used above that $\frac{1}{\cos\Theta_c} = \sqrt{1 + \tan^2\Theta_c}$. These steps will be used in the following:

$$\begin{aligned} E_{\mathrm{MC}}(q_{\parallel}) &= \hbar c \frac{q_c}{n_c} = \frac{\hbar c \pi}{n_c d \cos\Theta_c} = E_0 \sqrt{1 + \tan^2\Theta_c} \\ &= E_0 \sqrt{1 + \frac{q_{\parallel}^2 d^2}{\pi^2}} = E_0 \sqrt{1 + \frac{\hbar^2 q_{\parallel}^2}{E_0 \cdot m_{\mathrm{eff}}}}; \qquad m_{\mathrm{eff}} = E_0 \frac{n_c^2}{c^2} \\ &\approx E_0 + \frac{\hbar^2 q_{\parallel}^2}{2 m_{\mathrm{eff}}}. \end{aligned} \tag{2.8}$$

Thus, we expect to see in first approximation a parabolic function of the cavity mode. In the last line, the Taylor series for $\sqrt{1+x} \approx 1 + \frac{x}{2} - \frac{x^2}{8} + \cdots$ was used, so that the error of the approximation can be estimated from the neglected term of lowest order. In our case, $x = \tan\Theta_c$, for which the maximum angle which can be observed outside organic materials with $n \approx 1.8$ is $\Theta_c \approx 35°$. Thus, for $\Theta_0 = 90°$, the expected deviation from the parabola is 12%, while at $\Theta_0 = 40°$, it reduces even further to $< 5\%$.

Note that due to the differences between Equation 2.7 and Equation 2.8, care has to be taken when evaluating experimental data. When the energy is measured over the angle (e.g. using a goniometer), the dispersion of the cavity photon will not be parabolic but become flatter at large angles. Hence, the shape will be reminiscent of the dispersion relation of a lower polariton (see Section 2.4.1) even though the system is purely photonic. When the energy is instead measured using far-field imaging, the spectra will be resolved with respect to their spatial frequency, $q_{\parallel} = q_0 \cdot \sin\Theta_0$, which corresponds to the wave vector parallel to the mirrors. Therefore, far-field imaging recovers the well-approximated parabolic dispersion relation of Equation 2.8.

2.2.2 Metal mirrors vs distributed Bragg reflectors

There are two ways of reflecting light which are relevant in this thesis, either by metallic mirrors or by distributed Bragg reflectors (DBRs).

Below the plasma frequency, which lies for most metals well in the ultra-violet spectral region, electrons in metals can be approximately described as free electrons. As such, the absorption ($\propto k$) is a lot higher than the polarisability ($\propto n$) of the medium and the light penetrates very little into the mirror. We can express the reflectivity R of a surface via the reflection coefficient r from Fresnel equations (as will be discussed later, see Equation 3.7). At normal incidence, R only depends on the complex refractive indices, $\tilde{n}_1$, $\tilde{n}_2$ and for $\tilde{n}_1 = 1$ (i.e., vacuum or air) and $\tilde{n}_2 = n - ik$ (i.e., an arbitrary, absorbing material) it will become[85]

$$R^{\text{metal}} = |r|^2 = \left|\frac{(n-ik)-1}{(n-ik)+1}\right|^2 = \frac{(n-1)^2+k^2}{(n+1)^2+k^2}. \tag{2.9}$$

It follows that if $k \gg n$, as is the case for metals, $R \to 1$. In practice, the reflectance for metals of good optical quality (e.g. silver, gold, Al) is limited to $R_{\text{metal}} = 0.9 \cdots 0.98$. There, even though k is large, not much energy is dissipated because the light only penetrates for small

distances d_{pen} into the metal.[85] The effective cavity length d is thus increased with respect to the distance between the two mirrors, d_c: $d = d_c + 2d_{\text{pen}}$, where $d_c \gg d_{\text{pen}}$. If the thickness of the metal mirror is on the order of the penetration depth, some light will be transmitted through the mirror (i.e., it will be semitransparent) and the reflectance will be reduced.

The reflectance of a DBR, by contrast, relies on interference. A DBR consists of alternating layers of two different, transparent materials with refractive indices n_1 and n_2, see Figure 2.4b. Both layers have optical thickness $d_{\text{opt}} = \frac{\lambda_c}{4}$, which corresponds to a phase shift of $\frac{\pi}{2}$ for light with wavelength λ_c propagating through the layer. According to the Fresnel equations (Equation 3.7), light reflected on the surface from n_1 to n_2 will experience a phase shift of π if $n_1 < n_2$, i.e, only on every other interface. Transmission is never accompanied by a phase shift. As a consequence, all reflected light will interfere constructively, while a double-reflection into forward direction leads to cancellation of the electric field (see two bottommost layers in Figure 2.4b).

The concept of interference makes the DBR a highly tunable system, where the region and amount of reflection can be freely chosen by changing the thickness of the layers or the number of mirror pairs, N. The larger the number of mirror pairs in the DBR stack, the more effective the interference cancellation becomes and hence, the higher the reflectivity at λ_c. In quantative terms, this can be stated as[90]

$$R_{\text{DBR}} = 1 - 4\left(\frac{n_1}{n_2}\right)^{2N}, \qquad n_1 < n_2. \tag{2.10}$$

Equation 2.10 gives the maximum reflectance at normal incidence at λ_c. By increasing the number of layers in a DBR, one can thus increase the reflectance of the mirror to well above 99% and is only limited by the losses (scattering or absorption) in the mirror.[91] A full quantitative description with an explicit wavelength dependence including polarisation and angle dependence goes beyond the requirements for understanding the rest of this thesis and can be found for example in Panzarini *et al.* [92]. The overall shape of the DBR reflection spectrum will be described qualitatively, though, and is schematically illustrated in Figure 2.5a. From the considerations regarding the interference above, it is clear that both a change in angle and a change in wavelength will lead to a reduction of the maximum reflectance. Around the central wavelength λ_c, however, this change is small, so that a so-called stop band forms. Its width depends on the refractive index contrast $|n_1 - n_2|$. Outside this stop band, the reflectivity

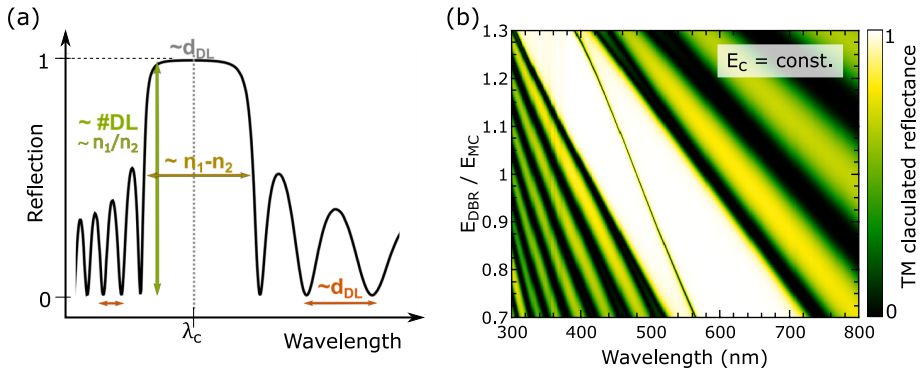

Figure 2.5: Properties of DBRs and DBR-based cavities. (a) Exemplary reflection spectrum of a DBR with indication of the parameters affecting the spectrum. DL stands for double layer, #DL for number of double layers. (b) Transfer matrix (TM) calculation of the mode shift originating from the phase matching when keeping the cavity thickness and energy (E_c) constant and only changing the stopband position (E_{DBR}) via the thickness of the DBR layers.

drops drastically and fringes are observed due to partially constructive or entirely destructive interference at different wavelengths. The relatively high transparency outside the stop band allows for coupling light efficiently into the cavity.

The confinement of the optical mode by interference leads to two particularities of the spatial mode profile inside a microcavity. First, the field does not necessarily vanish on the edges of the microcavity. If the refractive index adjacent to the cavity is smaller than that of the second material, the standing wave will have antinodes at the edges of the cavity (and a node in the centre of a $\frac{\lambda}{2}$-cavity).[90] In the opposite case, the field distribution resembles that of a metal cavity, with nodes on the edges. Second, the interference principle leads to a large penetration depth into the mirrors,[70]

$$d_{\mathrm{pen}}^{\mathrm{DBR}} = \frac{\lambda_c}{2n_c} \cdot \frac{n_1 n_2}{|n_1 - n_2|}, \tag{2.11}$$

which also depends on the refractive index inside the cavity, n_c. For a typical cavity used for the experiments presented in this thesis, $d_{\mathrm{pen}}^{\mathrm{DBR}} \approx 700$ nm $\approx 3 d_c n_c$. This large value results in the photonic mode volume being significant larger than in metal cavities, which will be of importance for the light–matter interaction discussed further below. A second effect of the large penetration depth into the DBR is a possible frequency shift of the mode due to phase matching. When the energy of maximum reflectance of the DBR, $E_{\mathrm{DBR}} = \frac{hc}{\lambda_c}$, differs from the cavity mode E_c (Equation 2.7), the energy E_{m} of the observed mode depends on both E_{MC} and

E_{DBR}:[92]

$$\begin{aligned} E_{\mathrm{m}} &= \frac{d_c \cdot E_{\mathrm{MC}}(\Theta) + d_{\mathrm{pen}}^{\mathrm{DBR}} \cdot E_{\mathrm{DBR}}(\Theta)}{d_c + d_{\mathrm{pen}}^{\mathrm{DBR}}} \\ &\approx \left(1 + \sin^2 \Theta_{\mathrm{eff}}\right) \frac{d_c \cdot E_{\mathrm{MC}}(\Theta = 0°) + d_{\mathrm{pen}}^{\mathrm{DBR}} \cdot E_{\mathrm{DBR}}(\Theta = 0°)}{d_c + d_{\mathrm{pen}}^{\mathrm{DBR}}} \end{aligned} \tag{2.12}$$

One thus observes a mode pulling towards the centre of the stop band upon detuning E_c from E_{DBR}. This is illustrated in the calculation of Figure 2.5b, where the mode (low reflectance in the stop band) is shifted upon changing E_{DBR}, even though E_c is kept constant. The second line in Equation 2.12 used the fact that E_{DBR} also depends on its internal angle Θ_{DBR} as $E_{\mathrm{DBR}} \propto \frac{1}{\cos \Theta_{\mathrm{DBR}}}$. On the assumption that $n_1, n_2, n_c \approx n_{\mathrm{eff}}$, it becomes clear that E_{m} is also expected to follow a parabola as function of $\sin \Theta_0$.

2.2.3 *Q*-factors

In order to define the quality of a microcavity, the concept of *Q*-factors is introduced. Qualitatively, the *Q*-factor of a purely photonic system describes how many round trips a photon can statistically take before it will leak through a mirror of the cavity. It is related to the photon lifetime τ like $\tau = Q \cdot \frac{\hbar}{E}$, where E is the energy of the mode. Q^{-1} gives the fraction of losses through the mirror and potentially by scattering (see discussion below). When an absorbing material is placed inside the microcavity, the photon can additionally lost by absorption inside the cavity. For this case, the definition of the *Q*-factor depends on the context. In the regime of strong light–matter coupling, the *Q*-factor is considered to be a property of the purely photonic system that can then potentially couple to the absorbing species. For weak light–matter coupling, by contrast, the cavity and material inside the cavity interact only perturbatively so that the *Q*-factor is regarded as a property of the full microcavity–material system.

Quantitatively, the Q-factor can be calculated as[86]

$$Q = \frac{E}{\delta E} = \frac{\lambda}{\delta \lambda}. \tag{2.13}$$

Here, E and λ represent the energy and wavelength of the mode and δE or $\delta \lambda$ its respective width. Even though the definition of Equation 2.13 strictly only applies for low-loss cavities with high *Q*-factors, it is used in this thesis to characterise all cavities in order to compare them quantitatively. Moreover, Q will be determined for lossless—i.e., empty—cavities when discussing strongly coupled systems to recover the properties of the uncoupled photon. In

spectral regions where the cavity material does not absorb, it can thus easily be determined experimentally from the cavity spectrum. In a symmetrical, lossless cavity, Q depends on the reflectance R of each mirror as[91]

$$Q = \frac{m\pi\sqrt{R}}{1-R}, \quad m = 1, 2, \ldots. \tag{2.14}$$

Depending on the type of mirror, Q thus varies between $Q \approx 30$ for metallic microcavities and up to $Q > 10^5$ for the latest DBR-clad microcavities of Fabry-Pérot type.[93]

By contrast, when referring to weakly coupled cavities, losses by absorption inside the cavity will also be taken into account. Then, Q can again be calculated from Equation 2.13 to the absorbing microcavity.[94,95] Equation 2.14, however, is clearly no longer applicable in this scenario.

2.3 Weak light–matter coupling

Weak light–matter coupling describes a regime in which the properties of matter are changed perturbatively by interaction with light. Prominent examples are the Purcell effect and photon lasing, both of which will be described in this Section.

2.3.1 Purcell effect

When light is confined in a microcavity, its density of states is changed with respect to free space. It is increased at the energy of the mode, E_m, and decreased everywhere else. This is important because according to Fermi's golden rule,[96] the transition rate Γ between an initial state $|\Psi_i\rangle$ and a final state $|\Psi_f\rangle$ depends on the final density of states, $D_f(E)$:[97]

$$\Gamma = \frac{1}{h} \left| \langle \Psi_i | H | \Psi_f \rangle \right|^2 D_f(E). \tag{2.15}$$

Here, H denotes the interactive perturbation and $\langle \Psi_i | H | \Psi_f \rangle$ is the transition dipole moment from $|\Psi_i\rangle$ to $|\Psi_f\rangle$, which depends on their overlap. By controlling the number of final states, one can thus control the probability of a particular transition. Hence, the relaxation of an excitation in a microcavity can, for example, be suppressed when the light emitted upon relaxation falls into the forbidden region of a cavity.[95] Likewise, the transition rate can be enhanced when bringing the cavity in resonance with the excitation, because the photon mode corresponds to

an increased $D_f(E)$ with respect to free space. This was first observed by Purcell *et al.* [98] and is thus called the Purcell effect. The enhancement of the transition rate at wavelength λ_c in a cavity (Γ_c) to the free-space rate (Γ_0) is proportional to the Purcell factor, F_P:[86]

$$\frac{\Gamma_c}{\Gamma_0} \propto F_\mathrm{P} = \frac{3}{4\pi^2}\left(\frac{\lambda_c}{n_c}\right)^3 \frac{Q}{V}. \tag{2.16}$$

The rate of radiative relaxation can thus be modified by either changing the Q-factor of a cavity, the refractive index n_c or mode volume V. Here, the Q-factor corresponds to the effective Q-factor of the entire system, i.e., respecting potential losses.

2.3.2 Photon lasing

Lasers use the process of **l**ight **a**mplification by **s**timulated **e**mission of **r**adiation. In order to realise a laser, an external pump of energy, a resonator and a material providing the gain are necessary. The gain process will be described in more detail as it relies on light–matter coupling.

First introduced by Einstein [99], the interaction between a two-level system and a photon distinguishes three processes. The system has two energy levels, $E_0 < E_1$, which are populated by N_0 and N_1 electrons, respectively. The thermal population of these levels depends on the temperature T and the energy difference of the levels according to the Maxwell-Boltzmann distribution:[85]

$$\frac{N_1}{N_0} = e^{-\frac{E_1 - E_0}{k_\mathrm{B} T}}. \tag{2.17}$$

Here, k_B is the Boltzmann constant. Spontaneous emission and thermal absorption processes will aim to maintain this distribution. When the energy difference, $E_1 - E_0$, is in the visible range and therefore $\gg k_\mathrm{B}T$, spontaneous emission aims at depleting E_1 by emitting photons of energy $\nu = E_1 - E_0$. This spontaneous emission is spatially and temporally incoherent and does not depend the electric field inside the cavity. The other two processes are called stimulated absorption and stimulated emission, as they are triggered by the interaction with a photon. They depend on the spectral energy density of the photon u_ν. The rate equations for the three transitions can be expressed via the Einstein A and B coefficients for spontaneous and stimulated processes, respectively:

$$\left.\frac{\mathrm{d}N_1}{\mathrm{d}t}\right|_{\text{spont em}} = -AN_1, \quad \left.\frac{\mathrm{d}N_0}{\mathrm{d}t}\right|_{\text{stim abs}} = -BN_0 u_\nu, \quad \left.\frac{\mathrm{d}N_1}{\mathrm{d}t}\right|_{\text{stim em}} = -BN_1 u_\nu. \tag{2.18}$$

Note that stimulated absorption and emission are both described by the same coefficient B.[100] Assuming equilibrium (i.e., the validity of Equation 2.17) and comparing the energy density distribution to the black body radiation, the form for u_ν is found to be[85]

$$u_\nu = \frac{A}{B}\left(\frac{1}{e^{\frac{h\nu}{k_B T}} - 1}\right), \quad \frac{A}{B} = \frac{8\pi h \nu^3}{c^3}. \tag{2.19}$$

The coefficients for spontaneous and stimulated absorption thus have a fixed ratio, which becomes larger (favouring spontaneous emission) for high frequencies.

Lasing becomes possible when stimulated emission becomes the dominant process, compared both to stimulated absorption and to spontaneous emission. A large energy density u_ν favours stimulated emission over spontaneous emission (see Equation 2.18). High densities u_ν are achieved by pumping the system externally and placing the gain material in which the amplification takes place inside a resonator that only enhances the resonant mode. It also follows from Equation 2.18 that lasing requires a population inversion, $N_1 > N_0$, so that the rate of stimulated emission dominates over that of stimulated absorption. However, this cannot be realised in a two-level system due to its equilibrium Maxell-Boltzmann distribution (Equation 2.17). When more electron levels are present, a population inversion can be attained by choosing an electron system with longer lifetimes in the E_1 level of the lasing transition compared to the E_0 level. This means that electrons which are pumped into a level $E_2 > E_1$ quickly relax into E_1, where they accumulate. When $N_1 > N_0$, stimulated emission will become the dominant process. In order for lasing to set in, the gain by stimulated emission moreover needs to outweigh the losses of the system, mainly through mirrors. The lasing threshold is thus determined by the reflectance of the mirrors, the frequency of the lasing transition (see Equation 2.19) and how readily population inversion can be achieved.

2.4 Strong light–matter coupling

The interaction between matter and light has been treated perturbatively in the previous chapter, discussing weak light–matter coupling. In the regime of strong light–matter coupling, by contrast, the interactions couple the cavity photons and the matter part in such a way that they can no longer be described separately. This coupling gives rise to new quasi particles called polaritons, which are a mix between the matter excitation and the cavity photon. The excitations in the matter can be of different nature—phonons, plasmons or electrons—but here,

we limit ourselves to the discussion of coupling of photons to excitons. The two can interact if they are on resonance and hence energy can be exchanged between photon and exciton. In order for strong light–matter coupling to set in, the absorption needs to happen faster than the decay of photons from the cavity and radiative relaxation of the exciton needs to happen faster than non-radiative decay. In the strong-coupling regime, the energy exchange becomes a coherent process and one can no longer distinguish between excitons and photons. The coupling fundamentally changes and mixes their properties to form exciton–polaritons or, briefly, polaritons. This section will present how these polaritons can be described theoretically and what properties they have—both in general and in particular when organic materials are used as active material inside the microcavity.

2.4.1 Theoretical description

Describing polaritons theoretically is key to understand their properties and measured signatures. Therefore, this Section shows how the simple coupled oscillator follows from the Hamiltonian of the coupled light–matter system and when it is valid. The difference between the experimentally easily accessible Rabi splitting and the coupling strength of the system is emphasised. Finally, the consequences of the strong light-matter coupling in the time domain are discussed.

2.4.1.1 Hamiltonian and coupled oscillator model

The simplest system of relevance contains a single cavity photon mode at energy E_C ($= E_\mathrm{C}(\Theta)$, see Section 2.2) and a single exciton at energy E_X, which are coupled by a coupling constant g. The corresponding Hamiltonian therefore consists of three terms, referring to the cavity photon (C), the exciton (X) and the interaction (ia). The Hamiltonian, similar to the Hamiltonian as derived by Hopfield,[101] has the following form[102,103]

$$\begin{aligned} \hat{H} &= \hat{H}_\mathrm{C} &&+ \hat{H}_\mathrm{X} &&+ \hat{H}_\mathrm{ia} \\ &= E_\mathrm{C}\,\hat{a}^\dagger\hat{a} &&+ E_\mathrm{X}\,\hat{b}^\dagger\hat{b} &&+ g\left(\hat{a}^\dagger + \hat{a}\right)\left(\hat{b}^\dagger + \hat{b}\right) \end{aligned} \tag{2.20}$$

Here, the creation, annihilation and number of photons (excitons) are described with the creation, annihilation and number operators $\hat{a}^\dagger$, $\hat{a}$ and $\hat{a}^\dagger\hat{a}$ ($\hat{b}^\dagger$, $\hat{b}$ and $\hat{b}^\dagger\hat{b}$), respectively. Equation 2.20 differs from the Hopfield Hamiltonian, because photon–photon interaction is neglected here.[103] This interaction would only lead to an offset in energy at a given excitation level,

which is not relevant for the present discussion. Note that the Hamiltonian for the interaction describes both rotating and counter-rotating wave contributions. The latter are the terms emerging $\hat{H}_{\mathrm{ia}}$ which do not conserve particle number, i.e., $\hat{a}^{\dagger}\hat{b}^{\dagger}$ and $\hat{a}\hat{b}$. They only play a role when either the electric field or the coupling strength is very large[102,104,105] and will be commented on in Section 2.4.2.2.

However, on the assumption of treating neither very strong fields nor very large coupling constants, $\hat{H}_{\mathrm{ia}}$ simplifies to $\hat{H}_{\mathrm{ia}} = g\left(\hat{a}^{\dagger}\hat{b} + \hat{a}\hat{b}^{\dagger}\right)$. With this so-called rotating-wave approximation, the Hamiltonian can be expressed as a 2×2 matrix and can now be solved exactly:

$$\hat{H} = \begin{pmatrix} E_{\mathrm{C}} - i\gamma_{\mathrm{C}} & g \\ g & E_{\mathrm{X}} - i\gamma_{\mathrm{X}} \end{pmatrix} \tag{2.21}$$

This is also referred to as the coupled oscillator (CO) model. For better readability, the dependence of the energy of the cavity photon on the viewing angle and cavity thickness, $E_{\mathrm{C}} = E_{\mathrm{C}}(\Theta_0, d)$, is not noted explicitly. In order to account for losses, damping terms $(\gamma_{\mathrm{C}}, \gamma_{\mathrm{X}})$ have been introduced in Equation 2.21. γ_{C} corresponds to the loss of cavity photons through the mirror and γ_{X} to the damping rate of excitons. Both damping terms have been claimed to be equivalent to the homogeneous linewidths of the underlying particle.[106] Yet, the nature of the excitonic damping is still debated, which will be discussed in Section 2.4.3.2.

It should be noted that while Equation 2.21 yields a fair description of polariton modes for a single oscillator, Hamiltonians describing realistic systems are often a lot more complex. These can include multiple excitonic transitions,[107] multiple photonic modes,[62] a vibronic substructure of the exciton,[46,108] disorder[109] and pumping as well as dissipation terms.[110] We will, however, not discuss these theoretical descriptions further here, but rather explain some of the effects of these terms in Section 2.4.2.

By solving the eigenvalue problem of Equation 2.21, two new eigenenergies of the system are found:

$$E_{\mathrm{UP/LP}} = \frac{E_{\mathrm{C}} + E_{\mathrm{X}}}{2} - i\frac{\gamma_{\mathrm{C}} + \gamma_{\mathrm{X}}}{2} \pm \sqrt{g^2 + \frac{1}{4}\left[E_{\mathrm{C}} - E_{\mathrm{X}} - i\left(\gamma_{\mathrm{C}} - \gamma_{\mathrm{X}}\right)\right]^2}. \tag{2.22}$$

The eigenstates corresponding to the eigenenergies of Equation 2.22 are called polaritons and their dispersion relation along the angle is sketched in Figure 2.6a. A coordinate transforma-

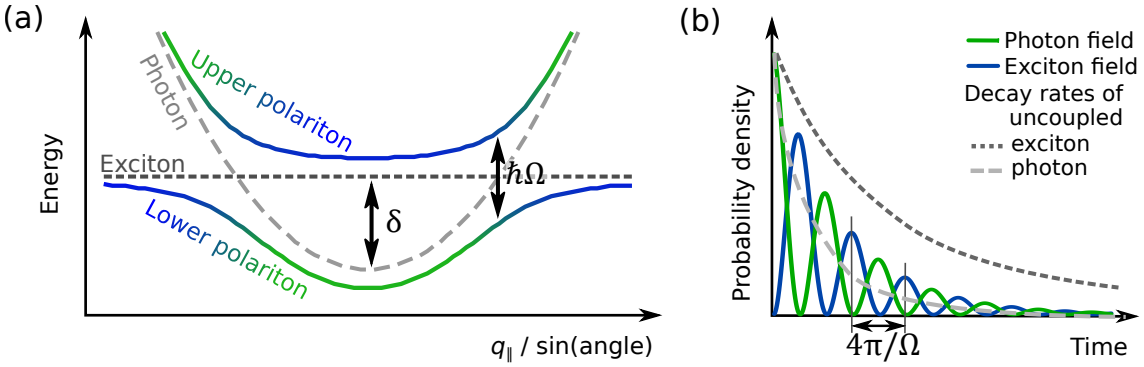

Figure 2.6: Polaritons in the energy and time domain. (a) Energy domain: dispersion relation of polaritons. The uncoupled constituents, cavity photon and exciton (dashed lines), give rise to exciton–polaritons (solid lines) when strongly coupled to each other. The photonic and excitonic fractions of each branch are represented by green and blue colour, respectively. (b) Time domain: Rabi oscillations. In the strong coupling regime, one finds coherent (damped) oscillations between photon (green) and exciton (blue) with the frequency $\Omega/2$. The schematic diagram shows a situation where initially only the photon field is excited and the polariton consists to equal parts of exciton and photon.

tion yields the new, mixed states from the eigentstates of exciton and photon:[88]

$$\begin{aligned} P_- &= X\,\hat{b} + C\,\hat{a} \\ P_+ &= -C\,\hat{b} + X\,\hat{a} \end{aligned} \quad , \qquad |C|^2 + |X|^2 = 1 \tag{2.23}$$

Here, P_- is the eigenstate of the lower polariton (LP), P_+ is the eigenstate of the upper polariton (UP), and X and C are the so-called Hopfield coefficients. $|X|^2$ and $|C|^2$ denote the exciton and photon fraction, respectively. Since the photon energy changes along $q_{\|}$ and with cavity thickness d, so do the polariton energies and thus, importantly, the excitonic and photonic fractions along the LP and UP branch (see Figure 2.6a). Impacts of the varying fractions on the polaritonic properties are discussed in Section 2.4.2.

While the derivation of the polariton states above is in agreement with quantum mechanics, the same result can be obtained from a fully classical, macroscopic model called linear dispersion theory.[111,112] This model relies on using appropriate dielectric functions for calculating the optical response of a microcavity using multi-beam interference from Maxwell's equations. Even though the applicability of this classical model cannot be assumed a priori, it was extensively validated (also for microcavities containing organic materials) to account for all localisation and broadening effects consistently.[113–115] Methods used for calculating the classical optical response of a cavity, like transfer matrix simulations, have since been used

routinely in the field of strongly coupled microcavities.[86,116,117] Therefore, transfer matrix calculations of reflectance and transmittance spectra are also used in this thesis for designing and characterising microcavities. The method will be explained in Chapter 3.1.

2.4.1.2 Rabi splitting vs coupling strength

From Equation 2.22, we can draw two further conclusions. First, we see that while the splitting between LP and UP changes with the energy of the cavity photon, it has an absolute minimum at resonance, where $E_C - E_X = 0$. This splitting is referred to as Rabi splitting ($\hbar\Omega$) in analogy to the splitting originally observed in a spin system coupled to a magnetic field.[118] The Rabi splitting is a measure for the coupling strength between photon and exciton since

$$\hbar\Omega = \sqrt{4g^2 - (\gamma_C - \gamma_X)^2}. \tag{2.24}$$

Second, it is obvious from the above that there is a fundamental limit for attaining the strong coupling regime. This threshold for the coupling strength follows from the difference of the loss terms of the photon and exciton, allowing for the strong coupling regime only if[90,119]

$$g > \frac{\gamma_C - \gamma_X}{2}. \tag{2.25}$$

γ_C corresponds to the linewidth of the cavity photon, but there exists a controversy about the nature of γ_X,[102,106,112,120,121] which will be discussed in further detail in Section 2.4.3.2. If the coupling strength is smaller than the threshold defined by cavity and material properties, the system is in the weak coupling regime (see Chapter 2.3).[86] Here, no splitting occurs and the interaction can be treated perturbatively.

Independent of the controversy about γ_X, it is emphasised that Equation 2.25 is different from the criterion of being able to observe the splitting. The threshold for the visibility of the splitting, g_{vis}, in contrast to the threshold of the strong coupling regime, depends on the sum of total widths (i.e., FWHM) of the uncoupled exciton and photon mode, σ_X and σ_C. g_{vis} is the minimum coupling strength for which two dips can be distinguished in the absorption spectrum and can be derived from linear dispersion theory to correspond to[90]

$$g_{vis} = \frac{\sigma_C + \sigma_X}{2}. \tag{2.26}$$

Next, the parameters which determine the coupling strength of a microcavity will be discussed. The coupling strength between a dipole of dipole moment μ and the vacuum field A inside a cavity is defined as[122–125]

$$g = \sqrt{N}\mu A/\hbar \propto A\sqrt{\frac{Nf}{V}}. \tag{2.27}$$

Here, N is the number of excitable sites which interact with the photons, f is the oscillator strength of the exciton and V is the cavity volume. All three variables are thus handles with which the coupling strength can be controlled and which can potentially drive the system between the weak and strong coupling system. Somewhat counter-intuitively, we also learn from $g \propto 1/\sqrt{V}$ that in metal-clad cavities, even though they have much smaller Q-factors, the coupling strength is inherently increased compared to DBR-clad cavities. The penetration depth into the mirrors, which is significantly larger for DBRs than for metal (see Section 2.2.2), results in an increased V—and hence decreased g—for DBR-clad cavities with respect to metal-clad cavities that are otherwise comparable.

2.4.1.3 Strong exciton–photon coupling in the time domain

Another way to understand strong light–matter coupling is in the time domain, which relates to the energy or frequency domain via Fourier transform.[126] In the time representation, the energy splitting of the strong coupling regime translates into coherent oscillations between excitons and photons (schematically shown in Figure 2.6b). This behaviour differs fundamentally from the weak coupling regime, where after an initial excitation, every exciton will emit independently, thus resulting in an exponential decay. More precisely, upon increasing the light–matter coupling, the emission lifetime is initially reduced from the spontaneous emission rate due to the Purcell effect, indicating the transition from an uncoupled to a weakly coupled regime.[86] Once the system enters the strong coupling regime, i.e. Equation 2.25 is fulfilled, damped oscillations of the form $\sin^2 \frac{\Omega t}{2}$ appear. The frequency of these oscillations is thus determined by the Rabi splitting. While Rabi splittings of a few meV in inorganic microcavities correspond to oscillation periods on the order of ps,[127] the large splittings observed in organic microcavities result in oscillations on the order of 10 fs.[128] The damping rate of the oscillation is a weighted average between those of the two bare constituents.[129]

Even though the investigations in the time domain can be technically challenging due

to the short time scales involved, the coherent nature of polaritons can be understood more intuitively. Importantly, the additional information on the time evolution of the oscillation also allows separating the effects of homogeneous and inhomogeneous broadening.[121] More recently, time-resolved excitation and probing experiments were able to explore the effect of pump and dissipation mechanisms in the non-equilibrium system and to control the dynamic evolution of the excited state.[130]

2.4.2 Properties of exciton–polaritons

This section describes the properties of polaritons, in which way they are linked to the properties of the uncoupled constituents; how polaritons can differ from the description above—either by violating the rotating-wave approximation or originating from the coupling of a photon to a system with more than two levels; and how their response to weak and strong excitation will be.

2.4.2.1 A mixture of light and matter

The properties of polaritons are inherently a mixture between the properties of their uncoupled constituents. As briefly touched upon previously, the character of the polariton changes along its branch and can thus be tuned by changing the probing angle or the cavity thickness (see Figure 2.6a). As a consequence, polaritons will sometimes behave more like a photon and at other times more like an exciton.

The behaviour of polaritons in the high-density regime is determined by their quantum statistics, i.e., by their spin. As quasiparticles, their spin is a superposition of the spin of the photon and of the exciton. Since both hole and electron have spin $\frac{1}{2}$, the alignment of their spins in the bound state will result in an exciton with integer spin (in organic materials, singlets or triplets), i.e., a boson.[75] When these excitons form a mixed particle with a photon—the epitome of bosonic spin-1 particles—the result will be another boson. Thus, Bose-Einstein statistics will govern the behaviour of polaritons at high densities (or low temperatures) and favour a macroscopic occupation of the ground state of the system.[54]

The photon-fraction of the polariton is crucial for being able to observe the polariton. It follows from Equation 2.23 that a polariton always consists to one part of a photon and as such, can decay from the cavity. Due to the conservation of momentum parallel to the mirrors,* prob-

*According to the Noether theorem, translational invariance in space corresponds to conservation of momentum.[97]

ing the photon field outside the microcavity gives us direct information on the polariton field inside.[70,125] Moreover, the optical signal outside the cavity at angle $\Theta = \Theta_0$ and wavevector q_0 relates to the in-plane wave vector of the polariton, $q_{\parallel}$, via $q_{\parallel} = q_0 \cdot \sin(\Theta)$.[125] This means that by measuring the optical response, we can directly infer the polaritonic dispersion relation. The second attribute of great importance inherited from the photon is the light mass close to the minimum of the dispersion relation, $m_{\mathrm{LP}} \sim 10^{-5} m_0$ (see Figure 2.6a and Section 2.2). This raises the critical temperature for Bose-Einstein condensation to above room temperature, as will be discussed in more detail later.

In contrast to photons, which are only weakly interacting particles, excitons are responsive to electric and magnetic fields. Via the excitonic fraction, this responsiveness is passed on to the polaritons and thus observable in the light leaking from the microcavity. This is manisfested, for instance, in the coupling strength—and thus energy of the polariton—being affected by electric fields, by changing the carrier density or by the number of excited dipoles.[39,131,132] A bias on the sample can, for example, control the polarisation of the photons detected outside the cavity.[133] Moreover, excitons can also be excited electrically, which means that the same holds for polaritons.[55,57] As in some materials, the oscillator strength changes with magnetic field, polaritons in these materials are also sensitive to external magnetic fields.[134] This sensitivity can then be used to distinguish bare cavity photons—irresponsive to magnetic fields—from photons originating from polaritons.[135]

Excitons also have much larger non-linearities compared to photons, originating from the Coulomb interaction between excitons, and so do excitonic polaritons. In fact, when considering polariton interaction and pumping terms, the Hamiltonian obtains a similar form as the nonlinear Schrödinger equation.[136] The nonlinearities give rise to effects like bistability or, in the region of negative band mass, bright solitons.[21,23] It should be noted at this point that this effect is more pronounced in inorganic than in organic polaritons because the excitons in the former have a larger exciton radius (see Section 2.4.3).

2.4.2.2 Ultra-strong coupling and hybrid polaritons

The following paragraphs will look at two 'special cases' of strong exciton–photon coupling. Ultra-strong coupling describes a regime where the coupling is large enough to affect the

While this is not the case in the direction of stratification (i.e., perpendicular to the mirrors), in the plane of the mirrors, translational variance and thus momentum are conserved.

ground state of the system. Hybrid polaritons are quasiparticles formed upon the coupling of one photon mode to more than one excitonic state.

It has been mentioned before that the simple description of polaritons with the coupled oscillator model (Equation 2.21) does not hold for large coupling strengths. When g is on the same order of magnitude as the exciton energy E_X, the counter-rotating terms in Equation 2.21 have to be taken into account, which means that the particle number is no longer conserved. This effect is called the ultra-strong coupling regime.[103] It has been observed in different material systems, ranging from intersubband transitions of quantum wells[137,138] over broad absorbers[52,139,140] to carbon nanotubes.[65] In the ultra-strong coupling regime, the splitting of UP and LP is no longer symmetric around $\frac{E_C+E_X}{2}$, a forbidden region opens up between the UP and the LP and changes to the ground state are expected.[103,139,141–143] Most of these changes—the energy shift of the ground state being the exception—generally do not scale with particle number, so that their effect is of little importance in the collective systems.[124,141] Recent studies have, however, found that the counter-rotating terms could drive changes in the high-excitation regime and open the possibility of new ordered phases that aim to lower the energy of the system by increasing the light–matter coupling.[144,145] Relative to the 'normal' strong coupling regime, the ultra-strong coupling regime results in a small dispersion and little change of the photonic and excitonic fractions along the LP branch.[140]

So far, we have considered a single exciton mode coupling to a photon mode. However, it was suggested by theory that the photon mode could also be used to couple two different exciton species to itself and to each other, thus forming a new hybrid polariton.[146] When the coupling strengths are larger than the energetic difference between two excitons, the hybrid polariton is formed in a narrow region on the newly arising middle polarition branch. Hybridisation has been realised for the excitons of different organic compounds, for different vibronic replicas of the same electronic transition and for mixing organic and inorganic excitons.[107,147,148] By using excitons that are degenerate in energy, the regime of hybridisation of two excitons can be extended over the entire upper and lower polariton branch.[149] For these truly hybrid polaritons, properties of both exciton species can be favourably combined to enhance the overall properties of the sample as originally suggested by theory.[59,146]

2.4.2.3 Polariton dynamics: linear response

The excitation of polaritons distinguishes between two regimes: the mainly linear regime at low excitation powers—i.e., below threshold where stimulated processes start to dominate the dynamics—and the nonlinear regime above threshold at high excitation powers, respectively. In the linear regime, interaction between polaritons plays a negligible role and the system behaves like a fully classical coupled oscillator. The nonlinear regime, by contrast, is defined by the interactions between polaritons, which become important at high densities and give rise to quantum effects like the Bose-Einstein condensation of polaritons.

In the linear regime, the microcavity is well described by the coupled oscillator model or the classical description of the linear dispersion theory.[134] The population in this regime depends on the effectiveness of relaxation mechanisms. Upon non-resonant excitation of microcavities, it was observed that the polariton population was often highest in the LP at large $q_{\parallel}$—before the slope of the dispersion relation, $\frac{\mathrm{d}E}{\mathrm{d}q_{\parallel}}$, increases towards smaller $q_{\parallel}$.[25,60,150] This was called the relaxation bottleneck and attributed to relaxation channels being less efficient for the region of large gradients.[151,152] For an efficient relaxation, by contrast, a thermal Maxwell-Boltzmann distribution is expected at low excitation powers and has since been observed.[25,60,93] The mechanisms for relaxation differ between organic and inorganic systems. In inorganic systems, polariton relaxation needs to conserve momentum and is mainly driven by phonon relaxation (towards the bottleneck) and exciton–exciton or polariton–polariton scattering.[89]

In organic microcavities, the dominant relaxation pathways vary between systems and largely depend on the properties of the uncoupled excited state, on the cavity structure and on the pumping mechanism.[43,153] Yet, only the relaxation following non-resonant pumping will be discussed here due to its relevance to the experiments presented later. An illustration of the processes discussed below is shown in Figure 2.7. Initially, non-resonant excitation generates highly excited states. Literature differs on where this initial energy is deposited, into the UP or into higher excitations of the (weakly coupled) excitonic states.[109,154] There is agreement, however, that this energy is transferred to the lowest-lying fully excitonic (i.e., uncoupled) states, the so-called exciton reservoir (ER), and that this transfer is fast ($\sim$ 100 fs).[109,154] From the ER, the UP branch can be populated either thermally or by spontaneous emission, depending on the temperature and energy differences. Scattering channels back into the exciton reservoir are, however, very efficient ($\sim$ 10 fs), so that the UP is generally depleted.[109,155]

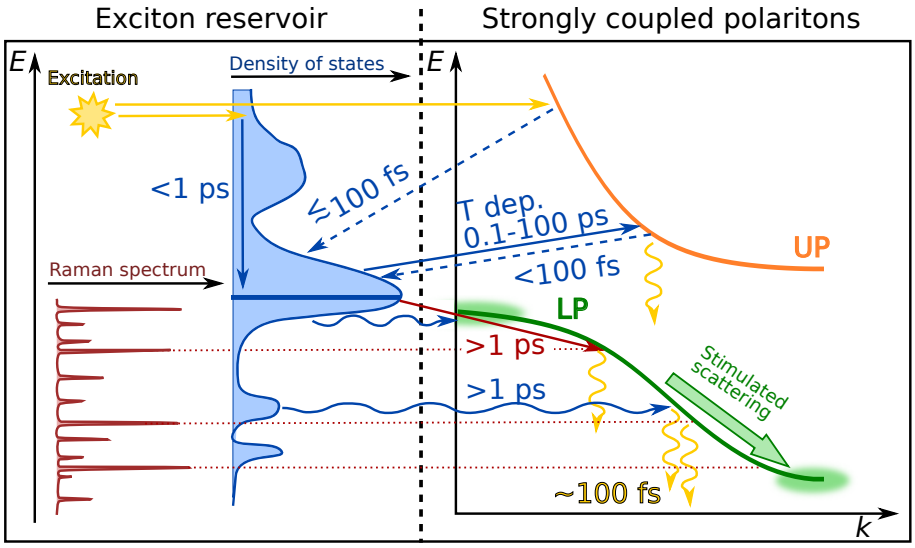

Figure 2.7: Illustration of possible relaxation pathways of organic polaritons under non-resonant excitation as described in the text. Time scales and efficiencies are estimates and depend on the concrete parameters of the system. Wriggly lines represent radiative processes, interaction with different electronic states of the exciton reservoir is indicated in blue and processes involving vibrational excitations in red.

The LP can be populated by two processes: radiative pumping or vibronically assisted scattering.[43,156,157] However, both these processes are slow (∼ 1 ps), so that a large fraction of the population (40%[120] up to >95%[154]) remains in the ER and thus localised. The core idea of radiative pumping is that only species of the highest oscillator strength are coupled to the cavity photon. Exciton species which lie lower in energy, e.g. excimers or those using other vibronic levels, can then populate the LP upon decay.[43,153] For materials with strong vibronic transitions and/or low PLQY in the microcavity, the vibronic transitions present the most efficient relaxation pathway.[41,157] Radiative and vibronically assisted pumping can also be combined in one process where the radiative transition does not end in the ground state, but in a vibronically excited state, which decays later.[153,158] Once the LP is populated, decay via the photonic fraction usually happens too fast (∼ 100 fs) for any further relaxation to occur.[109]

2.4.2.4 Polariton dynamics: nonlinear response

However, this situation changes significantly when densities become so large that interactions between polaritons do matter. Being bosons, their occupation number N_i of state i with energy

E_i follows the Bose-Einstein distribution,[159]

$$N_i = \frac{1}{e^{\frac{E_i-\mu}{k_B T}} - 1}, \tag{2.28}$$

where E_0 denotes the energetic ground state of the system, $\mu < E_0$ the chemical potential, k_B the Boltzmann constant and T the temperature. μ is a function of temperature and density. At high temperatures, where the chemical potential lies well below E_0, a Maxwell-Boltzmann distribution with a negligible occupation of the ground state is observed. It can be seen that in the limit $\mu \to E_0$ (or $T < T_c$), N_0 diverges, whereas N_i remains finite for $i > 0$.[29,160] When this phase transition occurs, the occupation of the ground state is maximised and becomes macroscopic. The new phase is called the Bose-Einstein condensate (BEC).[54] The critical temperature depends on the mass m and density ρ of the particles as[159]

$$T_c \approx 3.31 \frac{\hbar^2}{k_B m} \rho^{2/3} \tag{2.29}$$

and describes the point where the wave functions of the particles start to overlap. Two points of importance follow: (1) the low mass of the polariton favours a high T_c and (2) the system can be driven to condensate at constant temperature by increasing the density of the ground state.

It should be noted that BEC is originally only defined for 3D systems in equilibrium, whereas polaritons in microcavities are non-equilibrium particles in 2D. As a consequence, large systems show a Berezinskii-Kosterlitz-Thouless transition that is unique to 2D systems and that posesses a phase of higher order with bound vortex–antivortex pairs.[88] However, for systems of finite size—which is defined by the pump spot—, the phase of higher order is more similar to a BEC and thus termed quasi-BEC. Here, the steady state of the polaritons (including pumping and decay) can form a quasi-equilibrium outwith the bath.*[25,29] It has been argued, though, that the polariton condensate is distinct from a BEC, with distinct behaviour, and should thus not be called BEC.[161]

As microcavities containing polariton condensates emit coherent light, they are also referred to as polariton lasers.† This might be confusing since the underlying physical prin-

*Recently, microcavities of sufficiently high Q-factors have been fabricated to fully thermalise the polaritons before they leak from the cavity.[93]

†Sometimes, the distinction between polariton condensates and polariton lasers is made, depending on the extent of equilibrium,[152,162] but in this thesis, the two terms will be used interchangeably.

ciple differs fundamentally: photon lasing relies on the population inversion of a radiative transition—is thus inherently far from thermal equilibrium—and the bosonic stimulation acts on photons. By contrast, polariton condensation does not require a population inversion and the particles undergoing bosonic scattering/cooling are of mixed light–matter nature. The threshold for polariton condensation is thus expected to be lower than that for photon lasing.[54] Comparing the emission characteristics, however, the two processes look similar as both thresholds exhibit a non-linear increase of photon emission, linewidth narrowing (both in real and in momentum space) and the onset of temporal and spatial coherence.[29,85] A uniform polarisation across the spot is likewise expected in BECs and in most lasers.[29,163] Even a thermal-like distribution of the background and a spontaneous build-up of polarisation—previously thought to be the smoking gun for condensates[25,162]—have also been demonstrated in photon lasers.[164,165]

In order to unambiguously identify a condensate, two indicators need to be verified in addition to the features mentioned above. (1) Does the non-linear emission (still) arise from the coupled LP branch as opposed to the uncoupled branch of the cavity photon? (2) Does the emission show a small but continuous blue-shift with excitation power? The latter can be attributed to Coulomb repulsion of the polaritons, originating from their matter part. The attentive reader may notice an interdependence between (1) and (2), as the blue-shift will move the condensate in energy above the LP and towards the photon branch. This blue-shift should be small compared to $\hbar\Omega$, especially since lasing has also aready been shown to originate slightly red-shifted from the photon branch.[164] In organic microcavities, the blue-shift will be comparably small with respect to inorganic cavities due to the smaller exciton size and thus smaller nonlinearities (see Section 2.4.3). Nonetheless, ambiguities sometimes persist, especially in microcavities where LPs have a large photonic fraction and are thus very similar in energy to the energy of the uncoupled cavity photon.[63] Another proof to clearly distinguish polariton condensation from photon lasing is the presence of a second threshold at higher excitation powers. Here, the lower threshold corresponds to polariton lasing and the higher one to photon lasing. However, a demonstration of the second threshold is not always possible—in particular for organic materials. Low stability of the material can render the second threshold elusive, especially since the system can only be optimised for one of the phenomena.[27,62]

I conclude that although photon lasing and polariton condensation are fundamentally dif-

ferent bosonic effects, great care has to be taken to distinguish them experimentally.

2.4.3 Notes on organic polaritons

It has been mentioned before that organic microcavities differ in several aspects from inorganic microcavities. The first part of this section therefore compares the two systems directly. After that, the impact of the disorder, which prevails in many organic films, will be discussed in detail. This aspect is emphasised because the experiments discussed later in this thesis focus on the role and impact of disorder in the strong coupling regime.

2.4.3.1 Organic vs inorganic excitons

The difference between the behaviour of organic and that of inorganic semiconductors in the strong coupling regime is determined by the different properties of their excitons. Roughly speaking, organic semiconductors have larger oscillator strengths, larger binding energies and lower thermal stability than inorganic semiconductors. However, the large variety of representatives of each class blurs this simple categorisation. For example, there are organic compounds (e.g. carbon nanotubes) with a high thermal stability and likewise, there are inorganic semiconductors (e.g. GaN, ZnO) with binding exciton energies well above room temperature. This discussion focusses on those representatives mostly used in experiments. Table 2.1 compares the properties of organic and inorganic polaritons, using polymers and GaAs quantum wells as examples. Even though the exciton binding energy and oscillator strength of GaAs are on the lower end for inorganic semiconductors, this material is popular because it facilitates the epitaxial growth of high-quality microcavities.[89] Three differences between organic and inorganic excitons that have a large impact on the strong coupling regime will be explained in detail: the type of exciton, the oscillator strength and the disorder.

First, organic and inorganic materials have very different screening behaviour. Charge screening depends on the polarisability of the material and is proportional to the relative permittivity ϵ_r.[85] The higher ϵ_r, the better the material will screen the electron and hole from each other, i.e., the smaller their attraction (or binding energy) will be. $\epsilon_r \approx 3$ in organic materials, while in inorganic materials, $\epsilon_r \approx 15$, which is why they exhibit two very distinct types of excitons. At small screening, Coulomb interaction binds so-called Frenkel excitons tightly to have small Bohr radii (on one molecular unit) and large binding energies. Organic excitons are well described by the Frenkel picture and thus easily persist up to room temper-

Table 2.1: Comparison of organic and inorganic exciton parameters relevant for light–matter coupling: typical values for excitons in polymers and in GaAs quantum wells as representatives.

	Polymer	GaAs quantum well
Exciton type	Frenkel	Wannier-Mott
Schematic illustration	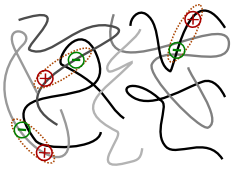	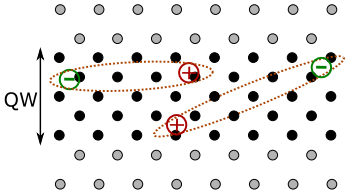
Energy diagram	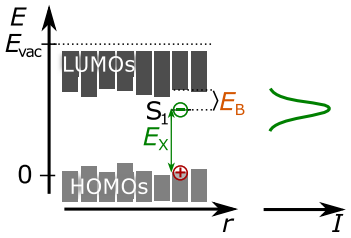	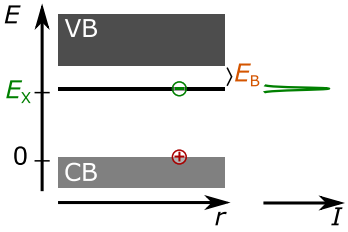
Relative permittivity ϵ_r[89]	3	15
Exciton binding energy E_B	0.3–1 eV[75,166]	16 meV[86]
Exciton radius a_B	15 Å[75]	80 Å[86]
Broadening: γ_{hom} vs. γ_{inh}	$\gamma_{hom} \ll \gamma_{inh}$	$\gamma_{hom} \sim \gamma_{inh}$[167]
Effective oscillator strength f_{eff}	$2 \cdot 10^{15}$ cm^{-2}*,[19]	$N \cdot 4 \cdot 10^{12}$ cm^{-2},[17]
Rabi splittings $\hbar\Omega$	0.1–1 eV[56,60]	4 – 20 meV[168]

*For lack of data in literature, this value is for a J-aggregate, not for a randomly disordered polymer.

ature.[169] This differs strongly from Wannier–Mott excitons, which are observed in inorganic semiconductors because there, electron and hole are well screened from each other. These excitons are delocalised over many lattice constants, even when confined in a quantum well, and often do not persist up to room temperature ($E_B < k_B T \sim 25$ meV).[86] Exceptions are GaN and ZnO with relatively low permittivities ($\epsilon_r^{GaN} \approx 6$ and $\epsilon_r^{ZnO} \approx 3$)[170,171] and therefore high exciton binding energies ($E_B^{GaN} \approx 35$ meV and $E_B^{ZnO} \approx 55$ meV)[172]. Hence, polaritons in these materials can be sustained up to room temperature. Yet, the epitaxial growth of GaN and ZnO materials is challenging[89] and the energy of the excitons would limit applications to the blue spectral range.[86,173] Finally, Bohr radii of Wannier–Mott excitons are a lot larger than those of Frenkel excitons; hence they interact much more at the same density and thus show larger nonlinearities.

Second, organic polaritons have a much larger oscillator strength. For the coupled micro-

cavity, the effective oscillator strength is of importance, which can be collectively enhanced, $f_{\text{eff}} = Nf$. Here, N is either the area density of molecules (for organic semiconductors) or the number of quantum wells (inorganic semiconductors). From Equation 2.27, we see that this directly affects the observable Rabi splitting. In contrast to inorganic polaritons, where Rabi splittings are on the order of 10 meV, organic semiconductors show splittings of 0.1–1 eV. Since the splittings are large, the requirements of the microcavity are reduced for observing organic polaritons, and even low-Q, metal-clad cavities have been shown to exhibit strong coupling.[72]

Third, disorder plays a much larger role in organic semiconductors. The lifetime of an organic exciton is on the order of 10^{-9} s, yielding a homogeneous broadening $\gamma_{\text{hom}} < 1$ μeV, while the total observed width is in general $\sigma > 10$ meV. In epitaxially grown inorganic semiconductors, inhomogeneous broadening is comparable to homogeneous broadening and can be tuned to be smaller or larger.[167] Since the effects of disorder are complex and manifold, but of great relevance for the thesis presented here, this is expanded on further below.

2.4.3.2 Effect of disorder

Disorder, though truly absent only in ideal systems, can be largely suppressed in high-quality inorganic microcavities. By contrast, in organic systems, disorder can generally not be neglected (see Section 2.1). In addition, absorption processes in typical organic semiconductors involve several vibronic transitions, which further increases the complexity of the system. The two aspects affect the linewidth of polaritons, the uniqueness of fits, and also give rise to subradiant polaritons. Moreover, they can potentially result in localisation and importantly, increase the threshold for the strong coupling regime. These effects will be explained below.

More important than the absolute amount of disorder, visible in the inhomogeneous broadening, is usually its relation to the coupling strength. When the coupling strength is larger than the inhomogeneous broadening, it can, for example suppress effects of disorder on the linewidth.[106] When the broadening related to disorder is larger or comparable to the Rabi splitting, the polariton linewidth on resonance is the average of the photon linewidth and the total linewidth of the exciton. In the weak disorder regime, where $\hbar\Omega \gg \sigma$, it is instead reduced to the average of the photon linewidth and the homogeneous linewidth of the exciton.[174,175]

The obvious effect of stronger disorder (compared to g) and the increase of inhomogeneous linewidths is the smearing out of modes (see Figure 2.8a). This relates directly to the

condition of the visibility of the strong coupling, see Equation 2.26, and can render the analysis of spectra ambiguous.[69] One broad transition in organic molecules can comprise a multitude of states of different energy, both due to disorder and to different vibro-electronic transitions. In this case, it is not clear how the coupling strength should be defined. On the one hand, it could be defined for the entire peak with the risk of gross overestimation. On the other hand, the situation could be viewed as a summation of several coupling strengths with suppressed middle polariton branches, so that the individual coupling strengths escape determination. Another ambiguity arises from the asymmetry of exciton absorption when deviating from the idealised Lorentz oscillator. In an asymmetric transition, the energy of the exciton could be defined either as the energy at peak absorption or at the centre of mass of the absorption.[176] The definition is crucial for employing the coupled oscillator model to analyse the polariton modes: different definitions of the energy of the exciton will yield different detunings, different coupling strengths and hence, different properties.[68]

Further, it was found that some samples exhibit a (weak) residual peak at the energy of the uncoupled exciton upon optical probing. This peak is generally more clearly visible in photoluminescence than in reflectance (see Figure 2.8b) and was attributed to disorder.[72,139,177,178] Even though initially, these states were explained by uncoupled excitonic states, they are now assumed to be coupled, but subradiant states.[106] They are referred to as vibrationally dressed states or dark vibronic polaritons.[124,179] When disorder is present and the coupling is large with respect to the vibronic transitions, dark vibronic polaritons couple several vibronic transitions to a single cavity mode. The larger the coupling strength is with respect to the disorder, the smaller is the intensity of the peak.[178]

Disorder can also lead to the localisation of polaritons, which can then no longer be described as wave packets.[112,120,180,181] Since the group velocity is a fundamental property of a wave packet, the latter is no longer defined when the broadening dominates over the gradient of the polariton. This leads to two regions of localisation (see Figure 2.8c), one at small angles (or $q_{\parallel} < q_{\mathrm{min}}$) and one at large angles ($q_{\parallel} > q_{\mathrm{max}}$), which differ fundamentally. While the region close to the bottom of the polariton dispersion is still a mixed light–matter state as defined above, this does not hold for $q_{\parallel} > q_{\mathrm{max}}$. Here, the excitations become similar to the weakly coupled, localised excitons, though the transition is gradual. This region is termed the exciton reservoir and plays an important role in relaxation processes (as discussed above).[109,182]

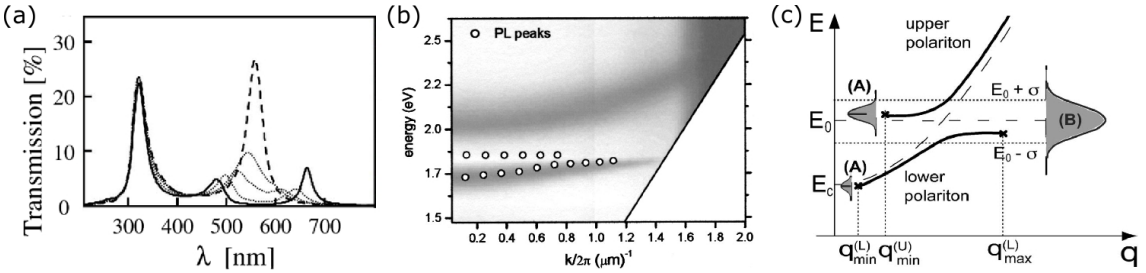

Figure 2.8: Effects of disorder on polaritons: (a) Transmission of an organic film of constant disorder with increasing coupling strength (dashed line: $g = 0$, solid line: maximum g). For intermediate coupling strengths, the anticrossing cannot be as clearly resolved as for large coupling strengths. Reprinted with permission from Schwartz *et al.* [139]. (b) Appearance of a peak in photoluminescence (PL, symbols), which is not as clearly visible in reflection (background). Reprinted with permission from Hobson *et al.* [72]. (c) Limited region of polaritons as delocalised wave packets. At regions where a group velocity can no longer be defined due to the to large uncertainty in energy/momentum, localisation occurs. While at $q_{\parallel} := q < q_{\mathrm{min}}$, the excitation is a polariton, it resembles an exciton for $q_{\parallel} > q_{\mathrm{max}}$. Reprinted with permission from Litinskaya & Reineker [180].

One of the most controversial topics in the context of disorder and strong coupling—though not necessarily treated as an open question—is whether the inhomogeneous broadening has an effect on the threshold for the onset of the strong coupling regime or not. In the absence of disorder, predictions from cavity quantum electrodynamics are unambiguous; the rate of interaction needs to be faster than the rate of decay from either of the constituents in order for the strong coupling regime to set in.[183] This corresponds to the condition formulated in Equation 2.25, that the threshold is solely determined by the lifetimes of the constituents and thus by their homogeneous linewidths.

This has been contested theoretically, mostly on the basis of linear dispersion theory (LDT), i.e., the approach to model the microcavity classically and macroscopically via its optical constants. LDT shows a reduction of the mode splitting in absorption starting from a broadened extinction coefficient, where the broadening does not depend on its origin.[102,106] It was also stated that inhomogeneous broadening effectively reduces the oscillator strength of the transition.[112] Experimentally, this is supported by experiments by Takemura *et al.* [167], who have shown that the strong coupling regime can break down at high pumping powers. This is attributed to the disorder introduced into the system by the excitation in the form of collisional broadening. The analogy of dynamic effects like collisional broadening to the predominantly static disorder encountered in organic systems, is, however, not evident.

Other reports do not find any reduction in the Rabi splitting when increasing the disorder in the material.[184] It has been pointed out by Savona *et al.* [90] that LDT predicts the splittings observed in reflection, absorption or transmission—and not the Rabi splittings. Analytic expressions derived from LDT yield different forms for reflection, absorption and transmission, all of which then depend on the total width of the exciton. Yet, these do not correspond directly to the (vacuum) Rabi splitting. Additionally, the mode positions can also appear to be shifted due to an overlap with the peak from subradiant polaritons states at the energy of the uncoupled exciton.[120] In fact, several authors explicitly mention that the threshold condition as defined in Equation 2.25 is a function of the damping rates, i.e., of the homogeneous broadening, and not of the total spectral width of the exciton.[45,90,106,114,119]

From this discussion, I draw the conclusion that the threshold might be influenced by inhomogeneous broadening of the excitonic transition. However, one cannot simply replace the homogeneous linewidth, γ_X, in Equation 2.25 with the total width, σ_X. Instead, the effect of the disorder broadening is—if it exists—more subtle and does not follow from the coupled oscillator model.[121,185] It is thus expected that inhomogeneous broadening will (in a certain range) lead to a reduction of the Rabi splitting, but it is not possible to give an analytical form for the threshold of the strong coupling regime. This is in agreement with most recent findings, according to which the Rabi splitting shows a different dependence on the homogeneous broadening than on the inhomogeneous broadening: Manceau *et al.* [175] demonstrate that the splitting is more robust with respect to disorder-induced broadening than to lifetime broadening.

The discussion of different aspects and effects of disorder presented here illustrates the complexity of the topic, which is difficult to address comprehensively both theoretically and experimentally. As a consequence, the validity of simple equations cannot be expected a priori when describing a system of strong disorder. Instead, simple, fundamental principles like the coupled oscillator model or the form of the coupling strength need to be questioned and investigated.

3

Materials and Methods

In order to perform the investigations presented in this thesis, different numerical and experimental methods were used, which will be described below. Transfer matrix simulations served to design suitable samples as well as to analyse experimental data. Microcavities were fabricated from thin films by combining different methods of deposition, involving spin coating, thermal evaporation and sputtering. Optical probing techniques like ellipsometry, reflection and luminescence measurements were employed for characterisation in order to obtain insight into the physics of the produced samples.

3.1 Simulations—the transfer matrix method

In general optics textbooks, the transfer matrix method (TMM) refers to a way to calculate the image response of an arbitrary optical system. From known optical transfer matrices of the different optical components in the system and the angle and position of the incident beam, the angle and position of the output beam can be deduced.[85] In the context of microcavities, the same principle of matrix multiplication is used to infer the overall reflection and transmis-

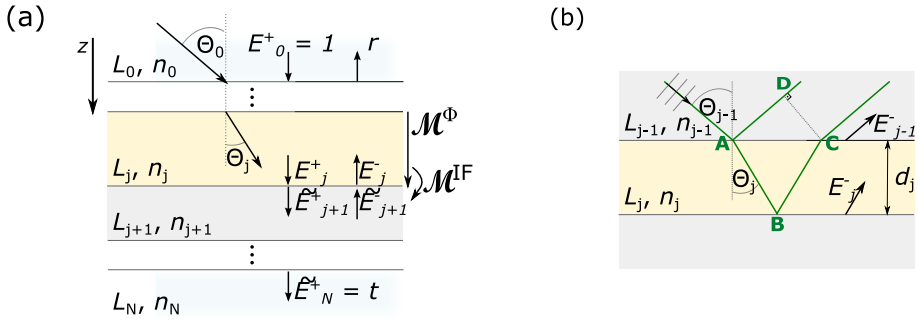

Figure 3.1: Schematic illustration of the transfer matrix method. (a) The optical system consists of a stack of $N+1$ layers L_j with refractive indices n_j. E_j^+ and E_j^- ($\tilde{E}_j^+$ and $\tilde{E}_j^-$) represent the field amplitude of waves propagating in $+z$ and $-z$ direction at the bottom (top) interface of layer L_j, respectively. The transfer matrix $\mathcal{M}^\Phi$ describes the phase shift induced by the propagation through a layer and the refraction matrix $\mathcal{M}^{IF}$ describes the refraction at an interface. (b) Illustration of light propagation across one layer. The phase shift across L_j in the transfer matrix $\mathcal{M}^\Phi$ can be determined from the path difference between beams reflected from the top of L_j and L_{j-1}.

sion of a well-defined* stack of different materials. This section is a synthesis of information found in Kavokin *et al.* [86], Byrnes [186], Troparevsky *et al.* [187], and Born & Wolf [188].

The optical response of an ideal stack which is stratified along the z axis consists of three main processes: transmission and reflection at interfaces and propagation across layers. In order to describe these, the electric field at the top and bottom interface of layer L_j is labelled as E_j^+ (E_j^-) and $\tilde{E}_j^+$ ($\tilde{E}_j^-$) for wave propagation in positive (negative) z direction, respectively (see Figure 3.1a). Introducing matrices to describe the refraction at an interface ($\mathcal{M}^{IF}$) and the propagation across a layer ($\mathcal{M}_j^\Phi$) allows us to relate the electric fields on either side of the stack:

$$\begin{pmatrix} E_0^+ \\ E_0^- \end{pmatrix} = \mathcal{M}_{01}^{IF} \cdot \mathcal{M}_1^\Phi ... \mathcal{M}_{N-1}^\Phi \cdot \mathcal{M}_{N-1,N}^{IF} \begin{pmatrix} \tilde{E}_N^+ \\ \tilde{E}_N^- \end{pmatrix} \tag{3.1}$$

Here, $\mathcal{M}_{j,j+1}^{IF}$ accounts for the refraction and transmittance at the interface between layers L_j and L_{j+1} and $\mathcal{M}_j^\Phi$ for the phase shift and attenuation caused by the propagation through layer L_j. Their mathematical form will be described later. By multiplying all matrices in the correct order, the optical response of the entire optical system can be described by a single matrix $\mathcal{M}_{tot}$. For the standard experimental case, where all light is incident from one side, e.g. the top of the stack, the incoming electric fields simplify to $E_0^+ = 1$ and $E_N^- = 0$. As a consequence, E_0^-

*As will be seen later, this requires the knowledge of the optical constants and thickness of all layers of the stack.

and E_N^+ can be identified with the total reflection coefficient r and transmission coefficient t of the system:

$$\begin{pmatrix} 1 \\ r \end{pmatrix} = \mathcal{M}_{\text{tot}} \begin{pmatrix} t \\ 0 \end{pmatrix} \tag{3.2}$$

This implies that once we know the form of $\mathcal{M}_{\text{tot}}$, we can determine the reflectivity R and the transmissivity T of the entire stack from the matrix elements M_{ij} of $\mathcal{M}_{\text{tot}}$ according to

$$\begin{aligned} T = \frac{n_N}{n_0} \cdot \frac{\cos\Theta_N}{\cos\Theta_0} \cdot t^2 \quad &= \frac{n_N}{n_0} \cdot \frac{\cos\Theta_N}{\cos\Theta_0} \cdot \left(\frac{1}{M_{11}}\right)^2 \\ R = r^2 \quad &= \left(\frac{M_{21}}{M_{11}}\right)^2. \end{aligned} \tag{3.3}$$

In order to find the optical response of the stack, R and T, we need to determine the form of $\mathcal{M}_{\text{tot}}$ and in consequence, the form of the matrices $\mathcal{M}^\Phi$ and $\mathcal{M}^{\text{IF}}$. This can be achieved by describing the change of the incident plane wave (1) due to propagation across a layer L_j (to yield $\mathcal{M}^\Phi$) and (2) due to refraction at an interface between L_j and L_{j+1} (to yield $\mathcal{M}^{\text{IF}}$).

First, we look at the form of the propagation matrix $\mathcal{M}^\Phi$. It follows from symmetry considerations that upon propagating across L_j, E_j^+ and E_j^- will have the same phase shift Φ_j, but in opposite directions, which gives the form of $\mathcal{M}^\Phi$:

$$\begin{aligned} E_{j-1}^+ &= e^{-i\Phi_j} E_j^+ \\ E_{j-1}^- &= e^{+i\Phi_j} E_j^- \end{aligned} \quad \Longrightarrow \quad \mathcal{M}_j^\Phi = \begin{pmatrix} e^{-i\Phi_j} & 0 \\ 0 & e^{i\Phi_j} \end{pmatrix}. \tag{3.4}$$

The phase shift Φ_j has the form

$$\Phi_j = \frac{2\pi\tilde{n}_j}{\lambda_0} \cdot \cos\Theta_j d_j. \tag{3.5}$$

Note that $\tilde{n}_j = n_j - ik_j$ is the complex index of refraction as introduced in Chapter 2.2 with n_j and k_j describing dispersion and absorption, respectively. Thus, the 'phase shift' Φ_j also accounts for attenuation of the electric field according to the extinction coefficient k. Since it is not intuitive why we multiply by $\cos\Theta_j$ instead of dividing by it in Equation 3.5, the form of Φ_j is derived in the following.

To understand the phase relation of two waves propagating in the same direction in adjacent layers (here E_j^- and E_{j-1}^-), we look at the beam path illustrated in Figure 3.1b. The

incident wave is partly reflected on the interface at the top of L_j and partly refracted with subsequent reflection at the bottom of L_j. Approximating the incident wave to be a plane wave, we are interested in the phase difference of the beams reflected off the top and bottom of L_j in the direction of propagation, i.e. on the wave front DC. The optical path difference on the wave front, Δ, is calculated as

$$\begin{aligned}\Delta &= n_{j-1} \cdot AD - n_j \cdot (AB + BC) \\ &= n_{j-1} \sin\Theta_{j-1} \cdot 2d_j \cdot \tan\Theta_j - \frac{2n_j d_j}{\cos\Theta_j} \\ &= 2n_j \cos\Theta_j d_j,\end{aligned} \tag{3.6}$$

where we used Snell's law, $n_j \sin\Theta_j = n_{j-1} \sin\Theta_{j-1}$. In order to determine the phase difference between the two beams propagating in the same direction, we use $\Phi_j = \frac{2\pi}{\lambda_0} \cdot \frac{\Delta}{2}$ and thus recover Equation 3.5.

The second process we need to describe with a matrix is the reflection and refraction of light on the interface from L_j to L_{j+1}. For better readability of the following equations, we set $j = 1$. At each interface, the fraction of the reflected and transmitted light (reflection coefficient r and transmission coefficient t, respectively) can be derived from the Maxwell equations and the boundary condition that the tangential part of the electric field is continuous across any interface. This results in the Fresnel equations, which give r and t with respect to the polarisation of the incoming light:

$$\begin{aligned}\text{TE-pol.:} \quad r_{12}^{\perp} &= \frac{n_1 \cos(\Theta_1) - n_2 \cos(\Theta_2)}{n_1 \cos(\Theta_1) + n_2 \cos(\Theta_2)}, \qquad t_{12}^{\perp} &= \frac{2n_1 \cos(\Theta_1)}{n_1 \cos(\Theta_1) + n_2 \cos(\Theta_2)} \\ \text{TM-pol.:} \quad r_{12}^{\parallel} &= \frac{n_2 \cos(\Theta_1) - n_1 \cos(\Theta_2)}{n_2 \cos(\Theta_1) + n_1 \cos(\Theta_2)}, \qquad t_{12}^{\parallel} &= \frac{2n_1 \cos(\Theta_1)}{n_2 \cos(\Theta_1) + n_1 \cos(\Theta_2)}\end{aligned} \tag{3.7}$$

Here, $\perp$ represents s-polarised or TE-polarised light, where the electric field is perpendicular to the plane of incidence and $\parallel$ represents p-polarised or TM-polarised light, where the electric field is parallel to the plane of incidence. It follows directly from the Fresnel equations that

$$\begin{aligned} r_{12} &= -r_{21}, \\ t_{12}t_{21} - r_{12}r_{21} &= 1,\end{aligned} \tag{3.8}$$

which will be useful later.

From Figure 3.1a, it is seen that the amplitudes of the electric field can be expressed with the help of the reflection and transmission coefficient as follows:

$$\begin{aligned} E_1^- &= r_{12}E_1^+ + t_{21}\tilde{E}_2^- \\ \tilde{E}_2^+ &= t_{12}E_1^+ + r_{21}\tilde{E}_2^- \end{aligned} \tag{3.9}$$

By inserting Equation 3.8 into Equation 3.9, this can be rearranged to yield the form of the refraction matrix $\mathcal{M}^{\mathrm{IF}}$:

$$\begin{aligned} E_1^+ &= \frac{1}{t_{12}}\left(\tilde{E}_2^+ + r_{12}\tilde{E}_2^-\right) \\ E_1^- &= \frac{1}{t_{12}}\left(r_{12}\tilde{E}_2^+ + \tilde{E}_2^-\right) \end{aligned} \quad \Longrightarrow \quad \mathcal{M}_{j,j+1}^{\mathrm{IF}} = \begin{pmatrix} \frac{1}{t_{12}} & \frac{r_{12}}{t_{12}} \\ \frac{r_{12}}{t_{12}} & \frac{1}{t_{12}} \end{pmatrix}. \tag{3.10}$$

The full response matrix, $\mathcal{M}_{\mathrm{tot}}$, is then obtained by multiplication of all transfer and propagation matricies (compare Equations 3.1 and 3.2).

A modification of the same principle was used to calculate the distribution of the electric field in the stack as reported by Pettersson *et al.* [189]. For this, the same equations (3.1, 3.4 and 3.10) are used, but $\mathcal{M}_{\mathrm{tot}}$ is not calculated for the entire stack as explained above. Instead, two additional variables are introduced, z for the absolute physical position inside the stack and $\tilde{z}$ for the relative position inside layer L_j. Now, the total transfer matrix needs to be evaluated before and after L_j, yielding $\mathcal{M}_{\mathrm{tot}}^{<j}$ and $\mathcal{M}_{\mathrm{tot}}^{>j}$, respectively, so that the full response corresponds to $\mathcal{M}_{\mathrm{tot}} = \mathcal{M}_{\mathrm{tot}}^{<j} \cdot \mathcal{M}_j^{\Phi} \cdot \mathcal{M}_{\mathrm{tot}}^{>j}$. Then, the electric field at position z can be calculated as[189]

$$E(z) = \frac{M_{11}^{>j} \cdot e^{-i\xi\left(d_j - \tilde{z}\right)} + M_{21}^{>j} \cdot e^{i\xi\left(d_j - \tilde{z}\right)}}{M_{11}^{<j} M_{11}^{>j} \cdot e^{-i\xi d_j} + M_{12}^{<j} M_{21}^{>j} \cdot e^{i\xi d_j}}, \tag{3.11}$$

where $\xi = \frac{2\pi\tilde{n}_j}{\lambda_0} \cdot \cos\Theta_j$. The electric field distribution can be calculated by calculating $E(z)$ for $0 \leq z \leq d_{\mathrm{tot}}$.

In the course of this thesis, the TMM was implemented into a matlab code to calculate the reflection and transmission of an arbitrary stack of materials and the distribution of the electric field therein. The core of the matlab code, which calculates either reflection or transmission of a given stack structure and wavelength or the electric field across, is given in the Appendix. This script is then called by a different script, in which the simulation parameters like variables, stack structure and probing methods, are defined.

3.2 Sample fabrication

In order to produce microcavities, films of different materials with thicknesses between 3 and 200 nm were deposited as multi-layer stacks on glass substrates. Depending on the deposited material, different techniques allow for the controlled deposition of such thin films. They will be explained in the following section. For more detailed information on the techniques, see for example Yonkoski & Soane [190], Frey & Khan [191], and Wasa *et al.* [192].

3.2.1 Spin coating: thin organic films from solution

Some materials can be dissolved in standard solvents, which enables them to be deposited in thin films by spin-coating. This process uses the large centrifugal forces on a substrate which is spun very quickly to reduce a large initial quantity of a solution on the substrate to a thin film.

After a solution of a specified concentration is created, it is drop-cast onto the substrate, which is held by suction to the spin-coater. When the substrate starts to rotate at high frequencies (500 to 5000 rpm), only the friction between solution and substrate and the viscosity of the solution act as centripetal force. Hence, most of the solution is carried off the substrate and only a thin, homogeneous film is retained on the substrate, from which the remaining solvent quickly evaporates. The film thickness can be controlled by varying the spin speed and/or the concentration of the solution. The advantage of this technique is that it can be carried out at ambient conditions and that it is quick and simple. However, not all materials can be deposited from spin coating since the process is, despite its technological simplicity, chemically complex. The formation of smooth films requires a solute–solvent pair with complementary properties regarding solubility, viscosity, vapour pressures, surface tensions and more.

Spin coating was used to deposited thin films of the polymers and of the J-aggregate described in Section 3.4, where processing parameters are given.

3.2.2 Thermal evaporation

The thermal evaporation process is schematically shown in Figure 3.2a. It relies on controllably heating the material which is to be deposited until the vapour pressure is sufficiently high to yield a stable evaporation rate. The high vacuum in the chamber ($\lesssim 10^{-6}$ Torr $\approx 10^{-4}$ Pa) ensures a ballistic transport of the evaporated atoms and molecules to the substrate and a

high purity of the deposited film. The ballistic nature of the propagation is important for high purities of the film (collisions increase the risk of contamination) and a directional evaporation. Mechanical shutters allow for control over the start and end of the deposition onto the substrate.

Materials have to fulfil two main requirements to allow for their thermal evaporation. Firstly, the temperatures for the desired vapour pressure need to be achievable with resistive heating. While for organic materials, this is not usually a restriction (evaporation temperatures generally $T_{\mathrm{evap}} < 500°\mathrm{C}$), and metals like silver can also be evaporated, in some other material classes, like oxides, melting points are too high to reach the necessary evaporation rates by resistive heating. Secondly, the temperature required for thermal evaporation needs to be lower than the temperature at which decomposition of the material sets in.[193] If this is not the case, e.g. for large, heavy molecules like polymers, the energy added to the system will first break bonds of the molecule before it will suffice to lift molecules into the gas phase.

In thermal evaporators, the thickness of the deposited film is controlled with a quartz crystal, of which the resonance frequency is monitored with great accuracy. The resonance frequency depends on the weight deposited on the crystal, so that from the knowledge of the density of the deposited material, a film thickness d_{QC} can be deduced. However, the quartz crystal is generally at a different (though fixed) position from the substrate and the evaporation rate depends on the position relative to the source (see below). Hence, the thickness deposited on the substrate, d_{S}, has to be inferred via the tooling factor t, which describes the fixed deposition ratio between substrate and crystal, via $d_{\mathrm{S}} = t \cdot d_{\mathrm{QC}}$.

Quartz crystal monitoring allows for high control over the film thickness, which, in a thermal evaporator, can be very homogeneous across the substrate. In order to obtain homogeneous films, the substrate rotates during deposition. The homogeneity also depends on the distance between source and substrate, since the evaporation rate Γ depends on the angle from the normal of the (small) evaporating surface, α, approximately like $\Gamma \propto \cos\alpha$. In the evaporator design, this is usually weighed against a larger waste of material for larger source–substrate distances.

Metal mirrors on solution-processed organic films were deposited from a single-source thermal evaporator by Edwards. An Evovac vacuum deposition system by Angstrom Engineering was used for fabricating microcavities containing thermally evaporated, organic materi-

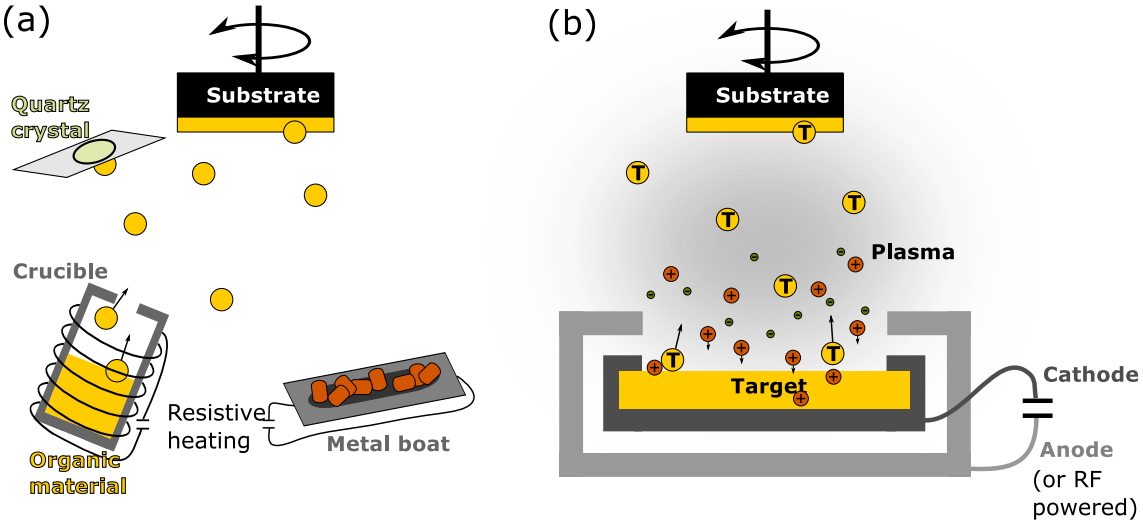

Figure 3.2: Schematic illustration of high-vacuum, thin-film fabrication methods. (a) Working principle of a thermal evaporator: materials are resistively heated, either via a coil around the crucible or of the boat directly, until their evaporation temperatures are reached. In the high vacuum, the evaporated molecules or atoms propagate ballistically to the substrate, where they condense and form a smooth, thin film. A quartz crystal is used for monitoring the thickness of the deposited film. (b) Working principle of the sputterer: ions of a plasma are accelerated onto a solid state target. By transferring their energy into the target, they eject atoms which propagate to the substrate, where they the thin film.

als. The Evovac system can hold up to ten different organic materials in crucibles and up to three materials evaporated from resistive boats. The substrate holder can hold up to sixteen 24 × 24 mm substrates. The thickness difference between the centre and the outermost point on the diagonal was 9%. The system contains movable wedges, allowing either for a thickness gradient along one direction or for different evaporation parameters between different rows. The organic materials C545T and MADN (see Section 3.4) were deposited by the Evovac evaporator.

3.2.3 Sputtering

For materials with very low vapour pressures at temperatures achievable with resistive heating, sputtering can be used for depositing thin films. In the process, as sketched in Figure 3.2, atoms of the target are 'catapulted' into the gas phase by ions impinging onto the surface of the target. The atoms then propagate to the substrate, where they form a thin film.

The ions impinging onto the substrate are part of a plasma, which is created by applying a voltage between cathode and anode (earthed). The plasma ignites when an electron is released

by a gas molecule via a random process (e.g. a collision). The voltage accelerates the electron, which collides with other gas molecules, thus triggering a cascade by setting further electrons free. Once the plasma is created, electrons are accelerated away from the target, ionising more molecules. At the same time, the ions are accelerated onto the solid-state target, thereby ejecting atoms from the target. Since this is not an equilibrium process, even materials with very strong binding energies in the solid state can be deposited in this way. In the sputtering process, the propagation of particles to the substrate is not ballistic but involves a few collisions with gas molecules or electrons. This is because the background pressure during a sputtering process is several mTorr ($\sim$ 0.1 Pa) to sustain the plasma, a pressure in which a mean free path length of less than 10 cm is expected. The gas used for the plasma is chosen to be relatively inert and heavy (e.g. Ar, N_2, Xe). However, it can be mixed with a reactive gas (e.g O_2) for improved stoichiometry of the deposited film.

There are several variants of the sputtering process, of which those that apply to the system and processes used in this thesis will be explained. For example, the voltage mentioned before can be either applied as a direct current (DC) or in a radiofrequency alternating current (RF). While DC sputtering can be employed for conducting materials, this process would cause problems for insulating materials like oxides. A non-conducting surface would become positively charged due to the collisions with ions, resulting in a repulsion positive ions by the surface and eventually in an end of the deposition. By contrast, RF sputtering avoids this issue by alternatingly accelerating electrons and ions onto the surface of the target, which leaves the target neutral overall. Finally, magnetic fields serve to confine the electrons—and hence, the plasma—in the space close to the target. Importantly, the localised plasma reduces the damage to the substrate. This is crucial for sputtering on top of organic materials, as the relatively low binding energies render organic materials sensitive to any interactions with high-energy particles.

For the experiments performed in this thesis, all sputtering was performed in a Nexdep 030 DC/RF magnetron sputtering system by Angstrom Engineering with in-situ control of the film thickness via quartz crystal monitoring. DC sputtering was employed for depositing metal mirrors. RF sputtering was used for depositing thin films of SiO_2 and distributed Bragg reflectors (DBRs, see Chapter 2.2) from SiO_2 and Ta_2O_5 films. Since the sputtering system was newly installed in St Andrews, the parameters for obtaining films and stacks of films of high quality were optimised within this PhD project. The energy for sputtering the oxides (90 W)

Table 3.1: Process parameters for sputtering metals and oxides.

Material	Power	P source	Process gases	Gas flows	Process pressure
Ag, Al	$\sim$ 45 W	DC	Ar	20 sccm	3 mTorr
SiO_2	90 W	RF	Ar	20 sccm	2 mTorr
Ta_2O_5	90 W	RF	Ar/O_2	20/4 sccm	3 mTorr

was supplied by a RF source, that for Al and Ag films by a DC source ($\sim$ 15 W). For metals, the rates were controlled and kept constant (at $\sim$ 1 Å/s). For the oxides, by contrast, the maximum sputtering power below the threshold for target damage were chosen and maintained throughout the sputtering process, so that only the end of the process was controlled by quartz crystal monitoring. While SiO_2 and metals were sputtered with a pure Ar plasma, an Ar/O_2 gas mixture of 1/5 was necessary to obtain Ta_2O_5 films of good quality. The minimum oxygen concentration at which no contamination with different tantalum oxides occurred was chosen in order to maintain a reasonable sputtering rate. The processing parameters for different materials are summarised in Table 3.1.

3.3 Optical characterisation

The optical probing methods explained below served to study the properties of single films and full microcavities. Variable angle ellipsometry allowed for determining optical constants and thicknesses of thin films. On the same instrument, angle-dependent reflection and transmission measurements were performed, from which the stack structure and positions of polariton modes could be deduced. Luminescence measurements further gave insight into the population and dynamics of the polaritons. The stability of the organic films was investigated with measurements of the photoluminescence quantum yield.

3.3.1 Ellipsometry

Ellipsometry measures the change of polarisation of an electric field when reflected from a stack of materials. From this change, film parameters like the optical constants, $\tilde{n} = n - ik$, or the film thickness d can be determined, as schematically illustrated in Figure 3.3. This is possible because the reflection and transmission coefficients of an electric field, which are a function of the complex optical constants, also depend on the plane of incidence (see Equation 3.7). As the components parallel and perpendicular to the electric field are changed in a different

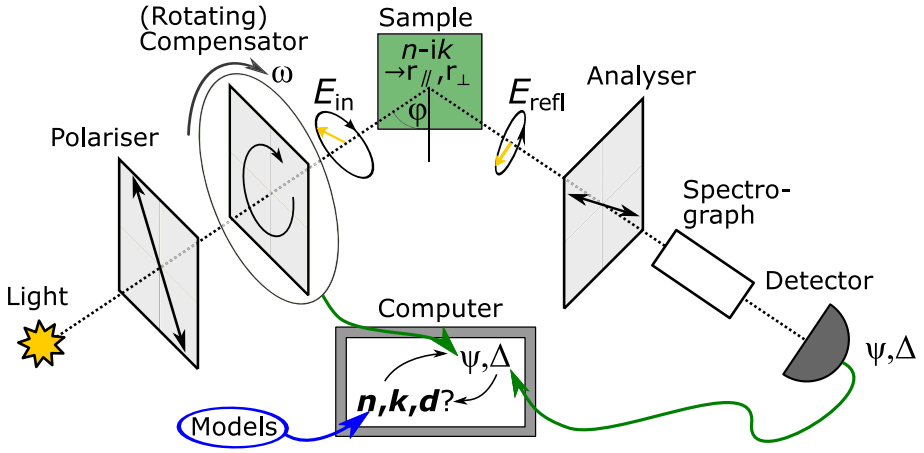

Figure 3.3: Working principle of a spectrographic ellipsometer with rotating compensator. White light is elliptically polarised by means of a linear polariser and rotating compensator. It is incident on the sample at angle φ. The polarisation of the reflected light, E_{refl}, is analysed with a second linear polariser and the spectral differentiation uses a spectrograph in combination with a CCD camera. An automated, iterative fit of a model of the sample to the measured ellipsometric parameters, Ψ and Δ, is used to determine e.g. the complex refractive index.

manner upon reflection and transmission, the polarisation of the light changes. This section will describe the theory behind ellipsometric measurements and is based on descriptions in Tompkins & Irene [194], J. A. Woollam Co., Inc. [195], and Cobet [196].

In order to record the change induced by the probed material, the electric field before and after incidence onto the surface needs to be determined and compared. Figure 3.3 shows that this is done by placing one linear polariser between source and sample and another as analyser between sample and detector. Additionally, a compensator or retarder can be built in after the polariser or before the analyser. This setup creates elliptically polarised light because polarisations along different axes of the compensator propagate at different speeds. The challenge of the method lies in determining the change of polarisation from a measurement of intensities on the detector. For this, the polarisation state of the light incident on the sample and of the analyser needs to be known. In order to obtain information on the properties of the sample, (i.e., to distinguish between absorption and suppression by different polarisations in analysed light and analyser) either of the polarisations needs to be varied, which is usually done by rotating one component continuously. An internal, instrument-dependent function then calculates the change in polarisation, from which the ellipsometric parameters can be determined. Depending on the nature of the sample, the number of parameters that are necessary to fully describe the optical response ranges from two (simplest, assuming in-plane isotropy) to six or more. In

this thesis, only two parameters were necessary to represent the optical response of the stacks:

$$\rho = \frac{r_{\parallel}}{r_{\perp}} := \tan(\Psi) \cdot e^{i\Delta}. \tag{3.12}$$

Here, ρ is the complex ratio of reflection coefficients for p-polarised and s-polarised light, $r_{\parallel}$ and $r_{\perp}$, respectively. Ψ and Δ serve to facilitate the analysis by splitting ρ into an amplitude and a phase term, respectively.

Similar to the transfer matrix method explained in Section 3.1, the change of the electric field is described with one matrix per optical component. The interaction with the sample is also described by matrices. Since the incident and reflected field are measured and the matrices for polariser, compensator and analyser are known, the reflectivity of p- and s-polarised light, and thus Ψ and Δ, can be deduced. Ψ and Δ are the output parameters of the measurement. However, it is not trivial to obtain the complex refractive index from this data—especially, when p- and s-polarisation are cross-correlated in anisotropic media.

In order to draw any conclusions about the properties of the sample from the knowledge of Ψ and Δ, a model of the sample needs to be built. This model represents all relevant interfaces with defined thickness and potential surface roughness, and all layers with their optical constants. The system is defined as well as possible (input of known parameters versus variables) to increase the specificity of the fit. All unknowns are set as variables, e.g. the thickness of the film and/or parameters in model functions for optical constants. In an iterative process, the variables in the model are then fitted to approximate the measured parameters. While the fitting process and the compliance with the Kramers–Kronig relations* for the optical constants are software controlled, the different models are defined by the user. Thus, the quality of the data obtained by ellipsometry measurements strongly depend on the adequacy of the chosen model and thus on the user.

In practice, the number of variables in the system is held as small as possible. Experimentally, this means that thin films are analysed on substrates with established optical constants and films are intended to be homogeneous with little surface roughness. The number of variables in the simulations is kept low by determining different parameters successively. For instance, a first fit to determine the thickness of the film only considers wavelengths far above

*The Kramers–Kronig relations link the real and imaginary part of an arbitrary complex function (the only restriction being analyticity for positive imaginary numbers) via the Cauchy Principal Value. Physically, this connection makes sense because both dispersion and attenuation are caused by dipole interaction with the incident light.

the bandgap. This is useful because the extinction coefficient k can be neglected in this range and the refractive index can be expected to follow a Cauchy model, $n(\lambda) = A + B/\lambda^2 + C/\lambda^4$. Once the thickness of the film and the background refractive index are established, a fit over the entire range yields the full set of isotropic optical constants obeying the Kramers-Kronig relations. Depending on the expected micro-structure of the sample, an anisotropic fit is performed subsequently using the isotropic optical constants as starting point.

The data presented in this work were obtained from a variable-angle spectroscopic ellipsometer with rotating compensator, M-2000DI by J.A. Woollam Co., Inc. In the instrument, white light by a Deuterium and a quartz tungsten halogen lamp is used to cover the spectral range from 200 to 1700 nm. Angles can be varied between 45° and 90° in reflection and arbitrarily in transmission mode, which is important for acquiring ellipsometric data close to the Brewster angle. The rotating-compensator configuration ensures high accuracy for the entire range of ellipsometric angles (Δ) across the entire wavelength range and enables to determine the sign of Δ. This is in contrast to rotating polariser or analyser configurations, where the accuracy drops for $\Delta \approx 0, \pi$ and the sign of Δ is not accessible. Ellipsometric data analysis is performed using the WVASE32 software by J.A. Woollam Co., Inc.

3.3.2 Reflection and transmission measurements

While ellipsometry is a very powerful technique for gaining detailed information about stratified stacks of thin films, spectrally resolved transmission and reflection measurements are more suitable for directly probing the modes of the system. They are also performed on the M-2000DI, but use a different measurement mode.

Both the transmission and reflection measurement require the acquisition of a reference spectrum to which the reflected or transmitted spectrum is compared. As for the ellipsometric data, the spectral range between 200 to 1700 nm is covered. Reflection can be measured between $40° \lesssim \varphi \lesssim 85°$ with an accuracy of $\Delta\varphi \leq 0.1°$ due to angle control by a micrometer screw gauge with Vernier scale. Transmission angles can be chosen arbitrarily—though due to the design of the sample holder only angles for $\varphi \lesssim 45°$ use the full intensity—with an accuracy of $\Delta\varphi \approx 2°$. The dynamic range is estimated from transmittance measurements of an opaque sample to cover four orders of magnitude.

3.3.3 Luminescence measurements

The reflection and transmission measurements described above provide information about the spectral position of the polariton modes. They cannot, however, give insight into the population of these states or of the dynamics of polaritons. Instead, luminescence measurements were performed on a custom-built setup, as sketched in Figure 3.4.

The exciting laser is an Opolette 355 by Opotek Inc. This instrument uses a pulsed Nd-YAG laser (1064 nm, pulse length 5 ns, repetition rate 20 Hz) that is frequency tripled (355 nm) to drive an optical parametric oscillator (OPO) consisting of a non-linear crystal and a resonator. The OPO enables a tunable output at wavelengths between 410 and 2400 nm by changing the resonance condition of the resonator that contains the non-linear crystal. Additionally, the lasing wavelength of the Nd-YAG laser is available as well as its frequency-doubled and frequency-tripled wavelengths at 532 nm and 355 nm, respectively. In the experiments shown here, either the 355 nm output or the tunable output at 420 nm was used with pulse repetition rates between 2 and 20 Hz.

Figure 3.4 illustrates the beam path in the optical setup, from the laser over the sample to the camera. The output light (blue beam path) is variably attenuated to probe the response of the sample to different pump powers. Moreover, residual stray light (especially of the 532 nm output) is filtered from the beam before the light enters the objective. Depending on the wavelength of the pump beam, a 400 or 450 nm shortpass filter is used. The objective lens focuses the pump beam onto the sample and, at the same time, collects the luminescence from the sample (green beam path). Using a beam splitter, the luminescence is guided through a longpass filter, which suppresses the pump light scattered and reflected from the sample. Optionally, a polariser can be inserted into the beam path to only look at TE- or TM-polarised light. An (optional) insertion of an additional 'Fourier lens' allows for Fourier imaging, which will be explained below. Finally, the imaging lens focuses the light onto a Shamrock 500i spectrograph with a Newton 971 EMCCD camera.

The $4f$-setup for acquiring far-field or Fourier images is illustrated in the inset of Figure 3.4. The setup is changed to Fourier mode by placing an additional lens at a position where its focal plane coincides with the back focal plane of the objective lens. It is known from ray optics that parallel rays will meet in the focal plane of a lens. Thus, in the back focal plane of the objective lens, light from different spots of the sample, but irradiating in the same direction, will meet

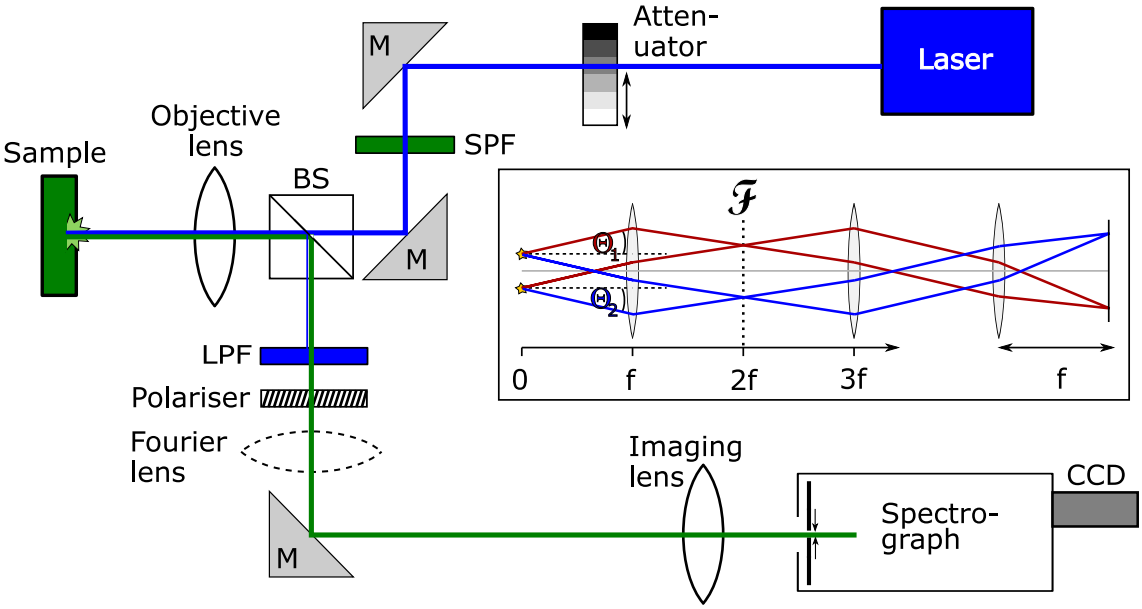

Figure 3.4: Optical setup for luminescence measurements. Light from the laser (blue path) is variably attenuated to control the power arriving on the sample. Before being guided into the objective lens, light of longer wavelength than the excitation wavelength is filtered out with a shortpass filter (SPF). The objective lens focuses the light onto the sample and collects luminescence from the spot (green path). Beam paths of excitation and collection are separated by a beam spliter (BS). A longpass filter (LPF) suppresses the excitation signal in the light collection. A Fourier lens and a linear polariser are optionally inserted into the beam path for measuring the Fourier image and filter out a single polarisation, respectively. An imaging lens focuses the light onto the entrance slit of the spectrograph, behind which the light is detected with a CCD camera. The inset shows a ray-optics illustration of the beam path for Fourier imaging using three lenses with the same focal length f. $\mathcal{F}$ denotes position of the Fourier plane.

in one spot. In other words, in the back focal plane, we see an image of the angle distribution of light from the sample. More rigorously, it can be derived that in the focal plane of a thin focusing lens, the Fourier transform of an aperture or object in the opposite focal length is observed. This transformation connects spatial frequency, which is the wave vector parallel to the sample surface, $q_{\parallel} = q \cdot \sin\Theta$, to the position x in the Fourier plane $\mathcal{F}$.[85] $\mathcal{F}$ can then be imaged onto any plane using two additional lenses. In the setup used, the magnification of the image onto the spectrograph is performed by the Fourier lens and the imaging lens, which magnify the image into the spectrograph. Due to the spectral discrimination in one plane, a 2-dimensional image forms on the detector. The image shows the intensity from the sample as a function of the wavelength of the light and of $q_{\parallel}$. Apart from lens aberrations, the Fourier image thus directly maps the dispersion relation of Equation 2.8 onto the detector.

3.3.4 Measurement of the photoluminescence quantum yield

The PLQY of luminescent materials is routinely determined with an integrating sphere. For this measurement, the sample is placed into a sphere with a white, scattering inside surface, where it is excited with monochromatic light at a chosen wavelength. Ideally, all light scattered or emitted from the sample is collected and analysed spectrally. From the difference in intensity at the pump energy between the sample and a reference measurement, the number of absorbed photons, n_{abs}, can be determined. Likewise, the number of emitted photons, n_{em}, is determined for longer wavelengths. The PLQY is then obtained from $\Phi = \frac{n_{\mathrm{em}}}{n_{\mathrm{abs}}}$ (see Chapter 2.1).

The setup used for determining the PLQY was the commercial C9920-02 instrument by Hamamatsu. It comprises a xenon light source and a monochromator (FWHM $\leq$ 10 nm) to generate the excitation light, an integrating sphere with optional N_2 purge, a spectrograph and analysis software. The setup is estimated to provide PLQY values that are accurate up to 2%.

3.4 Materials

Organic materials served as the active material in the microcavities investigated in this thesis. For different purposes, different materials were chosen, ranging from polymers over J-aggregating small molecules to amorphous small molecules. The chemical structures of all used materials are shown in Figure 3.5. The different mirror materials used are also described in this section.

3.4.1 Organic materials

Thin films of organic materials were processed either onto the bottom mirror of a cavity or directly onto silicon or glass substrates, which served to measure the properties of bare films via transmission, PLQY or ellipsometry measurements. Depending on the properties of the organic materials, they were processed by solution or by thermal evaporation.

3.4.1.1 Solution-processed films

Thin films of four different organic semiconductors were processed from solution: poly[9,9-dioctylfluorenyl-2,7-diyl] (PF8), poly[(9,9-dioctylfluorenyl-2,7-diyl)-alt-co-(1,4-benzo-2,1',3-

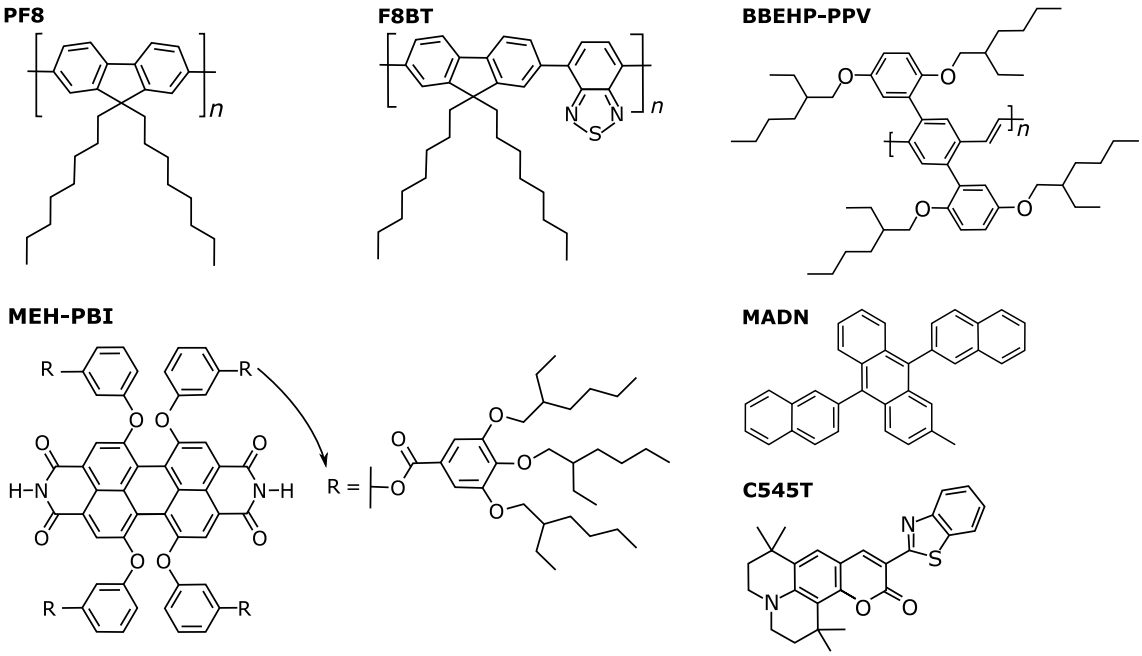

Figure 3.5: Chemical structure of the organic materials investigated in this thesis. The polymers PF8, F8BT and BBEHP-PPV and the J-aggregating small molecule MEH-PBI were deposited from solution. The small molecules C545T and MADN were thermally evaporated and used as active and matrix material, respectively.

thiadiazole)] (F8BT), poly[2,5-bis(2′,5′-bis(2″-ethyl-hexyl-oxy)phenyl)-p-phenylene vinylene] (BBEHP-PPV) and the J-aggregate forming dye MEH-PBI. The polyfluorenes PF8 and F8BT were purchased from American Dye Source, Inc. (ADS129BE and ADS133YE with a molecular weight of 40–150 kDa and 15–200 kDa, respectively). BBEHP-PPV and MEH-PBI were synthesised and provided by collaborators at the University of Strathclyde (group of Prof. P. Skabara) and Würzburg University (group of Prof. F. Würthner), respectively.

The different organic materials were dissolved using different protocols, which are summarised in Table 3.2. By changing the concentration of the solution (9–17 mg mL^{-1}) and the spin speed (1000–4000 rpm), both of which were varied between different samples and sample sets, thin films between 50 and 150 nm were fabricated from spin coating.

3.4.1.2 Thermally evaporated films

Thermal evaporation of the organic layer has the advantage over solution processing that in-situ control enables deposition of neat films or host–guest mixtures to a high level of accuracy. In order to fabricate more complex sample structures, the coumarin dye 2,3,6,7-tetrahydro-1,1,7,7,-tetramethyl-1H ,5H ,11H -10-(2-benzothiazolyl)quinolizino[9,9a ,1gh]coumarin (C545T)

Table 3.2: Process parameters for spin-coating polymers and J-aggregating small molecules.

Material	Solvent	Dissolution mechanism
PF8	Toluene	Stirring at 60 °C for 1/2 day
F8BT	Toluene	Stirring at 60 °C for 1/2 day
BBEHP-PPV	Chlorobenzene	Shaking manually at room temperature
MEH-PBI	Chloroform	Shaking manually at room temperature

was chosen as active material with 2-methyl-9,10-bis(naphthalen-2-yl)anthracene (MADN) as a matrix material (see Figure 3.5). Both were acquired from Lumtec (LT-E502 at a purity of $> 99\%$ and LT-E410 at a purity of $> 99.5\%$, respectively). Films of a thickness of 3–150 nm were fabricated with the C545T:MADN ratio varying between 1 and 1/99. The overall thickness was reproducible within a variation of $< 5\%$.

The intended doping concentrations were regulated by changing the evaporation rates of different materials. However, in order to have as small as possible variations on the doping concentration, the tooling factor of the dopant was artificially enhanced in order to increase the sensitivity:

$$t_{\mathrm{dop}} = t_{\mathrm{orig}} \left(\frac{1}{C} - 1 \right). \tag{3.13}$$

Here, C is the intended doping concentration, t_{orig} is the 'normal' tooling factor, determined from a neat film and t_{dop} is the artificial tooling factor, which serves to be able to evaporate both materials at (seemingly) the same rate. The success of this method was limited—especially at low doping concentrations, the concentration estimated from the absorption spectrum was two- to three-fold higher than intended. This high concentration, however, was then reproducible, so that in the end, nominal and measured concentrations did not differ noticeably. The actual concentrations were determined from the optical constants (k), which agreed with a comparison of PLQY measurements to literature and were thus deemed reliable. There are two possible reasons for the initial deviation of nominal and measured concentration: (1) It could be that in combination with MADN, the adsorption of C545T on the substrate is increased. This might be caused by interaction between the molecules that change the surface energy of the mixture. (2) The relative adsorption of C545T on the quartz crystal might be reduced at lower absolute evaporation rates. Such a behaviour could be tested by independently determining rate-dependent tooling factors, which was, however, not performed since a different way was found to make nominal and actual concentrations agree.

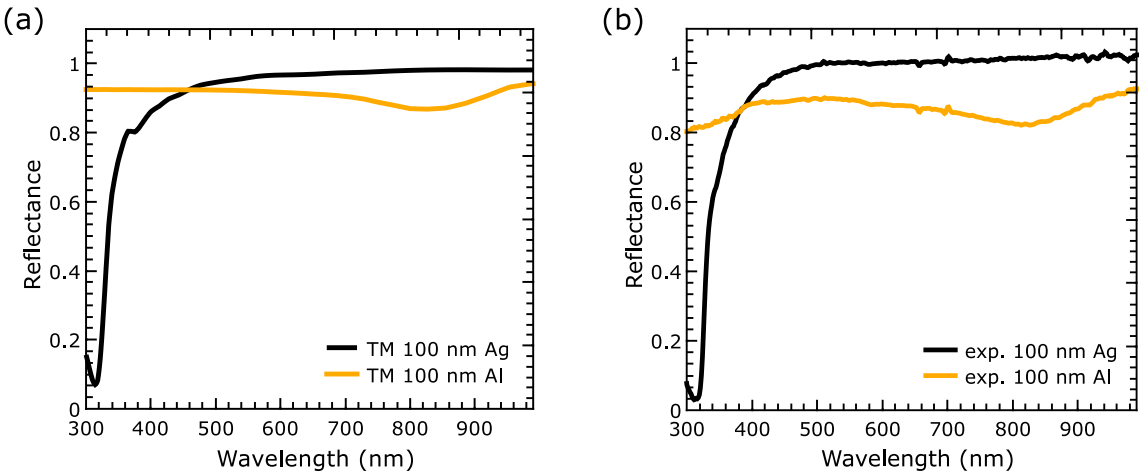

Figure 3.6: (a) Simulated and (b) experimental reflection spectra of 100 nm thick, sputtered films of silver (black lines) and Al (orange lines) at an angle of incidence of 40°.

3.4.2 Mirror materials

Mirrors form a crucial part of the microcavity; their reflectivity determines the Q-factor of the cavity and thus the lifetime of the cavity photon. Four different mirror materials were used in this thesis to study two different types of mirrors. Al and Ag were used to form metal-clad microcavities and stacks of alternating SiO_2/Ta_2O_5 served as high reflection, dielectric distributed Bragg reflectors (DBRs). Their fabrication and performance is discussed in Chapter 5.2.3. All sputtering targets were acquired from Angstrom Engineering at purities of $> 99.99\%$.

Al and Ag were thermally evaporated for microcavities with a solution-processed organic layer and sputtered for those with thermally evaporated organic layer. The evaporated materials were purchased from Sigma-Aldrich. No difference in the microcavity behaviour was observed between the two different deposition processes. Optical constants were assumed to be standard values as obtained from Winsemius *et al.* [197] for Al and from Rakić [198] for Ag. Figure 3.6 shows a comparison of measured and simulated reflection spectra from a single, 100 nm-thick film of either of the metals at an off-axis angle of 40°. The shape of the spectra agrees well, confirming both the TMM calculation as method for simulation and the optical constants to describe the real materials well. The absolute reflectances are slightly offset, being for Ag higher in the measurement than in the simulation and for Al lower. The lower values for Al could for example originate from a non-zero surface roughness of the sputtered film. The increased value for Ag, by contrast, can only be explained by (small) intensity fluctuations between the reference spectrum and the measurement.

Clearly, the choice for the best (metal) mirror material depends on the investigated spectral region. At wavelengths above 500 nm, Ag shows higher reflection and is thus to be preferred. However, at lower wavelengths, Al mirrors are more suitable for confining light, since the Ag reflection is greatly reduced in that spectral range due to plasmonic excitation.[199] Al was thus chosen as mirror material for all metal-clad microcavities but those containing an active material which absorbed in the red spectral range (MEH-PBI).

3.5 Fabrication of microcavities

The fabrication methods of microcavities differ between samples presented in different parts of this thesis. Chapter 4.1 discusses solution-processed materials in metal cavities with thermally evaporated mirrors. The entire fabrication process of these microcavities happened at ambient conditions in a class-10,000 clean room, the solution-processing on class-100 wet decks. By contrast, the microcavities containing thermally evaporated molecules were kept in nitrogen atmosphere or at vacuum throughout the entire fabrication process. For these vacuum–processed microcavities, which are presented in Chapter 4.2 and 5, metal mirrors were sputtered, as were all inorganic layers in combination with small molecules.

Samples were produced from bottom to top on glass substrates that were previously cleaned by sonification in acetone and in isopropyl alcohol after which substrates for vacuum processing were moreover plasma-cleaned. The stack was only characterised using reflectance measurements and TMM calculations after completion of the microcavity. Sometimes, organic films or mirrors were deposited in parallel to this component of the microcavity on a bare substrate to enable independent and direct determination of the layer thickness. However, this was not the case for every layer of every microcavity. Moreover, the film thickness varies across the area of the substrate holder for all vacuum deposition processes. In order to still obtain maximum information about the fabricated microcavities and measure different parts of the full microcavity independently, a mask was used during the sputtering steps (see Figure 3.7). The mask allowed for having regions on each 24 × 24 mm sample on which only some of the layers are present (i.e., only the organic film or the organic film and one of the mirrors), so that the different layers can be probed separately. Having the three non-cavity regions provided more information on the microcavity stack and thus allowed to attribute features of the entire microcavity to one of its parts. This was particularly used for DBR-clad microcavities.

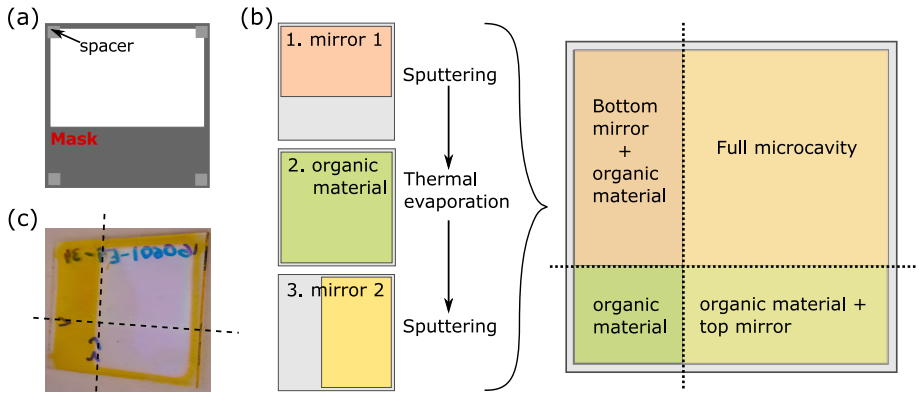

Figure 3.7: Illustration of the use of a mask for separating layer domains on sample. (a) Schematic illustration of mask. The dark grey region corresponds to the masked area. Light grey regions are small spacers in corner so that the mask does not touch the sample everywhere. (b) Illustration of the three-step process to divide the sample into non-equally sized quadrants of which only the largest contains a full microcavity. The other three contain only the organic material, the organic material plus bottom mirror and the organic material plus top mirror. (c) Picture of a DBR-clad, organic microcavity fabricated in the way illustrated in b. Dashed lines indicate borders between different quadrants.

It is also worthwhile to comment on the accuracy and reproducibility of the thickness of the organic layer. The thickness of bare organic films was measured using a profilometer (Dektak by Veeco) and ellipsometry, both yielding similar results within 10%. When producing microcavities, the thickness of the organic layer was determined by approximating the reflection spectrum of the microcavity by TMM calculations. When comparing the two measurements (bare films by ellipsometry versus films in microcavities by TMM simulations) for films produced with the same parameters, deviations of $\lesssim 20\%$ were observed. While this seems like a large number at first glance, it needs to be considered that the substrates for neat film measurements (glass and silicon wafers) differed from those of microcavities (bottom mirror: Al, Ag or DBRs ending with SiO_2 or Ta_2O_5). This could have an impact on the final film thickness already in the fabrication process. Moreover, during the deposition of the top mirror, reorganisation processes on the surface like desorption of organic molecules and diffusion of metal atoms into the organic films might change the physical thickness of the organic film. Considering these aspects, a deviation of 20% is deemed reasonable.

4

Organic materials in metal-clad microcavities

In many of the recent publications on organic polaritons, the confining mirrors of the microcavities are DBRs.[59,64,200,201] This is because metal-clad microcavities have significantly lower Q-factors than those achievable in microcavities with DBRs as mirrors. High Q-factors, in turn, are essential for prolonging the polariton lifetimes in order to observe nonlinear effects.[202] They are, however, not essential for observing strong light–matter coupling in microcavities containing organic molecules, owing to the large coupling strengths of organic materials. In this context, metal-clad cavities even have advantages over DBR-clad cavities with respect to simplicity of processing, the magnitude of the coupling strength and the spectral homogeneity of the reflectance.[72,203] This is why microcavities with metal mirrors are used here to study fundamental properties of organic polaritons.

It might be argued that the fundamental properties of strongly coupled light–matter systems are well known. Indeed, there is no controversy that for an ensemble of identical, lossless oscillators coupled to a cavity mode, the Rabi splitting is solely defined by the coupling strength, $\hbar\Omega = 2g$. In this idealised system, $g \propto A\sqrt{\frac{Nf}{V}}$ (with A being amplitude of the

electric field, N the number of interacting excitations, f the oscillator strength and V the mode volume) also follows from quantum electrodynamics (see Equation 2.27).[122] However, this assumption of identical oscillators is only a very rough approximation in organic microcavities, where individual excitons generally differ due to disorder in energy, in vibrational configuration and in rotational orientation. In fact, it has been shown that broad excitonic transitions with substructure do render the characterisation of the strongly coupled system ambiguous, both in organic and in inorganic systems.[68,69] In order to describe more realistic strongly coupled systems, losses have already been implemented in the description in the field of atom–photon coupling.[183] When taking losses into account, the coupled oscillator (CO) model predicts a threshold for the onset of the strong coupling regime which depends on the losses. In atom–photon systems, losses originate only from the finite lifetimes of the cavity photon and the excited state. In disordered systems, by contrast, it is debated how exactly the losses are affected by the presence of disorder, which might introduce additional dephasing.[102,106,112,121,167,175,185]

There is a number of publications studying the fundamental properties of organic polaritons, e.g. the dependence of the coupling strength on the number of absorbers or on the overlap of the excitons with the electric field.[19,42,50,71,72] Without belittling the importance of these findings, it should be noticed that there are two aspects limiting their generalisability. (1) All these reports on organic polaritons use J-aggregates as organic material, even though these form a very particular subset of organic semiconductors. J-aggregates show reduced disorder in comparison to other organic materials because of the increased long-range order that results from the stacking of molecules. Moreover, the absorption in J-aggregates is dominated by a single transition of the aggregate so that the presence of different vibronic levels in each individual molecule barely has an effect. (2) These studies do not consider any potential threshold attributed to losses which emerges from the CO model. Even though J-aggregates show reduced disorder, these losses cannot necessarily be neglected.

Here, experiments are presented which do not have the same limitations. The validity of fundamental predictions is tested for 'common' organic semiconductors, i.e., polymers, small molecules but also a J-aggregate. The large disorder and complex substructure of the electronic transition present in these systems renders them ideal for studying the properties of strongly coupled, disordered systems. Moreover, the analysis takes a potential threshold of the strong coupling regime into consideration. This improves the description of the results

and even allows for the observation of a non-zero threshold from experimental data. The results presented in Section 4.1 compare the properties of polaritons formed from different organic materials to the properties of the uncoupled materials. Most of these results have been published in Tropf *et al.* [73]. Section 4.2 then discusses how to transition between the weak and the strong coupling regime in two different ways; either by increasing the number of excitons in the microcavity or by increasing the overlap of a fixed number of excitons with the electric field. By studying the form of the dependence of the Rabi splitting on the parameter used for transitioning between weak and strong coupling, the onset of the strong coupling regime can be identified at non-zero values of the coupling strength. The greater part of the content of Section 4.2 has been published in Tropf & Gather [74].

4.1 Influence of bare excitonic properties on the strong coupling regime

In the scientific community working on organic polaritons, there seems to be no uniform picture of the effects of some properties of organic materials on the strong coupling regime. It has been argued that the disorder prevailing in organic semiconductors leads to a majority of the excitons remaining uncoupled to light, thus reducing the coupling strength.[112] This has been contested by recent results showing an immunity of the Rabi splitting with respect to inhomogeneous broadening to a certain extent.[175] Similar, albeit less explicit observations have been made already more than 20 years ago, when a homogeneous linewidth was recovered an inhomogeneously broadened system by increasing the coupling strength.[106] Nonetheless, early studies on organic polaritons favoured materials with narrow-linewidth transitions.[19,72,107,204–206] Up to date, many publications emphasize that narrow linewidths and small Stokes shifts of the materials inside the microcavities are beneficial—if not a necessity—for the strong coupling regime.[55,60,63,147,207–209] These conditions for the formation of polaritons seem violated by the often very broadband-absorbing materials in which ultra-strong coupling has been observed.[139,140,184]

All reports on fundamental properties of organic microcavities I am aware of demonstrate and characterise strong coupling in only a single material. However, since aspects like the concentration of excitons and film thickness as well as the choice of mirrors influence the properties of the strong coupling regime, a direct comparison between these different reports

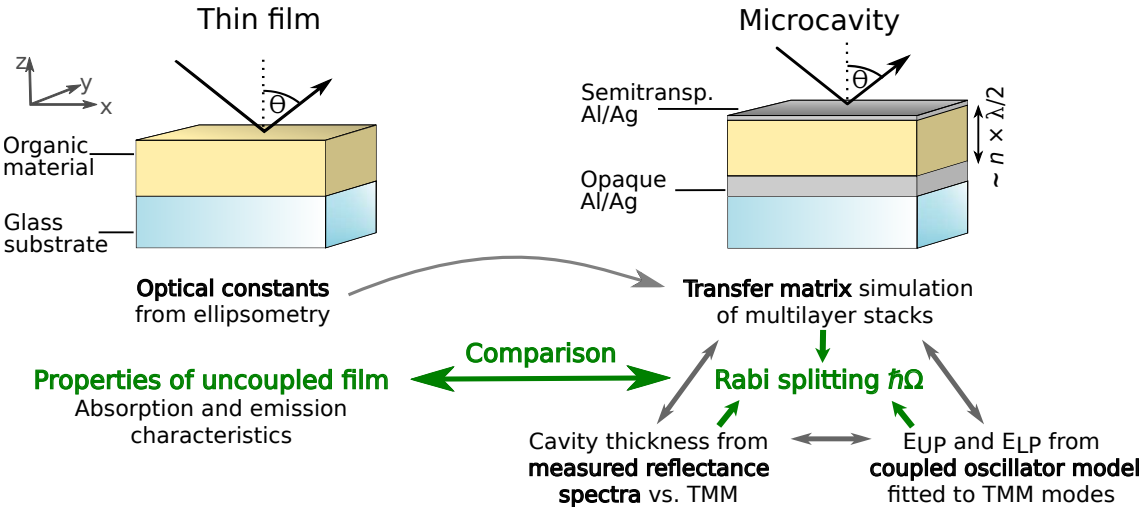

Figure 4.1: Schematic illustration of the comparison of materials in the uncoupled state and in the strong coupling regime. Different materials were analysed from thin films (ellipsometry) to obtain their uncoupled properties. The same materials are placed into microcavities. The optical response of the microcavity is also analysed, deducing $\hbar\Omega$ from a comparison of the experimental reflectance spectra with TMM calculations and the coupled oscillator (CO) model. In the last step, the Rabi splitting is tested for correlations with the properties of the uncoupled material.

is not possible. This calls for a systematic study comparing the relationship between different, uncoupled material parameters and the observed Rabi splitting. Therefore, this question was addressed within this PhD as illustrated in Figure 4.1 and the results are discussed below. First, the properties of uncoupled films of four materials were compared. Second, these materials were introduced into metal-clad microcavities and the Rabi splitting was determined for each material. This was done by comparing the measured reflectance spectra of fabricated microcavities to transfer matrix (TMM) calculations and to the coupled oscillator (CO) model. This Rabi splitting was then collated with the properties of the respective bare, uncoupled material. A correlation between the Rabi splitting and absorption characteristics was found; but none to other material parameters. Finally, the consistency of these results with a non-zero threshold for the onset of the strong coupling regime was tested and confirmed.

4.1.1 Organic materials and their properties in the uncoupled state

Four different materials were compared in the strong coupling regime, three polymers (PF8, F8BT and BBEHP-PPV) and one J-aggregate(MEH-PBI), all of which are introduced in Chapter 3.4. The four materials were chosen for different reasons. All of the polymers have been shown to possess excellent luminescence properties, which even persist in neat films.[210–213]

They were chosen to represent similar and dissimilar aspects of polymers: two are homopolymers (PF8 and BBEHP-PPV) and one is a co-polymer (F8BT) and they present two different, important classes of polymers, polyfluorenes (PF8 and F8BT) and poly-(*p*-phenylenes) (BBEHP-PPV).[214] By contrast, MEH-PBI represents a very distinct class of organic materials as it forms J-aggregates.[215] J-aggregates have been extensively studied in the strong coupling regime, selected for their narrow line widths and large oscillator strengths.[19,57,72,204,205] Even though MEH-PBI is unusual in the sense that it can show liquid crystal behaviour, it was chosen in order to cover different types of semiconductors.

The optical constants of the four materials were measured by ellipsometry and are shown in Figure 4.2. Note that the data of MEH-PBI has slightly changed with respect to Tropf *et al.* [73] because of an improved procedure for analysing ellipsometry data. However, this small adjustment does not change any of the presented outcomes qualitatively. The optical constants are of great significance for the sample design and characterisation as they are fed into the TMM code to calculate the optical response of microcavities. This is why the optical constants will be discussed in detail. The analyses of the ellipsometric data yield a better agreement between measurement and simulation when assuming an anisotropic material. A good correspondence was found for one set of optical constants describing the optical response of the material in the plane of the film surface (*xy*) and another for the response perpendicular to the surface (z). This anisotropy is likely to stem from the film fabrication by spin-coating, which is a highly anisotropic process.

In polymers, the film deposition by spin-coating causes the backbones of polymer chains to preferentially align parallel to the surface than perpendicular to it. Since the dipoles in polymers are oriented along the backbone,[216] this results in a higher oscillator strength parallel to the plane than perpendicular to it. This is confirmed by the data presented in Figure 4.2a–c, where the main peak of the extinction coefficient is more pronounced for the in-plane optical constants (k_{xy}) than for out-of-plane optical constants (k_z). Note that this corresponds to a stronger absorption and emission normal to the film surface.

In MEH-PBI, the optical response in z-direction is no longer simply a reduced version of the optical response in the *xy*-plane (Figure 4.2d). Instead, there are two peaks in the spectrum, one at wavelengths $\lambda \sim$ 500–670 nm, which is more pronounced in k_{xy}, and another at $\lambda \sim$ 640 nm, which is more pronounced in k_z. A comparison of these data to a detailed analysis

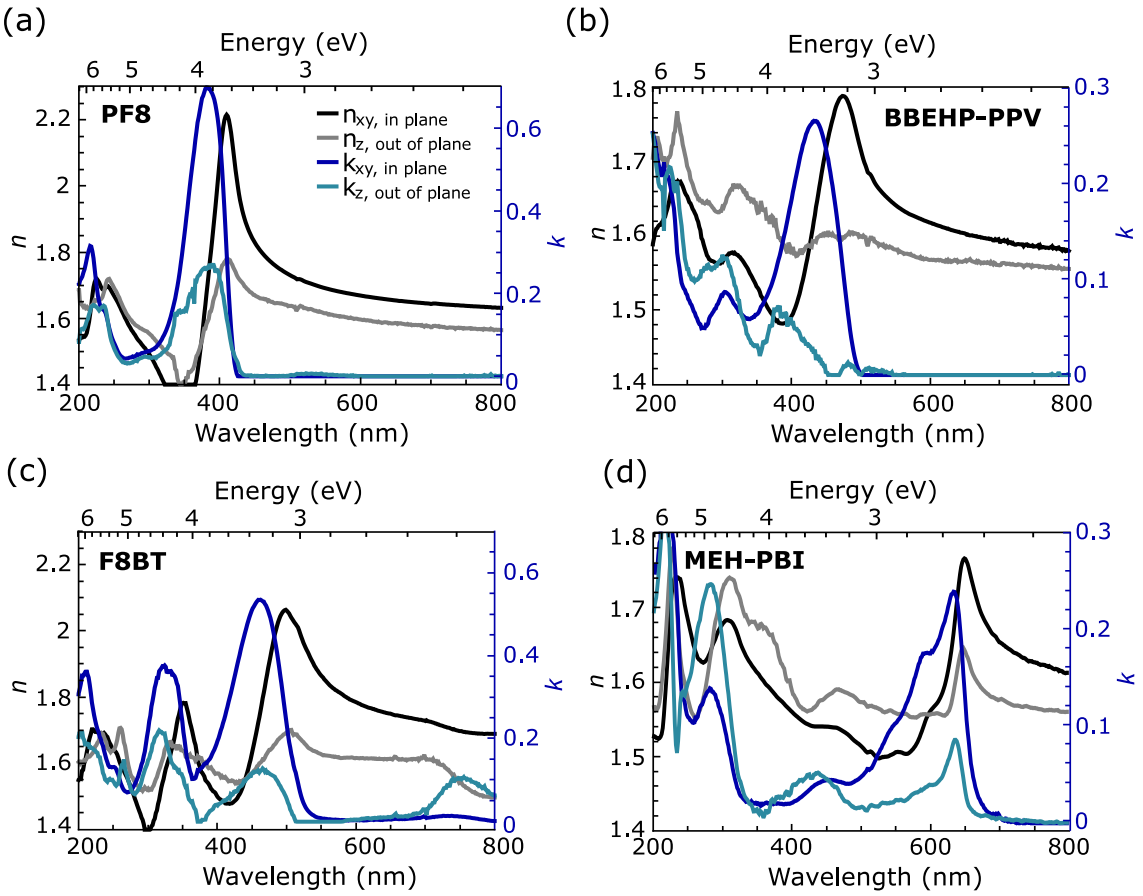

Figure 4.2: Optical constants of (a) PF8, (b) BBEHP-PPV, (c) F8BT and (d) MEH-PBI as measured by ellipsometry. The left axis corresponds to the anisotropic real part of the refractive index (black and grey lines for in-plane and out-of-plane n, respectively) and the right axis to the extinction coefficient (dark and light blue lines for in-plane and out-of-plane k, respectively).

of anisotropic J-aggregate absorption[217] suggests that the peaks have different origins. The monomer dipole (S_0–S_1 transition at 563 nm) lies in the molecular plane.[218] This plane can be assumed to be parallel to the film surface, given the planar structure of the molecule and the film deposition via spin coating, so that $k_{xy}(560\text{ nm}) > k_z(560\text{ nm})$. The transition dipole of the J-aggregate is red-shifted with respect to the monomer (appearing at $\lambda \sim 640$ nm). These dipoles are oriented along the aggregated filaments, which in turn lie in the plane of the film. Hence, the absorption from aggregated MEH-PBI, which is the most intense absorption feature, is also more pronounced in k_{xy} than in k_z. Note that the peak at $\lambda = 500\cdots670$ nm is thus a combination of two different, coexisting excited states—one representing the J-aggregated stack (intense and narrow) and the other the S_0–S_1 transition of the monomer with several vibronic replica. The blue-shifted absorption at 440 nm, which is more pronounced in k_z, i.e.,

perpendicular to the film, could indicate the spectral position of the S_0–S_2 transition.

In order to compare the four materials, several quantities are introduced to characterise the properties of the uncoupled materials. They comprise several aspects of the absorption and some quantities related to the emission of light and are summarised in Table 4.1. The absorption is characterised by its position and width. The energetic position of the extinction peak describes the energy of the exciton, E_X, which ranges from $E_X^{\mathrm{MEH-PBI}} = 1.94$ eV in the red to $E_X^{\mathrm{F8BT-X2}} = 3.82$ eV in the ultra-violet spectral range. The full width at half maximum (FWHM) of the absorption peak, δE_{FWHM}, comprises homogeneous and inhomogeneous broadening as well as several vibronic replica. δE_{FWHM} is smallest for MEH-PBI (0.26 eV) with a nearly three-fold width in X_2 of F8BT (0.68 eV). This is contrasted with the homogeneous linewidth δE_{hom}, which can be calculated from literature values of the lifetime of the exciton with the Heisenberg uncertainty relation. In all materials, $\delta E_{\mathrm{hom}} \lesssim 1$ μeV, which means that the inhomogeneous broadening by disorder and the existence of several vibronic replica dominate the linewidth of the transition. This is typical for organic materials. Thus, the inhomogeneous broadening, $\delta E_{\mathrm{inhom}}$, can be determined from the width of the individual vibro-electronic transitions. This is done by fitting the absorption peak with several Gaussians that are equally spaced in energy E_{vib}:

$$k(E) = \sum_{m=0}^{2} A_m \cdot \exp\left\{-\left[\frac{E-(E_0+m\cdot E_{\mathrm{vib}})}{\sigma_m}\right]^2\right\}, \tag{4.1}$$

Here, A_m, E_0, E_{vib} and σ_m are fit parameters denoting the peak height, the lowest transition, the vibronic energy quantum and the peak width, respectively. $\delta E_{\mathrm{inhom}}$ is then quantified as the average FWHM of the dominant Gaussians. $\delta E_{\mathrm{inhom}}$ spans values from 0.19 eV for MEH-PBI to 0.47 eV for X_2 of F8BT.

The strength of the absorption is described by the peak absorption coefficient, α_{max}, and by the integrated absorption over the peak, α_{int}.* These two values are chosen because δE_{FWHM} is larger than the linewidth of the microcavity so that it is not clear if the entire absorption peak will contribute to the coupling strength or not. α_{max} represents the limit of the cavity photon only coupling to a very narrow range of the exciton and ranges from $0.4\cdot10^5$ cm^{-1} in MEH-PBI to $1.6\cdot10^5$ cm^{-1} in PF8. α_{int}, which represents the limit of the photon coupling to the

*The absorption coefficient is calculated from the (measured) peak extinction coefficient as $\alpha_{\mathrm{max}} = \frac{4\pi k_{\mathrm{max}}}{\lambda_0}$, where λ_0 denotes the spectral position of the absorption peak.

Table 4.1: Summary of the optical properties of thin films of PF8, BBEHP-PPV, F8BT and MEH-PBI comparing: the exciton energy E_X, the width of absorption peak at half maximum δE_{FWHM}, homogeneous linewidth δE_{hom}, inhomogeneous linewidth δE_{inhom}, maximum absorption coefficient α_{max}, the absorption integrated over the relevant exciton peak, α_{int}, photoluminescence quantum yield (PLQY) in a neat film and Stokes shift between lowest energy absorption and highest energy emission peak, Δ_{Stokes}. For F8BT, X_1 and X_2 denote the two transitions.

	E_X (eV)	δE_{FWHM}	δE_{hom} (eV)*	δE_{inhom} (eV)	$\alpha_{max}/10^5$	α_{int} (a.u.)	PLQY	Δ_{Stokes}
PF8 X_1	3.27	0.52 eV	$\sim 1 \cdot 10^{-6}$	0.32	1.6 cm^{-1}	1	0.53[219]	0.31 eV
PF8 X_2	5.28							
BBEHP-PPV	2.84	0.58 eV	$\sim 5 \cdot 10^{-7}$	0.32	0.8 cm^{-1}	0.53	0.84[220]	0.36 eV
F8BT X_1	2.68	0.50 eV	$\sim 2 \cdot 10^{-7}$	0.37	0.9 cm^{-1}	0.55	0.58[211]	0.38 eV
F8BT X_2	3.82	0.68 eV		0.47	1.2 cm^{-1}	0.89		
F8BT X_3	5.30							
MEH-PBI	1.94	0.26 eV	$\sim 5 \cdot 10^{-8}$	0.19	0.4 cm^{-1}	0.12	0.13[218]	0.04 eV

* δE_{hom} was calculated from the Heisenberg uncertainty relation using the lifetimes of the excitons found in literature: $\tau_{PF8} = 227$ ps,[211] $\tau_{BBEHP-PPV} = 650$ ps,[212] $\tau_{F8BT} = 2028$ ps,[211] $\tau_{MEH-PBI} = 6800$ ps.[218]

ensemble of vibro-electronic transitions, is proportional to the oscillator strength as defined in Equation 2.1. α_{int} is also largest in PF8, by a factor of ~ 8 larger than α_{int} in MEH-PBI.

In addition to the absorption characteristics, some parameters in Table 4.1 describe the luminescence properties of the four materials. These give information about non-radiative relaxation pathways, via the PLQY, or the difference in energy between the absorbing and the emitting transition, i.e., the Stokes shift. The PLQY ranges from 0.13 in MEH-PBI[218] to 0.84 in BBEHP-PPV[220], where all polymers show a PLQY > 0.5. The Stokes shift, which is a measure of the conformational reorganisation of the materials, is smallest in MEH-PBI (0.04 eV) and ~ 0.35 eV in the three polymers.

Each of the optical properties listed in Table 4.1 covers a span of values differing by more than a factor of two for the different materials. Moreover, the values are not strictly correlated (although there is an inherent connection between $\delta E_{FWHM} \cdot \alpha_{max}$ and α_{int}). Hence, a comparison of these parameters with the properties of the strongly coupled system should allow to identify parameters of the uncoupled system that have a large impact on the latter.

4.1.2 Properties of different materials in metal-clad microcavities

This section discusses the properties of the four materials inside microcavities. For this, they were sandwiched between two metal mirrors of which the bottom mirror was opaque, whereas the semitransparent top mirror allowed for probing of the properties of the microcavities.

Cavities containing films of MEH-PBI had silver mirrors; all others had Al mirrors. Samples of different cavity thickness were fabricated in order to produce cavities at different detunings by controlling the thickness of the organic film. This was achieved by varying the spin-coating parameters between different samples. The reflectance of these samples was measured at an angle $\Theta = 0°$ (BBEHP-PPV) or $\Theta = 45°$ (PF8, F8BT and MEH-PBI). These measurements were compared to TMM calculations (which used the previously measured optical constants) and to the CO model. This comparison was used to extract the Rabi splitting $\hbar\Omega$ for the different materials, as illustrated in Figure 4.1.

In order to illustrate the methodology of the analysis with TMM calculations, an exemplary reflectance spectrum of a microcavity filled with MEH-PBI is shown in Figure 4.3 (black line). Also shown are calculations of reflectance spectra for different, schematically illustrated scenarios. These comprise a bare film of anisotropic MEH-PBI (Structure D, blue line), an empty cavity containing a non-absorbing, dispersionless layer (Structure C, orange line) and two microcavities containing isotropic and anisotropic MEH-PBI, respectively. The difference of Structures C and D to the experimental microcavity is obvious; they represent the bare cavity and the bare excitonic film, respectively. The reflectance of both structures only shows a single dip—that of the empty cavity being much more narrow than that of the excitonic film—which contrasts starkly with the two dips observed in the experimental spectrum. Furthermore, the minima in reflectance in Structures C and D coincide with the peak between the two dips in the experimental spectrum. This indicates an anticrossing of the modes of the experimental spectrum around the modes of the uncoupled exciton and cavity photon, which is characteristic for strongly coupled systems.

The difference between Structures A and B is more subtle: both represent full microcavities containing an MEH-PBI film of the same thickness (140 nm, chosen for best agreement between Structure A and the experimental spectrum). Yet, the structures have different optical constants, which were obtained by fitting the ellipsometric data with an isotropic and anisotropic model for Structure B (grey line) and A (green line), respectively. Even though both spectra show the double-peak feature indicative for the strong coupling regime, the shape of the anisotropic microcavity resembles the experimental spectrum more closely. Both the shape of the measured dips and the distance between them is in better agreement with the spectrum calculated from Structure A than with that from Structure B. This confirms that MEH-PBI is optically anisotropic and hence the considerations presented above for the choice of anisotropic

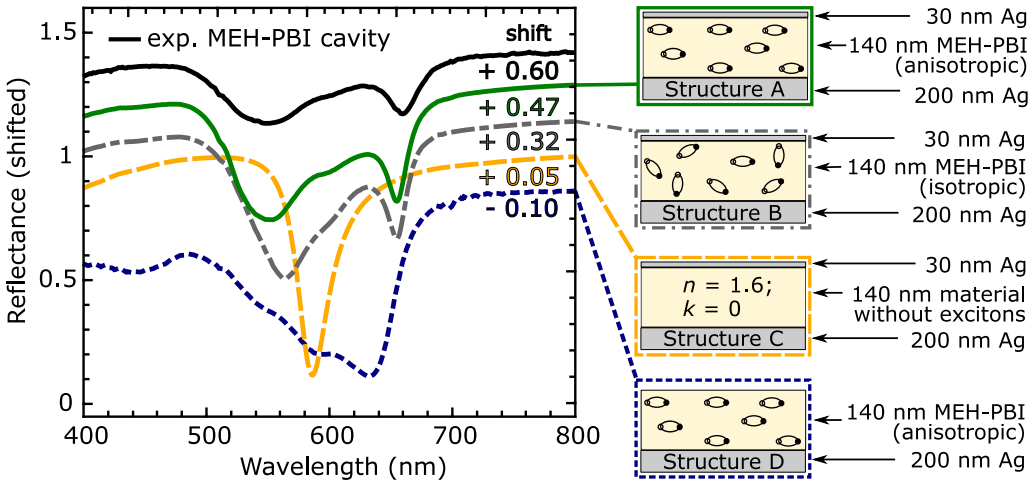

Figure 4.3: Exemplary reflectance spectrum of a microcavity containing MEH-PBI. This is compared to TMM calculations of different structures, which are illustrated schematically to the right of the spectra. Apart from the most realistic case, i.e., a microcavity containing anisotropic material (Structure A, green, solid line), calculations are performed for microcavities containing isotropic material (Structure B, grey, dash-dotted line), for an empty microcavity (Structure C, orange, dashed line) and for a bare film of (anisotropic) MEH-PBI (Structure D, blue, dotted line).

optical constants. A similar behaviour—i.e., a satisfactory agreement between TMM calculations and experimental data only when assuming optical anisotropy—was also observed for the three polymers. These results demonstrate the importance of taking potential anisotropies into account for predicting the optical response of a microcavity since they can influence the coupling strength. This is in agreement with reports in molecular crystals, fully aggregated films of J-aggregates and carbon nanotubes.[65,221,222] All calculations presented in this section consider the anisotropy of the investigated materials.

Reflectance spectra similar to the one shown in Figure 4.3 were acquired for at least three microcavities of each material. For each material, different microcavities have a different thickness because they contain a film of different thickness. The individual thicknesses were determined by comparing the measured spectra to TMM calculations of microcavities. The essence of these experimental spectra—the spectral position of the modes—was then compared to TMM simulations of the spectrally resolved reflectance as a function of the continuously varied thickness of the organic film. This is shown in Figure 4.4, demonstrating that the experimental modes (orange symbols) coincide well with the modes expected from TMM calculations (grey background, dark regions indicate dips). However, since the thickness of the cavity was determined from TMM calculations, this agreement is anticipated.

In order to compare these modes to an independent method, the CO model was used to analyse the shape of the modes. For this, the mode of the cavity photon was calculated according to Equation 2.7. The angle was fixed to the value used in the experiment (and TMM calculations). The background refractive index n_c and the penetration depth into the metal mirror were treated as constrained variables, i.e., they were only allowed a variation within a physically sensible interval.* For PF8, F8BT and BBEHP-PPV, both the fundamental and the first harmonic mode of the microcavity were taken into account. The energy of the excitons was fixed at the peak value of the extinction coefficient from the measurement of the optical constants, see Table 4.1.

The eigenenergies of the polaritons were calculated according to Equation 2.21, which was extended as shown by Armitage *et al.* [223] to comprise two and three excitons for PF8 and F8BT, respectively. Note that the effect of the second and third exciton considered for PF8 and F8BT, respectively, are at higher energies than the presented range and are thus not visible in Figure 4.4 (for values, see Table 4.1). g_{eff}, n_c and d_{pen} were varied to obtain maximum agreement between the modes from TMM calculations and the polariton modes from the CO model. The losses of the photon and of the exciton were neglected because the relevant parameter is the difference in losses, of which one—the loss in the excitonic, disordered system—is difficult to estimate. Thus, the fit parameter corresponds to an effective coupling strength $g_{\text{eff}} = \frac{\hbar\Omega}{2} = \sqrt{g^2 - (\gamma_C - \gamma_X)^2/4}$ rather than to g. However, this is not a problem here, because only $\hbar\Omega$ is extracted from the presented data and the width of the modes was not analysed.

In addition to the TMM calculations and the experimental modes, Figure 4.4 shows all modes from the CO model: cavity modes as dashed or dash-dotted lines, exciton modes as dotted lines and polariton modes as green, solid lines. An anticrossing of the polariton modes at the resonance of the photon and each exciton energy is clearly visible. Moreover, the thickness dependence of the measured and of the TMM-calculated modes is evidently consistent with the CO model. The calculations of CO model thus demonstrate that the microcavities with all four studied materials are in the strong coupling regime. This allows us to attribute the dif-

*n_c was maintained at values similar to the value measured at large wavelengths. The approximate penetration depth into the metal mirrors was determined using TMM calculations from the difference between the optical thickness of an empty cavity and of its resonant wavelength. This yielded ≈ 30 nm for Al and ≈ 60 nm for Ag (summed up penetration depth into both mirrors). Yet, this value varies with the wavelength of the resonance and, since it is on the order of the semitransparent top mirror, with the thickness of this mirror. This is why some variation ($\lesssim$ 10%) was allowed for.

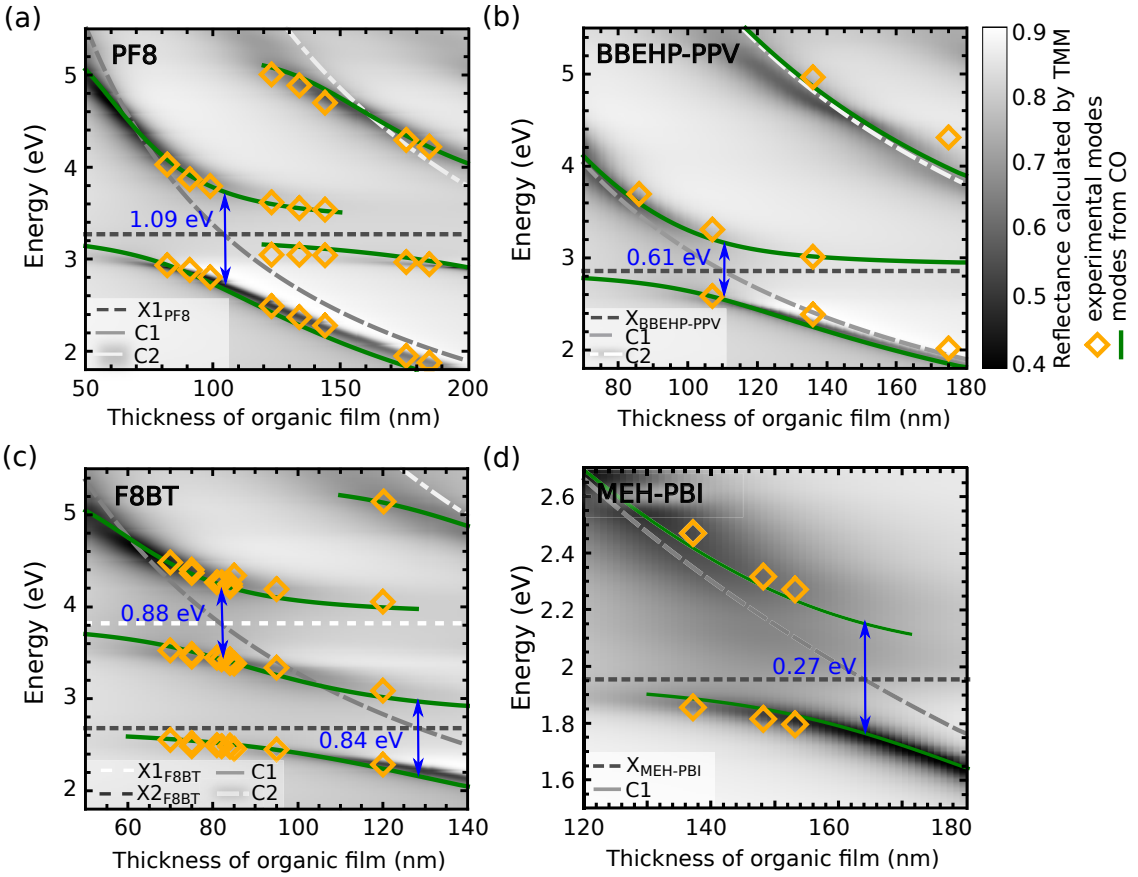

Figure 4.4: Data for determining the Rabi splitting of (a) PF8, (b) BBEHP-PPV, (c) F8BT and (d) MEH-PBI. The position of the modes of experimental reflectance spectra (orange symbols) is compared to TMM calculations (grey background) and modes from the CO model (green, solid lines). The modes of cavity photons (C_1 and C_2) and excitons (X_1 and X_2) used in the CO model are indicated by grey, dotted and dashed lines.

ferent modes of the experimental spectra to LPs, middle polaritons (MPs) and UPs for the fundamental and the first harmonic mode in the microcavity. For PF8 and more clearly for F8BT, MPs are observed. This is because at different thicknesses of the cavity, different excitonic transitions are in resonance with the cavity photon. At some intermediate cavity thickness, the cavity photon hybridises the two excitations so that MPs are hybrid polaritons. Hybrid polaritons have been frequently observed in organic and in organic–inorganic systems and they can for example increase the charge transfer between different exciton species.[107,147,149,209] In F8BT, the MP forms between the S_0–S_1 transition at 2.7 eV and the excitation at 3.8 eV, the nature of which was not investigated further. This MP in F8BT thus corresponds to a coherent exchange of energy between collective excitations of all three constituents: X_1, X_2 and the cavity photon. In the context of comparing the coupling strength of different systems, MPs are

valuable because they represent the coupling around two (different) excitations in the same system. Further, they can potentially show the effect of interaction between these excitons on the coupling strength around either of the excitons.

In order to compare the different materials quantitatively, the extent of the minimal splitting, i.e., the Rabi splitting, was determined for each transition (blue labels in Figure 4.4). The presented value is the average between the minimal mode splitting of the modes from TMM calculations and $2g_{\text{eff}}$ of the CO model. The Rabi splittings determined from these two methods differed by less than 0.05 eV. The observed Rabi splitting is largest for PF8 (1.09 eV) and smallest for MEH-PBI (0.27 eV). For the materials with large splitting, i.e., PF8 and F8BT-X1, these large Rabi splittings are indicative of the ultra-strong coupling regime, corresponding to 33% and 31% of the energy of the exciton. However, all Rabi splittings observed in these materials were relatively large, $\hbar\Omega \gtrsim 0.1E_{\text{X}}$ and for all polymers, $\hbar\Omega \lesssim 0.2E_{\text{X}}$.

4.1.3 Comparing the Rabi splitting to properties of the uncoupled materials

Finally, the Rabi splittings were compared to the properties of the uncoupled materials discussed in Section 4.1.1. Moreover, different relationships between the measured Rabi splitting and the underlying coupling strength were assumed, testing different parameters to determine the offset between g and $\hbar\Omega$.

In Figure 4.5, the Rabi splitting is plotted as a function of different characteristics of the uncoupled materials in order to test for any correlation between the Rabi splitting and the respective parameter. Neither for the Stokes shift (blue squares), nor for the total linewidth of the exciton peak in absorption (δE_{FWHM}, grey circles), for the PLQY (blue stars) or for the estimated homogeneous linewidth of the material (δE_{hom}, grey diamonds), any correlation is apparent. Even though the smallest Rabi splitting in MEH-PBI coincides with its smallest value in these four parameters, the distribution of values for the polymers is clearly random. Only in the right panel, where the Rabi splitting is plotted as a function of the maximum and the integrated absorption coefficient (grey triangles and blue crosses, respectively), the parameters seem to be related to the extent of the Rabi splitting.

This potential correlation between $\hbar\Omega$ and α_{max} and/or α_{int} was tested by fitting the Rabi splitting with a linear function ($A \cdot \alpha + B$, not shown) and with a square root function ($\sqrt{A \cdot \alpha + B}$, dashed lines). For both parameters, the square root fit yielded a larger coefficient

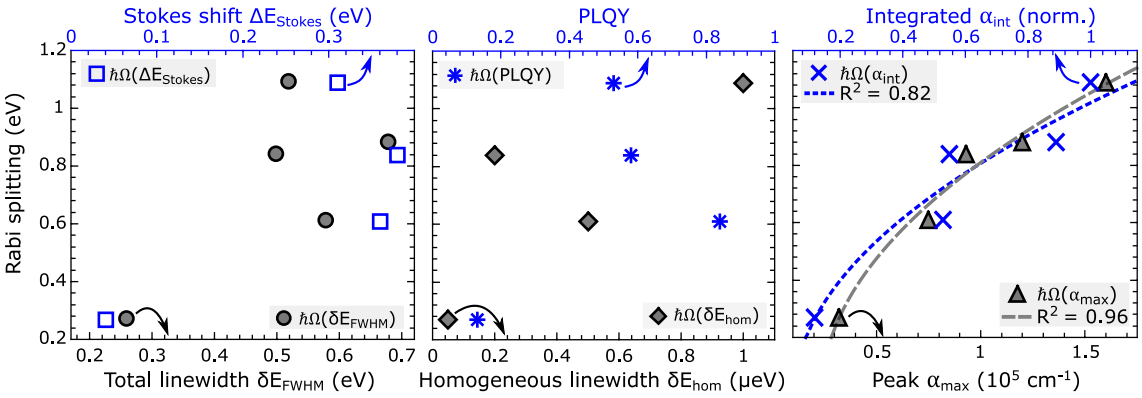

Figure 4.5: Comparison of the Rabi splitting $\hbar\Omega$ to different properties of the uncoupled material. Grey symbols refer to the bottom x-axis and blue symbols to the top x-axis. In the left and central graph, $\hbar\Omega$ is plotted as a function of the Stokes shift ΔE_{Stokes} (blue squares), the total linewidth δE_{FWHM} (grey circles), the PLQY (blue stars) and the homogeneous linewidth δE_{hom} (grey diamonds). In the right graph, $\hbar\Omega$ is shown as a function of both the integrated and the peak absorption, α_{int} (blue crosses) and α_{max} (grey triangles), respectively. These data are fitted with a square root function ($\sqrt{A \cdot \alpha + B}$, dashed lines), of which the coefficients of determination are given in the legend.

of determination; $R^2_{\sqrt{x}} = 0.82$ versus $R^2_{\text{lin}} = 0.80$ for α_{int} and $R^2_{\sqrt{x}} = 0.96$ versus $R^2_{\text{lin}} = 0.89$ for α_{max}. This is in agreement with theoretical predictions of the coupling strength (Equation 2.27), according to which $g \propto \sqrt{f}$ and not $g \propto f$. The oscillator strength f, however, is proportional to the integral over the absorption coefficient, not to its peak value (see Chapter 2.1). Thus, it is not expected from these predictions that the correlation is more obvious for the peak value of the absorption coefficient ($R^2_{\sqrt{x},\text{max}} = 0.96$) than for the integrated absorption coefficient ($R^2_{\sqrt{x},\text{int}} = 0.82$).

There are two possible explanations for this. (1) Since the width of the absorption is much larger than the spectral width of the cavity photon ($\delta E_{\text{C}} \sim 0.1$ eV), the photon might only couple to a subset of excitonic states. If the spectral range was narrow and the same for all materials, α_{max} would be a better measure for this reduced, coupling oscillator strength. (2) The seeming deviation from theory could stem from the fact that the measured quantity was not the coupling constant g but rather the Rabi splitting $\hbar\Omega$. According to the CO model, there is an offset between g and $\hbar\Omega$ which stems from the losses of the uncoupled photon (γ_{C}) and exciton (γ_{X}): $\hbar\Omega = \sqrt{4g^2 - (\gamma_{\text{C}} - \gamma_{\text{X}})^2}$. Since the losses might differ between different materials, $\hbar\Omega$ might only be loosely related to the parameter g, for which the correlation is expected.

Therefore, g is extracted from the value of the Rabi splitting using estimates for the loss terms. γ_C was determined for each material from the FWHM of the TMM-calculated mode in an empty cavity at the approximate spectral position of the exciton. With the mirror material and Θ as used experimentally, this yielded $\gamma_C = 0.10 \ldots 0.13$ eV. The determination of the excitonic loss term γ_X is less straightforward, although this is crucial for determining the relationship between g and $\hbar\Omega$. As discussed in Chapter 2.4.3, it is still debated what value γ_X can be identified with: is it the entire width of the electronic transition, δE_{FWHM}, is it the homogeneous broadening δE_{hom} caused by the finite lifetime of the exciton or is it the inhomogeneous broadening around each vibronic transition, $\delta E_{\mathrm{inhom}}$? Hence, all three parameters for $\gamma_X = \{\delta E_{\mathrm{FWHM}}, \delta E_{\mathrm{hom}}, \delta E_{\mathrm{inhom}}\}$ are used to calculate a test coupling strength, $g_{\mathrm{test}} = \{g_{\mathrm{FWHM}}, g_{\mathrm{hom}}, g_{\mathrm{inhom}}\}$, from the Rabi splitting. Assuming the validity of $g \propto \sqrt{f}$, the agreement between $g_{\mathrm{test}} \propto \sqrt{\alpha_{\mathrm{int}}}, \sqrt{\alpha_{\mathrm{max}}}$ can be used both to verify the previous observation from the fit to the Rabi splitting ($f \propto \alpha_{\mathrm{max}}$?) and as an indicator for the value of γ_X.

The results of this test are shown in Figure 4.6, where the test coupling strength calculated assuming that $\gamma_X = \delta E_{\mathrm{FWHM}}$ (g_{FWHM}, grey symbols), $\gamma_X = \delta E_{\mathrm{hom}}$ (g_{hom}, blue symbols) and $\gamma_X = \delta E_{\mathrm{inhom}}$ (g_{inhom}, orange symbols). Each series of data points was fitted with a square root function ($A \cdot \sqrt{\alpha}$, dotted lines of the same colour as the symbols) as a function of α_{max} (Figure 4.6a) and α_{int} (Figure 4.6b). The R^2 values for each fit are indicated in the legend. Note that here, the fit function originates from (0,0) because no threshold-like behaviour is expected for g (in contrast to the situation for $\hbar\Omega$). For the three versions of g_{test}, a difference in the fit quality is found between α_{max} and α_{int}. While the coefficients of determination for α_{int} lie in the range of $R^2_{\mathrm{int}} = 0.86 \cdots 0.95$, for α_{max}, they are reduced to $R^2_{\mathrm{max}} = 0.80 \cdots 0.86$. All fits as a function of α_{max} seem to deviate systematically from the data points, indicating an inappropriate form of the fit function for the data. Indeed, it is found that when allowing for an additional offset on the g-axis, the fits improve for α_{max}, with R^2-values increasing to $0.93 \cdots 0.95$. Yet, since no threshold-like behaviour is expected for $g \propto \sqrt{f}$, this increase of R^2 is unphysical and only shows that $f \not\propto \alpha_{\mathrm{max}}$.

A closer look at Figure 4.6b reveals differences between the individual g_{test} that use different hypotheses for the value of γ_X. Here, the deviation of the data points from the fit functions consists of a random scattering of values around the orange and blue dashed lines, not of a systematic deviation as observed for α_{max}. Hence, this refined analysis shows in agreement to expectations that $g \propto \sqrt{\alpha_{\mathrm{int}}} \propto \sqrt{f}$. This indicates that the cavity photon couples to

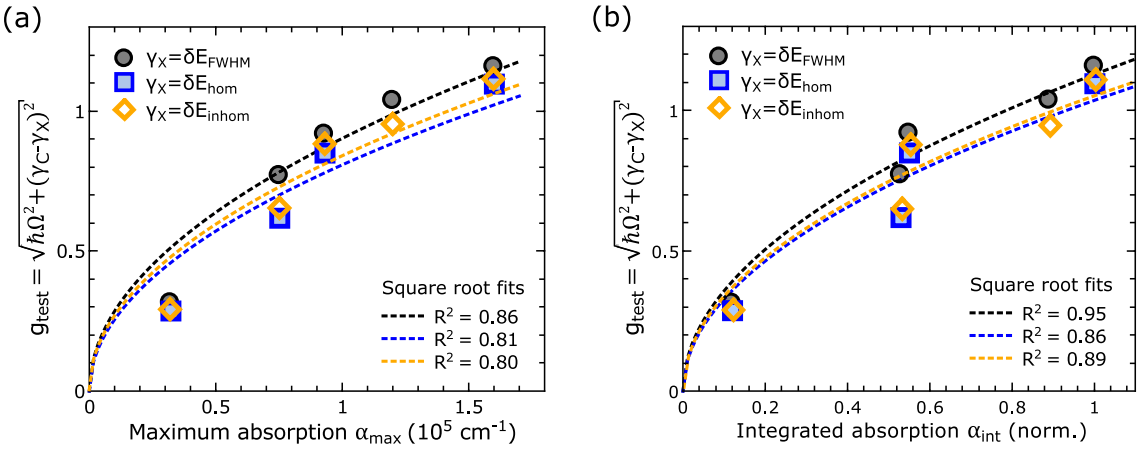

Figure 4.6: Testing different excitonic loss terms: The coupling strength is calculated from the Rabi splitting with the linewidth of the cavity photon γ_C and testing three different values for the excitonic losses: δE_{FWHM} (grey symbols), δE_{hom} (blue symbols) and $\delta E_{\mathrm{inhom}}$ (orange symbols). Dotted lines of the same colour as the symbols represent square root fits ($A \cdot \sqrt{\alpha}$) of which the R^2 value is noted in the figures. The three hypothetical coupling strengths g_{test} are plotted (a) over the maximum absorption coefficient and (b) over the normalised integrated absorption coefficient.

the entire excitonic transition and not only to a subset thereof. Moreover, it is apparent that the difference between g_{hom} and g_{inhom} is small. The similarity between g_{hom} and g_{inhom} is also visible from the similarity in fit functions for the two parameters. This is because both $(\gamma_C - \delta E_{\mathrm{hom}})^2 \ll \hbar\Omega^2$ and $(\gamma_C - \delta E_{\mathrm{inhom}})^2 \ll \hbar\Omega^2$, so that $g_{\mathrm{hom}} \approx g_{\mathrm{inhom}} \approx \hbar\Omega$. Nonetheless, the coefficients of determination point to a better agreement for $\gamma_X = \delta E_{\mathrm{inhom}}$; $R^2_{\mathrm{inhom}} = 0.89$ versus $R^2_{\mathrm{hom}} = 0.86$. By contrast, g_{FWHM} differs visibly from g_{hom} and g_{inhom}, owing to the large total widths of the transition. For g_{FWHM}, the data points lie closer to the fit function, which is confirmed by a much larger coefficient of determinations, $R^2 = 0.95$. This value is high, especially when considering that the fit function only has one variable. The presented data thus suggest that the full width of the excitonic transition, δE_{FWHM}, best estimates the losses of the exciton. This means that not only the finite lifetime of the exciton, but also the broad band of available states reduces the coherence between exciton and photon. While this has been assumed previously,[61] this is not necessarily expected from quantum electro-dynamics or from other recent investigations of the impact on the inhomogeneous broadening.[90,175,184]

To summarise, the comparison of different organic materials in metal-clad microcavities has yielded four main results: (1) It is important to take the anisotropy into account when predicting the response in the strong coupling regime. This holds even for materials in which

the anisotropy is not as striking as for instance in organic crystals. The preferential in-plane orientation of the dipoles of the investigated materials leads to an increased coupling strength for light incident normal to the mirror surface. (2) All four investigated materials show strong coupling in metal-clad microcavities, clearly indicated by the anticrossing of photonic and excitonic modes. For F8BT, strong coupling was observed around two excitations, which resulted in one hybrid polariton. The large Rabi splitting observed in PF8 and F8BT-X_1 ($\hbar\Omega > 0.3E_X$) even places these materials in the ultra-strong coupling regime. (3) The comparison of the Rabi splitting to the properties in the uncoupled materials showed that the Rabi splitting only correlated with parameters related to the absorption strength. No correlation was observed for other investigated parameters like the PLQY or the Stokes shift. (4) Three parameters were tested to correspond to the loss term γ_X, which defines the threshold for the onset of the Rabi splitting: the full width of the transition, the homogeneous linewidth calculated from the lifetime of the exciton and the inhomogeneous linewidth extracted from multi-peak Gaussian fits to the extinction coefficient. This yielded the best agreement between theory and experiment when assuming that the losses can be estimated from the full width of the excitonic transition. Moreover, the analysis confirmed that the effective oscillator strength, which determines the coupling strength, is proportional to the integrated absorption coefficient and not merely to its peak value—even in these strongly disordered systems with several vibroelectronic transitions. Owing to the variety of materials studied, these results are trusted to be widely applicable to organic, strongly coupled systems.

4.2 Investigating the onset of the strong-coupling regime

The experiments presented in this section aim to quantitatively verify the dependence of the coupling strength on the electric field A and on the number of absorbers N in strongly disordered microcavities. The form of the coupling strength has been previously investigated in organic materials, confirming that $\hbar\Omega \propto \sqrt{N}$,[19,44,50,72,139] $\hbar\Omega \propto A$,[42,71] and $\hbar\Omega \propto \sqrt{\frac{1}{V}}$.[72] All these investigations study the dependence of the Rabi splitting on the different parameters. However, it was shown in the previous section that the difference $\hbar\Omega$ and g can have an effect on the validity of claims. Moreover, as mentioned before, these investigations use J-aggregates as the active material, which are not strongly disordered compared to other organic materials.

Here, the relationship between the coupling strength (not the Rabi splitting) and single parameters that determine the coupling strength according to theory is carefully tested. Even

though direct measurements only allow for the unambiguous determination of the Rabi splitting, g can be retrieved from $\hbar\Omega$ by the systematic variation of one isolated parameter. In this way, it is tested if $g \propto A$ and if $g \propto \sqrt{N}$. This distinction between g and $\hbar\Omega$ is a significant difference to previous studies that investigate the form of the coupling strength. Moreover, the discrimination between g and $\hbar\Omega$ allows to determine the offset between the two parameters, i.e., the threshold of the strong coupling regime, experimentally. To the best of my knowledge, this has not been shown before.

The variety of materials used in the previous experiment was important for comparing many independent properties of the materials. However, it would not be suitable for isolating the effect of a single parameter. Thus, the experiments discussed in the following aim to vary only one parameter of the strongly coupled system. Previous reports studying the relationship between $\hbar\Omega$ and N varied N by increasing the concentration of molecules in a uniform film filling the cavity.[19,44,72,139] To my best knowledge, the only studies on the proportionality of $g \propto \sqrt{N}$ at constant concentrations were performed on inorganic semiconductors.[168,224] However, the concentration of chromophores is known to potentially change their behaviour in many ways, for instance affecting the nature of excited states or relaxation pathways.[225] Hence, this approach was not used in the experiments presented here. Instead, N was varied by changing the thickness of a film of constant concentration (neat film). This required for the cavity thickness to be varied independently of the thickness of the organic film, i.e., a multi-layered microcavity.

A sketch illustrating the experiments and analysis process of these investigations is shown in Figure 4.7. Two different sample series were designed; the d_{org} series to study the relationship between g and N (top row) and the *OVL* series to study the relationship between g and A (bottom row). The microcavities of the d_{org} series contain organic films of different thickness, and thus a different number of excitons, N. In this series, the energy of the cavity photon is tuned independently of the thickness of the C545T film by introducing additional SiO_2 buffer layers below and above the organic film. In this way, the film of C545T is localised in the centre of the cavity and the cavity thickness is controlled ($d_{\mathrm{opt}} \approx \lambda_{\mathrm{X}}/2$). By tuning the cavity through resonance, the Rabi splitting can be determined. The form of g is then tested by analysing the dependence of the Rabi splitting on the film thickness. The threshold for the strong coupling regime can be determined from the intercept with the $\hbar\Omega$-axis.

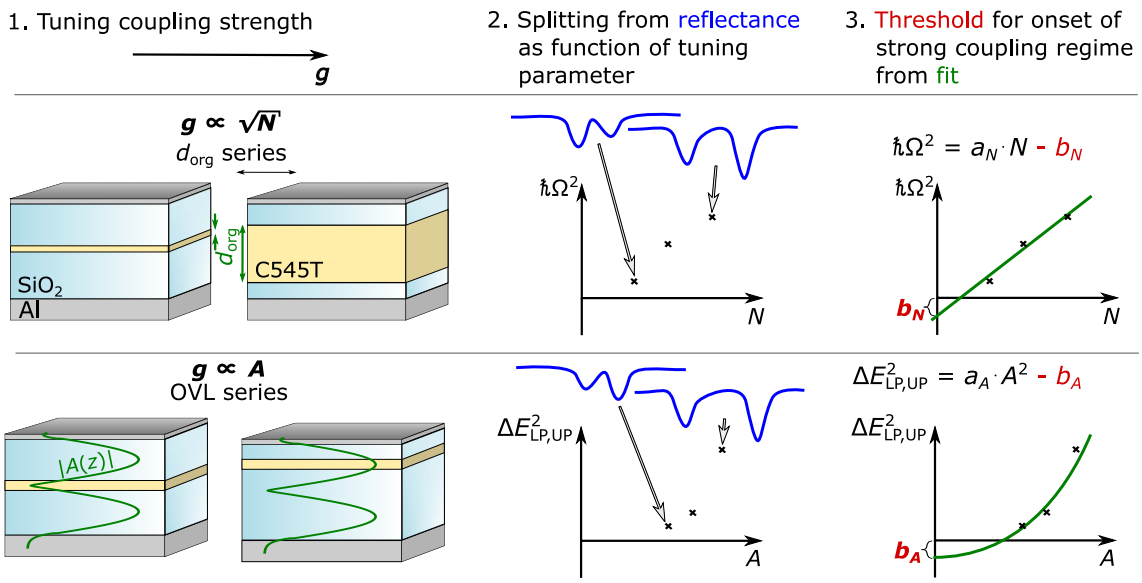

Figure 4.7: Schematic illustration of procedure for determining the threshold for the onset of the strong coupling regime. The coupling strength is tuned in two different ways, by changing the thickness of the organic film (d_{org} series, top) and by changing the overlap between a thin film of the organic material with the electric field A (*OVL* series, bottom). From the different samples, the Rabi splitting (d_{org} series) or the mode splitting (*OVL* series) is determined from reflectance spectra as a function of the tuning parameter. From fitting the data points with a fit function suggested by theory, the y-intercept can be used to determine the threshold for the onset of the strong coupling system.

The second sample series, the *OVL* series, obtains is name because its varies the overlap of a thin, organic film with the electric field by changing the position of the film inside the cavity. In order to be able to compare the samples, the thickness of the organic film and of the cavity was kept constant in the *OVL* series. From probing the reflectance of the *OVL* series, the energy splitting of LP and UP is determined at the same detuning. Again, the dependence of the splitting on the overlap with the electric field A provides information both about the validity of $g \propto A$ and about the threshold for the onset of the strong coupling regime predicted by the CO model.

The studied microcavities used Al mirrors, thin films of the coumarin dye C545T and additional SiO_2 buffer layers. This organic material was chosen because it absorbs strongly and, belonging to the class of small molecules, its thickness can be well controlled by thermal evaporation. C545T has been reported to be an efficient emitter at low concentrations, both in electrically pumped light-emitting devices (LEDs)[226] and in optically pumped organic lasers.[227] More importantly, however, it has a broad absorption spectrum, comprising several vibronic

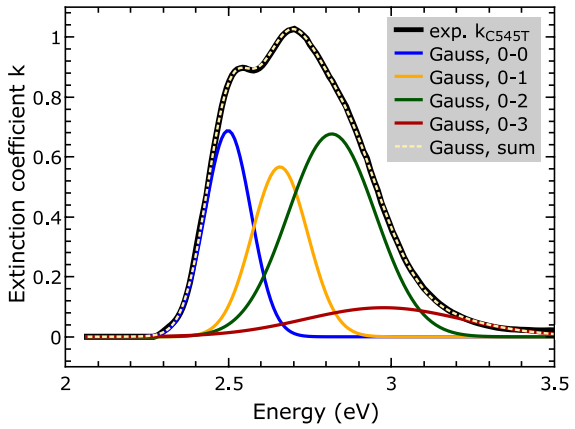

Figure 4.8: Extinction coefficient of C545T. The measured k_{C545T} (black line) is compared to the individual peaks (non-black, solid lines) of a multi-Gaussian fit (yellow, dashed line), for which the distance between different peaks is fitted to a constant value E_{vib}. The different Gaussians thus correspond to transitions from $n_{\mathrm{vib}} = 0$ of S_0 to $n_{\mathrm{vib}} = 0, 1, 2, 3$ of S_1.

replica, as shown in Figure 4.8. These have been identified by fitting a multi-Gaussian function to the measured extinction coefficient (see Equation 4.1), which describes the absorption very well ($R^2 = 0.99992$). The 0–0 transition is found to be at $E_0 = 2.50$ eV and the vibrational energy is determined to be $E_{\mathrm{vib}} = 0.16$ eV. The inhomogeneous broadening is of the same order of magnitude as E_{vib}, with the FWHM of the individual Gaussians ranging between $\delta E_0 = 0.16$ eV to $\delta E_3 = 0.56$ eV.

Section 4.2.1 describes the experiments and analysis of the d_{org} series and Section 4.2.2 explains the investigations on the *OVL* series. The following section (4.2.3) then discusses how the analyses of the d_{org} series and of the *OVL* series were used to determine the threshold for the onset of the strong coupling regime and how this compares to the thresholds expected from the CO model. Like this, a threshold for the onset of the strong coupling regime is found that is consistent with predictions from the CO model.

4.2.1 Coupling strength as a function of the number of absorbers

In the samples of the d_{org} series presented here, the number of absorbers is changed at constant concentration, i.e., in a neat film, by changing the thickness d of the organic film ($N \propto d$).

Figure 4.9 shows the data of three exemplary sets of samples of the d_{org} series, one without any C545T (a), one containing 15 nm of C545T (b) and one containing 40 nm of C545T (c). Reflectance spectra (second row) show that cavities of positive and negative detuning were

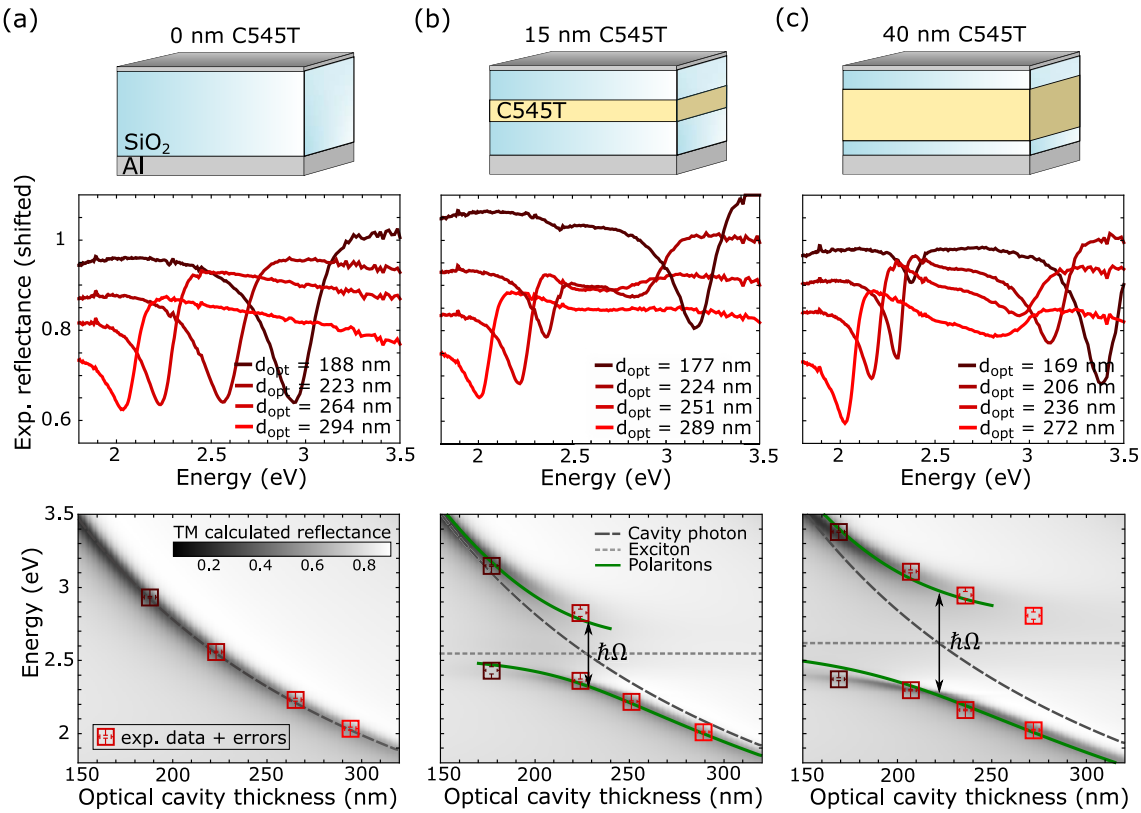

Figure 4.9: Characterisation of the d_{org} series from reflectance spectra. Each column shows a set of samples containing a C545T film of different thickness. (a) left: no C545T, (b) centre: 15 nm C545T, (c) right: 40 nm C545T. The top row shows an illustration of the microcavities and the second row the experimental reflectance spectra for cavities with different cavity thickness (optical thickness d_{opt} indicated in legend). The bottom row compares the mode position of the experimental spectra (red symbols) to TMM calculations (grey background). Dotted, dashed and solid lines represent modes calculated from the CO model. Arrows indicate the position and the extent of the Rabi splitting.

produced ($E_{\mathrm{X}} \approx 2.5$ eV). By comparison to TMM calculations, the optical thickness of the microcavities was determined. In order to determine the Rabi splitting for each of the cavities, the reflectance of corresponding structures was calculated using the TMM. Additionally, TMM calculations were performed for a continuous variation of the thickness of the SiO_2 films, see the background in the third row of Figure 4.9. The mode positions extracted from the experimental spectra are overlaid (red symbols) and agree well with the TMM calculations.

Moreover, green, solid lines from CO calculations demonstrate that the shape of the modes follows that expected for a strongly coupled system. In agreement with expectations, the plots show an increased Rabi splitting for larger thicknesses of the organic film inside the microcavity. Note, however, that in order to obtain the agreement between TMM and CO

calculations, not only the coupling constant g was changed. Instead, the energy of the cavity mode (grey, dashed line) had to be changed slightly via the background refractive index of the microcavity and the exciton energy (grey, dotted line) also had to be adjusted between different sets. The small adjustments of n_{eff} might be due to misestimations of the background refractive index of SiO_2 and/or C545T. The changes in E_X are more noticeable; the best agreement for the samples with 15 nm C545T is found for $E_X = (2.52 \pm 0.05)$ eV, while samples with 40 nm C545T require $E_X = (2.62 \pm 0.05)$ eV. Even though the change in E_X is not drastic, the observed increase of E_X for increasing thickness of C545T was continuous. The small values of E_X, which are observed for small Rabi splittings, roughly correspond to the energy of the 0–0 transition (see Figure 4.8). At large Rabi splittings, by contrast, $E_X \lesssim 2.67$ eV is found, which is similar to the position of the peak value of the entire absorption band (at 2.7 eV). This shift in E_X could indicate an asymmetry in the splitting, as would be expected for the ultra-strong coupling regime.[103] Since the simple CO model used here does not take into account any counter-rotating terms, an asymmetry might be misinterpreted as a shift in exciton energy (with symmetric splitting). Indeed, TMM calculations show that for $d_{\text{C545T}} \gtrsim 20$ nm, $\hbar\Omega \gtrsim 0.5$ eV, which would correspond to $\hbar\Omega \approx 0.2E_X$ and thus limit the applicability of the rotating-wave approximation on which the CO model relies. Since we only care about the extent of the splitting here, the assumed spectral position of the exciton does not matter and we only accept this discrepancy.

The Rabi splitting was determined from the TMM calculations as the energy of the minimal splitting between two modes. These values agreed well (±0.04 eV) with the values of the splitting obtained from the CO model. Figure 4.10a shows the squared Rabi splitting (symbols) determined in this way as a function of the thickness of the C545T film, d_{C545T}, which is proportional to the number of excitons, N. In agreement with expectations, the Rabi splitting increases with increasing d_{C545T}. However, even though theory predicts that $g \propto \sqrt{d}$, the linear fit (green line) fails to describe the data well; a systematic deviation of the data from the fit is visible. This systematic nature of the deviation is confirmed by obtaining very different fit parameters when only fitting a subset of the values. This points to a hidden variable influencing the coupling strength, which is identified as the electric field. Since the electric field forms a standing wave inside the microcavity with nodes at its edges, films of different thickness will not be exposed to the same average field, $\overline{A}$ (see middle panel of Figure 4.10). This means that for the d_{org} series, g is not only affected by the change in N, but also by changes in A.

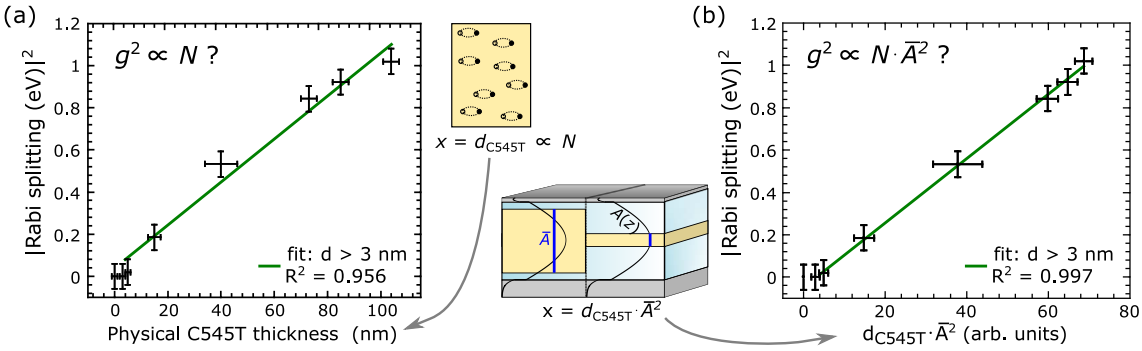

Figure 4.10: Squared Rabi splitting of the d_{org} series as a function of different parameters: (a) as a function of the physical thickness of the organic film, d_{C545T}, and (b) as a function of $d_{\text{C545T}} \cdot \bar{A}^2$, considering the average electric field overlapping with the organic film (see blue lines in central panel). Each symbol represents one set of microcavities with samples of constant thickness of the organic film. The experimental data are fitted with a linear fit for the entire range where a finite splitting was observed (green, solid lines). R^2 values for the fits are indicated in the legend. The central panel illustrates the difference between the x-axes of (a) and (b).

Assuming the correctness of Equations 2.24 and 2.27, this can be accounted for by considering both variables in the fit:

$$\begin{aligned} \hbar\Omega^2 &= 4g^2 && -(\gamma_{\text{X}} - \gamma_{\text{C}})^2 \\ &= a_N \cdot d_{\text{C545T}} \cdot \bar{A}^2 && - b_N . \end{aligned} \tag{4.2}$$

Hence, a linear fit with a_N and b_N as fit parameters can be used to test the validity of Equation 4.2 with $x = d_{\text{C545T}} \cdot \bar{A}^2$ as the dependent variable.

While plotting $\hbar\Omega$ as a function of d_{C545T} is straightforward, the calculation of $\bar{A}$ deserves a few comments. In order to determine $\bar{A}$(C545T), $A(z)$ was calculated for an empty microcavity with $E_{\text{C}} \approx E_{\text{X}}$. The average electric field $\bar{A}$ was calculated from the knowledge of the position (centre, z_0) and optical thickness of the film of C545T ($d_{\text{C545T}} \cdot n$, where $n = 1.8$). This value was then normalised to the maximum value of the average electric field $\bar{A}_{\text{max}}$ that was measured in any of the subsets:

$$\bar{A} = \int_{z_0 - d_{\text{C545T}}/2}^{z_0 + d_{\text{C545T}}/2} A(z)\,\mathrm{d}z \cdot \left[d_{\text{C545T}} \cdot n \cdot \bar{A}_{\text{max}} \right]^{-1} . \tag{4.3}$$

This might seem an oversimplified method, given that the electric field inside the microcavity is certainly changed by introducing a strongly absorbing material into the cavity. Not only is

the refractive index no longer constant, but the mode positions change. Hence, the electric field inside the strongly coupled microcavities is negligible at E_C. This is, however, also the reason why it is difficult to compare the electric field in different cavity structures directly from corresponding TMM calculations. The described method, which was also used by Wang *et al.* [42], Schouwink *et al.* [71], and Hobson *et al.* [72], was thus chosen as an estimate of $\overline{A}$. The normalised values for $\overline{A}$ ranged from 0.81 for the thickest film (104 nm) to 1 for the thinnest film (3 nm) of C545T.

In order to test Equation 4.2, the Rabi splitting in Figure 4.10b is plotted as a function of $d_{\mathrm{C545T}} \cdot \overline{A}^2$. This corresponds to a rescaling of the physical film thickness for the average electric field overlapping with the film. A linear fit was performed on all sample sets for which a finite Rabi splitting was detected, i.e., for $d_{\mathrm{C545T}} > 3$ nm (see green lines in Figure 4.10). The coefficients of determination for each fit are indicated in the legend. Clearly, not only the coefficient of determination improves when changing taking the overlap with the electric field into account ($R^2 = 0.96 \rightarrow R^2 = 0.997$). Also, no systematic deviation of the data from the fit is observed; the remaining deviations between data and fit are of a random nature. The experiment thus confirms that $g \propto \sqrt{N}$. However, a comparison between $x = d_{\mathrm{C545T}}$ and $x = d_{\mathrm{C545T}} \cdot \overline{A}^2$ also shows that in the studied samples, the effect of the electric field is small compared to the changes induced by changing d_{C545T}. Subtle deviations from a $g \propto A$ dependence would thus not necessarily have been obvious in the previously discussed results. Therefore, the next section will look at the effect of the electric field in detail.

4.2.2 Coupling strength as a function of the electric field

In order to isolate the effect of the electric field A, the *OVL* series was produced. The design of the *OVL* series aimed to keep all parameters the same between samples apart from the overlap of a thin, organic film with the electric field. Thus, a set of microcavities was fabricated that contains thin films of C545T of the same thickness but at different positions inside the cavity (see Figure 4.11a). The position of the film inside the microcavity was controlled by changing the thickness ratio of the top and bottom SiO_2 films, yet keeping the sum of the two constant. The experimental variation of the thickness of the organic film was minimised by depositing the film of C545T on all samples in the same evaporation run.

In contrast to all previously discussed samples, a λ microcavity was chosen for the *OVL* series because of the greater variation of the amplitude of the electric field. In a $\lambda/2$ cavity,

the field is non-zero even at the edges of the cavity, due to the penetration depth of the field into the metal. The λ cavity, by contrast, has a node in the centre, where $A \equiv 0$. Moreover, the organic film can be placed with its centre coinciding with the central node, which further reduces the average amplitude over the film in comparison to being placed on the edge of a $\lambda/2$ cavity. As illustrated in Figure 4.11a, the set contains four microcavities in which the film of C545T is gradually shifted from the centre of the microcavity to the maximum of the electric field. According to their overlap with the electric field, the samples are labelled *OVL0* for minimal overlap to *OVL3* for maximal overlap. In addition to these four microcavities, one reference cavity without organic film is produced (*OVLx*) and one cavity *OVL1b*, which is mirror-symmetric to *OVL1*. This means that the organic film has a similar overlap with the electric field as *OVL1*, but it is localised in the other lobe than *OVL1–3*, closer to the opaque mirror.

Figure 4.11b shows the reflectance spectra of samples *OVLx* and *OVL1–3*, measured at different angles between 45° and 75°. This variation of angle served to fine-tune the energy of the cavity photon to be the same in all cavities. The photon energy can be compared at $E_{C,1} \approx 1.2$ eV, which is considered to be uncoupled to the exciton as a result of being far off resonance. It can be verified from the spectra that $E_{C,1}$ is at the same energy for all samples and thus, that the cavities have the same detuning.

The reflectance spectra clearly show that, even though the cavity mode has the same energy in all samples, the reflectance differs greatly around $E \approx 2.5$ eV, where the exciton is close to resonance with the first harmonic cavity mode, $E_{C,2}$. The reflectance of sample *OVL0* (blue line), in which the thin film of C545T is exposed to the smallest average electric field, is very similar to the reflectance of the uncoupled, empty reference cavity, *OVLx* (black line): both only show a single dip at approximately the same energy (mode position indicated by grey symbols). When increasing the overlap of the organic film with the electric field, this single dip is observed to split into two dips, one at lower and one at higher energies. This splitting becomes larger and more pronounced with increasing overlap with the electric field, i.e., moving from *OVL1* (green line) over *OVL2* (orange line) to *OVL3* (red line). The observed behaviour is characteristic for the onset of the strong coupling regime, evidenced by the splitting and anticrossing of modes. Between these samples, the only varied parameter is the position of the thin film of C545T inside the microcavity. Therefore, this transition from the weak to the strong coupling regime is probably driven by the change of electric field to which the organic

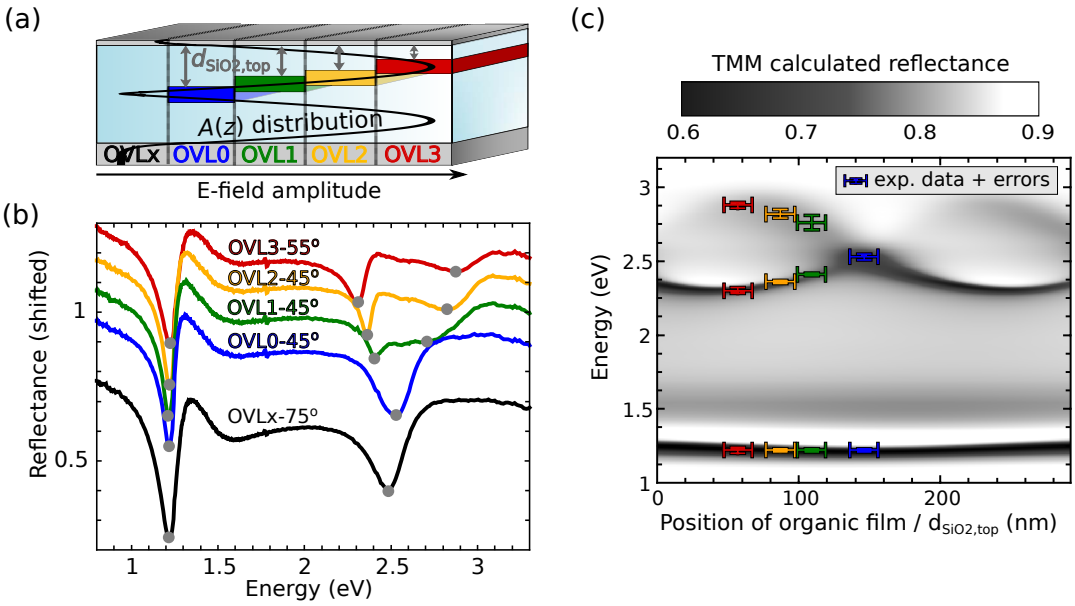

Figure 4.11: Reflectance from the *OVL* series: (a) schematic illustration of the samples; (b) experimental reflectance spectra at different angles, so that the position of the fundamental cavity mode is at the same spectral position; (c) Mode position of measured spectra (symbols, for colour code, see (a)) versus TMM calculation of reflectance (background).

film is exposed.

In order to get a fuller picture of the situation, the measured reflectance spectra are compared to TMM calculations. For this, first the experimental spectra were analysed with the help of TMM calculations to find the total cavity thickness and the position of the microcavity. The thickness of the active layer of C545T was determined from ellipsometry measurements of a bare organic film that was fabricated in the same evaporation run as the samples of the *OVL* series. The thickness of the C545T film inside the microcavities was then fixed to the measured value ($d_{\mathrm{C545T}} = 42$ nm) to reduce the number of variables in the calculation. Since the total thickness of the cavity (and thus of the SiO_2 layers) can be deduced from the position of $E_{\mathrm{C},1}$, the position of the film was the only variable for determining the spectrum. Like this, the thickness of the top and bottom SiO_2 layers could be determined reliably.

With this information, the mode positions from the experimental spectra (symbols) were collated to TMM-calculated spectra of the reflectance as a function of the position of the organic film in the cavity, see Figure 4.11c. Even though the TMM calculation assumes $\Theta = 45°$, the experimental mode positions of *OVL3* were taken from a spectrum measured at 55°. This is because E_{C} is fixed within the calculation, which can—due to experimental variations—only

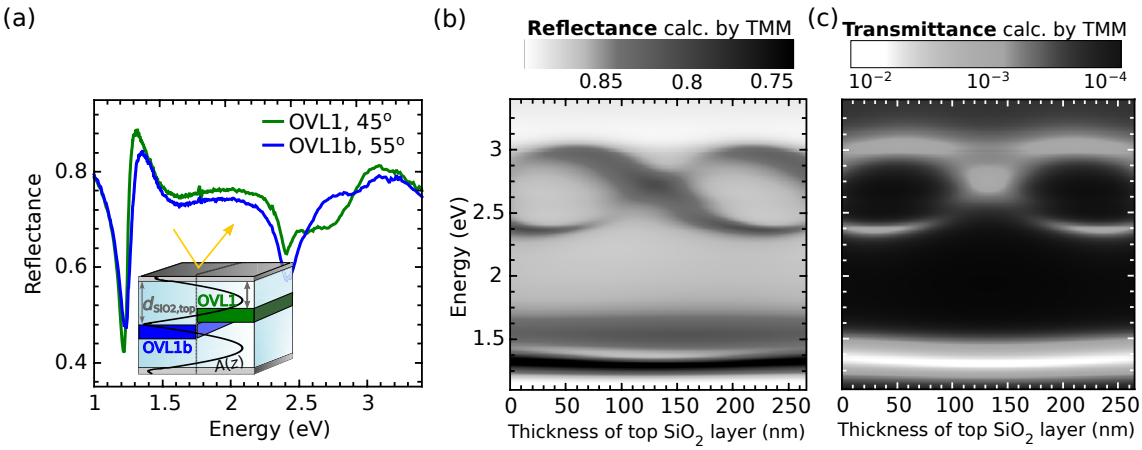

Figure 4.12: Asymmetry of reflectance in the *OVL* series. (a) Experimental reflectance of samples *OVL1* and *OVL1b*; the inset is an illustration of the cavities. (b–c) TMM calculations of (b) the reflectance and (c) the transmittance of a fully symmetric cavity (25 nm Al for both mirrors) containing a 42-nm film of C545T at different positions, which are defined by the thickness of the top SiO_2 layer (x-axis).

be maintained for *OVL3* if $\Theta_{OVL3} = 55°$. Evidently, the measured spectra agree well with predictions using the TMM. The full calculation shows that indeed, there is a transition from a single dip if the film is situated in the centre to two separate dips if the film is located closer to the antinodes of the electric field.

Moreover, the calculations suggest that the splitting is not axis-symmetric with respect to the centre of the cavity. This was not expected, since the distribution of the electric field inside the microcavity is expected to be symmetric (except in regions of close vicinity to the mirrors). Yet, this asymmetry was confirmed experimentally by comparing the reflectance of samples *OVL1* and *OVL1b* (see Figure 4.12a). Both the positions and the depths of especially the mode at higher energy differ. An initial guess assumed the asymmetry of the mirrors (the bottom mirror is opaque whereas the top mirror is semitransparent) to be the origin of this dissimilarity. However, TMM calculations of a symmetric microcavity with two semitransparent mirrors exhibited a similar reflectance map that is not mirror-symmetric with respect to the centre of the cavity (see Figure 4.12b). The TMM-calculated transmittance map of the same structure, however, is symmetric around the centre (Figure 4.12c). This indicates that the asymmetry is linked to the probing method. It is, however, not entirely clear where this asymmetry comes from.

One reason could be that even though the mirrors define the 'main' microcavity, there

exist two 'sub-microcavities' in each sample. These are a result of the difference in refractive indices of C545T and SiO_2*, which means that there will be some reflection on both sides of the SiO_2 films. Since the two sub-microcavities differ in thickness, the spectral mode enhancement and suppression by interference will differ in the top and in the bottom sub-microcavity. When probing the microcavity in transmittance, both sub-microcavities will be probed equally—hence, mirror symmetry is expected. However, when probing the reflectance for instance from the top, the top subcavity will be probed predominantly. Therefore, the spectrum of the main microcavity—from which the observed signatures of the strong coupling regime originate—will be enveloped by a function which mainly represents the interference spectrum of the top microcavity.

Since the comparability of *OVL1b* to samples *OVL0–3* cannot be judged, only samples *OVL0–3* were analysed quantitatively. For this, the splitting in energy was plotted as a function of the average electric field to which the organic film was exposed in each sample. This was calculated according to Equation 4.3, apart from not normalising the field to the maximum value. Since the material, the thickness of the material, and the mode volume are the same for all samples of the *OVL* series, the coupling strength should only depend on the average electric field: $g \propto \bar{A}$. However, it has been extensively discussed that g cannot be accessed directly experimentally and here, not even the Rabi splitting was measured but only the mode splitting at non-zero detuning, $\Delta E_{\mathrm{LP,UP}}$. From Equation 2.22, it follows that the square value of $\Delta E_{\mathrm{LP,UP}}$ can be described as

$$\begin{aligned} \Delta E_{\mathrm{LP,UP}}^2 = &\quad 4g^2 &&+ (E_\mathrm{C} - E_\mathrm{X})^2 - (\gamma_\mathrm{C} - \gamma_\mathrm{X})^2 - 2i\,(E_\mathrm{C} - E_\mathrm{X})(\gamma_\mathrm{C} - \gamma_\mathrm{X}) \\ = &\quad a_A \cdot \bar{A}^2 &&+ b_A. \end{aligned} \tag{4.4}$$

Here, a_A and b_A are fit parameters, where $b_A = (E_\mathrm{C} - E_\mathrm{X})^2 - (\gamma_\mathrm{C} - \gamma_\mathrm{X})^2$. Note that the imaginary term can be neglected because only the mode position is analysed and not its width (or losses). The validity of Equation 4.4 requires all samples to be at the same detuning, but as mentioned before, this was ensured by taking measurements at an angle where the uncoupled modes are at the same position. The measured values of $\Delta E_{\mathrm{LP,UP}}^2$ (black symbols) are shown along with the parabolic fit (green line) in Figure 4.13. The errors for the splitting are conservatively

*The contrast in refractive indices in the relevant spectral region (2.4–3 eV) is mainly due to the large change in refractive index of C545T ($\Delta n = 1.4$) in that region due to the S_0–S_1 absorption band. Therefore, the sub-microcavities will form for any transparent buffer layer since this will show little variation in refractive index due to the Kramers–Kronig relation.

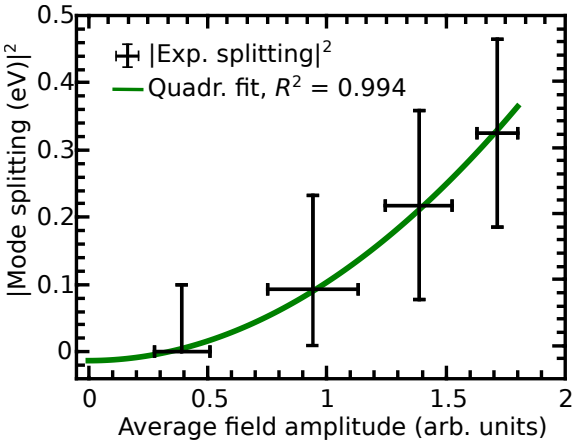

Figure 4.13: Mode splitting as a function of the average field amplitude. The experimental splitting at the same but non-zero detuning is determined from the experimental spectra of samples *OVL0–3*. Its square value is plotted over the average amplitude of the electric field to which the organic film is exposed to in each sample (black symbols). The data is fitted with a parabola (green line), yielding an R^2 value of $R^2 = 0.994$.

estimated from the width of the modes observed in reflectance (see Figure 4.11b) and those for the electric field from the change of this value for small variations of the thickness or position of the organic film. The fit is found to describe the data very well ($R^2 = 0.994$). This suggests that the errors might have been overestimated. Nonetheless, the value of $\Delta E_{\mathrm{LP,UP}} = 0$ at $\overline{A} = 0.4$ (i.e., the data from *OVL0*) should be treated with caution: from Equation 4.4, it follows that $\Delta E_{\mathrm{LP,UP}} = 0$ for all values of g fulfilling $4g^2 + (E_{\mathrm{C}} - E_{\mathrm{X}})^2 < (\gamma_{\mathrm{C}} - \gamma_{\mathrm{X}})^2$. Hence, it is not guaranteed that there might not be samples with a larger overlap between the excitons and the electric field which will also exhibit $\Delta E_{\mathrm{LP,UP}} = 0$. Yet, the data of *OVL0* is also important as it gives a lower limit of $\overline{A}$ at which $\Delta E_{\mathrm{LP,UP}} = 0$ is observed.

The *OVL* series has shown that when carefully designing a sample series in which all parameters but the overlap between the electric field and the organic film are kept constant, $g \propto A$ can be shown unambiguously. The reflectance data showed a transition from the weak coupling regime (single mode) to the strong coupling regime (two anticrossing modes) when increasing the overlap with the electric field. Moreover, it was found that the reflectance spectrum differs depending on which half of the microcavity the thin film of absorbing material is situated in. This asymmetry might originate from microcavity effects due to the contrast of the refractive indices of the active and the transparent buffer material.

4.2.3 Threshold of the strong-coupling regime

The experiments presented in this chapter have used hetero-structure microcavities to systematically vary one parameter at a time. Both when varying the number of absorbers in the d_{org} series and when changing the overlap of an organic film with the electric field in the *OVL* series, an excellent agreement with theoretical predictions was found. In this section, these data will be used further to investigate the strong coupling regime with respect to a potentially non-zero threshold, which is predicted by the CO model. It has been explained, however, that the CO model is very simple in comparison to the complex nature of organic semiconductors and thus, its validity is not evident. The threshold is predicted to correspond to the losses of the organic system but as discussed in Chapter 2.4.3, it is debated if these losses correspond only to lifetime broadening, the inhomogeneous broadening or to the entire structural and disorder broadening.

As explained before, the threshold of the strong-coupling regime can be determined from the y-intercept of the fit curves which describe the Rabi or energy splitting as a function of the varied parameter. Thus, the threshold for the onset of the strong coupling regime can be calculated from the d_{org} series from the fit parameter b_N according to (see Equation 4.2)

$$g_{\mathrm{thr}}^{d_{\mathrm{org}}} = \frac{\sqrt{b_N}}{2} = (0.11 \pm 0.02)\ \mathrm{eV}. \tag{4.5}$$

The error was determined from the error given by the fit ($\delta b_N = 0.014\ \mathrm{eV}^2$).

For the *OVL* series, the threshold is deduced from Equation 4.4 to be

$$g_{\mathrm{thr}}^{OVL} = \frac{\sqrt{(E_{\mathrm{X}} - E_{\mathrm{C}})^2 - b_A}}{2} = (0.07 \pm 0.03)\ \mathrm{eV}. \tag{4.6}$$

Here, the error was propagated from the estimated error of the energy of the exciton ($\delta E_{\mathrm{X}} = 0.04$ eV), the estimated error of the energy of the photon ($\delta E_{\mathrm{C}} = 0.01$ eV) and of the error of the fit parameter ($\delta b_A = 0.007\ \mathrm{eV}^2$). The error of E_{X} is presumed to be relatively large (1) because the exciton energy estimated from TMM calculations and from the coupled oscillator model differ and (2) because of the inherent ambiguity of E_{X} stemming from the broad absorption band (i.e., it is not clear if E_{X} corresponds to the energy of the central position of the electronic transition, of the 0–0 transition or of some intermediate value). Note that the way

g_{thr}^{OVL} was determined might underestimate the threshold. This is because of the zero splitting observed in *OVL0*, which represents not necessarily the largest overlap at which zero splitting can be observed. Ideally, one would want to measure the largest overlap of the excitons with the electric field for which no splitting occurs to determine the threshold. The higher this value of the electric field is, the larger the calculated threshold will be. The value from *OVL0* was taken into account despite these considerations because it can serve as a lower limit of the threshold. Moreover, discarding the data of *OVL0* would only leave three values to be fitted by the two-variable fit function (Equation 4.4), which would be more arbitrary.

Although $g_{\mathrm{thr}}^{d_{\mathrm{org}}}$ and g_{thr}^{OVL} differ, the difference is moderate and within the intervals of confidence. It is emphasised that this is the case even though different samples were analysed and the coupling strength was tuned with different variables. Note that the potential underestimation of g_{thr}^{OVL} is consistent with its lower value compared to $g_{\mathrm{thr}}^{d_{\mathrm{org}}}$.

A quantitative comparison of these values with the CO model requires a calculation of the theoretically predicted threshold. This follows from Equation 2.25 to be

$$g_{\mathrm{thr}}^{\mathrm{CO}} = \frac{|\gamma_{\mathrm{C}} - \gamma_{\mathrm{X}}|}{2}. \tag{4.7}$$

It is straightforward to determine γ_{C} from the linewidth of an empty cavity. Here, the cavity spectrum was calculated using the TMM method, which produces $\gamma_{\mathrm{C}} = (0.13 \pm 0.02)$ eV. The error was estimated considering that TMM calculations correspond to idealised cavities, from which the experimental values might deviate. The value for γ_{X}, in contrast, is still disputed. This is why, similar to Section 4.1, we test three different scenarios for what defines the losses of the exciton: (1) Assuming that the lifetime broadening dominates the losses and assuming $\tau \gg 1$ ps, which is generally the case for organic semiconductors,[75] the excitonic losses are $\gamma_{\mathrm{X}}^{\mathrm{hom}} \ll 10^{-4}$ eV. (2) When assuming the losses related to disorder only to be dominant, these can be determined from the multi-Gaussian fit to k_{C545T} (see Figure 4.8), and one obtains $\gamma_{\mathrm{X}}^{\mathrm{inhom}} = (0.23 \pm 0.06)$ eV. An average of the three dominant peaks was taken as an estimate for $\gamma_{\mathrm{X}}^{\mathrm{inhom}}$. The large error of $\gamma_{\mathrm{X}}^{\mathrm{inhom}}$ is a result of the large spread of peak widths of the individual Gaussian peaks. (3) Finally, when both the disorder and the vibronic substructure of the electronic transition is taken into account, the excitonic losses will be determined from the FWHM of the excitonic peak. This yields $\gamma_{\mathrm{X}}^{\mathrm{FWHM}} = (0.51 \pm 0.02)$ eV with the relatively small error reflecting the straightforward determination. Substituting these values into Equation 4.7,

we obtain three different values for theoretical predictions of the threshold depending on the assumptions for the excitonic losses:

$$g_{\mathrm{thr}}^{\mathrm{theo}} = \begin{cases} (0.07 \pm 0.01)\ \mathrm{eV} & \text{if losses are predominantly homogeneous;} \\ (0.05 \pm 0.06)\ \mathrm{eV} & \text{if losses are predominantly inhomogeneous;} \\ (0.19 \pm 0.02)\ \mathrm{eV} & \text{if the entire absorption width defines the losses.} \end{cases} \tag{4.8}$$

These theoretically predicted values will now be compared to the thresholds obtained from the experimental investigations with the d_{org} series and the *OVL* series. First, note that the order of magnitude of the two experimentally determined values agrees with the values expected from studying the losses of the coupled system. Thus, it can be concluded that the threshold for the onset of the strong coupling regime, which is observed with both independent, experimental methods, is consistent with predictions from the CO model.

The analysis of how exactly the losses from the excitonic part contribute, is, however, less clear. This is partly due to the similarity in values of $g_{\mathrm{thr}}^{\mathrm{theo}}$. Even though the values for γ_{X} span several orders of magnitude, the values of $g_{\mathrm{thr}}^{\mathrm{theo}}$ lie much closer and vary by less than a factor of four. That difference stems from the form of the threshold, which depends on the difference between the losses and not on the absolute values of the losses. Especially the values of $g_{\mathrm{thr}}^{\mathrm{hom}}$ and $g_{\mathrm{thr}}^{\mathrm{inhom}}$ are very similar—not even distinguishable when taking the large errors of the values into account. A discrimination between effects of $g_{\mathrm{thr}}^{\mathrm{hom}}$ and $g_{\mathrm{thr}}^{\mathrm{inhom}}$ would be possible if one of the values was controlled. Hence, the inhomogeneous broadening in C545T was attempted to be reduced by cooling thin films to cryogenic temperature and by annealing the organic films (data not shown here). However, none of the methods yielded a reduction in $\delta E_{\mathrm{inhom}}$ so that the indistinguishability could not be lifted experimentally. Thus, the theoretical values do not allow for any distinction between excitonic losses being defined by lifetime broadening or instead being strongly affected by disorder.

The second difficulty when comparing $g_{\mathrm{thr}}^{\mathrm{exp}}$ to $g_{\mathrm{thr}}^{\mathrm{theo}}$ is the (small) difference of the experimentally determined thresholds. There are two ways to compare them to the theoretical values; one could either take their average to yield $g_{\mathrm{thr}}^{\mathrm{exp}} = (0.09 \pm 0.03)$ eV or argue that $g_{\mathrm{thr}}^{d_{\mathrm{org}}}$ is more reliable and hence deduce that $g_{\mathrm{thr}}^{\mathrm{exp}} = (0.11 \pm 0.02)$ eV. Either way, $g_{\mathrm{thr}}^{\mathrm{exp}}$ lies between the theoretically predicted values—it is larger than $g_{\mathrm{thr}}^{\mathrm{hom}} \approx g_{\mathrm{thr}}^{\mathrm{inhom}}$ and smaller than $g_{\mathrm{thr}}^{\mathrm{FWHM}}$—so that no clear distinction can be made. Hence, this set of data, although more quantitative

than the comparison of different materials, does not allow for determining the nature of the excitonic losses in the CO model.

The analysis discussed in this section shows that by systematically changing one parameter of the system, a threshold for the onset of the strong coupling regime can be determined from experiments. This was done by mostly investigating samples well above the threshold, where the splitting was clear and not blurred by the broad modes. This increases the reliability of the method. The existence of the threshold confirms the validity of the CO model. The data was further used to test if the losses of the exciton are defined by homogeneous broadening, inhomogeneous broadening or by the entire width of the electronic transition. Here, however, the data did not allow for singling out one particular loss mechanism.

4.3 Discussion

The experiments presented in this chapter all investigate the same question: 'To what extent are the simple models commonly used valid for the complex, large-disorder systems of organic semiconductors?' The answer to this question is not obvious, given the number of particularities found in the organic strongly coupled microcavities (see Chapter 2.4.3). For answering the question, different parameters were varied in distinct samples series: the material in the microcavity, the number of absorbers at constant concentration or the overlap of a film of constant thickness with the electric field. The discussed investigations fully confirm the validity of the simple form of the coupling strength, $g \propto A\sqrt{Nf}$—in view of the complexity of the organic material, perhaps somewhat surprisingly. Likewise, the results are consistent with the prediction from the coupled oscillator model of a threshold for the onset of the strong coupling regime that depends on the losses in the system.

On the more subtle points, however, observations are less clear-cut. The first subtle point relates to the definition of the oscillator strength in such a strongly broadened material. It classifies as textbook knowledge that the oscillator strength of a transition is proportional to the integral over the absorption coefficient α_{int}.[75] However, the investigation comparing the Rabi splitting of different materials could not confirm this uniformly. On the one hand, when testing different values as loss terms to determine g from $\hbar\Omega$, the highest agreement was obtained for $g_{\text{FWHM}} \propto \sqrt{\alpha_{\text{int}}}$. This fit assumed the losses to be defined by the full width of the absorption and the oscillator strength by the integrated absorption—and yielded a coefficient of deter-

mination of $R^2 = 0.95$. On the other hand, a comparison between fitting $\hbar\Omega \propto \sqrt{\alpha_{\mathrm{int}}}$ and $\hbar\Omega \propto \sqrt{\alpha_{\mathrm{max}}}$ (the integrated and peak absorption, respectively) showed a higher agreement when assuming $f \propto \alpha_{\mathrm{max}}$ ($R^2_{\mathrm{max}} = 0.95$ versus $R^2_{\mathrm{int}} = 0.83$).

When evaluating these two results which seem contradictory at first sight, two aspects ought to be considered: (1) the number of hidden variables and (2) the number of fit parameters. (1) From Equation 2.24, it follows that the Rabi splitting depends on the coupling strength minus the losses in the system. The losses cannot be assumed to be the same across the samples because the materials differed. Thus, the losses are an extra unknown parameter hidden in $\hbar\Omega$ which is not present in g. All potential extra variables in g, by contrast, will also appear in $\hbar\Omega$. As a consequence, the dependence between g and any variable (contained in g) is expected to be more meaningful than the relationship of that variable to $\hbar\Omega$. (2) Due to the threshold predicted by the CO model, the fit of $\hbar\Omega$ allowed for a non-zero y-intercept and thus in total for two fit parameters. Since for fitting g there was only one variable (y-intercept fixed to zero), the fit for g will be more consequential in that regard as well. I conclude therefore that even though the (adjusted) R^2 values are the same between the two investigations, $g \propto \sqrt{\alpha_{\mathrm{int}}}$ is more trustworthy. Thus, the experiments confirm (1) that $g \propto \sqrt{f}$ and (2) that the entire S_0–S_1 transition couples to the photon, $f \propto \int \alpha(\nu)\,\mathrm{d}\nu$.

In addition to analysing the form of the coupling strength, the data from all three different sample sets was used to examine the threshold for the onset of the strong coupling regime quantitatively. This was done to discriminate different potential loss terms of the exciton between pure lifetime losses ($g^{\mathrm{hom}}_{\mathrm{thr}}$), losses dominated by the disorder ($g^{\mathrm{inhom}}_{\mathrm{thr}}$) and losses due to the full range of available states ($g^{\mathrm{FHWM}}_{\mathrm{thr}}$). In this regard, the investigations comparing different materials yielded the clearest result: for these samples, it could be shown that when assuming $g^{\mathrm{FHWM}}_{\mathrm{thr}}$, $g \propto \sqrt{f}$ could be reproduced to a greater coefficient of determination ($R^2 = 0.95$) than when assuming $g^{\mathrm{inhom}}_{\mathrm{thr}}$ ($R^2 = 0.89$) or $g^{\mathrm{hom}}_{\mathrm{thr}}$ ($R^2 = 0.86$). Yet, this test was not clearly pinning down of the value of γ_{X}, but rather testing them for consistency with different assumed hypotheses. Furthermore, the samples of this series showed an overall much greater variance from the fit function than the more controlled d_{org} series or *OVL* series.

The more sophisticated layout of the d_{org} series and of the *OVL* series allowed for a more reliable quantitative evaluation of the data. The results were insofar satisfying as they all confirmed the existence of the threshold and allowed for determining its order of magnitude

($\sim$ 0.1 eV), which was estimated to be similar to prevailing losses. However, they did not provide a consistent picture of the underlying mechanism of the excitonic losses. Within the errors of the values, the threshold was estimated to being somewhere between $g_{\mathrm{thr}}^{\mathrm{hom}}$, $g_{\mathrm{thr}}^{\mathrm{inhom}}$ and $g_{\mathrm{thr}}^{\mathrm{FWHM}}$.

These results are obviously neither conclusive nor unambiguous. This might, on the one hand, be due to experimental constraints and errors which do not allow for a further specification. On the other hand, however, it might also be the physical circumstance that the losses cannot be identified with exactly one of these tested values. Losses corresponding to a value between $\gamma_{\mathrm{X}}^{\mathrm{inhom}}$ and $\gamma_{\mathrm{X}}^{\mathrm{FWHM}}$ would explain thresholds of $g_{\mathrm{thr}}^{\mathrm{exp}} \sim 0.1$ eV well. This assumption would also not necessarily contradict the observations from the material comparison, where both $\gamma_{\mathrm{X}}^{\mathrm{inhom}}$ and $\gamma_{\mathrm{X}}^{\mathrm{FWHM}}$ yield the highest agreement between data and fit. Finally, such a partial robustness to disorder would be in agreement with observations on the linewidth of polaritons and on the extent of the Rabi splitting.[106,175]

5

Photoluminescence from strongly coupled, organic microcavities

Luminescence measurements are essential for obtaining information about the dynamics of emissive systems. Dynamics, in turn, determine which states are populated to which extent and thus provide insight into the ongoing relaxation processes.[75,109] For example, the stimulated scattering of polaritons into the ground state is indicated in the luminescence by a concentration of emission from the ground state minimum as a function of both energy and momentum.[25] Moreover, a comparison of PL measurements from strongly coupled microcavities to the theory established for weakly coupled systems allows to detect peculiarities of the strongly coupled system. In order to study PL, this chapter focusses on microcavities with distributed Bragg reflectors (DBRs) as mirrors and blended films of C545T and MADN as active material. First, the uncoupled system was investigated, for which Section 5.1 discusses the optical properties of thin films of C545T:MADN at different ratios. Section 5.2 is dedicated to experimental challenges which were faced when attempting to demonstrate polariton conden-

sation in this material system. In particular, investigations aiming at finding the reason why these attempts were unsuccessful are discussed. Finally, Section 5.3 looks at the relationship between the PL intensity from strongly coupled microcavities and the intensity expected from a weakly coupled system. First, this is studied for the *OVL* series presented in Chapter 4.2, i.e., metal-clad cavities with the same uncoupled properties. The last part then discusses the PL from DBR-clad microcavities with different blends of C545T and MADN and with different Q-factors.

5.1 Optical properties of uncoupled, blended films

In order to understand the effect the strong coupling regime imposes on the material, the properties of the uncoupled material need to be known. This includes the optical constants of the bare films and—since this chapter studies the luminescence from polaritons—their luminescence properties. Both are expected to vary significantly for different blending ratios of the two materials, C545T and MADN, where C545T acts as chromophore and MADN as matrix material. MADN was chosen as a host material complementary to C545T as it absorbs at larger energies. Moreover, the C545T:MADN system has been demonstrated to enable efficient electroluminescent devices.[228]

5.1.0.1 Optical constants with different C545T:MADN blending ratios

Changing the concentration of a blended film is a powerful tool for controlling the optical properties of organic materials. While absorption generally depends linearly on the concentration C of a chromophore (Beer's law, $k \propto C$)[229], this is the case for luminescence only for very dilute chromophores.[230] For higher concentrations, self-absorption and the processes discussed in Chapter 2.4.3 reduce the luminescence efficiency. At small distances between chromophores, so-called concentration quenching sets in, which denotes that the PLQY not only saturates but decreases.[225] Concentration quenching can be reduced by spacing the conjugated segment of molecules further apart, e.g. with the help of additional side groups. This is the reason why the polymers studied in Chapter 4.1 maintain a high PLQY even in neat films.[211,219,220] C545T, by contrast, has been shown to emit most efficiently at very low concentrations in a host matrix ($\lesssim 1\%$).[226,231] The absorption and emission properties of a blended C545T:MADN film are thus expected to show different trends with increasing concentration of C545T.

Figure 5.1 shows the real (a) and the imaginary part (b) of the measured refractive index

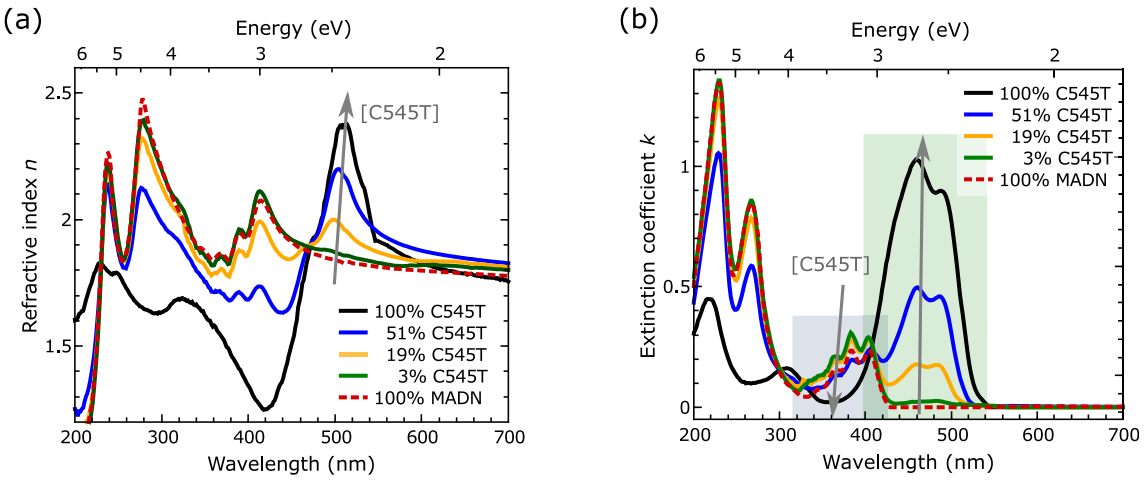

Figure 5.1: Optical constants of a film of blended C545T:MADN with different concentrations (0 to 100% C545T) from ellipsometry measurements. Grey arrows indicate increasing concentration of C545T. The concentration of the films was determined from the peak height of their extinction coefficient. (a) Real part of the refractive index, n. (b) Imaginary part of the refractive index, extinction coefficient k. The green and blue shading indicates the spectral region of the S_0–S_1 absorption of C545T and MADN, respectively.

of films containing different mixing ratios of co-evaporated C545T:MADN (ranging from 0 to 1). The extinction coefficient peaks for C545T at $\lambda \approx 480$ nm and for MADN at $\lambda \approx 370$ nm. At long wavelengths with respect to this absorption, the refractive index takes a value of $n \approx 1.8$ for all different mixing ratios. In the spectral range where either C545T or MADN absorb, the refractive index shows an oscillatory behaviour in agreement with Kramers–Kronig relations. As the crucial property for strong coupling in organic semiconductors is the extinction coefficient (see Chapter 4.1), this will be discussed quantitatively in the following.

The extinction coefficient for different concentrations of C545T in MADN is shown in Figure 5.1b. At 100% concentration of C545T (black solid line), nearly the entire absorption takes place at 400 nm $\lesssim \lambda \lesssim$ 540 nm and at 0% C545T (i.e., 100% MADN, red dashed line) the S_0–S_1 absorption peak is at 320 nm $\lesssim \lambda \lesssim$ 420 nm. Ignoring absorption features in the far UV, which corresponds to absorption to higher excited states, these absorption peaks were analysed by fitting them with an ensemble of four Gaussian peaks, see Equation 4.1 ($m_{\mathrm{max}} = 3$). This form of the fit function was chosen to account for a vibronic substructure in a disordered material, which is typical for organic semiconductors. Fit parameters for the absorption peak of both pure C545T and pure MADN are given in Table 5.1. Both fits yield high coefficients of determination, $R^2_{\mathrm{C545T}} = 0.9996$ and $R^2_{\mathrm{MADN}} = 0.9988$. While this is partly owed to the large number of fit parameters, it also validates the assumptions underlying Equation 4.1. The

Table 5.1: Fit parameters for the peak of the extinction coefficient of C545T and MADN according to Equation 4.1. The measured peaks were fitted with four Gaussians each, where a vibronic structure with fixed ground state energy E_0 and vibronic energy E_{vib} was assumed. R^2 denotes the value of the coefficient of determination of the fit.

Material	R^2	E_0 (eV)	E_{vib} (eV)
C545T	0.9996	2.501	0.163
MADN	0.9988	3.062	0.174

	Peak heights (arb. units)				Peak widths (eV)			
Material	A_0	A_1	A_2	A_3	σ_0	σ_1	σ_2	σ_3
C545T	0.720	0.676	0.634	0.146	0.101	0.121	0.167	0.243
MADN	0.224	0.224	0.145	0.076	0.090	0.093	0.092	0.102

vibronic spacing is slightly smaller for C545T than for MADN, $E_{\text{vib}}^{\text{C545T}} = 0.16$ eV and $E_{\text{vib}}^{\text{MADN}} = 0.17$ eV, respectively, while the vibronic broadenings σ_m are larger for C545T. This results in an absorption peak of C545T which has less features of the vibronic substructure discernible compared to MADN. The 0–0 transition of C545T lies at lower energies, $E_0^{\text{C545T}} = 2.50$ eV ($\lambda = 496$ nm) compared to $E_0^{\text{MADN}} = 3.06$ eV ($\lambda = 405$ nm), and the entire absorption is more pronounced. Strong coupling is sought around the excitons of C545T.

Upon blending the two materials (blue, yellow and green solid lines), no additional features, which would be attributed to coupled excited states, appear. As a consequence, Beer's law can be assumed to be valid. Thus, the actual C545T content of each sample was determined from the measured height of the absorption peak of C545T (at $\lambda = 486 \pm 3$ nm), $\widehat{k}$, interpolating linearly between $\widehat{k}(0\%\,\text{C545T}) = 0$ and $\widehat{k}(100\%\,\text{C545T}) = 0.91$. From this method, the C545T concentration was found to be larger than the nominal concentration, i.e., the intended concentration which was controlled by quartz crystal monitoring during the evaporation process using separately determined tooling factors for each material. Possible reasons for this deviation are discussed in Chapter 3.4. Table 5.2 summarises the optical properties of blended films for selected concentrations of C545T.

5.1.1 Photoluminescence as a function of different C545T:MADN ratios

After the optical constants, the PL properties of pure C545T and blended C545T:MADN films were investigated in an integrating sphere, see Figure 5.2. All PL spectra are red-shifted with respect to the absorption (see Figure 5.1). The extent of the red-shift increases with increasing concentration of C545T (see also Table 5.2). Comparing the film containing 3% C545T with

Table 5.2: Summary of the optical properties (absorption and PL) of blended films of C545T and MADN at different ratios. $\lambda(\mathrm{PL_{max}})$ denotes the spectral position of the peak PL. k–PL shift describes the energetic difference between the lowest absorption peak (E_0) and peak emission.

[C545T]	k(486 nm)	$\lambda(\mathrm{PL_{max}})$	k–PL shift	PLQY
3%	0.03	505 nm	0.04 eV	0.58
19%	0.18	557 nm	0.27 eV	0.20
43%	0.39	568 nm	0.32 eV	0.11
100%	0.91	602 nm	0.44 eV	0.06

the pure MADN film, a very distinct PL spectrum is observed. This indicates that the energy, which is mainly absorbed by MADN, is efficiently transferred to C545T. Of all PL spectra, only that of the very low-concentration film (3% C545T, green line) shows a substructure which can be attributed to vibronic replicas. All other spectra only consist of a single, broad peak. Both the shift of high-concentration C545T films and the spectral shape are in agreement with other reports.[232,233] Therein, the red-shift and the spectral change with concentration was explained with the formation of excimers. Excimers arise from a large Coulomb interaction between two resonant, excited molecules. While their absorption is unchanged with respect to the monomer, the emission is red-shifted and no longer shows any vibronic structure.[75] The extent of the red-shift observed here is in agreement with Liu *et al.* [233] for intermediate concentrations of C545T, but it is much larger than the red-shift observed by Rhee *et al.* [232] for pure films (measured peak at 602 nm vs literature value at 573 nm). However, since the formation of the excimer depends on the interaction between different excitons, a continuous shift with increasing concentration is expected.[234] The signature of excimer emission dominates in the PL of films with high C545T concentrations in MADN. Hence, it is deduced that only at very low C545T concentrations, the emission is expected to originate from the exciton.

Together with the red-shift of the PL, the PLQY drops strongly with increasing concentration of C545T (see Figure 5.2b). In very good agreement with literature, the highest PLQY is observed at the lowest concentration, $\Phi([\mathrm{C545T}] = 1\%) = 0.7$.[228] The decay of the PLQY with concentration can be attributed to concentration quenching, as done before for the efficiency of electroluminescence in devices containing C545T.[231] Yet, for electroluminescence, non-radiative decay channels like triplet–triplet annihilation and triplet–polaron annihilation are expected to quench luminescence,[83,232] which are both negligible in PL. Thus, even though the reduction in efficiency is on the same order of magnitude as reported in literature, the

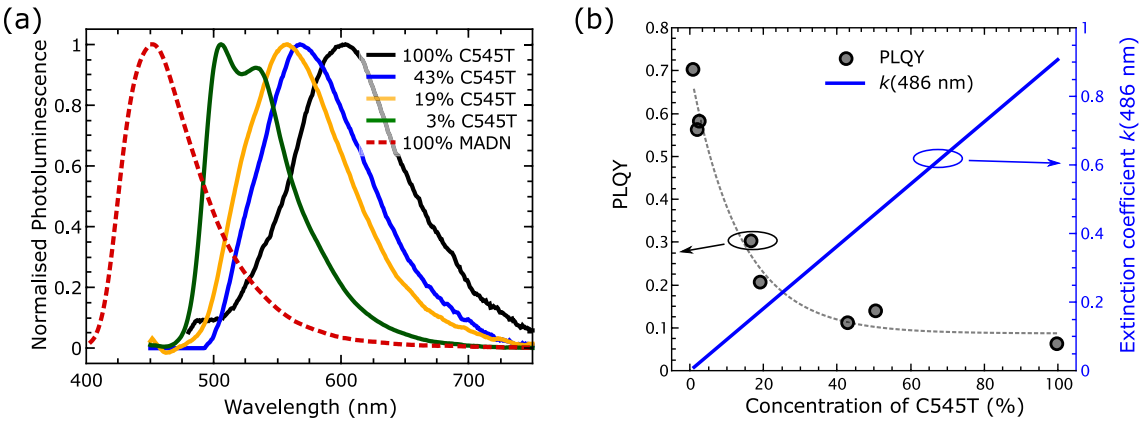

Figure 5.2: Luminescence properties of C545T:MADN-blended films with different concentrations (0 %to 100% C545T) from measurements in the integrating sphere. (a) Photoluminescence spectra (smoothed, background-corrected and normalised). All samples containing C545T were excited at 420 nm, while the pure MADN film was excited at 355 nm. (b) Left axis: PLQY as a function of the C545T concentration in the film (grey symbols), which was determined from the value of the extinction coefficient at (486 ± 3) nm (blue solid line, right axis). The grey, dashed line is a single exponential fit and acts as a guide to the eye.

quenching mechanisms are probably different for the PL shown here. The investigations shown above demonstrate that by tuning the concentration of C545T in the organic layer, the absorption and the spectral position as well as the efficiency of the luminescence can be controlled. These parameters cannot be tuned independently, though. Instead, an increase in absorption will always be concomitant with a decrease in PLQY of the bare film at constant layer thickness for a given host–guest material system (see Figure 5.2b).

The behaviour of the optical properties of the material with concentration of the dye observed here is well known for organic molecules. However, it is not obvious how this behaviour will be affected by the strong coupling regime. On the one hand, the cavity photon has been shown to mediate energy transfer between different exciton species and improve the PLQY.[41,107,235] On the other hand, different investigations support the picture that the scattering from the exciton reservoir to the polariton branches is slow.[109] As a consequence, excimers have even been found to play an active role in the population of the polariton branches by radiative pumping.[43] The concentration-dependent studies presented in the following sections aim to clarify this picture.

5.2 Experimental challenges: Organic materials in high-Q microcavities

A large fraction of this PhD was dedicated to optimising microcavities in order to achieve polariton condensation, but was unsuccessful in this respect. To the best of my knowledge, the understanding of which parameters are critical for polariton condensation in organic microcavities is limited at present. To date, a number of different materials with very distinct properties have shown to support polariton lasing.[27,60–63] These publications mostly focus the properties of polariton condensates in organic microcavities and its peculiarities, which is undoubtedly exciting and important science. Yet, the limited overall number of reports over the course of eight years shows that achieving polariton condensation in organic materials is not straightforward. Nonetheless, no systematic study on which parameters are crucial for polariton lasing has been published. Dietrich *et al.* [62] comment on the dependence of the threshold for condensation on the detuning of cavity photon and exciton. However, the highly tunable system of organic microcavities allows for the variation of many more parameters. These comprise the coupling strength, the cavity detuning, the PLQY of the organic material, the Q-factor of the microcavities and different pump parameters.

This section discusses the systematic study on optimising a many-variable system for polariton condensation. The first part describes the different handles used in the optimisation and the investigated parameter space. Thereafter, possible reasons for why the non-linear regime was not reached are discussed. The demonstration of photon lasing in the same material system in the last part serves as validation of the design and fabrication process.

5.2.1 Optimising microcavities for polariton condensation

The chosen material system to be optimised were DBR-clad microcavities filled with blended films of organic material. The optimisation involved an iterative combination of simulations, fabrication and characterisation. Figure 5.3 illustrates the different parameters which might influence the condensation threshold and which were thus controlled. The effect of the different parameters will be briefly explained in the following. A summary of the parameters of fabricated and analysed samples is found in Table 5.3.

By changing the concentration of C545T in the matrix MADN (2% to 100%), both the

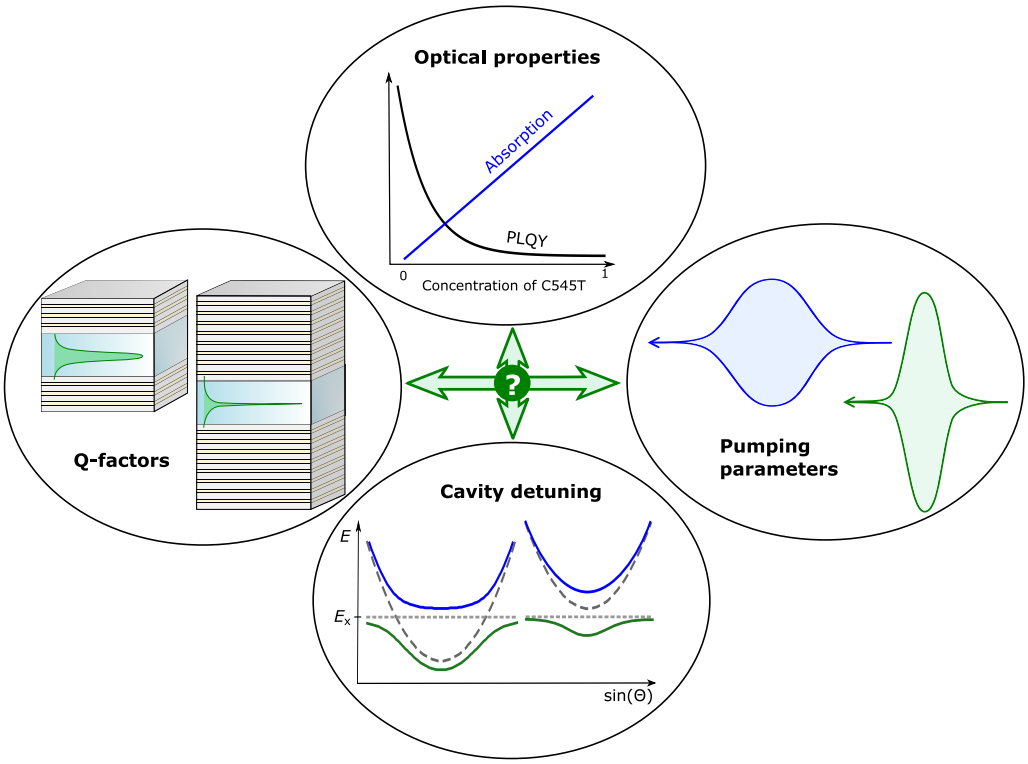

Figure 5.3: Illustration of experimental parameters which were varied during the optimisation of the system for polariton condensation. The *Q*-factor of the cavity was varied by changing the number of mirror pairs, the optical properties of the cavity material were tuned via the C545T:MADN ratio, exciton–photon detuning was controlled via the cavity thickness and different pumping conditions were tested.

coupling strength (via the absorption, see Chapter 4.1) and the PLQY can be controlled. The two are, however, linked (see Figure 5.2) in a way that an increase in absorption will result in an exponential reduction of the PLQY. By combining sputtering and thermal evaporation in the fabrication process, both the *Q*-factor of the cavity and its thickness could be chosen at liberty. Sputtering a different number of mirror pairs in the DBRs (3.5 to 9.5 pairs) provided control over the *Q*-factor. An upper limit for these *Q* factors was obtained from transfer matrix (TMM) calculations, which yielded $70 < Q < 6,700$ (see Table 5.3). Cavities using > 5.5 mirror pairs are thus expected to exceed the *Q*-factors of 600, for which polariton condensation has been previously achieved by Daskalakis *et al.* [61]. By varying the thickness of the microcavity (i.e., the thickess of the organic material), different—positive and negative—detunings were chosen for each combination of concentration and mirrors. Like this, the photonic and excitonic fraction and thus at the same time the relaxation pathways could be varied despite the fixed angle pumping ($\Theta \approx 0°$) and probing ($\Theta = 0 \ldots 30°$) of the samples. Finally, different excita-

Table 5.3: Summary of samples produced for polariton condensation and the experimental pumping parameters. # DBR pairs, Q, [C545T], $d_{\text{min}}-d_{\text{max}}$, Δd and λ_{pump} denote the number of pairs of alternating refractive index in the DBR, the resulting Q-factor, the concentration of C545T in an MADN matrix, the range of thicknesses covered in the samples, the thickness interval between different samples and the excitation wavelength, respectively.

Sample parameters					**Pumping parameters**	
# DBR pairs	Q	[C545T]	d_{min}–d_{max} (nm)	Δd (nm)	Pulse length	λ_{pump} (nm)
3.5; 7.5	70; 340	3%	80–160	~ 25	5 ns; 180 fs	355, 420; 343
		19%	75–160	~ 30	5 ns; 180 fs	355, 420; 343
		43%	80–170	~ 30	5 ns; 180 fs	355, 420; 343
		100%	70–110	~ 15	5 ns	355, 420
7.5	1,500	43%	50–200	10	5 ns; CW	355; 440
9.5	6,700	2%	100–160	~ 8	5 ns; 180 fs	420; 343
		51%	100–160	~ 8	5 ns; 180 fs	420; 343

tion parameters were used. The microcavties were pumped with 5 ns pulses at 355 nm or at 420 nm (see Figure 3.4), and some additionally by an optical parametric amplifier providing 180 fs pulses at 343 nm. For the latter, I acknowledge the help by Sai K. Rajendran and permission to use the equipment by Ifor D.W. Samuel. The pump power was increased until the point of visible damage to the sample. Both the pump wavelength and the pulse duration play an important role in the optimisation. Pumping the microcavities at different wavelengths will influence the pumping efficiency. The use of fs-pulsed laser light has so far been necessary for most demonstrations of polariton lasing (excepting Dietrich *et al.* [62]). There are three reasons why short pulses of excitation are beneficial for increasing the density of excited states in the system. (1) Due to the short excited-state lifetime in organic semiconductors ($\lesssim 1$ ns), the excitation energy has to be delivered within a short period. Increasing the time span of excitation means that some of the excitons will have decayed by the time the last excitons get excited. (2) Even though the formation of triplets is not a very common process, these excited states are very long-lived (~ 100 ns).[75] Thus, a continuous excitation would decrease the number of excitable states, which will be avoided when triplets can decay between pulses. (3) Finally, all non-radiative processes during the relaxation of excitons will heat the organic material. Pumping the material with short pulses allows for the heat to diffuse and dissipate between excitation events. In this way, the damage to the sample by heating can be greatly reduced.

As mentioned before, none of the samples produced a polariton condensate. The angular

emission was studied as a function of PL intensity (peak intensity and angular distribution), of the width of the PL peak and of its spectral position. These values were extracted from the Fourier image with the help of a Matlab script (developed in the course of this PhD) that fitted the 1D-spectrum of each pixel in momentum space by a Lorentzian. This was intended to show the signatures of the non-linear threshold, e.g. a continuous spectral blue-shift of the PL and a concentration of the PL intensity at the bottom of the LP. None of these effects were observed. Luminescence generally originated from the bottom of the LP, not showing any sign of a relaxation bottleneck. This remained unchanged when increasing the power—apart from an observed increase in PL intensity—up to the point where the sample was damaged and the mode became darker and broader.

One obvious problem of the produced samples was that many did not show any mode in the stopband at all. When modes were observed, they were located at the edge of the stopband, where the reflectance of the DBRs and hence the *Q*-factor of the microcavity is reduced. This, one could argue, might be a problem of poorly designed samples, where the mode should not be expected within the stopband. However, Figure 5.4a proves that this was not the case. The Figure shows a data series of 14 microcavities with 7.5 mirror pairs of nominal thicknesses between 50 nm and 200 nm. On this series, reflectance, transmittance and PL measurements were performed. Modes from the experimental spectra, when appearing in the stopband, are marked in a 2D plot with red, blue and yellow symbols respectively. They are compared to TMM calculations of a corresponding structure (grey-shaded background). Mostly, the measurements agree with each other and with the TMM calculation. However, none of the samples between 100 and 140 nm show any mode—in agreement with the calculations. The transmission of the organic quadrant (see Chapter 3.5) on the same samples (Figure 5.4b), demonstrates that the absorption (and hence the real thickness) increases monotonically with nominal thickness of the organic film. In consequence, this means that there is a range of cavity thicknesses—which corresponds, in fact, to resonance of photon and exciton—where no mode is visible.

With this, four potential reasons have been identified that could impede polariton condensation: (1) damage of the organic material during the fabrication process, (2) a large discrepancy between the *Q*-factors from calculations and from real microcavities, (3) mode suppression in DBR-clad microcavities and (4) bimolecular quenching upon high excitation levels. All four points will be discussed in the following.

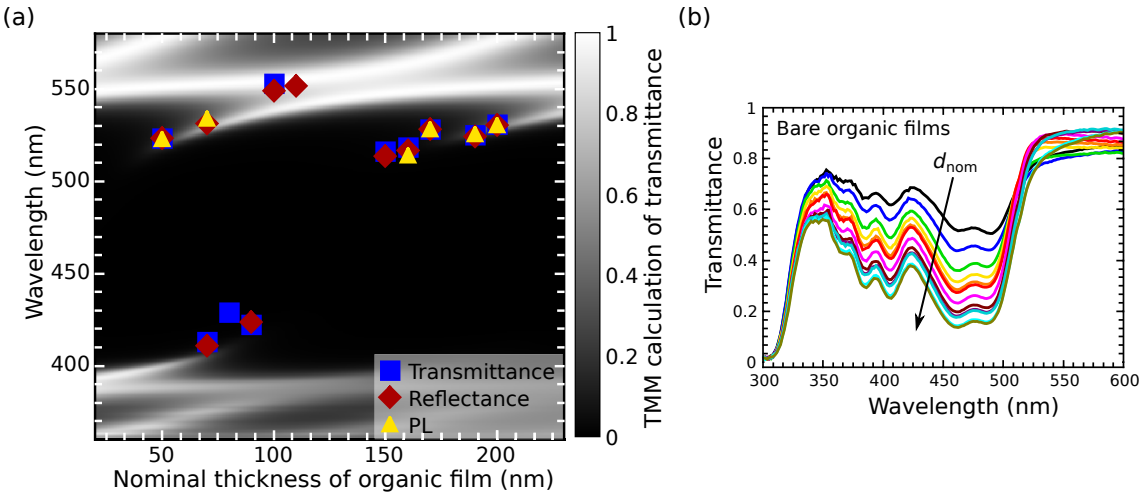

Figure 5.4: (a) Mode positions in microcavities with 7.5 mirror pairs filled with 43% C545T, measured in transmittance (blue symbols), reflectance (red symbols) or PL (yellow symbols) at $\Theta = 0°$. Background: TMM calculation of thickness-dependent, spectral transmittance of corresponding microcavities. (b) Transmittance of the quadrant with the bare organic film. The dip in transmission increases monotonically with nominal thickness of the organic film.

5.2.2 Sample stability

It is well established that high-*Q* microcavities are crucial for polariton condensation.[202] The fabrication of the highly reflective DBRs necessary for these high-*Q* cavities relies on techniques like molecular beam epitaxy, sputtering or electron-beam evaporation. These are associated with high substrate temperatures, plasmas or charged particles.[236,237] Organic materials, by contrast, often degrade easily and are very sensitive, whether this regards exposure to heat, light, water or oxygen.[238,239] Hence, elaborate approaches have been developed to avoid sputtering on top of the organic film in the fabrication of high-*Q* microcavities.[221] Yet, there have been reports of depositing DBRs on top of organic films,[240,241] which could in more recent years even demonstrate good functionality of the organic film.[60,61] Establishing a protocol for incorporating organic films of C545T between sputtered, highly reflective DBRs without damaging them was thus expected to be possible, but challenging. This is why the effect of different parameters of the sputtering process on the organic film was studied with the help of PLQY measurements. The effect of storing the samples in air on the PLQY was also tested. It was necessary to determine the impact of storage in air because all setups for sample characterisation and excitation were established outside gloveboxes, i.e., in air.

One crucial factor for obtaining films of high quality between DBRs turned out to be the

substrate temperature relative to ambient temperature. Any amount of heating during the sputtering process ($T_{\mathrm{min,test}} = 50°$) turned out to have a negative effect on the homogeneity and stability of the organic film. Although this was initially unexpected from the reported glass transition temperature of C545T ($T_g = 100$ °C)[226], the sensitivity at lower temperatures is likely to be caused by the high vacuum in the chamber before the start of the process. Once sample damage by heating of the substrate was avoided, the quality of the organic film might still be deteriorated by the conditions inherent to the sputtering process or by the sample storage. First, sputtering on top of organic films could be detrimental because of the high-energy particles or heat present in the plasma.[236–238,242] Second, the exposure to oxygen and water can quench luminescence, particularly in electroluminescent or phosphorescent devices.[75,239,243] In our system, degradation—though not as severe—is also expected, especially in combination with irradiation.[244] Both effects were investigated by PLQY measurements and the results are presented in this section.

In order to quantify the damage to the sample by sputtering on top of organic films, thin films of C545T:MADN were produced in the same evaporation run. These are expected to have the same C545T concentration and thus the same PLQY. On the surface of some of these samples, an oxide film was deposited by sputtering, after which the PLQY of these different films was compared. Figure 5.5a shows the results of two sample sets, one set of samples containing 17% C545T and the other 1% C545T in MADN. The first set distinguishes three scenarios: (1) only taking the sample into air, (2) sputtering SiO_2 on top and subsequently taking the sample into air and (3) taking the sample into air and only then sputtering SiO_2on top. The second set compares the PLQY of one film taken directly out of the glove box and the other one taken out after having a Ta_2O_5film sputtered onto its surface. Both the effect of SiO_2 and of Ta_2O_5 is tested because the materials are sputtered with different gas mixtures. Ta_2O_5 required 17% of oxygen to be mixed into the argon gas in order to obtain films at the right stoichiometry. Figure 5.5a clearly shows that all sputtering processes degrade the film quality. Comparing the cases of direct sputtering and sputtering after exposure to air, it becomes apparent that the exposure to air in itself decreases the PLQY. Moreover, while direct sputtering of SiO_2 decreases the PLQY by less than 20% (0.30 → 0.25), the deposition of Ta_2O_5reduces the PLQY by more than 50% (0.70 → 0.34). However, due to the high refractive index of Ta_2O_5 ($n(Ta_2O_5) \approx 2.15$), some of the apparent reduction in PLQY could be caused by wave-guiding. An estimation of this effect assumes isotropic emission and complete loss of

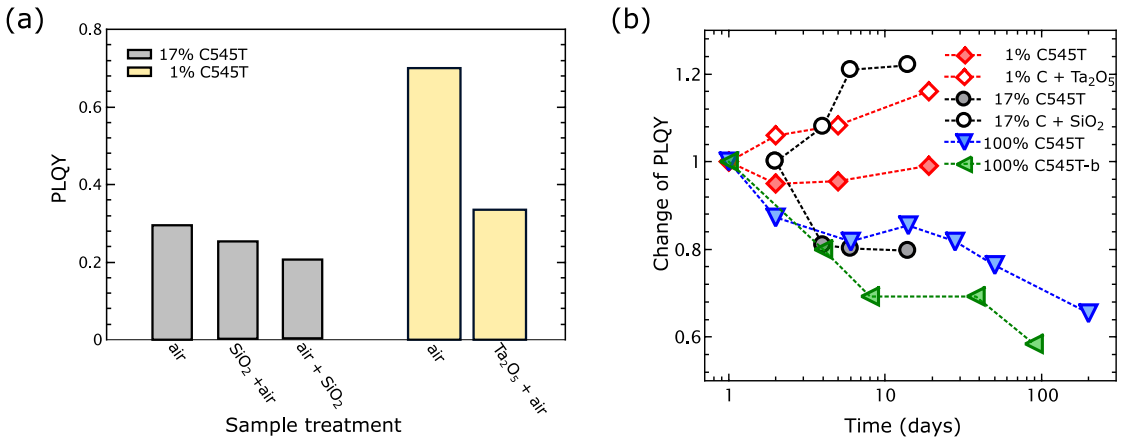

Figure 5.5: Degradation of C545T:MADN films with different concentrations (1% to 100% C545T) from measurements of their PLQY. The impact of (a) sputtering on top of the organic film and (b) the storage in air on the PLQY was measured. In the legend, C is an abbreviation for C545T and the green and blue symbols represent different samples from different fabrication runs. The dashed lines are intended to act as guide to the eye.

the photons when wave-guided. This puts an upper limit to the reduction in PLQY caused by wave-guiding of 17%. Hence, it is probable that although the damage to the material might be less than 50%, it is still larger than when depositing SiO_2. Overall, it should be noted that while the sputtered samples show a reduced PLQY, the material is not completely destroyed; but its luminescence efficiency is decreased by $\lesssim 50\%$. This is in agreement with literature, where the damage of sputtering to organic films is reported to not quench a major fraction of the luminescence.[242] However, the extent of the damage depends on processing parameters like pressure, sputtering power and gas mixture and the correlation is sometimes counter-intuitive.[245,246]

The development of the PLQY with time of storage in air is shown in Figure 5.5b, where different concentrations and film treatments are compared. All PLQY values are normalised to the PLQY on the first day of measurement. Thereafter, samples are stored in a dark, ambient environment and measured at intervals. Three main observations follow from this investigation. First, although all untreated samples (no sputtering, filled symbols) deteriorate when exposed to air, the PLQY is never entirely suppressed but remains above 50% of its original value even after 200 days. Second, the higher the C545T concentration, the greater the degradation over time. In particular, the film with the lowest concentration barely shows any degradation over the investigated time span of 19 days. Third, the films which were sputtered upon (open symbols) behave very differently: their PLQY increases with time. Since three independent

samples (two shown) confirm this trend of an increasing PLQY with time after sputtering on the surface, this is understood as a real effect. A stabilisation of the PLQY with time could be explained by the sputtered layer protecting the surface of the organic material from e.g. oxygen. Some reports also have shown that the sputtering process need not necessarily deteriorate the luminescence properties.[246] The continuing increase in PLQY, by contrast, is not currently understood.

To summarise the investigations regarding the damage of the material over time and with sputtering, a detrimental impact of both aspects is found. The damage over time by exposure to air can be reduced by measuring samples soon after fabrication and storing them in an oxygen-free environment (i.e., the glovebox). This was generally the followed protocol.

5.2.3 Q-factors of DBRs: calculations vs measurements

DBRs were fabricated from alternating SiO_2 and Ta_2O_5 films by magnetron sputtering. DBRs of high reflectivity can only be obtained if all films have a homogeneous thickness over the entire surface, negligible surface roughness and all layers have a thickness of exactly $\frac{\lambda_0}{4n}$. Here, λ_0 is the central wavelength of the stopband and n is the refractive index of the oxide layers. Any deviation from this ideal cavity will result in a reduction in Q-factor. The process, once optimised, was set up for maximum reproducibility. This was obtained when using constant sputtering power (instead of constant rates), always the same gas mixture and flows and no heating of the substrate. Generally, for sputtering high quality or even crystalline films, it is advised to keep the substrate at an elevated temperature, $T_s > 300$ °C.[247] However, as mentioned before, sputtering at ambient temperature turned out to be necessary to avoid degradation of the organic film, which requires two remarks. (1) The overall temperature on the substrate was found to heat up by ~ 15 °C during the sputtering process. The maximum measured substrate temperature, $T_s = 35$ °C, is still well below the glass transition temperature of C545T at ambient temperatures ($T_g = 100$ °C)[226], so that the properties of the film were expected to be largely maintained throughout the sputtering process. In terms of reorganisation of the sputtered particles on the surface of the substrate, the inherent increase in T_s corresponds only to a small increase in kinetic energy ($\sim 5\%$). Hence, the gradient of material properties in the sputtered film appearing during the heating process over the first 10–20 nm of the DBR stack is expected to be small. (2) The effect of lowering the sputtering temperature from 80 °C to ambient temperature (i.e., 35 °C) was investigated via the transmission of

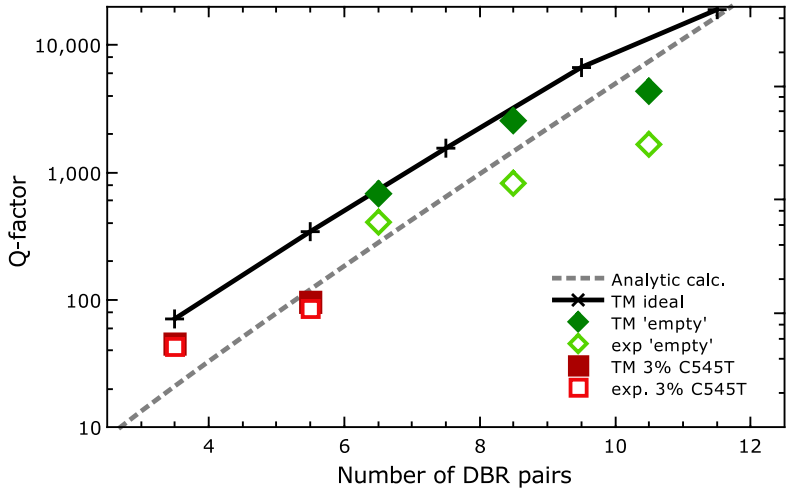

Figure 5.6: Comparison of *Q*-factors as a function of the number of DBR pairs: simulated vs real microcavities. The black line shows transfer matrix simulations of empty cavities with the mode positioned in the centre of the stop band. The grey dashed line shows the analytic calculation from Equations 2.10 and 2.14, which describes the microcavity in the limit of a large number of mirror pairs. Open symbols show the measured *Q*-factors from microcavities containing 3% C545T (red) and 1% C545T where the cavity mode is far off the absorption band ('empty', green). Solid red and green symbols represent the *Q*-factors obtained from TMM calculations matching the spectra of the real cavities (i.e., assuming the presence of absorbers inside the cavity and mode positions away from the centre of the stop band).

fully grown DBRs and the surface roughness of the top layer of these DBRs. Upon decreasing the substrate temperature, the minimum of transmission in the stopband in comparable DBRs increased by 27% (from 2.2% to 2.9% for DBRs with 7.5 mirror pairs). This confirms the expectation of poorer film quality at lower substrate temperatures. At the same time, measurements by atomic force microscopy of the surface roughness, for which I acknowledge Nils Kronenberg, showed that the surface roughness barely increased upon lowering the temperature (1.5 ± 0.4 nm vs 1.6 ± 0.4 nm). Hence, the reason for the increase in transmittance is not fully understood.

The quality of DBRs sputtered at room temperature was further assessed via the *Q*-factors of microcavities. In ideal DBRs—consisting of only perfectly transparent, plane parallel films of a thickness of exactly $\frac{\lambda_0}{4n}$—the reflectivity in the stopband can be enhanced infinitely by only increasing the number of layers (see Equation 2.10). However, any amount of absorption or scattering inside the mirrors will reduce the coherence and thus the maximum reflectivity. TMM simulations serve as 'ideal' microcavities to which the measured transmittance spectra of real microcavities are compared in order to evaluate the performance of the DBRs, see Figure

5.6. While the simulations take into account the potential absorption in SiO_2 and Ta_2O_5 via the measured refractive indices, they correspond to ideal microcavities as they assume perfect, parallel interfaces and have the mode in the centre of the stop band. The analytic formulae presented in Chapter 2.2 are also used to calculate the Q-factors expected from ideal DBRs. Yet, these underestimate the Q-factor because they are only valid for a large number of mirror pairs, as it can be seen from the convergence of the analytical and the TMM result for large N.

Additionally, Figure 5.6 compares experimentally measured Q-factors (open symbols) to Q-factors from simulated cavities with corresponding structures (filled symbols). The difference between these simulations and simulations of ideal cavities (black line) is the spectral position of the cavity mode with respect to the stopband. Clearly, the experimental Q-factors are lower than the simulated reference. The two sets of experimental microcavities illustrate two points why an experimental approach might under-estimate the maximum Q-factor achievable with these sputtered mirrors in an empty microcavity. It is important to acknowledge this difference because while the experimental approach is straight forward, the relevant quantity for the properties of the uncoupled cavity photon is the Q-factor of an empty microcavity. In the microcavities represented by red symbols, the cavity mode was in a spectral region of absorption of C545T although this only made up 3% of the material inside the microcavity. Once this absorption was considered in the TMM calculations (red, filled symbols), the experimental Q-factor nearly matched the simulation. These additional losses by absorption are not inherent to the mirrors so that an experimental determination of the Q-factor is not appropriate here.

The second series of microcavities (green symbols) can be considered to be empty, since the cavity mode was red-shifted with respect to the absorption of the material in the microcavity. Here, however, the cavity mode was not centred in the stop band. Comparative TMM calculations (green, filled symbols) were performed for cavities containing an adjusted thickness of the cavity material so that the mode position coincided with that of the experimental microcavity. Accounting for the mode position in the stop band reduced the Q-factor with respect to the TMM calculation of an ideal cavity. This reduction in Q-factor is real—at the position of the cavity mode, the mirrors are less reflective and hence, more energy is lost in each round trip. It can be seen that a discrepancy between Q-factors from TMM simulations and from measurements decreases when accounting for the offset between cavity mode and centre of the stop band, but does not vanish. This will be due to the scattering introduced by non-zero surface roughnesses and not perfectly identical optical thicknesses in the layers

throughout the stack.

From Figure 5.6, two trends are deduced. First, the larger the number of DBR pairs and the predicted Q-factor, the larger the deviation of the quality of the real microcavity with respect to an ideal cavity. This is because the larger the number of layers in the DBR, the larger the effect of any irregularity that introduces decoherence. Second, even though being smaller than the values of ideal microcavities, Q-factors of real microcavities reached values up to $Q = 1,600$ (with 10.5 mirror pairs). Previous reports on polariton lasing using SiO_2 and Ta_2O_5 as materials for the DBRs use six mirror pairs on top and bottom (reporting $Q = 600$) or six and nine mirror pairs for top and bottom mirrors (Q not specifed).[60,61] The mirror investigation shown here thus proves that the process established within this PhD produced microcavities with properties that are compatible with polariton lasing.

5.2.4 Mode suppression in DBR-clad microcavities

The cavity mode in DBR-clad microcavities can be very narrow, $\delta\lambda_C < 1$ nm. The absorption of C545T, by contrast, is very broad, $\delta\lambda_X \approx 90$ nm. In order to understand how this broad absorption affects the polariton modes, TMM calculations were performed on simulated toy materials.

The optical constants of these hypothetical materials were defined to have a Lorentzian absorption peak in k, with n obeying the Kramers-Kronig relation, see Figure 5.7a. They were designed such that Materials A and B (blue and grey) have the same height of the absorption peak, Materials A and C have the same width of the absorption peak (blue and green) and materials B and C (grey and green) have the same integrated absorption. All three materials, A, B and C, have the same background refractive index, $n = 1.8$

For these materials, the polariton modes are calculated as a function of thickness d of a layer of the hypothetical material inside the cavity, as shown in Figure 5.7b–d. All three materials show two distinct modes. For both narrow materials, Material A and Material C, these modes clearly anticross, i.e., there is a range of thicknesses in which two modes appear in the stop band. These can then be unambiguously identified with the LP and UP branch. The extent of the splitting, as well as the range of thicknesses over which both UP and LP exist is larger for Material C with the larger extinction coefficient. This indicates a larger coupling strength in Material C, which is expected because its overall oscillator strength is larger (see

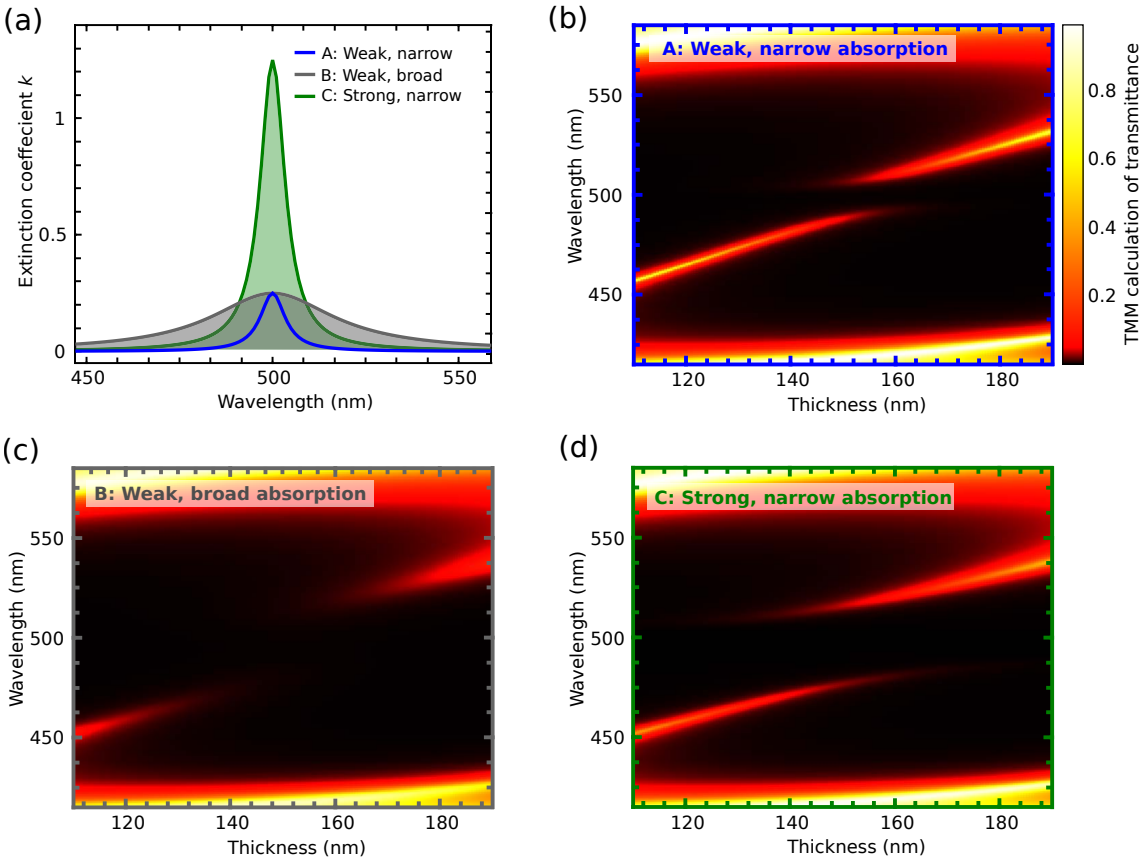

Figure 5.7: The effect of broad absorbers inside a DBR-clad microcavity. (a) Extinction coefficients of three different, hypothetical materials representing Lorentzian absorbers. The absorption is characterised by the maximum extinction value ('weak' or 'strong') and by the width of the peak ('narrow' or 'broad'). The Materials A (blue, 'weak, narrow') and B (grey, 'weak, broad') have the same maximum absorption, while B and C (green, 'strong, narrow') have the same integrated absorption. (b–d) Transfer matrix calculations of the transmittance over cavity thickness of Material A (b), Material B (c) and Material C (d).

Equations 2.1 and 2.27). When comparing Material B (weak and broad absorption) to A and C, it is striking that there is no region of mode overlap, i.e., no range of thickness where two modes are observed. Instead, Material B shows a region of thicknesses where no mode is visible. It is thus difficult to identify the existing modes with UP and LP since the anticrossing of modes, which is the key signature for strong light–matter coupling, is absent.

The peak of the extinction coefficient in C545T is roughly as large as that of Material C ($k_{\mathrm{max}} \approx 1$) and wider than that of Material B ($\delta\lambda_{\mathrm{C545T}} \approx 90$ nm vs $\delta\lambda_{\mathrm{B}} \approx 40$ nm). The observed effects are thus expected to be more pronounced than in Figure 5.7c: due to the large coupling constant, the modes will be pushed further away from each other and at the same time, the region without any visible mode will increase. Note that the vanishing of modes

is not singular to C545T; other publications also report regions of suppressed modes instead of their anticrossing.[61,120]

Further simulations show that this effect is stronger the larger the absorption (or concentration) of the excitons is and the larger the number of DBR pairs—i.e., the larger the Q-factor. The effect of mode suppression has also been observed in metal-clad microcavities of λ-type, albeit to a smaller extent. Here, too, a major difference between cavities of type $\lambda/2$ and λ is the increased Q-factor for λ cavities.

There are two possible ways to explain the disappearance of the modes: a lack of impedance matching or additional absorption by detuned excitonic states. On the one hand, matched impedances, that is, losses, are a condition for two oscillators to couple to each other.[248] Since the impedances of photon and exciton correspond to their losses, not directly to their linewidths, this effect is difficult to estimate. The impedance of the cavity photon is simply the inverse of the Q-factor (10^{-3} for good microcavities), but for the exciton, the situation is less clear. Nonetheless, the observation that the suppression of the modes is enhanced for increasing Q-factors corroborates this mechanism to affect the light–matter coupling. On the other hand, the vanishing of the modes could also be caused by absorption from uncoupled excitons. The presence of excitonic levels over a large range of energies leads to a range of detunings between the cavity photon and different excitons. As a consequence, some of those excitonic states—those far from resonance—will not be strongly coupled to the cavity photon and thus, will be able to absorb the energy stored in the polaritonic modes. Due to the absorption, there will no longer be many photons leaking from the polariton modes so that the modes—although present in the system—will not be visible from the outside.

5.2.5 Inhibition of high exciton densities by bimolecular quenching

Bimolecular quenching processes become pronounced at high excitation levels or at high densities of chromophores.[249] This can be a problem for achieving the large densities of excitons required for polariton condensation, as an extensive study by Akselrod *et al.* [250] revealed. The system studied here consists of relatively densely packed C545T in order to achieve sufficient absorption for the strong coupling regime. Moreover, aiming for polariton condensation, the microcavities were highly excited (up to their damage threshold). Both aspects increase the risk of bimolecular quenching. Therefore, the microcavities were tested for exciton–exciton annihilation in two ways; the time-dependent exciton decay and the PL intensity as a function

of the pump power were studied.

In ideal excitonic states with one radiative transition, a mono-exponential decay is expected.[75] The appearance of several exponential decays with different time scales are an indication for additional processes going on, e.g. for several different decay channels. When exciton–exciton annihilation becomes dominant, a mono-exponential decay no longer describes the data well. Instead, a function of intensity over time can be deduced from the knowledge of the rate equation for exciton–exciton annihilation (see Eq. 2.3):[250]

$$I(t) = \frac{I_{\text{in}}}{e^{\frac{t}{\tau}} \cdot \left(1 + \frac{\gamma\tau}{2} \cdot n_0\right) - \frac{\gamma\tau}{2} \cdot n_0} \tag{5.1}$$

Equation 5.1 holds on the assumption of short pumping pulses with respect to the excitonic lifetime τ. Here, I_{in} represents the pump intensity, γ the annihilation rate constant and n_0 the exciton density at $t = 0$. Note that light–matter interactions are not taken into account in Equation 5.1.

The exciton lifetime of bare organic films was measured in two ways; by time-correlated single photon counting (TCSPC, not shown) and with the help of a streak camera. I acknowledge M. Tariq Sajjad and Sai K. Rajendran for helping me with these measurements and Ifor D. W. for access to his equipment. The two methods differ in the excitation power (single photon level for TCSPC and ≥ 20 μW for the measurements with the streak camera) and in dynamic range (10^4 for TCSPC and 10^2 for the measurement with streak camera). Qualitatively, both measurements showed a similar trend: the higher the concentration of C545T in MADN, less the time-resolved luminescence corresponded to the mono-exponential decay expected for a simple emitting process. From the TCSPC measurement, the largest decay rate (shortest time) increased steadily with increasing the concentration of C545T. This behaviour is an indication that for films with concentrated C545T, some relaxation happens via fast, non-radiative processes already at extremely low excitation powers.

Figure 5.8 shows the time-resolved decay of PL from microcavities with different concentrations of C545T and at different pump powers measured with the streak camera. In order to understand the underlying mechanisms, both mono-exponential decays ($A \cdot e^{t/\tau}$; orange, dashed lines) and functions of the same form as Equation 5.1 ($A \cdot \left[e^{t/\tau} \cdot (1 + c) - c\right]^{-1}$; red, dotted lines; referred to as XX fit in the following) were fitted to the time-resolved PL. At low concentrations (3% C545T in MADN; Figure 5.8a) and low pump powers (black line), both

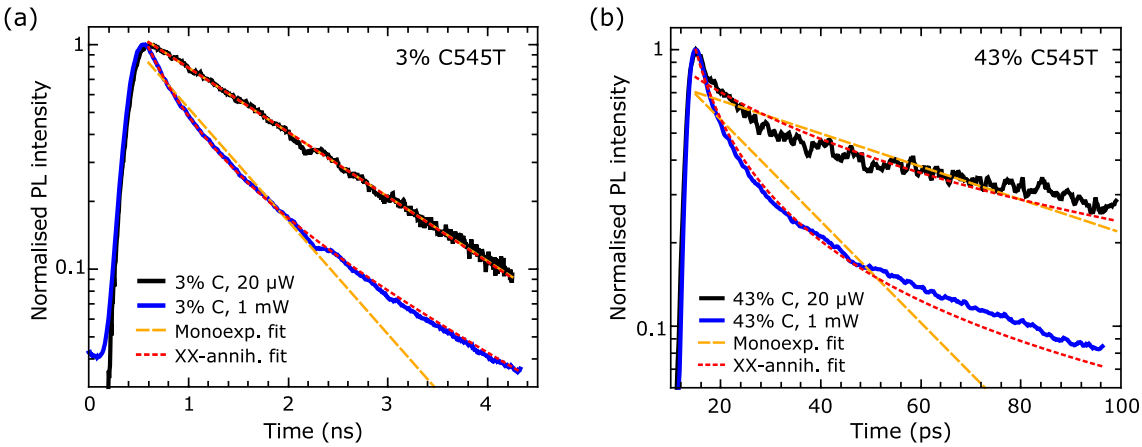

Figure 5.8: Time-resolved decay of PL in microcavities measured by a streak camera after excitation by a 180-fs laser pulse. The decay after excitation with low power (20 μW, black line) and high power (1 mW, blue line) is fitted with a mono-exponential decay (orange, dashed line) and a function assuming exciton-exciton annihilation (red, dotted line). The microcavities with 5.5 mirror pairs contain 3% C545T in MADN (a) and 43% C545T in MADN (b). Note the different time scales of (a) and (b).

curves fit the measured data well and are barely distinguishable. The coefficient of determination is the same for both fits, $R^2 = 0.9986$, despite more fit variables in the XX fit. It follows that bimolecular quenching does not play a dominant role in the decay at these conditions. The situation changes, however, upon increasing the pump power by a factor of 50. Now, τ was fixed in the XX fit to the value obtained from the mono-exponential fit for the PL at low power ($\tau = 1.5$ ns) so that both fit functions had two variables. Nonetheless, XX fit describes the time-resolved PL at high pumping values much better ($R^2_{\mathrm{XX}} = 0.9992$ vs $R^2_{\mathrm{m-exp}} = 0.98$). The data are thus an example for bimolecular quenching driven by high pump intensities.

At much higher concentrations of C545T in MADN (43%), the mono-exponential decay only provides a poor fit for the PL both at low and at high excitation densities ($R^2_{20\mu\mathrm{W}} = 0.84$ and $R^2_{1\mathrm{mW}} = 0.85$), see Figure 5.8b. The XX fit ($\tau = 1.5$ ns fixed) for the 20 μW excitation yields $R^2 = 0.92$, which is smaller than the R^2 values observed in the low-concentration sample. This might partly be due to the data being quite noisy due to the relatively low PLQY at that concentration. However, it could also be an effect of the light–matter coupling, which is expected to be strong at such high concentrations of C545T, but is not considered in the fit equation. When increasing the pump power on the sample, the XX fit still provides an adequate description of the PL data, $R^2 = 0.992$. The study of time-resolved PL thus supports the hypothesis of bimolecular quenching reducing the number of excitons. Yet, exponential

decays with three terms (which have 6 fit parameters) also provide a satisfactory description of the data. Additionally, further non-radiative processes attributed to concentration quenching would be expected at concentrations of 43% of C545T, like the formation of non-radiative excited states of coupled excitons. Moreover, the light–matter interaction is expected to play a role—at least in the samples with high densities of C545T—, so that the applicability of Equation 5.1 is debatable, despite the remarkably good fits to the data.

In order to confirm that exciton–exciton annihilation has a significant contribution to the exciton population, the PL intensity was investigated as a function of pump power. Here, the samples were pumped with a 5-ns-pulsed OPO at 420 nm. For dominant exciton–exciton annihilation, a square root dependence is expected, PL $\propto \sqrt{I_{\mathrm{pump}}}$. Results of two representative microcavities are shown in Figure 5.9, one containing a film of low C545T concentration (3%, blue symbols) and one of high C545T concentration (43%, black symbols). Clearly, the intensity grows sublinearly with pump power in both samples. Power-law fits were applied to the data ($y = A \cdot x^b$, dashed lines), yielding an exponent of $b < 0.5$ for both microcavities. This suggests strong bimolecular quenching. Even though the exponent varied between different samples with the same concentration of C545T, b was consistently highest for microcavities with lowest C545T concentrations and vice versa. This exponent in high-concentration samples, which is smaller than 0.5, points to an additional pump-power dependent loss term with increasing C545T concentration in MADN. Yet, its origin cannot be deduced from the presented and performed measurements.

Both the time-dependent and the power-dependent study of the PL intensity are consistent with the assumption of exciton–exciton annihilation as a dominant non-radiative loss channel. The reduction in lifetime and in the ratio of input and output power was more pronounced for samples with higher concentrations of C545T in MADN. For very low concentrations, the expected effects of exciton–exciton annihilation are not yet visible at low pump powers. Since bimolecular quenching is well-known to impede the build-up of large exciton populations, this could well be one reason for the absence of polariton condensation. The extent of the impact of bimolecular quenching could be investigated by studying microcavities containing a material where the bimolecular annihilation rate γ is tunable and independent of other material properties, although it is not clear what this should be. This was beyond the scope of this PhD.

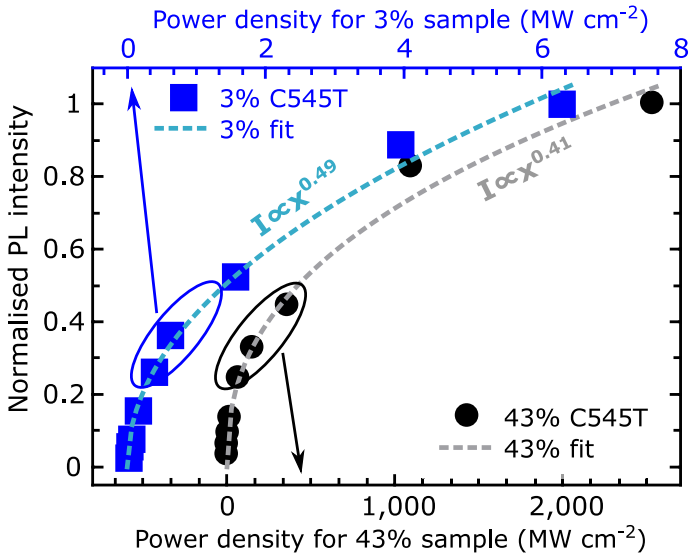

Figure 5.9: PL intensity as a function of pump power for a microcavity with 3.5 mirror pairs containing 3% C545T (blue symbols and top x-axis) and for a microcavity with 5.5 mirror pairs containing 43% C545T in MADN (black symbols). The data points are fitted with a power law (dashed lines).

5.2.6 Photon lasing

The investigations described above have shown that the fabrication process established during the course of this PhD should yield well functioning microcavities. Potential challenges are the suppression of polariton modes and bimolecular quenching. The suppression of polariton modes prohibits access to polaritons where largest coupling strengths are expected. Hence, it is not possible to experiment with all different detunings for obtaining polariton lasing. Moreover, due to the lack of a second mode, it is difficult to determine parameters like photon or exciton character or even to identify the existing modes with LP and UP. Bimolecular quenching is a problem that scales with concentration of the chromophore, and thus with coupling strength (see Equation 2.27). However, it should not dominate the relaxation dynamics at very low concentrations. These findings could be jointly confirmed by the demonstration of a photon laser using this material system and this fabrication process.

As outlined in Chapter 2, the requirements for photon lasing and polariton condensation differ. While for polariton condensation, efficient relaxation to bottom of the LP is crucial, photon lasing requires high PLQYs and an amplification of the mode in the spectral range of optical gain.[251] The build-up of a population inversion in turn relies on high Q-factors of the resonators. This is manifested in thresholds for polariton and photon lasing that depend

on the spectral position of the lasing mode. In particular, it has been observed that optimal conditions for photon lasing are red-shifted with respect to those of polariton condensation.[62] Thus, photon lasing will occur in a spectral range away from the absorption, so that the mode suppression is not relevant. Finally, because the coupling to light does not need to be strong, the concentration of the dye (C545T) in the matrix (MADN) can be reduced. This reduces concentration quenching and exciton–exciton annihilation, so that a large PLQY can be maintained also at high pump powers. All these aspects point to the possibility of observing photon lasing with C545T despite the elusiveness of polariton lasing.

The series of samples aiming for photon lasing consisted of 12 microcavities grouped in three sets of four microcavities containing a C545T:MADN film with 1% doping concentration. At this low doping concentration, the maximum PLQY was observed, $\Phi_{1\%\text{C545T}} = 0.7$. Within one set, the intended thickness of the organic film was varied between 154 and 179 nm, in order to obtain cavity modes between 528 and 564 nm. Between the three different sets, the number of DBR pairs was varied from 6.5 over 8.5 to 10.5 pairs. The DBRs were designed to be centred around $\lambda_c = 550$ nm. The measured transmittance of these microcavities showed stop bands centred around $\lambda \approx 540$ nm with mode positions between 540 and 573 nm. All modes thus lie well in the region where gain is expected for C545T (500–570 nm)[227], at wavelengths higher than the absorption edge (530 nm) and within its luminescence band (470–620 nm). Amplified spontaneous emission, which is an indicator of the gain region, was observed at 535 nm for C545T.[252]

All microcavities were pumped at 440 nm on the outside of the stop band with the set-up described in Chapter 3.3 and measured in Fourier space. Most samples showed homogeneous PL from the cavity modes (transverse electric and transverse magnetic), as seen in Figure 5.10a, across the entire range of pump energies. Figure 5.10d compares the PL of different microcavities at the bottom of the cavity mode as a function of pump power. For all cavities clad with DBRs of 8.5 mirror pairs or less (blue symbols), the PL increased steadily with pump power. By contrast, for microcavities of 10.5 mirror pairs and a photonic mode at $\lambda_m = 548$ nm or $\lambda_m = 550$ nm (black and grey symbols, respectively), a sharp increase in PL with pump power is observed at 10 nJ and 25 nJ pump power (corresponding to $\lesssim 30$ mJ/cm^{-2} and $\lesssim 80$ mJ/cm^{-2}), respectively. Fourier spectra of the cavity with $\lambda_m = 548$ nm at and above the sharp increase are shown in Figure 5.10b and c. At the point of superlinear increase in PL, an intense peak appears at the bottom of the cavity mode, which shows a large spread

in angles with respect to the minimum of the cavity mode. The angular spread (half-angle Θ) of the far-field diffraction pattern of a circular aperture at wavelength λ is limited by the diameter D of the aperture: $\Theta \approx \frac{1.22\lambda}{D}$.[100] Since the luminescence from the lasing mode has a much larger spread in k-space than the photon mode, this demonstrates that its spot size in real space is much smaller. This, in turn, means that the photon lasing only occurs in a very small, localised region within the pump spot, where the mode is confined e.g. by inhomogeneities of the microcavity. Upon further increasing the pump energy ($E = 64$ nJ), the PL from the cavity mode becomes weaker with respect to this intense peak. At the same time, the intensity of the peak is only slightly increased with respect to its value at $E = 16$ nJ.

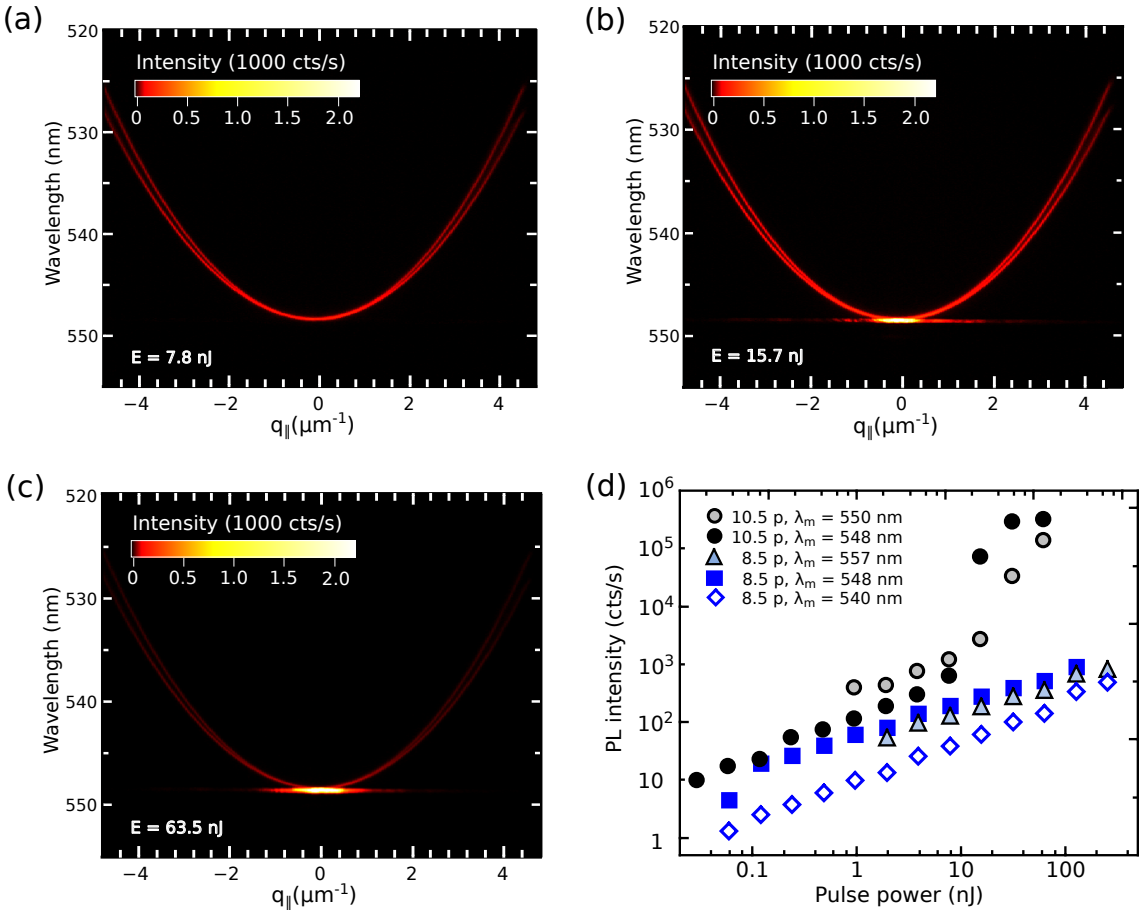

Figure 5.10: Photon lasing with C545T. (a-c) Fourier spectra of a microcavity clad with 10.5-pair DBRs and containing ∼ 155 nm of MADN doped with 1% C545T (mode position $\lambda_m = 548$ nm). The pump power increases from (a) to (c) as indicated in bottom left corner of each sub-figure (energy per 5-ns pulse). (d) PL intensity at $q_{\|} = 0$ of the different microcavities as a function of the energy of the pump pulse. All samples were measured up to the point of damage. Blue symbols represent microcavities with 8.5 pairs of DBRs at different mode positions (see legend), black symbols represent microcavities with 10.5 pairs of DBRs at different mode positions.

The sudden increase in PL and its localisation in the minimum of the cavity mode are both indicators for photon lasing. Polariton lasing, which would have similar signatures, can be ruled out because (1) the low concentration of C545T results in a very low coupling strength according to Equation 2.27; (2) the cavity mode is so far red-shifted from the absorption peak that any excitonic fraction would be negligible; and (3) polariton lasing is expected to be concomitant with a collapse of the PL in q-space,[25] which is not observed here. Another signature of photon lasing which should accompany the threshold-like behaviour in luminescence is a significant reduction in linewidth.[253] This, however, was not observed in the presented microcavities. Just below threshold, a full width half maximum of $\delta\lambda = 0.200 \pm 0.009$ nm and a good agreement with a Lorentzian line shape was observed ($R^2 = 0.98$). Above threshold, the peak was less well described by a Lorentzian ($R^2 = 0.91$), the linewidth only decreased slightly to $\delta\lambda = 0.17 \pm 0.02$ nm and actually increases at the highest measured pulse energy ($E = 64$ nJ) to $\delta\lambda = 0.26 \pm 0.02$ nm. One potential reason for not observing a significant narrowing could be that the values are close to the resolution of the spectrometer used (0.05 nm). Also, the sample was probably not homogeneous over the probing spot, e.g. in composition or thickness. The latter argument is supported by the fact that lasing in these samples was not observed over the entire sample, that the emission from the lasing mode showed a large spread in k-space and that the threshold showed a minor dependence on the local spot on the sample. Furthermore, the pump spot had an area of $\gtrsim 31$ μm^2, across which several independent lasing modes at slightly different energies could be possible. Such an ensemble of lasing modes could both explain why the spectral width of the PL does not reduce by much and why the spectra above the threshold no longer have a strictly Lorentzian shape. Moreover, the persistence of luminescence from the cavity mode—albeit weaker at higher pump energies—is another indicator that several coexisting, locally separated regions of no lasing and lasing at different thresholds make up the observed spectrum. It is thus concluded that the intense luminescence above a sample- and spot-dependent threshold corresponds to lasing from a slightly inhomogeneous cavity.

The evidence for photon lasing presented in Figure 5.10 clarifies two aspects of the fabrication process. (1) As lasing threshold is sensitive to the gain of the organic material, the observation of lasing proves that sputtering DBRs (first layer Ta_2O_5) on top of the organic films does not fundamentally damage the organic films. (2) The Q-factors of the fabricated microcavities are large enough to support lasing and play a crucial role in lowering the lasing

thresholds below the damage threshold of the material.

5.3 Luminescence from organic polaritons in the linear pumping regime

This section discusses the luminescence from strongly coupled, organic microcavities in the linear pumping regime. It has been found by Ballarini *et al.* [41] that the PLQY of an organic dye can be enhanced by placing it into the coupling regime. The up to ten-fold increase of PLQY in the microcavity with respect to a bare film was attributed to an efficient, phonon-assisted scattering mechanism from the exciton reservoir to the LP. However, this picture was not unanimously confirmed. While Schwartz *et al.* [254] observed a much smaller increase in luminescence efficiency (×2), Grant *et al.* [43] even reported a small decrease in efficiency in the strong coupling regime. Such a large spread in results is likely due to the large spread in material properties, e.g. in the PLQYs. The reports investigating the relationship between the luminescence intensity and the strong coupling regime use blended films of a dye in a matrix. This means that the complex excitation scheme in organic materials is further complicated by additional excitonic states and the energy transfer between strongly coupled and uncoupled exciton species.

Here, PL measurements from two different systems were studied. One type of microcavity combined neat films of C545T with metal mirrors and the other combined blended films of C545T in an MADN matrix with DBRs. Section 5.3.1 compares the PL from the *OVL* series, a series of metal-clad microcavities with thin, neat films of C545T. In these samples, the coupling strength is varied by changing the overlap of the organic molecules with the electric field in the microcavity. Section 5.3.2 then compares the PL in DBR-clad microcavities, which are filled with with films of different blending ratios of C545T and MADN. The data are quantitatively analysed, taking into account aspects like the the luminescence efficiency at the spectral position of the polariton or photon mode. The results of the experiments are not conclusive, but they emphasise the importance of taking the properties of the uncoupled film into account when evaluating the impact of strong coupling on these properties.

5.3.1 Photoluminescence from the metal-clad *OVL* series

In order to study the PL as a function of the coupling strength, the *OVL* series was revisited (see Chapter 4.2). This was done because, while the coupling strength differs between the different samples in the series, all other, uncoupled properties should be the same. The *OVL* series consists of metal-clad microcavities of λ-type, i.e., the optical thickness is the same as the wavelength of the exciton transition. Five cavities in the series contain thin films of pure C545T of the same thickness (42 nm). With the help of SiO_2 spacer layers, the position of the organic film is controlled by changing the ratio of top and bottom SiO_2 film in the microcavity (see Figure 4.11a). The work discussed in Chapter 4.2 has shown that the mode splitting can be increased from 0 to 0.5 eV only by changing the position of the film in the cavity. At the same time, all uncoupled films show the same properties. This is why the *OVL* series is well suited to understand the link between the PL properties of bare films and those of strongly coupled microcavities.

Here, we investigate the PL of the microcavities of the *OVL* series upon pumping with an intense halogen lamp filtered through an ultraviolet band-pass filter ($\lambda_{\text{pump}} = 370 \ldots 390$ nm) from the broad lamp spectrum. The microcavities were excited at an angle of $0° < \Theta < 48°$ and the luminescence was likewise collected for $0° < \Theta < 48°$ through the same objective (NA = 0.75). For each sample, the PL was collected on the quadrant of the full microcavity and on the quadrant of the bare organic film (see Chapter 3.5. The measured PL spectra, which where acquired with the help of Marcel Schubert, are shown in Figure 5.11a. The spectra for the bare films were comparable, as expected for organic films of the same thickness and concentration.

By contrast, the spectra of the microcavities differ strongly in maximum PL and in the spectral position of the luminescence peak—as would be expected from the analysis of Chapter 4.2. From *OVL0* to *OVL3*, a continuous red-shift of the luminescence is observed, which is accompanied by an increase in PL intensity of the samples. The only exception is sample *OVL1b*, which showed the weakest luminescence of all samples, despite being approximately as far red-shifted as sample *OVL2*. In order to understand the nature of the luminescence peak, the PL spectra are compared to reflectance spectra of the *OVL* series at 0° (see Figure 5.11b). Two aspects of the reflectance spectra should be noted: (1) The spectra of samples *OVL1* and *OVL2* show a dip at the absorption of bare C545T ($\lambda \sim 480$ nm). These features stem most probably from the beam in reflectance partially hitting the bare organic quadrant

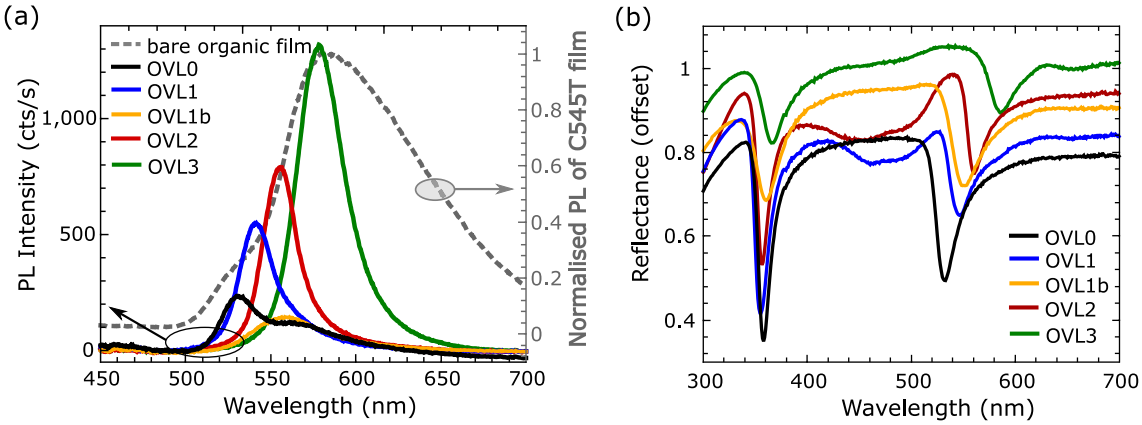

Figure 5.11: PL spectra of the *OVL* series (see Chapter 4.2). All samples were pumped at the same pump energy at $\lambda_{\text{pump}} = 300 \ldots 380$ nm. (a) PL from microcavites *OVL0* to *OVL3* (solid lines). Residual light from the excitation was fitted by an exponentially decaying function and substracted from the raw data and the spectra were smoothed by a 5 point moving average. The dashed line shows a normalised PL spectrum from a bare organic film in samples of the *OVL* series averaged by 5 point moving average (right axis). (b) Reflectance spectra of *OVL0* to *OVL3* at 0°, vertically shifted for clarity.

of the sample and they are not considered to be related to the response of the microcavity. (2) More importantly, it can be observed that although the uncoupled dips at 360 nm are all well aligned—indicating a similar cavity thickness for all microcavities—the dips at larger wavelengths shift from 532 nm in *OVL0* to 587 nm in *OVL3*. This mode shift is attributed to the coupling of the photon mode to the exciton which absorbs at $\lambda \lesssim 520$ nm. In contrast to the reflectance spectra measured at large angles (see Figure 4.11), the UP is not visible here, possibly because of its too low photonic fraction.* It follows from the increasing shift of the modes around $\lambda \sim 550$ nm from sample *OVL0* to *OVL3* that the coupling between light and matter continually increases, in agreement with the results presented in Chapter 4.2. The comparison of luminescence and reflectance spectra demonstrates that the peak positions of the luminescence are dictated by the mode position of the samples.

Quantitatively, the PL of sample *OVL3* is more than five times as intense as that of sample *OVL0*. Hence, the presented PL spectra seem to indicate that the light–matter interaction enhances the luminescence efficiency of the material inside the microcavity. Yet, the peak intensity of the microcavities also seems to roughly follow the PL spectrum of the bare organic film (grey, dashed line in Figure 5.11). In order to evaluate the possible enhancement quanti-

*Curiously, simulations show that in these λ-cavities—in contrast to $\frac{\lambda}{2}$-cavities of a comparable structure—show a similar mode suppression to that observed in DBR-clad microcavites (see Section 5.2.4). Possibly, this is a result of the higher Q-factor of the λ-cavity with respect to the $\frac{\lambda}{2}$-cavity.

tatively, an estimate of the PL intensity as expected from weak coupling theory is performed. For this, all quantities which differ between the cavities and which influence the luminescence response—except for potential effects of the light–matter coupling—are measured or simulated to calculate the expected relative luminescence intensity of the samples. Note that this analysis does not aim to calculate the absolute PL intensity but rather the ratio of luminescence between the samples. In order to predict a theoretically expected response, I_{theo}, the efficiencies for pumping the film inside the cavity, η_{pump}, for the internal conversion, η_{int}, and for coupling light out of the cavity, η_{out}, need to be considered:

$$I_{\mathrm{theo}} \propto \overbrace{I_{\mathrm{pump}}(\lambda)\cdot k(\lambda_{\mathrm{pump}})\cdot T\left(\lambda_{\mathrm{pump}}\right)\cdot A\left(\lambda_{\mathrm{pump}}, z_{\mathrm{C545T}}\right)}^{\eta_{\mathrm{pump}}}\cdot\overbrace{\Phi\left(\lambda_{\mathrm{out}}\right)\cdot A\left(\lambda_{\mathrm{out}}, z_{\mathrm{C545T}}\right)}^{\eta_{\mathrm{int}}}\cdot\overbrace{T\left(\lambda_{\mathrm{out}}\right)}^{\eta_{\mathrm{out}}}. \tag{5.2}$$

η_{pump} is determined by the (measured) spectral shape of the pump light $I_{\mathrm{pump}}(\lambda)$, by the corresponding extinction coefficient $k(\lambda_{\mathrm{pump}})$, by the transmittance of the top mirror at the pump wavelengths, $T\left(\lambda_{\mathrm{pump}}\right) = 1 - R(\lambda_{\mathrm{pump}})$, and by the magnitude of the electric field at the pump wavelength, A. Since the pump light was spectrally broad, the absorbed light into the cavity was calculated by first multiplying the spectrally resolved I_{pump}, k, and T and then integrating over the thus calculated spectrally resolved absorption. The electric field, which was evaluated at two different wavelengths of the absorbed light, depends on the position inside the microcavity and needs to be evaluated at the position of the thin C545T film in the cavity, z_{C545T}. A was calculated for two different wavelength of the broad absorption spectrum and averaged. In the weak coupling regime, the relative η_{int} can be obtained from the PL intensity of the uncoupled organic film at the spectral position of the emitting wavelength, $\Phi\left(\lambda_{\mathrm{out}}\right)$. Moreover, the emission efficiency will depend on the overlap of the electric field at the emission wavelength with the thin film of C545T. This is considered because an increased amplitude of the field will correspond to an increased density of final states for the excitonic transition and thus should increase the PL efficiency according to Fermi's Golden Rule. While the PL intensity is in principle also proportional to the Q-factor, the effect is not expected to change the relative PL because the reflectance suggests similar Q-factors (~ 20) for all samples in the *OVL* series. Finally, the relative η_{out} is given by the transmittance of the microcavity at the emitting wavelength, $T\left(\lambda_{\mathrm{out}}\right)$.

From evaluating Equation 5.2 at the mode position of the different samples, a theoretical prediction for the peak PL, I_{theo}, can be obtained. It is emphasised that I_{theo} assumes the

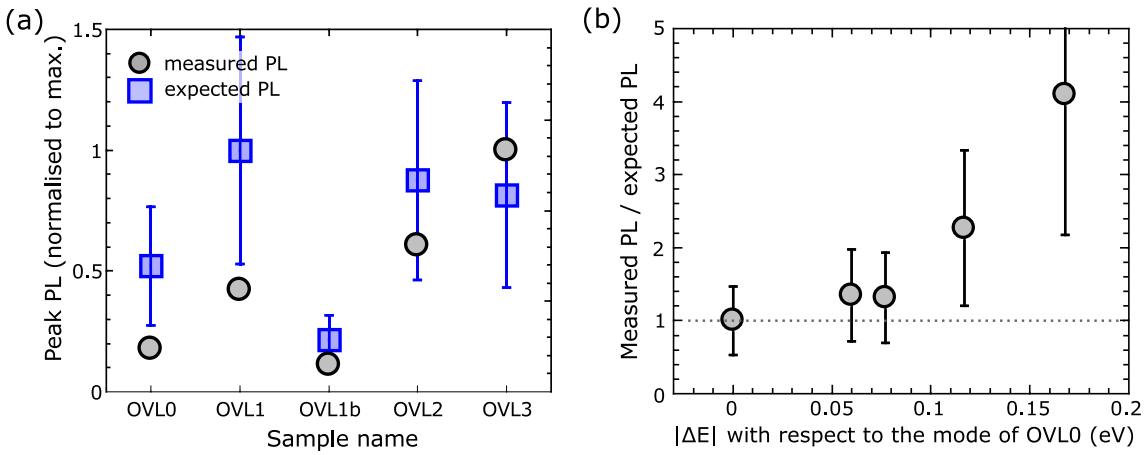

Figure 5.12: Comparison of measured PL of *OVL* series and expected PL. (a) Values for peak PL from measured data (grey symbols) and calculations neglecting strong coupling effects with indicated error estimation (blue symbols). (b) Ratio of peak measured PL versus calculated PL as a function of the mode shift of the λ-mode (at $\lambda \sim 550$ nm) with respect to that of sample *OVL0*. The dashed line indicates the same ratio of calculated and measured PL as observed in *OVL0*

internal PL efficiency to be that of the uncoupled C545T film—which we do not necessarily expect to describe the strongly coupled microcavities. In Figure 5.12a, I_{theo} (blue symbols) is compared to the measured peak PL, I_{meas} (black symbols), for the different samples. The large error of the theoretical value (47%) is a result of depending on five different parameters, the error for each of which was estimated to be between 10% and 30%. The comparison of the measured and predicted values does not indicate a clear correlation to the measured values. Even though both the theoretical and measured PL intensity are lowest for sample *OVL1b*, the calculation predicts the highest value for *OVL1*, which is in fact only the third highest value measured. While the calculated absorption of light into the cavity and $T(\lambda_{\text{out}})$ are similar for all samples, $A\left(\lambda_{\text{pump}}, z_{\text{C545T}}\right)$, $A\left(\lambda_{\text{out}}, z_{\text{C545T}}\right)$ and $\Phi(\lambda_{\text{out}})$ each vary by more than a factor of two between the samples.

In order to obtain a clearer picture of the relationship, Figure 5.12b plots the ratio of measured to predicted PL (normalised to *OVL0*) for all samples of the *OVL* series. Note that here, the x-axis denotes the shift of the mode at $\lambda \sim 550$ nm with respect to the mode of sample *OVL0*. This unusual x-axis is chosen because it can serve as an indication for the light–matter interaction in these samples. The mode splitting measured for the *OVL* series at larger angles (Chapter 4.2) cannot serve as a meaningful measure here since the different coupling strengths of the samples will result in a different energetic range over which photon and exciton will

be mixed. It is emphasised that it is only possible to use the mode shift relative to *OVL0* as a measure for the exciton–photon coupling because the mode at $\lambda \sim 350$ nm proves that the photonic mode is expected to be at the same position for all samples. Figure 5.12b shows a clear trend: all samples with a larger overlap of the organic film with the electric field than *OVL0* (i.e., all samples but *OVL0*) show a relatively increased PL signal. Moreover, the larger the mode shift is with respect to *OVL0*, the larger is the observed enhancement of PL intensity—up to a factor of 4.1 in *OVL3*. The similarity of the enhancement factor between *OVL1* and *OVL1b* is also remarkable; these two samples show a difference in absolute PL intensity by a factor of three but have a similar mode shift with respect to the mode of *OVL0*. Note, however, that the method of calculating the enhancement, though it is necessary for any meaningful evaluation of the results, is highly sensitive to errors in each factor considered for calculating I_{theo}.

The enhancement of the PL signal observed here is on the same order of magnitude as that observed by Ballarini *et al.* [41] and Schwartz *et al.* [254]. A comparison to literature indicates what the origin of the increased PL intensity might be. Herrera & Spano [255] predict that in low-Q, metal-clad cavities, an enhancement in PL intensity is caused by an efficient pumping of the polariton, from which the excitation can relax very efficiently via the photonic fraction of the polariton. The efficient pumping into the LP occurs by radiative transitions that involve at least one vibronic transition. Yet, this enhancement is expected to only set in when the coupling strength is in the same range as the vibrational energy, $g \approx E_{\text{vib}}$. From the analysis the extinction coefficient of C545T, $E_{\text{vib}} \approx 0.16$ eV is found (see Table 5.1). This value is confirmed by Raman spectroscopy on a neat film of C545T, see Figure 5.13, where the strongest Raman modes in the range between 1,400 cm^{-1} and 1,600 cm^{-1} correspond to an energy $E_{\text{vib}} \approx 0.19$ eV. The spectrum was acquired on a custom-built setup by Mingzhou Chen in the laboratory of Kishan Dholakia.

It is, however, not obvious how the coupling strength g should be evaluated. The Rabi splitting is estimated from simulations for *OVL0*, *OVL1*, *OVL2* and *OVL3* to be $\hbar\Omega = 0.14$ eV, 0.31 eV, 0.46 eV and 0.53 eV, respectively. From this, one would expect for *OVL1*, *OVL2* and *OVL3* to fall into the regime of vibronic enhancement, which is consistent with the results. However, since the samples are off resonance, it is not evident if the Rabi splitting describes the light–matter interaction adequately. Alternatively, the mode shift at $\Theta = 0^\circ$ with respect to the presumably uncoupled mode of *OVL0* could be seen as an indication for the coupling

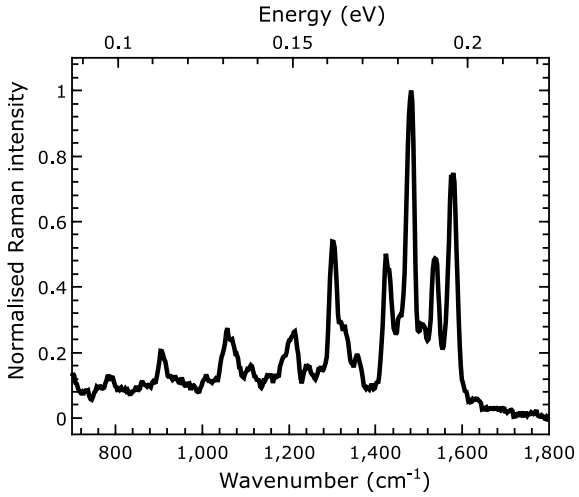

Figure 5.13: Raman spectrum of a neat film of C545T.

strength. This hypothesis is supported by the fact that the enhancement of samples *OVL1* and *OVL1b*, where the mode shift is only on the order of $E_{\mathrm{vib}}/2$, is only moderate (factor 1.3). Since the work by Herrera & Spano [255] does not specify which behaviour would be expected away from resonance, it is difficult to prefer one of the methods to estimate the coupling strength over the other. Nonetheless, the observed behaviour is consistent with the theoretical prediction, showing a continuous enhancement of the PL intensity up to a factor of four for the emission from polaritons (*OVL1*–*OVL3*) with respect to a largely photonic mode (*OVL0*).

Moreover, the presented data demonstrate the importance of considering all effects that might change the emission before jumping to a conclusion: while the PL spectra in Figure 5.11a suggest that e.g. *OVL1* is two times as bright as *OVL0*; and *OVL1b*—with a similar mode shift as *OVL1*—only half as bright as *OVL0*, the more careful analysis of Figure 5.12 shows that both samples show a moderate, but similar PL enhancement with respect to sample *OVL0*.

5.3.2 Photoluminescence from broad absorbers in DBR-clad microcavities

A major advantage of DBRs over metal mirrors is their extensive tunability—both the position and the reflectance of the stop band can be chosen at liberty (see Figure 5.6). This makes them indispensable for microcavities of the high Q-factors necessary for observing non-linear processes in strongly coupled microcavities. Yet, it has been observed that when these microcavities contain materials with a spectrally broad absorption, modes are suppressed at conditions

where photon and exciton are on resonance (see Section 5.2.4). This renders the characterisation in terms of light–matter coupling difficult. It is anticipated that this is not a problem of DBRs in particular, but rather that the mode suppression stems from the unbalanced loss of coherence between high-Q cavities and the material therein. This section will discuss a method for determining the character of the mode—bare cavity or mixed light–matter—from its Fourier image. For this method, microcavities with different blends of C545T and MADN and with different Q-factors were compared. In the second part, the PL of these microcavities is investigated and compared to predictions from weak coupling theory.

Fourier images of the PL from six different microcavities are compared in the following, as shown in Figure 5.14. Microcavities with 3.5 or 5.5 mirror pairs (a–c and d–f, respectively) filled with blended C545T:MADN films at concentrations of C545T ranging from 3% (left column) over 19% (centre column) to 43% (right column). In the following, they will be abbreviated according to the concentration C and the number of mirror pairs as C%-L and C%-H for 3.5 and 5.5 mirror pairs (low and high Q-factor), respectively. The shape of these spectra is analysed and compared to the parabolic shape of the dispersion expected for bare cavity modes (Equation 2.8). This less straightforward method is necessary because the mode position itself does not provide information about the mixed character of the mode: TMM fits of transmittance spectra at 0° revealed an increasing thickness of the organic film with increasing concentration of C545T, which could explain a mode shift to lower energies at least qualitatively.

In order to still obtain information about the mixing of light and matter in the different microcavities, the shape of the mode was analysed. With the help of a Matlab script, key characteristics of the mode—like position, width and height—were extracted from the 2D image by fitting the spectrum of each pixel with a Lorentzian curve. The due to a distortion of the peak shape for higher angles, however, the mode position was better described by simply finding the most prominent peak. Nonetheless, the data obtained from the Lorentzian fits are important because they also give a measure for the mode width—which was confirmed as a valid measure also for distorted peaks. The mode position of these six samples is plotted as a function of $q_{\parallel}$ in Figure 5.14g–i. The full width of the detector corresponds to approximately $-30° \lesssim \Theta \lesssim 30°$, which is determined by the numerical aperture of the objective (0.55).

These modes were then fitted with parabolas in a small range around the minimum ($\frac{1}{a} \cdot$

$x^2 + E_0$ for $-1.3\ \mu m^{-1} < q_{\parallel} < 1.3\ \mu m^{-1}$), where all minima could be approximated with quadratic function to a satisfactory degree ($R^2 > 0.83$ for all modes, which could be increased by noise reduction via a 5-point moving average to $R^2 > 0.98$). The shape of Bragg modes was also analysed for comparison (not shown). Since the scaling factor a is proportional to the inverse of the curvature of the mode, it is proportional to its effective band mass and will in the following be referred to as mass factor.

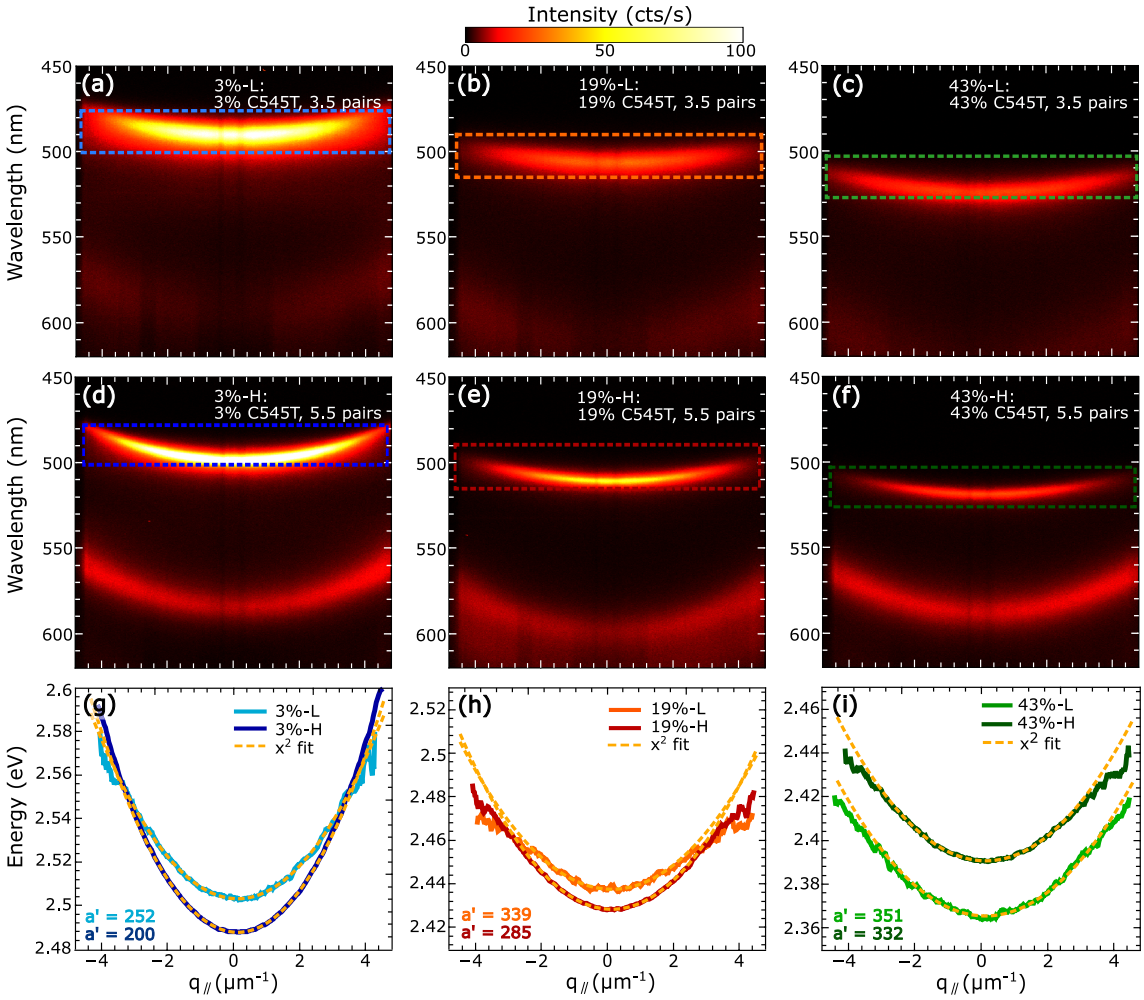

Figure 5.14: PL from microcavities as a function of C545T concentration and Q-factor. Microcavities in the first, second and third column contain 3%, 19% and 43% C545T in MADN, respectively. The first row (a–c) shows PL from microcavities with 3.5 mirror pairs, the second row (d–f) from microcavities with 5.5 mirror pairs. Dashed boxes indicate the spectral region shown in the third row. The third row (g–h) shows the modes extracted from images (a–f), smoothed by a 5-point moving average. These are compared to parabolic functions ($\frac{1}{a}x^2 + E_0$, orange, dashed lines) that were fitted in the region $-1.3\ \mu m^{-1} < q_{\parallel} < 1.3\ \mu m^{-1}$ and then plotted over the entire range of $q_{\parallel}$. The unitless mass factor $a' = a/(\ eV^{-1}\mu m^{-2})$, which is proportional to the effective mass of the mode, is noted for each curve in the figure.

This mass factor a, which is noted unitless as $a' = a/(\ \mathrm{eV}^{-1}\mu\mathrm{m}^{-2})$ in Figures 5.14g–i, ranged from $a_{3\%-\mathrm{H}} = 200\ \mathrm{eV}^{-1}\mu\mathrm{m}^{-2}$ to $a_{43\%-\mathrm{L}} = 351\ \mathrm{eV}^{-1}\mu\mathrm{m}^{-2}$. As a comparison, the Bragg modes—which are supposed to be purely photonic—on average have a mass factor of $a = (220 \pm 20)\ \mathrm{eV}^{-1}\mu\mathrm{m}^{-2}$, slightly larger than the lightest mass observed of a mode in the stopband. The similarity of values between 3%-H and the Bragg modes indicates that 3%-H has a similar mass to that of a purely photonic mode and is thus mostly photonic. However, it is not clear if the side fringes follow the same dispersion relation as the cavity mode, so that the absolute values of a are rather compared to calculations of a purely photonic mode according to Equation 2.8, from which it follows that $a = \frac{2E_0 \cdot n_c^2}{\hbar^2 c^2}$. Evaluating this expression for organic microcavities ($n_c \approx 1.8$) with a mode energy of $E_0 \approx 2.45$ eV yields a mass factor of $a \approx 400\ \mathrm{eV}^{-1}\mu\mathrm{m}^{-2}$. It is not clear where this deviation of a factor of 2 stems from, so the absolute values of the mass factor ought to be handled with caution.

Relatively between the samples, however, an interesting observation is made: there is a general trend of a to be larger for higher concentrations of C545T and for lower Q-factors. If all modes were purely photonic, the relationship $\frac{a}{E_0 \cdot n_c^2}$ should be constant. Since the background refractive index of C545T and MADN is the same, so will that of different mixtures of the materials be—i.e., $n_c \approx$ constant (see Figure 5.1). Given that E_0 also only varies within 6%, the increase in mass factor from 3%-H to 43%-L by over 50% must be driven by something else. An admixture of excitonic fraction into the photon mode would result in an increase of the effective band mass, and hence the mass factor. This has been observed within this PhD in previous experiments in Al-clad microcavities (not shown). For the samples presented here, films with a higher concentration of C545T (i.e., excitons) are expected to have a larger coupling strength, and thus an increased excitonic fraction in the mode. Thus, the increase of the mass factor a with higher concentrations is in agreement with the expectation of a greater light–matter coupling. It is emphasised that this increase in mass factor (and potentially increase in excitonic fraction) is observed with increasing concentration of C545T although $|E_0(43\%) - E_\mathrm{X}| > |E_0(19\%) - E_\mathrm{X}| > |E_0(3\%) - E_\mathrm{X}|$ (with exciton energy $E_\mathrm{X} = 2.50$ eV). If all coupling strengths were the same, a decrease in excitonic fraction would be expected with greater distance from the excitonic mode. Thus, the increase in excitonic fraction implies an increase in coupling strength.

In the next step of the analysis, the parabolic fit of the restricted range was plotted over the entire detector range ($-5\ \mathrm{eV}^{-1}\mu\mathrm{m}^{-2} < q_\parallel < 5\ \mathrm{eV}^{-1}\mu\mathrm{m}^{-2}$) and compared to the mea-

sured shape of the mode. Here, differences between the different samples become even more pronounced. The only curve which is (slightly) narrower than the parabolic fit towards the edges of the detector is 3%-H, the sample which had the steepest parabola, and for which the lowest light–matter interaction is expected. All other modes tend to flatten away from the parabola at large angles. For modes which are roughly at the same energy and concentration, the flattening is generally more subtle for the modes in the high-Q microcavity. In the sample containing an organic film with 43% C545T, the modes are offset by 0.03 eV, where the low-Q sample 43%-L is found at lower energies and further away from the exciton. Assuming that the broadening as well as the flattening of the parabola at large angles are caused by an increase in light–matter interaction, this would imply a larger coupling strength for the low-Q cavities.

Both parts of the analysis of the mode shape thus yield results that agree with each other: (1) The exciton fraction and coupling strength both increase with concentration of C545T, which is consistent with Equation 2.27. It is emphasised that this is not obvious with only a single visible mode (i.e., no clear anticrossing), nor is it clear from only looking at the Fourier images of the luminescence (Figure 5.14). (2) The coupling strength appears to be larger for microcavities with a lower number of mirror pairs (i.e., lower Q-factors), which is not expected. Yet, comparing the mode distribution between cavities with high and low Q-factors, the mode volume is found to be larger by a factor of 1.4 for microcavities with 5.5 mirror pairs. Since $g \propto \sqrt{1/V}$ (see Equation 2.27), this would result in an increase in coupling strength from high-Q to low-Q cavities by a factor of ~ 1.2. Furthermore, the mass factor measured for the modes of samples 19%-L and 19%-H, which are at approximately the same energy, differ by a factor of 1.2. Thus, the smaller mode volume in low-Q cavities could explain the extent of the increase in exciton fraction even quantitatively.

After the coupling inside these microcavities has been analysed, their measured PL intensity is compared to theoretical predictions from weak coupling theory. In contrast to the samples discussed in Section 5.3.1, the material properties in these DBR-clad microcavities differ strongly from each other. The samples differ in concentration of C545T, C, (i.e., in PLQY Φ and extinction coefficient k), in Q-factor of the cavity and in mode volume V. All these parameters will have an impact on the luminescence of the cavity, which we would from weak

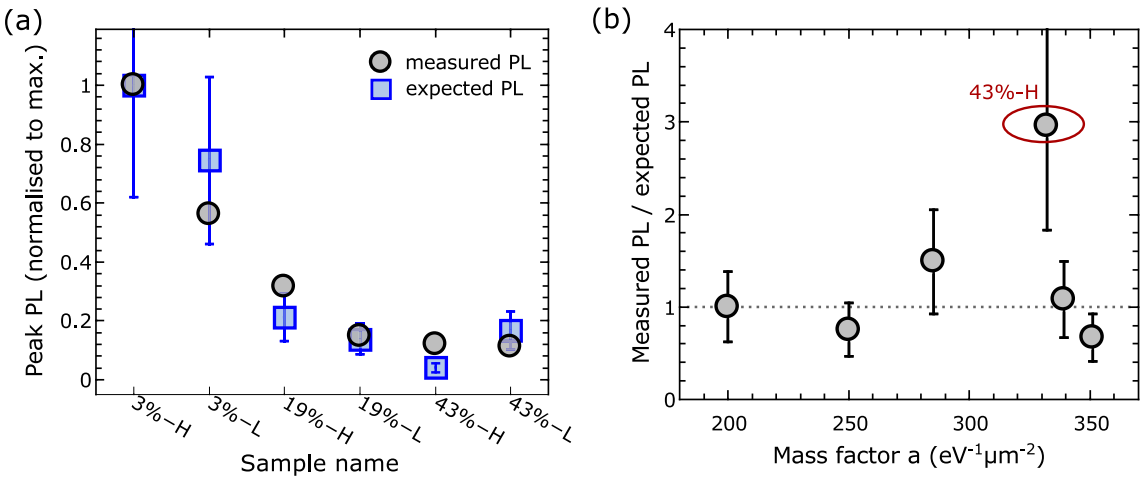

Figure 5.15: PL intensity of DBR-clad microcavities versus theoretical predictions. (a) Peak PL intensity (normalised to maximum) of samples presented in Figure 5.14, as measured (grey symbols) and predicted PL intensity according to Equation 5.3 (normalised to maximum) (blue symbols with error bars). (b) Ratio of measured over predicted PL intensity as a function of the mass factor a (see Figure 5.14), normalised to the ratio at smallest a, i.e., 3%-H. The dotted line indicates values where $\mathrm{PL}_{\mathrm{meas}}/\mathrm{PL}_{\mathrm{theo}} = 1$. The value for 43%-H is circled.

coupling theory expect to correspond to

$$\mathrm{PL}_{\mathrm{theo}} = \overbrace{T\left(\lambda_{\mathrm{pump}}\right) \cdot d_{\mathrm{org}} \cdot k\left(\lambda_{\mathrm{pump}}\right)}^{\eta_{\mathrm{pump}}} \cdot \overbrace{\Phi(C) \cdot \Phi\left(\lambda_{\mathrm{m}}\right) \cdot \frac{Q \cdot \lambda_{\mathrm{m}}^3}{V}}^{\eta_{\mathrm{int}}} \overbrace{T\left(\lambda_{\mathrm{m}}\right)}^{\eta_{\mathrm{out}}}. \tag{5.3}$$

As before, η_{pump}, η_{int} and η_{out} correspond to the pumping efficiency, the internal efficiency and the outcoupling efficiency, respectively. Since the emission originates from a mode defined by the microcavity, the PLQY is a function of both the concentration, $\Phi(C)$, and the spectral efficiency, $\Phi\left(\lambda_{\mathrm{m}}\right)$. Moreover, η_{int} takes into account the Purcell factor, $F_{\mathrm{P}} \propto \frac{Q \cdot \lambda_{\mathrm{m}}^3}{V}$, which depends on the Q-factor, the mode position λ_{m} and the mode volume V. Note that here, the Q-factor is not determined for an empty cavity, but from the experimental spectrum. The reason for this is that the increase of the radiative rate by the Purcell effect is a consequence of the increased final density of states, which, in turn, depends on the Q-factor. However, when an absorbing material is introduced into the microcavity, the coherence of the cavity mode will be reduced and so will the final density of states be. Therefore, the losses inside the microcavity by absorption should be accounted for when calculating the Purcell factor, which is done by determining the Q-factor from the experimental width of the mode.

Figure 5.15a shows a comparison of the measured values of the peak PL (grey symbols) to

the theoretical predictions explained above (blue symbols). The large error of the theoretical PL intensity (38%) originates from the large number of different factors with conservatively estimated, relative errors between 3% and 20% that contribute to the overall error. Both the measured and the expected PL signal decrease when increasing the concentration of C545T in the absorber or lowering the Q-factor.

In order to obtain a more quantitative understanding of the relationship between these values, the ratio of the measured PL intensity over that of the predicted PL intensity is plotted in Figure 5.15b as a function of the mass factor a. This x-axis is chosen in this way because the previous analysis has suggested that a is directly linked to the light–matter mixing of the mode. Hence, if there was a trend with light–matter interaction to be observed, it should appear along a. However, the data in Figure 5.15b does not indicate any clear trend. Instead, most values lie at ±50% around the PL ratio calculated for the presumably uncoupled mode of 3%-H. The only outlier is the PL ratio of 43%-H, for which a three-fold increase with respect to the ratio of 3%-H is observed. It is not clear from the data why the PL intensity of this microcavity should be increased. Both the measured and the predicted value of 43%-H are small, so that a small absolute error in the measurement of the PL intensity of 43%-H would correspond to a large relative error. Since all five other samples show a similar trend, the value of 43%-H is thus discarded. The remaining DBR-clad microcavities do not show any trend of increase in PL signal with the mass factor a (which is linked to the coupling strength as discussed above).

At first glance, this result—i.e., no enhancement in PL with light–matter coupling—seems contradictory to the steady increase of PL signal observed in the metal-clad microcavities in Section 5.3.1. However, one should not forget that the nature of the metal-clad samples is very different from those discussed here. The samples discussed in Section 5.3.1 are metal-clad microcavities with a lower Q-factor and the bare material properties of the films are the same throughout the entire sample series. Here, by contrast, the active material in the microcavities consists of blended films of different concentrations and the cavities have different Q-factors. It is difficult to directly compare the coupling strengths between the metal-clad and the DBR-clad microcavities, since in both series, different indirect measures for the coupling strength were used. In absolute terms, the higher concentration and the smaller mode volume in the metal-clad cavities there needs to be weighed against the overall greater thickness of the organic film here. It might simply be the case that the coupling strength in this DBR-clad series is too small to enable the vibrationally assisted pumping of the LP branch. It is also possible that

the Q-factors of the DBR-clad microcavities analysed here are too high (up to ~ 130 when considering intra-cavity losses and $Q > 300$ for calculations of an empty cavity) for the theory of Herrera & Spano [179, 255] to hold, which was specified for low-Q microcavities.

From the investigations presented in this section, two lessons are learned: (1) Introducing blended films into microcavities significantly increases the complexity of the system. Experimentally, it would thus be preferable to either involve more samples, e.g. with different thicknesses for each of the six sample categories presented here, or reduce the experimental fluctuations (which accompany the greater freedom in design), e.g. with commercially acquired DBRs. Nonetheless, most of the DBR-clad microcavities studied here did not show an increase of PL intensity with coupling strength. (2) Analysing the shape of a single, visible mode was found to be a method which could provide some information about its mixed light–matter character. Even though this did not provide information like the absolute coupling strength, relative coupling strengths could be deduced.

6

Conclusions and outlook

To summarise, this thesis has presented experimental investigations of organic microcavities, looking into basic relationships between the properties of the strongly coupled microcavity and those of its uncoupled constituents. In contrast to previous reports addressing similar questions, the work here has focussed on disordered organic materials which exhibit a pronounced vibronic progression and has distinguished between the measured Rabi splitting and the underlying coupling strength. In general, the results confirm the validity both of the form of the coupling strength and of the coupled oscillator model, even for complex, disordered materials. Studying the photoluminescence , a moderate increase with the coupling strength was found in metal-clad microcavities, whereas no significant increase was found in DBR-clad microcavities.

First, the optical properties of four different active materials (PF8, F8BT, BBEHP-PPV and MEH-PBI) were compared in the uncoupled state (Chapter 4.1). Contrasting these values with the Rabi splitting, which was measured for metal-clad microcavities containing the four materials, only showed a correlation between the Rabi splitting and the absorption character-

istics. No correlation was observed for any of the other investigated parameters, including the linewidth of the transition and the Stokes shift. Hence, the results showed that the absorption strength is the key property of all investigated material characteristics to define the coupling strength, in agreement with predictions. An additional analysis tested the relationship between the Rabi splitting and the coupling strength by examining the three different terms for the excitonic losses—assuming them to be predominantly of homogeneous or inhomogeneous nature or assuming the entire band width of the transition to contribute to the losses. From this, the coupling strength showed the clearest proportionality to the integrated absorption coefficient when assuming the losses to be defined by the total width of the transition. In this way, the results are shown to be consistent with the coupled oscillator model.

However, when changing the materials inside the microcavity, many parameters were changed at the same time, which were partly shown to have a minor influence on the coupling strength (like the width of the transition). Hence, two further sets of microcavities aimed to isolate and vary one single parameter at a time and thus to access a possible onset of the strong coupling regime more directly (Chapter 4.2). Again, a material with pronounced disorder and vibronic progression was chosen for the investigations, namely C545T. From a variation of the number of absorbers—in contrast to previous reports, at constant concentration—the coupling strength was found to be proportional to the square root of the number of absorbers. In an independent experiment, the overlap between a thin, organic film and the electric field was controlled by controlling the position of the film inside the microcavity. This demonstrated the coupling strength to be directly proportional to the electric field, so that both sample series quantitatively confirm the predicted form of the coupling strength. In fact, the data agreed so well with the expectation ($R^2 > 0.99$ for both series) that the offset between the coupling strength and the Rabi splitting could be determined. This offset, which corresponds to a threshold for the onset of the strong coupling regime, was determined for both independently fabricated and analysed sample sets to be $g_{\mathrm{thr}}^{\mathrm{exp}} = 0.10 \pm 0.03$ eV. This experimentally determined threshold was compared to the loss terms of photon and exciton, which determine the threshold of the strong coupling regime according to the coupled oscillator model. Again, three different scenarios were considered for the excitonic losses. Depending on the assumption for the excitonic losses, theoretical values of $g_{\mathrm{thr}}^{\mathrm{theo}} = 0.06 \ldots 0.19$ eV were found for the threshold. Even though the data did not allow for identifying the excitonic losses which determine the threshold, the agreement in the order of magnitude clearly validated the coupled

oscillator model also for materials with strong disorder and vibronic broading.

The second part of this thesis was dedicated to studying the photoluminescence from microcavities (Chapter 5.2). A large parameter space was scanned in order to find the best conditions for polariton lasing in a blended host:guest material system. Yet, although the optical properties of the blended film, the *Q*-factors of the microcavities, the detuning between exciton and photon and excitation parameters were varied, polariton lasing was not achieved. The reason for this was not the fabrication process, which was proven by the demonstration of photon lasing in a separately designed microcavity. Instead, two other effects were identified which potentially impede polariton lasing: (1) the disappearance of modes when photon and exciton are on resonance (instead of their anticrossing) and (2) bimolecular quenching, which hinders the build-up of large exciton densities. While the first is probably a consequence of the present impedance mismatch, i.e., of the large difference between the excitonic and photonic linewidth, the latter is unrelated to the linewidth of the exciton and only depends on its decay dynamics.

These two aspects are compared to the publications by Daskalakis *et al.* [61] and Dietrich *et al.* [62], which report polariton lasing with materials of a large bandwidth. The angle-resolved reflectivity spectra of Daskalakis *et al.* [61] also do not show anticrossing over a large angular range, though the effect is not as pronounced as in the present material. In particular, there is only a single mode at $\Theta = 0°$, i.e., at the bottom of the lower polariton branch. Yet, polariton lasing was observed in this broad absorber. Dietrich *et al.* [62] do not observe a similar behaviour because they couple the broad excitonic absorption band to a multitude of photonic modes by increasing the thickness of the organic film. The authors emphasize, however, the role of the bimolecular quenching. Indeed, in both materials, the exciton–exciton annihilation is shown to set in only above a certain threshold, which contrasts with the materials here, where a sublinear optical response is observed even for the lowest measured excitation powers. This difference indicates that the extent of strong bimolecular quenching has a larger impact on polariton condensation than the disappearance of modes.

As mentioned, the non-linear, strongly coupled regime was not reached for the cavities produced within this PhD. However, the photoluminescence intensity was probed in the linear regime as a function of the coupling strength (Chapter 5.3). Yet, it follows from the discussion above about the suppression of modes that the mode splitting can no longer act as an indicator

for the coupling strength: there is only a single mode. In order to still determine the character of the modes observed in luminescence, their shape was analysed by fitting a parabola to a small region restricted around the minimum of the mode. A correlation of the expected light–matter interaction to the width of this parabola and to its deviation from the measured mode at large angles was observed. Both trends are consistent with a larger excitonic fraction of the mode. Hence, this method proves to be an indicator for the light–matter mixture of the mode in the absence of anticrossing. When comparing the photoluminescence intensity of these different modes to the predictions from weak coupling theory, no enhancement of photoluminescence with coupling strength was observed in this cavity series. By contrast, a series of metal-clad microcavities, in which the coupling strength is the only parameter modified between samples, showed a clear increase of the luminescence with coupling strength up to a factor of four. This enhancement of luminescence can possibly be explained by vibrationally assisted scattering into the polariton branch when the coupling strength tunes into resonance of twice the vibrational energy.[256] This scattering is only predicted for low-Q, metal-clad cavities, so that the absence of enhancement in the DBR-clad microcavities is not necessarily contradictory to this hypothesis.

The work discussed in this thesis has brought some clarity into the description of strongly disordered organic semiconductors—especially by experimentally confirming a non-zero threshold for the onset of the strong coupling regime. Yet, more questions remain: (1) What quantity of the excitonic transition determines the excitonic losses that influence the threshold for the strong coupling regime? The presented data do not provide a conclusive picture, but indicate that the excitonic losses are probably not defined by the homogeneous linewidth. An investigation that systematically varies only the inhomogeneous broadening might shed more light on the precise form the the excitonic losses. (2) Which parameters of the organic microcavity are crucial for achieving polariton lasing? The discussion above has shown that one important quality of the material is probably to maintain high quantum efficiencies up to high excitation densities. This would have to be confirmed in a systematic comparison of materials with different quantum efficiencies in the highly excited strong coupling regime. (3) What effect does the suppression of modes at resonance between the broad mode of an absorber and the narrow mode of a cavity have? Even though the absence of anticrossing suggests the absence of efficient light–matter coupling, the analysis of the mode shape indicated an admixture of the exciton onto the mode. Time-resolved measurements on the time-scale of the Rabi frequency

could provide more insight into the interaction between the cavity photon and the exciton in this ambiguous case.

Appendix

In the following, the core of the Matlab script, which was developed in the course of this PhD project and used for TM calculations, is presented. It is called by an external function, in which all parameters of the stack (thickness, refractive index) and the wavelength of the light are specified.

```
%% TM_core
% Function to calculate reflectance, transmittance or E-field distribution
% over defined stack of materials using matrix optics with Fresnel's
% equations and the phase shift due to propagation.
% Equations adapted from Pettersson et al., JAP vol. 86 (1999)
% Main tools:   Tif(jj) - Matrix to account for reflectance/transmittance
%                         at interface between layers jj-1 and jj (eq. 1)
%               Tps(jj) - Matrix to account for phase shift while
%                         propagating through layer jj (eq. 5, use inverse
%                         signs due to sign convention in n_c=n_r +- i*k)
%               Ttot(jj) - combining effect of all scatterings /
%                         propagations up to layer jj by matrix multipl. (eq
    . 8)
% input:    x - wavelength/energy, at which refl/tran are calculated
%           stackd - stack of thicknesses of different layers
%           stackn - stack of refr. indices at this wl/en of each layer
%           xdep - specifier: wavelength 'la' or energy 'en'?
%           th1 - angle of incidence
%           pol - 'p' or 's'?
%%
function [outdata,d_inl]=TM_core(x,stackd,stackn,xdep,th0,pol,datatype,
    posd)
```

```
switch xdep
    case 'la'
        la=x*1e-9;
    case 'en'
        la=wl2en(x)*1e-9;
end
% adapt to n=n+ik in JAP
stackn=conj(stackn);

% reduce stacks to layers where material actually exists, add air on both
% sides (thickness = 0, n=1)
stackd=[0;stackd;0];
stackn=[1;stackn;1];


if or(strcmpi(datatype,'refl'),strcmpi(datatype,'tran'))
    Ttot=eye(2); %Initialise matrix with unity matrix

    for jj=2:length(stackd)
        % use functions IF_r, IF_t, psfac, qfac as defined below
        Tif=[1,IF_r(jj-1,jj,pol,th0); IF_r(jj-1,jj,pol,th0),1] /IF_t(jj-1,
            jj,pol,th0);  % eq. 1
        Tps=[exp(-1i*psfac(jj,th0,la)*stackd(jj)),0;0,exp(1i*psfac(jj,th0,
            la)*stackd(jj))]; % eq. 5
        Ttot=Ttot*Tif*Tps; % eq. 8
    end

    %resulting matrix is of the form [1/tr,-ref/tr;-ref/tr,1/tr], where tr
    %is transmissivity and ref is reflectivity at this wavelength
    if strcmp(datatype,'tran')
        outdata=abs(1/Ttot(1,1))^2; % only true if n_0 = n_N
    elseif strcmp(datatype,'refl')
        outdata=abs(Ttot(2,1)/Ttot(1,1))^2;
    end
```

```
elseif strcmpi(datatype,'Efield')

    dsum=cumsum(stackd);     %summed up thickness
    outdata=zeros(1,length(posd));
    lno=1; % counter for layer number in stack
    for ipos=1:length(posd)
        % only if a layer border is crossed, do recalculate Tbef, Taft
        if posd(ipos) > dsum(lno)
            % Matrices describing effect of stack on electric field before
            % and after layer where field strength is calculated,
                respectively.
            Tbef=eye(2);
            Taft=eye(2);

            %in case there are layers with 0 thickness in stack.
            while posd(ipos) > dsum(lno)
                lno=lno+1;
            end

            % effect of stack before current layer: Tbef
            for jj = 2 : lno
                Tif = [1,IF_r(jj-1,jj,pol,th0); IF_r(jj-1,jj,pol,th0),1] /
                     IF_t(jj-1,jj,pol,th0);  % eq. 1
                Tps = [exp(-1i*psfac(jj-1,th0,la)*stackd(jj-1)),0;0,exp(1i
                    *psfac(jj-1,th0,la)*stackd(jj-1))]; % eq. 5
                Tbef = Tbef*Tps*Tif; % eq. 8
            end

            % effect of stack after current layer: Taft
            for jj = lno+1 : length(stackd)
                Tif = [1,IF_r(jj-1,jj,pol,th0); IF_r(jj-1,jj,pol,th0),1] /
                     IF_t(jj-1,jj,pol,th0);  % eq. 1
                Tps = [exp(-1i*psfac(jj,th0,la)*stackd(jj)),0;0,exp(1i*
                    psfac(jj,th0,la)*stackd(jj))]; % eq. 5
                Taft = Taft*Tif*Tps; % eq. 8
            end
```

```
        end

        % calculating field at position ipos according to eq. 21
        d_inl = posd(ipos) - dsum(lno-1); % thickness in current layer
        E_enum11 = Taft(1,1) * exp(-1i*psfac(lno,th0,la)*(stackd(lno)-
            d_inl)) ;
        E_enum21 = Taft(2,1) * exp(1i*psfac(lno,th0,la)*(stackd(lno)-d_inl
            ))  ;
        E_denom11 = Tbef(1,1) * Taft(1,1) * exp(-1i*psfac(lno,th0,la)*
            stackd(lno));
        E_denom21 = Tbef(1,2) * Taft(2,1) * exp(1i*psfac(lno,th0,la)*
            stackd(lno));
        outdata(ipos) = (E_enum11 + E_enum21)/(E_denom11 + E_denom21);
    end
end

%% qfac - factor ~ wavelength 'stretching' due to non-zero angle and n > 1
    (eq. 4)
% qa = na *cos(tha) - reformulate via snells law as function of th0
% difference to Pettersson: omits sin^2, whereas ^2 should be there from
% derivation (LB3, p.136)
    function qa = qfac(na,th0)
        qa=sqrt(na^2-stackn(1)^2*(sin(th0))^2);
    end

%% reflectivity at interface between stackpos1 and stackpos 2
    function r = IF_r(stackpos1,stackpos2,pol,th0)
            n1=stackn(stackpos1);
            q1=qfac(n1,th0);
            n2=stackn(stackpos2);
            q2=qfac(n2,th0);
        if strcmp(pol,'s') % Fresnel r_s = TE
            r = (q1-q2)/(q1+q2);       % eq. 2a
        elseif strcmp(pol,'p') % Fresnel r_p = TM
            r = (n1^2*q2 - n2^2*q1)/(n1^2*q2 + n2^2*q1); % -1*(eq. 3a) -
                error in paper!
```

```
        end
    end

%% transmissivity at interface between stackpos1 and stackpos 2
    function t=IF_t(stackpos1,stackpos2,pol,th0)
            n1=stackn(stackpos1);
            q1=qfac(n1,th0);
            n2=stackn(stackpos2);
            q2=qfac(n2,th0);
        if strcmp(pol,'s')          % Fresnel t_s = TE
            t = 2*q1/(q1+q2);         % eq. 2b
        elseif strcmp(pol,'p')      % Fresnel t_p = TM
            t = 2*n1*n2*q1/(n2^2*q1 + n1^2*q2);    % eq. 3b
        end
    end

%% phase-shift factor depending on angle, refractive index and k-vector/wl
    (eq. 6)
    function ps = psfac(stackpos, th0, la)
        n1=stackn(stackpos);
        q1=qfac(n1,th0);
        ps = 2*pi/la * q1;
    end

end
```

Bibliography

1. Directorate-General for Health and Consumers and Scientific Committee on Emerging and Newly Identified Health Risks. *Light Sensitivity* (European Commission, 2008).
2. Lenard, P. Über die lichtelektrische Wirkung. *Annalen der Physik* **313,** 149–198 (1902).
3. Einstein, A. Über einen die Erzeugung und Verwandlung des Lichtes betreffenden heuristischen Gesichtspunkt. *Annalen der Physik* **322,** 132–148 (1905).
4. Gordon, J. P., Zeiger, H. J. & Townes, C. H. The Maser—New Type of Microwave Amplifier, Frequency Standard, and Spectrometer. *Physical Review* **99,** 1264–1274 (1955).
5. Maiman, T. H. Stimulated Optical Radiation in Ruby. *Nature* **187,** 493–494 (1960).
6. European Commission. *Energy roadmap 2050* (Publications Office of the European Union, 2012).
7. Royal Swedish Academy of Sciences. *Scientific Background: Efficient blue light-emitting diodes leading to bright and energy-saving white light sources* (Nobel Prize, 2014).
8. Ilberg, W. *et al. Physikalisches Praktikum fur Anfänger* 6th ed. (BSB B.G. Teubner Verlagsgesellschaft, 1982).
9. Agranovich, V. & Malshukov, A. Surface polariton spectra if the resonance with the transition layer vibrations exist. *Optics Communications* **11,** 169–171 (1974).
10. Aberra Guebrou, S. *et al.* Coherent Emission from a Disordered Organic Semiconductor Induced by Strong Coupling with Surface Plasmons. *Physical Review Letters* **108,** 066401 (2012).
11. Törmä, P. & Barnes, W. L. Strong coupling between surface plasmon polaritons and emitters: a review. *Reports on Progress in Physics* **78,** 013901 (2015).

12. Huang, K. On the interaction between the radiation field and ionic crystals. *Proceedings of the Royal Society A: Mathematical, Physical and Engineering Sciences* **208,** 352–365 (1951).

13. Shalabney, A. *et al.* Enhanced Raman Scattering from Vibro-Polariton Hybrid States. *Angewandte Chemie International Edition* **54,** 7971–7975 (2015).

14. Sanchez-Mondragon, J. J., Narozhny, N. B. & Eberly, J. H. Theory of Spontaneous-Emission Line Shape in an Ideal Cavity. *Physical Review Letters* **51,** 550–553 (1983).

15. Meschede, D., Walther, H. & Müller, G. One-Atom Maser. *Physical Review Letters* **54,** 551–554 (1985).

16. Rempe, G., Walther, H. & Klein, N. Observation of quantum collapse and revival in a one-atom maser. *Physical Review Letters* **58,** 353–356 (1987).

17. Weisbuch, C., Nishioka, M., Ishikawa, A. & Arakawa, Y. Observation of the coupled exciton-photon mode splitting in a semiconductor quantum microcavity. *Physical Review Letters* **69,** 3314–3317 (1992).

18. Houdré, R. *et al.* Room-temperature cavity polaritons in a semiconductor microcavity. *Physical Review B* **49,** 16761–16764 (1994).

19. Lidzey, D. G. *et al.* Strong exciton-photon coupling in an organic semiconductor microcavity. *Nature* **395,** 53–55 (1998).

20. Forrest, S. R. The path to ubiquitous and low-cost organic electronic appliances on plastic. *Nature* **428,** 911–918 (2004).

21. Baas, A., Karr, J., Eleuch, H. & Giacobino, E. Optical bistability in semiconductor microcavities. *Physical Review A* **69,** 023809 (2004).

22. Amo, A. *et al.* Polariton Superfluids Reveal Quantum Hydrodynamic Solitons. *Science* **332,** 1167–1170 (2011).

23. Sich, M. *et al.* Observation of bright polariton solitons in a semiconductor microcavity. *Nature Photonics* **6,** 50–55 (2011).

24. Deng, H. *et al.* Condensation of Semiconductor Microcavity Exciton Polaritons. *Science* **298,** 199–202 (2002).

25. Kasprzak, J. *et al.* Bose–Einstein condensation of exciton polaritons. *Nature* **443,** 409–414 (2006).

26. Christopoulos, S. *et al.* Room-Temperature Polariton Lasing in Semiconductor Microcavities. *Physical Review Letters* **98,** 126405 (2007).

27. Kéna-Cohen, S. & Forrest, S. R. Room-temperature polariton lasing in an organic single-crystal microcavity. *Nature Photonics* **4,** 371–375 (2010).

28. Wouters, M. & Carusotto, I. Excitations in a Nonequilibrium Bose-Einstein Condensate of Exciton Polaritons. *Physical Review Letters* **99,** 140402 (2007).

29. Keeling, J. & Berloff, N. G. Exciton–polariton condensation. *Contemporary Physics* **52,** 131–151 (2011).

30. Klembt, S. *et al.* Exciton-Polariton Gas as a Nonequilibrium Coolant. *Physical Review Letters* **114,** 186403 (2015).

31. Sturm, C. *et al.* Nonequilibrium polariton condensate in a magnetic field. *Physical Review B* **91,** 155130 (2015).

32. Werner, A., Egorov, O. A. & Lederer, F. Exciton-polariton patterns in coherently pumped semiconductor microcavities. *Physical Review B* **89,** 245307 (2014).

33. Bobrovska, N. *et al.* Dynamical Instability of a Nonequilibrium Exciton-Polariton Condensate. *ACS Photonics* **5,** 111–118 (2017).

34. Berloff, N. G. *et al.* Realizing the classical XY Hamiltonian in polariton simulators. *Nature Materials* **16,** 1120–1126 (2017).

35. Schachenmayer, J., Genes, C., Tignone, E. & Pupillo, G. Cavity-Enhanced Transport of Excitons. *Physical Review Letters* **114,** 196403 (2015).

36. Feist, J. & Garcia-Vidal, F. J. Extraordinary Exciton Conductance Induced by Strong Coupling. *Physical Review Letters* **114,** 196402 (2015).

37. Orgiu, E. *et al.* Conductivity in organic semiconductors hybridized with the vacuum field. *Nature Materials* **14,** 1123–1129 (2015).

38. Hagenmüller, D. *et al.* Cavity-Enhanced Transport of Charge. *Physical Review Letters* **119,** 223601 (2017).

39. Graf, A. *et al.* Electrical pumping and tuning of exciton-polaritons in carbon nanotube microcavities. *Nature Materials* **16,** 911–917 (2017).

40. Zhong, X. *et al.* Non-Radiative Energy Transfer Mediated by Hybrid Light-Matter States. *Angewandte Chemie International Edition* **55,** 6202–6206 (2016).

41. Ballarini, D. *et al.* Polariton-Induced Enhanced Emission from an Organic Dye under the Strong Coupling Regime. *Advanced Optical Materials* **2,** 1076–1081 (2014).

42. Wang, S. *et al.* Quantum Yield of Polariton Emission from Hybrid Light-Matter States. *The Journal of Physical Chemistry Letters* **5,** 1433–1439 (2014).

43. Grant, R. T. *et al.* Efficient Radiative Pumping of Polaritons in a Strongly Coupled Microcavity by a Fluorescent Molecular Dye. *Advanced Optical Materials* **4,** 1615–1623 (2016).

44. Hutchison, J. A. *et al.* Modifying Chemical Landscapes by Coupling to Vacuum Fields. *Angewandte Chemie* **124,** 1624–1628 (2012).

45. Ebbesen, T. W. Hybrid Light–Matter States in a Molecular and Material Science Perspective. *Accounts of Chemical Research* **49,** 2403–2412 (2016).

46. Herrera, F. & Spano, F. C. Cavity-Controlled Chemistry in Molecular Ensembles. *Physical Review Letters* **116,** 238301 (2016).

47. Feist, J., Galego, J. & Garcia-Vidal, F. J. Polaritonic Chemistry with Organic Molecules. *ACS Photonics* (2017).

48. Eizner, E. *et al.* Organic Photodiodes with an Extended Responsivity Using Ultrastrong Light–Matter Coupling. *ACS Photonics* **5,** 2921–2927 (2018).

49. Martínez-Martínez, L. A. *et al.* Polariton-Assisted Singlet Fission in Acene Aggregates. *The Journal of Physical Chemistry Letters* **9,** 1951–1957 (2018).

50. Stranius, K., Hertzog, M. & Börjesson, K. Selective manipulation of electronically excited states through strong light–matter interactions. *Nature Communications* **9,** 2273 (2018).

51. Polak, D. *et al.* Manipulating matter with strong coupling: harvesting triplet excitons in organic exciton microcavities. *arXiv:1806.09990* (2018).

52. Mazzeo, M. *et al.* Ultrastrong light-matter coupling in electrically doped microcavity organic light emitting diodes. *Applied Physics Letters* **104,** 233303 (2014).

53. Held, M. *et al.* Ultrastrong Coupling of Electrically Pumped Near-Infrared Exciton-Polaritons in High Mobility Polymers. *Advanced Optical Materials* **6,** 1700962 (2018).

54. Imamoğlu, A., Ram, R., Pau, S. & Yamamoto, Y. Nonequilibrium condensates and lasers without inversion: Exciton-polariton lasers. *Physical Review A* **53,** 4250–4253 (1996).

55. Christogiannis, N. *et al.* Characterizing the Electroluminescence Emission from a Strongly Coupled Organic Semiconductor Microcavity LED. *Advanced Optical Materials* **1,** 503–509 (2013).

56. Genco, A. *et al.* Bright Polariton Coumarin-Based OLEDs Operating in the Ultrastrong Coupling Regime. *Advanced Optical Materials,* 1800364 (2018).

57. Tischler, J. *et al.* Strong Coupling in a Microcavity LED. *Physical Review Letters* **95,** 036401 (2005).

58. Lodden, G. H. & Holmes, R. J. Electrical excitation of microcavity polaritons by radiative pumping from a weakly coupled organic semiconductor. *Physical Review B* **82,** 125317 (2010).

59. Paschos, G. G. *et al.* Hybrid organic-inorganic polariton laser. *Scientific Reports* **7,** 11377 (2017).

60. Plumhof, J. D. *et al.* Room-temperature Bose–Einstein condensation of cavity exciton–polaritons in a polymer. *Nature Materials* **13,** 247–252 (2013).

61. Daskalakis, K. S., Maier, S. A., Murray, R. & Kéna-Cohen, S. Nonlinear interactions in an organic polariton condensate. *Nature Materials* **13,** 271–278 (2014).

62. Dietrich, C. P. *et al.* An exciton-polariton laser based on biologically produced fluorescent protein. *Science Advances* **2,** e1600666 (2016).

63. Cookson, T. *et al.* A Yellow Polariton Condensate in a Dye Filled Microcavity. *Advanced Optical Materials* **5,** 1700203 (2017).

64. Scafirimuto, F. *et al.* Room-Temperature Exciton-Polariton Condensation in a Tunable Zero-Dimensional Microcavity. *ACS Photonics* **5,** 85–89 (2018).

65. Gao, W., Li, X., Bamba, M. & Kono, J. Continuous transition between weak and ultrastrong coupling through exceptional points in carbon nanotube microcavity exciton–polaritons. *Nature Photonics* **12,** 362–367 (2018).

66. Barachati, F. *et al.* Tunable Third-Harmonic Generation from Polaritons in the Ultrastrong Coupling Regime. *ACS Photonics* **5,** 119–125 (2018).

67. Coles, D. M. *et al.* Strong Exciton–Photon Coupling in a Nanographene Filled Microcavity. *Nano Letters* **17,** 5521–5525 (2017).

68. Oulton, R. F. *et al.* Strong coupling in organic semiconductor microcavities. *Semiconductor Science and Technology* **18,** S419–S427 (2003).

69. Faure, S. *et al.* Comparison of strong coupling regimes in bulk GaAs, GaN, and ZnO semiconductor microcavities. *Physical Review B* **78,** 235323 (2008).

70. Skolnick, M. S., Fisher, T. A. & Whittaker, D. M. Strong coupling phenomena in quantum microcavity structures. *Semiconductor Science and Technology* **13,** 645–669 (1998).

71. Schouwink, P., Berlepsch, H., Dähne, L. & Mahrt, R. Dependence of Rabi-splitting on the spatial position of the optically active layer in organic microcavities in the strong coupling regime. *Chemical Physics* **285,** 113–120 (2002).

72. Hobson, P. A. *et al.* Strong exciton–photon coupling in a low-Q all-metal mirror microcavity. *Applied Physics Letters* **81,** 3519–3521 (2002).

73. Tropf, L. *et al.* Influence of optical material properties on strong coupling in organic semiconductor based microcavities. *Applied Physics Letters* **110,** 153302 (2017).

74. Tropf, L. & Gather, M. C. Investigating the Onset of the Strong Coupling Regime by Fine-Tuning the Rabi Splitting in Multilayer Organic Microcavities. *Advanced Optical Materials,* 1800203 (2018).

75. Köhler, A. & Bässler, H. *Electronic Processes in Organic Semiconductors: An Introduction* (Wiley-VCH Verlag GmbH & Co. KGaA, Weinheim, Germany, 2015).

76. Demtröder, W. *Atoms, molecules and photons: an introduction to atomic-, molecular- and quantum-physics* 2. ed (Springer, Heidelberg, 2010).

77. Riedel, E. *Anorganische Chemie* 4. Aufl (de Gruyter, Berlin, 1999).

78. Bässler, H. Charge Transport in Disordered Organic Photoconductors a Monte Carlo Simulation Study. *physica status solidi (b)* **175,** 15–56 (1993).

79. Atkins, P. W. & Ludwig, R. *Kurzlehrbuch Physikalische Chemie* 3. Aufl., 2. Nachdr. 859 pp. (Wiley-VCH, Weinheim, 2007).

80. Barford, W. *Electronic and optical properties of conjugated polymers* (Clarendon Press, Oxford, 2005).

81. Würthner, F., Kaiser, T. E. & Saha-Möller, C. R. J-Aggregates: From Serendipitous Discovery to Supramolecular Engineering of Functional Dye Materials. *Angewandte Chemie International Edition* **50,** 3376–3410 (2011).

82. Bricks, J. L., Slominskii, Y. L., Panas, I. D. & Demchenko, A. P. Fluorescent J-aggregates of cyanine dyes: basic research and applications review. *Methods and Applications in Fluorescence* **6,** 012001 (2017).

83. Murawski, C., Leo, K. & Gather, M. C. Efficiency Roll-Off in Organic Light-Emitting Diodes. *Advanced Materials* **25,** 6801–6827 (2013).

84. Swenberg, C., Geacintov, N. & Pope, M. Bimolecular quenching of excitons and fluorescence in the photosynthetic unit. *Biophysical Journal* **16,** 1447–1452 (1976).

85. Hecht, E. *Optics* 4th ed (Addison-Wesley, Reading, Mass, 2002).

86. Kavokin, A. V., Baumberg, J. J., Malpeuch, G. & Laussy, F. P. *Microcavities Series on semiconductor science and technology* **no. 16** (Oxford University Press, Oxford ; New York, 2007).

87. Kavokin, A. Exciton-polaritons in microcavities: Recent discoveries and perspectives. *physica status solidi (b)* **247,** 1898–1906 (2010).

88. Deng, H., Haug, H. & Yamamoto, Y. Exciton-polariton Bose-Einstein condensation. *Reviews of Modern Physics* **82,** 1489–1537 (2010).

89. Sanvitto, D. & Kéna-Cohen, S. The road towards polaritonic devices. *Nature Materials* **15,** 1061–1073 (2016).

90. Savona, V., Andreani, L., Schwendimann, P. & Quattropani, A. Quantum well excitons in semiconductor microcavities: Unified treatment of weak and strong coupling regimes. *Solid State Communications* **93,** 733–739 (1995).

91. Lalanne, P. & Hugonin, J. Bloch-wave engineering for high-Q, small-V microcavities. *IEEE Journal of Quantum Electronics* **39,** 1430–1438 (2003).

92. Panzarini, G. *et al.* Exciton-light coupling in single and coupled semiconductor microcavities: Polariton dispersion and polarization splitting. *Physical Review B* **59,** 5082–5089 (1999).

93. Sun, Y. *et al.* Bose-Einstein Condensation of Long-Lifetime Polaritons in Thermal Equilibrium. *Physical Review Letters* **118,** 016602 (2017).

94. Kleppner, D. Inhibited Spontaneous Emission. *Physical Review Letters* **47,** 233–236 (1981).

95. Bayer, M. *et al.* Inhibition and Enhancement of the Spontaneous Emission of Quantum Dots in Structured Microresonators. *Physical Review Letters* **86,** 3168–3171 (2001).

96. Dirac, P. A. M. The Quantum Theory of the Emission and Absorption of Radiation. *Proceedings of the Royal Society A: Mathematical, Physical and Engineering Sciences* **114,** 243–265 (1927).

97. Klingshirn, C. F. *Semiconductor Optics* (Springer Berlin Heidelberg, Berlin, Heidelberg, 2012).

98. Purcell, E. M., Torrey, H. C. & Pound, R. V. Resonance Absorption by Nuclear Magnetic Moments in a Solid. *Physical Review* **69,** 37–38 (1946).

99. Einstein, A. Zur Quantentheorie der Strahlung. *Physikalische Zeitschrift* **18,** 121–128 (1917).

100. Siegman, A. E. *Lasers* (University Science Books, Mill Valley, California, 1986).

101. Hopfield, J. J. Theory of the Contribution of Excitons to the Complex Dielectric Constant of Crystals. *Physical Review* **112,** 1555–1567 (1958).

102. Pau, S. *et al.* Microcavity exciton-polariton splitting in the linear regime. *Physical Review B* **51,** 14437–14447 (1995).

103. Ciuti, C., Bastard, G. & Carusotto, I. Quantum vacuum properties of the intersubband cavity polariton field. *Physical Review B* **72,** 115303 (2005).

104. Shore, B. W. & Knight, P. L. The Jaynes-Cummings Model. *Journal of Modern Optics* **40,** 1195–1238 (1993).

105. Milonni, P. W., Ackerhalt, J. R. & Galbraith, H. W. Chaos in the Semiclassical N-Atom Jaynes-Cummings Model: Failure of the Rotating-Wave Approximation. *Physical Review Letters,* 966–969 (1983).

106. Houdré, R., Stanley, R. P. & Ilegems, M. Vacuum-field Rabi splitting in the presence of inhomogeneous broadening: Resolution of a homogeneous linewidth in an inhomogeneously broadened system. *Physical Review A* **53,** 2711–2715 (1996).

107. Lidzey, D. G. *et al.* Photon-Mediated Hybridization of Frenkel Excitons in Organic Semiconductor Microcavities. *Science* **288,** 1620–1623 (2000).

108. Ćwik, J. A., Rehur, S., Littlewood, P. B. & Keeling, J. M. J. Polariton condensation with saturable molecules dressed by vibrational modes. *Europhysics Letters* **105,** 47009 (2014).

109. Michetti, P., Mazza, L. & La Rocca, G. C. *Organic Nanophotonics* (ed Zhao, Y. S.) 39–68 (Springer Berlin Heidelberg, Berlin, Heidelberg, 2015).

110. Keeling, J., Marchetti, F. M., Szymańska, M. H. & Littlewood, P. B. Collective coherence in planar semiconductor microcavities. *Semiconductor Science and Technology* **22,** R1–R26 (2007).

111. Zhu, Y. *et al.* Vacuum Rabi splitting as a feature of linear-dispersion theory: Analysis and experimental observations. *Physical Review Letters* **64,** 2499–2502 (1990).

112. Agranovich, V., Litinskaia, M. & Lidzey, D. Cavity polaritons in microcavities containing disordered organic semiconductors. *Physical Review B* **67,** 085311 (2003).

113. Ell, C. *et al.* Influence of Structural Disorder and Light Coupling on the Excitonic Response of Semiconductor Microcavities. *Physical Review Letters* **80,** 4795–4798 (1998).

114. Houdré, R. Early stages of continuous wave experiments on cavity-polaritons. *physica status solidi (b)* **242,** 2167–2196 (2005).

115. Bradley, M. S., Tischler, J. R., Shirasaki, Y. & Bulović, V. Predicting the linear optical response of J -aggregate microcavity exciton-polariton devices. *Physical Review B* **78,** 193305 (2008).

116. Houdré, R., Stanley, R. P., Oesterle, U. & Weisbuch, C. Strong coupling regime in semiconductor microcavities. *Comptes Rendus Physique* **3,** 15–27 (2002).

117. Holmes, R. & Forrest, S. Strong exciton–photon coupling in organic materials. *Organic Electronics* **8,** 77–93 (2007).

118. Rabi, I. I. Space Quantization in a Gyrating Magnetic Field. *Physical Review* **51,** 652–654 (1937).

119. Houdré, R. *et al.* Room-temperature cavity polaritons in a semiconductor microcavity. *Physical Review B* **49,** 16761–16764 (1994).

120. Michetti, P. & La Rocca, G. C. Polariton states in disordered organic microcavities. *Physical Review B* **71,** 115320 (2005).

121. Savona, V. & Weisbuch, C. Theory of time-resolved light emission from polaritons in a semiconductor microcavity under resonant excitation. *Physical Review B* **54,** 10835–10840 (1996).

122. Fabre, C. *Confined Photon Systems* (eds Benisty, H. *et al.*) 1–37 (Springer Berlin Heidelberg, 1999).

123. Khitrova, G. *et al.* Vacuum Rabi splitting in semiconductors. *Nature Physics* **2,** 81–90 (2006).

124. Ćwik, J. A., Kirton, P., De Liberato, S. & Keeling, J. Excitonic spectral features in strongly coupled organic polaritons. *Physical Review A* **93,** 033840 (2016).

125. Houdré, R. *et al.* Measurement of Cavity-Polariton Dispersion Curve from Angle-Resolved Photoluminescence Experiments. *Physical Review Letters* **73,** 2043–2046 (1994).

126. Bracewell, R. N. *The Fourier transform and its applications* 3. ed., internat. ed (McGraw Hill, Boston, Mass., 2000).

127. Norris, T. B. *et al.* Time-resolved vacuum Rabi oscillations in a semiconductor quantum microcavity. *Physical Review B* **50,** 14663–14666 (1994).

128. Rajendran, S. K. *et al.* Direct evidence of Rabi oscillations and antiresonance in a strongly coupled organic microcavity. *Physical Review B* **91,** 201305 (2015).

129. Agarwal, G. S. Vacuum-field Rabi oscillations of atoms in a cavity. *Journal of the Optical Society of America B* **2,** 480 (1985).

130. Dominici, L. *et al.* Ultrafast Control and Rabi Oscillations of Polaritons. *Physical Review Letters* **113,** 226401 (2014).

131. Fisher, T. A. *et al.* Electric-field and temperature tuning of exciton-photon coupling in quantum microcavity structures. *Physical Review B* **51,** 2600–2603 (1995).

132. Flatten, L. C. *et al.* Electrically tunable organic–inorganic hybrid polaritons with monolayer WS_2. *Nature Communications* **8,** 14097 (2017).

133. Dreismann, A. *et al.* A sub-femtojoule electrical spin-switch based on optically trapped polariton condensates. *Nature Materials* **15,** 1074–1078 (2016).

134. Tignon, J. *et al.* From Fermi's Golden Rule to the Vacuum Rabi Splitting: Magnetopolaritons in a Semiconductor Optical Microcavity. *Physical Review Letters* **74,** 3967–3970 (1995).

135. Schneider, C. *et al.* An electrically pumped polariton laser. *Nature* **497,** 348–352 (2013).

136. Biswas, A. & Milovic, D. Bright and dark solitons of the generalized nonlinear Schrödinger's equation. *Communications in Nonlinear Science and Numerical Simulation* **15,** 1473–1484 (2010).

137. Anappara, A. A. *et al.* Cavity polaritons from excited-subband transitions. *Applied Physics Letters* **91,** 231118 (2007).

138. Günter, G. *et al.* Sub-cycle switch-on of ultrastrong light–matter interaction. *Nature* **458,** 178–181 (2009).

139. Schwartz, T., Hutchison, J. A., Genet, C. & Ebbesen, T. W. Reversible Switching of Ultrastrong Light-Molecule Coupling. *Physical Review Letters* **106,** 196405 (2011).

140. Kéna-Cohen, S., Maier, S. A. & Bradley, D. D. C. Ultrastrongly Coupled Exciton-Polaritons in Metal-Clad Organic Semiconductor Microcavities. *Advanced Optical Materials* **1,** 827–833 (2013).

141. Galego, J., Garcia-Vidal, F. J. & Feist, J. Cavity-Induced Modifications of Molecular Structure in the Strong-Coupling Regime. *Physical Review X* **5,** 041022 (2015).

142. Todorov, Y. *et al.* Ultrastrong Light-Matter Coupling Regime with Polariton Dots. *Physical Review Letters* **105,** 196402 (2010).

143. Kockum, A. F. *et al.* Ultrastrong coupling between light and matter. *Nature Reviews Physics* **1,** 19–40 (2019).

144. Cortese, E., Lagoudakis, P. G. & De Liberato, S. Collective Optomechanical Effects in Cavity Quantum Electrodynamics. *Physical Review Letters* **119,** 043604 (2017).

145. Keeling, J. & Kirton, P. G. Orientational alignment in cavity quantum electrodynamics. *Physical Review A* **97,** 053836 (2018).

146. Agranovich, V., Benisty, H. & Weisbuch, C. Organic and inorganic quantum wells in a microcavity: Frenkel-Wannier-Mott excitons hybridization and energy transformation. *Solid State Communications* **102,** 631–636 (1997).

147. Holmes, R. J. & Forrest, S. R. Strong Exciton-Photon Coupling and Exciton Hybridization in a Thermally Evaporated Polycrystalline Film of an Organic Small Molecule. *Physical Review Letters* **93,** 186404 (2004).

148. Holmes, R. J., Kéna-Cohen, S., Menon, V. M. & Forrest, S. R. Strong coupling and hybridization of Frenkel and Wannier-Mott excitons in an organic-inorganic optical microcavity. *Physical Review B* **74,** 235211 (2006).

149. Slootsky, M., Liu, X., Menon, V. M. & Forrest, S. R. Room Temperature Frenkel-Wannier-Mott Hybridization of Degenerate Excitons in a Strongly Coupled Microcavity. *Physical Review Letters* **112,** 076401 (2014).

150. Müller, M., Bleuse, J., André, R. & Ulmer-Tuffigo, H. Observation of bottleneck effects on the photoluminescence from polaritons in II–VI microcavities. *Physica B: Condensed Matter* **272,** 476–479 (1999).

151. Tassone, F. *et al.* Bottleneck effects in the relaxation and photoluminescence of microcavity polaritons. *Physical Review B* **56,** 7554–7563 (1997).

152. Byrnes, T., Kim, N. Y. & Yamamoto, Y. Exciton–polariton condensates. *Nature Physics* **10,** 803–813 (2014).

153. Mazza, L., Kéna-Cohen, S., Michetti, P. & La Rocca, G. C. Microscopic theory of polariton lasing via vibronically assisted scattering. *Physical Review B* **88,** 075321 (2013).

154. Virgili, T. *et al.* Ultrafast polariton relaxation dynamics in an organic semiconductor microcavity. *Physical Review B* **83,** 245309 (2011).

155. Coles, D. M. *et al.* Temperature dependence of the upper-branch polariton population in an organic semiconductor microcavity. *Physical Review B* **84,** 205214 (2011).

156. Chovan, J., Perakis, I. E., Ceccarelli, S. & Lidzey, D. G. Controlling the interactions between polaritons and molecular vibrations in strongly coupled organic semiconductor microcavities. *Physical Review B* **78,** 045320 (2008).

157. Coles, D. M. *et al.* Vibrationally Assisted Polariton-Relaxation Processes in Strongly Coupled Organic-Semiconductor Microcavities. *Advanced Functional Materials* **21,** 3691–3696 (2011).

158. Herrera, F. & Spano, F. C. Theory of Nanoscale Organic Cavities: The Essential Role of Vibration-Photon Dressed States. *ACS Photonics* **5,** 65–79 (2018).

159. Merhav, N. *Statistical Physics for Electrical Engineering* 65–73 (Springer International Publishing, Cham, 2018).

160. Pitaevskii, L. & Stringari, S. *Bose-Einstein Condensation and Superfluidity* (Oxford University Press, 2016).

161. Butov, L. V. & Kavokin, A. V. The behaviour of exciton–polaritons. *Nature Photonics. Correspondence* **6** (2012).

162. Baumberg, J. J. *et al.* Spontaneous Polarization Buildup in a Room-Temperature Polariton Laser. *Physical Review Letters* **101,** 136406 (2008).

163. Renk, K. F. *Basics of laser physics: for students of science and engineering* Second edition (Springer, Cham, 2017).

164. Bajoni, D., Senellart, P., Lemaître, A. & Bloch, J. Photon lasing in GaAs microcavity: Similarities with a polariton condensate. *Physical Review B* **76,** 201305(R) (2007).

165. Ohadi, H. *et al.* Spontaneous Symmetry Breaking in a Polariton and Photon Laser. *Physical Review Letters* **109,** 016404 (2012).

166. Conwell, E. Definition of exciton binding energy for conducting polymers. *Synthetic Metals* **83,** 101–102 (1996).

167. Takemura, N. *et al.* Dephasing effects on coherent exciton-polaritons and the breakdown of the strong coupling regime. *Physical Review B* **92,** 235305 (2015).

168. Brodbeck, S. *et al.* Experimental Verification of the Very Strong Coupling Regime in a GaAs Quantum Well Microcavity. *Physical Review Letters* **119,** 027401 (2017).

169. Kéna-Cohen, S. & Forrest, S. R. *Exciton Polaritons in Microcavities: New Frontiers* (eds Timofeev, V. & Sanvitto, D.) 349–375 (Springer Berlin Heidelberg, Berlin, Heidelberg, 2012).

170. Kawashima, T. *et al.* Optical properties of hexagonal GaN. *Journal of Applied Physics* **82,** 3528–3535 (1997).

171. Stelling, C. *et al.* Plasmonic nanomeshes: their ambivalent role as transparent electrodes in organic solar cells. *Scientific Reports* **7** (2017).

172. Hong, J. S. *et al. Exciton binding energies in wurtzite ZnO/MgZnO quantum wells 2006 IEEE Nanotechnology Materials and Devices Conference* (IEEE, Gyeongju, South Korea, 2006), 324–325.

173. Lai, Y.-Y., Lan, Y.-P. & Lu, T.-C. Strong light–matter interaction in ZnO microcavities. *Light: Science & Applications* **2,** e76–e76 (2013).

174. Borri, P. *et al.* Microcavity polariton linewidths in the weak-disorder regime. *Physical Review B* **63,** 035307 (2000).

175. Manceau, J.-M. *et al.* Immunity of intersubband polaritons to inhomogeneous broadening. *Physical Review B* **96,** 235301 (2017).

176. Armitage, A. *et al.* Modelling of asymmetric excitons in organic microcavities. *Synthetic Metals* **111-112,** 377–379 (2000).

177. Lidzey, D. G. *et al.* Experimental study of light emission from strongly coupled organic semiconductor microcavities following nonresonant laser excitation. *Physical Review B* **65,** 195312 (2002).

178. Canaguier-Durand, A. *et al.* Thermodynamics of Molecules Strongly Coupled to the Vacuum Field. *Angewandte Chemie International Edition* **52,** 10533–10536 (2013).

179. Herrera, F. & Spano, F. C. Dark Vibronic Polaritons and the Spectroscopy of Organic Microcavities. *Physical Review Letters* **118,** 223601 (2017).

180. Litinskaya, M. & Reineker, P. Loss of coherence of exciton polaritons in inhomogeneous organic microcavities. *Physical Review B* **74,** 165320.

181. Litinskaya, M. Propagation and localization of polaritons in disordered organic microcavities. *Physics Letters A* **372,** 3898–3903 (2008).

182. Agranovich, V. M., Gartstein, Y. N. & Litinskaya, M. Hybrid Resonant Organic–Inorganic Nanostructures for Optoelectronic Applications. *Chemical Reviews* **111,** 5179–5214 (2011).

183. Kimble, H. J. Strong Interactions of Single Atoms and Photons in Cavity QED. *Physica Scripta* **T76,** 127 (1998).

184. Gambino, S. *et al.* Exploring Light–Matter Interaction Phenomena under Ultrastrong Coupling Regime. *ACS Photonics* **1,** 1042–1048 (2014).

185. Savona, V. Effect of interface disorder on quantum well excitons and microcavity polaritons. *Journal of Physics: Condensed Matter* **19,** 295208 (2007).

186. Byrnes, S. J. Multilayer optical calculations. *arXiv:1603.02720* (2016).

187. Troparevsky, M. C., Sabau, A. S., Lupini, A. R. & Zhang, Z. Transfer-matrix formalism for the calculation of optical response in multilayer systems: from coherent to incoherent interference. *Optics Express* **18,** 24715 (2010).

188. Born, M. & Wolf, E. *Principles of optics: electromagnetic theory of propagation, interference, and diffraction of light* 5th ed (Pergamon Press, Oxford, New York, 1975).

189. Pettersson, L. A. A., Roman, L. S. & Inganäs, O. Modeling photocurrent action spectra of photovoltaic devices based on organic thin films. *Journal of Applied Physics* **86,** 487–496 (1999).

190. Yonkoski, R. K. & Soane, D. S. Model for spin coating in microelectronic applications. *Journal of Applied Physics* **72,** 725–740 (1992).

191. *Handbook of thin-film technology* (eds Frey, H. & Khan, H. R.) (Springer, Berlin Heidelberg, 2015).

192. *Handbook of sputter deposition technology: fundamentals and applications for functional thin films, nanomaterials and MEMS* 2nd ed (eds Wasa, K., Kanno, I. & Kotera, H.) (William Andrew, Waltham, MA, 2012).

193. Kovacik, P. *et al.* Vacuum-Deposited Planar Heterojunction Polymer Solar Cells. *ACS Applied Materials & Interfaces* **3,** 11–15 (2011).

194. *Handbook of ellipsometry* (eds Tompkins, H. G. & Irene, E. A.) (William Andrew Pub. ; Springer, Norwich, NY : Heidelberg, Germany, 2005).

195. J. A. Woollam Co., Inc. *Guide to using WVASE32*

196. Cobet, C. *Ellipsometry of Functional Organic Surfaces and Films* (eds Hinrichs, K. & Eichhorn, K.-J.) 1–26 (Springer Berlin Heidelberg, Berlin, Heidelberg, 2014).

197. Winsemius, P., Kampen, F. F. v., Lengkeek, H. P. & Went, C. G. v. Temperature dependence of the optical properties of Au, Ag and Cu. *Journal of Physics F: Metal Physics* **6,** 1583–1606 (1976).

198. Rakić, A. D. Algorithm for the determination of intrinsic optical constants of metal films: application to aluminum. *Applied Optics* **34,** 4755–4767 (1995).

199. Gong, J., Dai, R., Wang, Z. & Zhang, Z. Thickness Dispersion of Surface Plasmon of Ag Nano-thin Films: Determination by Ellipsometry Iterated with Transmittance Method. *Scientific Reports* **5,** 9279 (2015).

200. Nishimura, T. *et al.* Quantitative evaluation of light–matter interaction parameters in organic single-crystal microcavities. *Optics Letters* **43,** 1047 (2018).

201. Lerario, G. *et al.* Room-temperature superfluidity in a polariton condensate. *Nature Physics* **13,** 837–841 (2017).

202. Bajoni, D. Polariton lasers. Hybrid light–matter lasers without inversion. *Journal of Physics D: Applied Physics* **45,** 313001 (2012).

203. Finlayson, C. E., Vijaya Prakash, G. & Baumberg, J. J. Strong exciton-photon coupling in a length tunable optical microcavity with J-aggregate dye heterostructures. *Applied Physics Letters* **86,** 041110 (2005).

204. Lidzey, D. G. *et al.* Room Temperature Polariton Emission from Strongly Coupled Organic Semiconductor Microcavities. *Physical Review Letters* **82,** 3316–3319 (1999).

205. Schouwink, P., Berlepsch, H., Dähne, L. & Mahrt, R. Observation of strong exciton–photon coupling in an organic microcavity. *Chemical Physics Letters* **344,** 352–356 (2001).

206. Tartakovskii, A. I. *et al.* Raman scattering in strongly coupled organic semiconductor microcavities. *Physical Review B* **63,** 121302(R) (2001).

207. Wenus, J., Connolly, L. G. & Lidzey, D. G. New organic materials and microcavity structures for strong exciton-photon coupling. *physica status solidi (c)* **2,** 3899–3902 (2005).

208. Coles, D. M. *et al.* Temperature dependence of the upper-branch polariton population in an organic semiconductor microcavity. *Physical Review B* **84,** 205214 (2011).

209. Coles, D. M. *et al.* Polariton-mediated energy transfer between organic dyes in a strongly coupled optical microcavity. *Nature Materials* **13,** 712–719 (2014).

210. Heliotis, G. *et al.* Blue, surface-emitting, distributed feedback polyfluorene lasers. *Applied Physics Letters* **83,** 2118–2120 (2003).

211. Xia, R., Heliotis, G., Hou, Y. & Bradley, D. D. Fluorene-based conjugated polymer optical gain media. *Organic Electronics* **4,** 165–177 (2003).

212. Rose, A. *et al.* Sensitivity gains in chemosensing by lasing action in organic polymers. *Nature* **434,** 876–879 (2005).

213. Tsiminis, G. *et al.* Nanoimprinted Organic Semiconductor Laser Pumped by a Light-Emitting Diode. *Advanced Materials* **25,** 2826–2830 (2013).

214. Akcelrud, L. Electroluminescent polymers. *Progress in Polymer Science* **28,** 875–962 (2003).

215. Herbst, S. *et al.* A Columnar Liquid-Crystal Phase Formed by Hydrogen-Bonded Perylene Bisimide J-Aggregates. *Angewandte Chemie International Edition* **56,** 2162–2165 (2017).

216. Landreth, B. M. & Stupp, S. I. Dipole orientation in a liquid-crystal polymer: a study by electric field FTIR. *Macromolecules* **20,** 2083–2089 (1987).

217. Roodenko, K. *et al.* Anisotropic Optical Properties of Thin-Film Thiacarbocyanine Dye Aggregates. *The Journal of Physical Chemistry C* **117,** 20186–20192 (2013).

218. Herbst, S. *private communication* 2015.

219. Ariu, M. *et al.* The effect of morphology on the temperature-dependent photoluminescence quantum efficiency of the conjugated polymer poly(9, 9-dioctylfluorene). *Journal of Physics: Condensed Matter* **14,** 9975–9986 (2002).

220. Wang, Y. *et al.* LED pumped polymer laser sensor for explosives: LED pumped polymer laser sensor for explosives. *Laser & Photonics Reviews* **7,** L71–L76 (2013).

221. Kéna-Cohen, S. & Forrest, S. R. Giant Davydov splitting of the lower polariton branch in a polycrystalline tetracene microcavity. *Physical Review B* **77,** 073205 (2008).

222. Oda, M. *et al.* Strong exciton-photon coupling and its polarization dependence in a metal-mirror microcavity with oriented PIC J-aggregates. *physica status solidi (c)* **6,** 288–291 (2009).

223. Armitage, A. *et al.* Polariton-induced optical asymmetry in semiconductor microcavities. *Physical Review B* **58,** 15367–15370 (1998).

224. Tredicucci, A. *et al.* Controlled Exciton-Photon Interaction in Semiconductor Bulk Microcavities. *Physical Review Letters* **75,** 3906–3909 (1995).

225. Kawamura, Y. *et al.* Intermolecular Interaction and a Concentration-Quenching Mechanism of Phosphorescent Ir(III) Complexes in a Solid Film. *Physical Review Letters* **96,** 017404 (2006).

226. Chen, C. H. & Tang, C. W. Efficient green organic light-emitting diodes with stericly hindered coumarin dopants. *Applied Physics Letters* **79,** 3711–3713 (2001).

227. Duarte, F. J., Liao, L. S., Vaeth, K. M. & Miller, A. M. Widely tunable green laser emission using the coumarin 545 tetramethyl dye as the gain medium. *Journal of Optics A: Pure and Applied Optics* **8,** 172–174 (2006).

228. Pu, Y.-J. *et al.* Optimizing the Charge Balance of Fluorescent Organic Light-Emitting Devices to Achieve High External Quantum Efficiency Beyond the Conventional Upper Limit. *Advanced Materials* **24,** 1765–1770 (2012).

229. Lakowicz, J. R. *Principles of fluorescence spectroscopy* 3rd ed. 954 pp. (Springer, New York, 2006).

230. Williams, R. T. & Bridges, J. W. Fluorescence of solutions: A review. *Journal of Clinical Pathology* **17,** 371–394 (1964).

231. Feng, S.-W., Shih, M.-C., Huang, C. & Chung, C.-T. Impacts of dopant concentration on the carrier transport and recombination dynamics in organic light emitting diodes. *Thin Solid Films* **517,** 2719–2723 (2009).

232. Rhee, S. H. *et al.* Heavily Doped, Charge-Balanced Fluorescent Organic Light-Emitting Diodes from Direct Charge Trapping of Dopants in Emission Layer. *ACS Applied Materials & Interfaces* **7,** 16750–16759 (2015).

233. Liu, Z., Helander, M. G., Wang, Z. & Lu, Z. Efficient Single-Layer Organic Light-Emitting Diodes Based on C545T-Alq $_3$ System. *The Journal of Physical Chemistry C* **114,** 11931–11935 (2010).

234. Avis, P. & Porter, G. Effect of concentration on the absorption and fluorescence spectra of pyrene in a solid solution of poly(methyl methacrylate). *Journal of the Chemical Society, Faraday Transactions 2* **70,** 1057 (1974).

235. Coles, D. M. *et al.* Polariton-mediated energy transfer between organic dyes in a strongly coupled optical microcavity. *Nature Materials* **13,** 712–719 (2014).

236. Chaneliere, C., Autran, J., Devine, R. & Balland, B. Tantalum pentoxide (Ta2O5) thin films for advanced dielectric applications. *Materials Science and Engineering: R: Reports* **22,** 269–322 (1998).

237. Nishio, R., Tuchida, K., Tooma, M. & Suzuki, K. Origins of charged particles in vapor generated by electron-beam evaporation. *Journal of Applied Physics* **72,** 4548–4555 (1992).

238. Brenner, P. *et al.* Degradation mechanisms of polyfluorene-based organic semiconductor lasers under ambient and oxygen-free conditions. *Journal of Polymer Science Part B: Polymer Physics* **53,** 1029–1034 (2015).

239. Scholz, S., Kondakov, D., Lüssem, B. & Leo, K. Degradation Mechanisms and Reactions in Organic Light-Emitting Devices. *Chemical Reviews* **115,** 8449–8503 (2015).

240. Anni, M. *et al.* Organic μ cavities based on thermally evaporated TeOx-LiF distributed Bragg reflectors. *Applied Physics Letters* **79,** 1381–1383 (2001).

241. Song, J.-H. *et al.* Exciton-polariton dynamics in a transparent organic semiconductor microcavity. *Physical Review B* **69,** 235330 (2004).

242. Suzuki, H. & Hikita, M. Organic light-emitting diodes with radio frequency sputter-deposited electron injecting electrodes. *Applied Physics Letters* **68,** 2276–2278 (1996).

243. Schaer, M. *et al.* Water Vapor and Oxygen Degradation Mechanisms in Organic Light Emitting Diodes. *Advanced Functional Materials* **11,** 116–121 (2001).

244. Samuel, I. D. W. & Turnbull, G. A. Organic Semiconductor Lasers. *Chemical Reviews* **107,** 1272–1295 (2007).

245. Chung, C.-H. *et al.* Improvement in performance of transparent organic light-emitting diodes with increasing sputtering power in the deposition of indium tin oxide cathode. *Applied Physics Letters* **86,** 093504 (2005).

246. Lei, H. *et al.* Low Damage Sputter Deposition of ITO Films on Organic Light Emitting Films. *Transactions of the Materials Research Society of Japan* **34,** 321–324 (2009).

247. Greene, J. E. Review Article: Tracing the recorded history of thin-film sputter deposition: From the 1800s to 2017. *Journal of Vacuum Science & Technology A: Vacuum, Surfaces, and Films* **35,** 05C204 (2017).

248. Zanotto, S. *et al.* Perfect energy-feeding into strongly coupled systems and interferometric control of polariton absorption. *Nature Physics* **10,** 830–834 (2014).

249. Kuehne, A. J. C. & Gather, M. C. Organic Lasers: Recent Developments on Materials, Device Geometries, and Fabrication Techniques. *Chemical Reviews* **116,** 12823–12864 (2016).

250. Akselrod, G. M. *et al.* Exciton-exciton annihilation in organic polariton microcavities. *Physical Review B* **82** (2010).

251. Schütte, B. *et al.* Continuously tunable laser emission from a wedge-shaped organic microcavity. *Applied Physics Letters* **92,** 163309 (2008).

252. Nakanotani, H., Furukawa, T. & Adachi, C. Light Amplification in an Organic Solid-State Film with the Aid of Triplet-to-Singlet Upconversion. *Advanced Optical Materials* **3,** 1381–1388 (2015).

253. Samuel, I. D. W., Namdas, E. B. & Turnbull, G. A. How to recognize lasing. *Nature Photonics* **3,** 546–549 (2009).

254. Schwartz, T. *et al.* Polariton Dynamics under Strong Light-Molecule Coupling. *ChemPhysChem* **14,** 125–131 (2013).

255. Herrera, F. & Spano, F. C. Theory of Nanoscale Organic Cavities: The Essential Role of Vibration-Photon Dressed States. *ACS Photonics* **5,** 65–79 (2018).

256. Herrera, F. & Spano, F. C. Absorption and photoluminescence in organic cavity QED. *Physical Review A* **95,** 053867 (2017).